

**Meteorological applications
of a
surface network of
Global Positioning System
receivers**

Siebrén de Haan

Promotor : Prof. dr. A. A. M. Holtslag,
Hoogleraar in de Meteorologie, Wageningen Universiteit

Copromotoren : Dr. ir. H. van der Marel,
Universitair docent, Technische Universiteit Delft

Dr. I. Holleman,
Senior onderzoeker, KNMI, De Bilt

Promotiecommissie : Prof. ir. B. A. C. Ambrosius, Technische Universiteit Delft
Dr. A. J. van Delden, Universiteit Utrecht
Prof. dr. C. Mätzler, Universiteit Bern, Zwitserland
Prof. dr. ir. R. Uijlenhoet, Wageningen Universiteit

Meteorological applications of a surface network of Global Positioning System receivers

Meteorologische toepassingen van een grondnetwerk van Global Positioning System ontvangers

Proefschrift

ter verkrijging van de graad doctor
op gezag van de rector magnificus
van Wageningen Universiteit,
Prof. dr. M. J. Kropff,
in het openbaar te verdedigen
op dinsdag 27 mei 2008
des namiddags te vier uur in de Aula.

ISBN : 978-90-8504-881-7

Contents

| | |
|--|-----------|
| Voorwoord | v |
| Abstract | ix |
| 1 Introduction | 1 |
| 1.1 Atmospheric water vapour | 1 |
| 1.2 The Global Positioning System | 4 |
| 1.3 GPS Meteorology | 9 |
| 1.4 Meteorological Applications | 11 |
| 1.5 Outline | 12 |
| 2 Background | 13 |
| 2.1 Water vapour observations | 13 |
| 2.1.1 Radiosonde | 13 |
| 2.1.2 GPS surface networks | 14 |
| 2.1.3 Other water vapour observations | 15 |
| 2.2 Temporal variations and correlations of water vapour | 16 |
| 2.3 Signal delay from atmospheric models | 20 |
| 2.3.1 Zenith algorithm | 22 |
| 2.3.2 Slant algorithm | 23 |
| 2.4 Data quality and validation | 26 |
| 2.4.1 ZTD comparison | 27 |
| 2.4.2 IWV comparison | 29 |
| 2.5 Summary | 31 |
| 3 The influence on GPS estimates of NWP derived mapping functions | 33 |
| 3.1 Introduction | 33 |
| 3.2 Mapping functions | 34 |
| 3.2.1 Niell mapping function | 34 |
| 3.2.2 Mapping functions derived from NWP | 35 |
| 3.2.3 Mapping functions derived from radiosondes | 36 |
| 3.3 Influence of mapping functions on GPS parameters | 36 |
| 3.4 Case study | 38 |
| 3.4.1 Niell and NWP mapping functions difference | 39 |

| | | |
|----------|---|-----------|
| 3.4.2 | Niell and radiosonde mapping functions difference | 40 |
| 3.4.3 | Influence on GPS parameters | 41 |
| 3.5 | Conclusions | 43 |
| 4 | Synergetic use of GPS water vapour and Meteosat images for synoptic weather forecasting | 45 |
| 4.1 | Introduction | 45 |
| 4.2 | Cold front passage | 47 |
| 4.3 | Discussion | 49 |
| 4.4 | Conclusion | 52 |
| 5 | Measuring atmospheric stability with GPS | 53 |
| 5.1 | Introduction | 53 |
| 5.2 | Data | 55 |
| 5.3 | Methodology | 58 |
| 5.4 | Results | 61 |
| 5.5 | Conclusions | 65 |
| 6 | Real-time water vapour maps from a GPS surface network and the application for nowcasting of thunderstorms | 67 |
| 6.1 | Introduction | 67 |
| 6.2 | Observations and infrastructure | 68 |
| 6.2.1 | Radiosonde | 69 |
| 6.2.2 | Weather radar | 70 |
| 6.2.3 | Lightning detection network | 70 |
| 6.2.4 | Numerical weather model data | 71 |
| 6.2.5 | Timeseries analysis | 72 |
| 6.3 | Integrated water vapour field analysis | 72 |
| 6.4 | Integrated water vapour field validation | 74 |
| 6.5 | Nowcasting cases | 78 |
| 6.5.1 | A severe thunderstorm on 8 June 2007 | 78 |
| 6.5.2 | Two thunderstorm events on 20 July 2007 | 80 |
| 6.6 | Conclusions | 80 |
| 7 | Comparison of GPS slant delay measurements to a numerical Model: case study of a cold front passage | 83 |
| 7.1 | Introduction | 83 |
| 7.2 | Computation of slant delays from GPS | 84 |
| 7.3 | Derivation of slant delays from NWP | 86 |
| 7.4 | Non-stratified slant wet delay comparison | 87 |
| 7.5 | Conclusions | 91 |

| | |
|--|------------|
| 8 Observing three-dimensional water vapour using a surface network of GPS receivers | 93 |
| 8.1 Introduction | 94 |
| 8.2 Water vapour observations from GPS | 95 |
| 8.3 Variational analysis method | 98 |
| 8.3.1 Background error covariances | 99 |
| 8.3.2 Slant observation error covariances | 101 |
| 8.3.3 Systematic observation error correlations | 102 |
| 8.4 Variational analysis experiments | 103 |
| 8.4.1 Observation simulation system experiment | 104 |
| 8.4.2 Realistic experiments | 106 |
| 8.5 Conclusions | 113 |
| 9 Summary, outlook and recommendations | 115 |
| 9.1 Conclusions | 115 |
| 9.2 Outlook | 117 |
| 9.3 Recommendations | 120 |
| References | 122 |
| Samenvatting | 131 |
| A Constants and definitions | 135 |
| A.1 Constants | 135 |
| A.2 Saturated water vapour pressure | 135 |
| B Acronyms | 137 |
| List of Publications | 138 |
| Curriculum Vitae | 141 |
| Acknowledgement | 143 |

“Now the sun, moving as it does, sets up processes of change and becoming and decay, and by its agency the finest and sweetest water is every day carried up and is dissolved into vapour and rises to the upper region, where it is condensed again by the cold and so returns to the earth. This, as we have said before, is the regular course of nature.”

Aristotle (Physics, Book II)

Voorwoord

Dit proefschrift is het resultaat van een aantal jaar onderzoek aan meteorologische toepassingen van het “Global Positioning System” (kortweg GPS). Mijn allereerste kennismaking met GPS-meteorologie was ongeveer negen jaar geleden, eind september 1999 in Brussel waar één van de eerste vergaderingen van de COST716-werkgroep werd gehouden. Ik kon toen nog niet vermoeden dat dit eigenlijk het begin was van mijn proefschrift.

Onder leiding van Sylvia Barlag heb ik me tijdens het COST716-project gericht op de toepassing van GPS voor de kortetermijnweersverwachting. Hier lag een vrij simpele reden aan ten grondslag: het numerieke weermodel dat indertijd op het KNMI draaide kon de GPS-informatie nog niet gebruiken tijdens de initialisatie. Onze pragmatische insteek was in de trant van “zonde om er niets mee te doen”, want de atmosferische gegevens uit GPS kwamen geleidelijk aan steeds meer beschikbaar. Sylvia, dankzij jouw inzichten, enthousiasme, (subtiele) sturing en discussies ben ik me met veel plezier in GPS-meteorologie gaan vastbijten. Ontzettend bedankt voor de ruimte die je me geboden hebt!

Het COST716-project bracht de geodetische en meteorologische werelden bij elkaar. Tijdens dit project kreeg ik steeds meer vat op hoe het schatten van atmosfeer-parameters met GPS nu precies werkt. Vooral de nauwe en vruchtbare samenwerking met Hans van der Marel van de TU Delft heeft daar aan bijgedragen. Hans, ik ben je dan ook ontzettend veel dank verschuldigd voor de antwoorden op mijn vragen, het samen schrijven van artikelen en projectvoorstellen en de fantastische zeiltochten op “de Rust”.

In 2002 kon ik eindelijk een groot deel van mijn tijd aan GPS-meteorologie gaan besteden, met subsidie van SRON. Het NIVR heeft in 2005 een project gefinancierd om de GPS-waarnemingen uit het bestaande netwerk van GPS-stations in Nederland te berekenen. Beide projecten waren in samenwerking met Hans van der Marel. Tegelijkertijd was het Kadaster, in samenwerking met Rijkswaterstaat, begonnen met het opzetten van landelijk dekkend GPS-referentienetwerk voor landmeetkundige toepassingen. Op een drietal afgelegen KNMI-waarneemstations zijn in dit kader GPS-antennes geplaatst en dankzij deze samenwerking wordt de totale waterdamp van 35 locaties in Nederland in “real-time” berekend. Dit mooie resultaat was niet mogelijk geweest zonder de inzet van o.a. Joop van Buren van het Kadaster, Ronald van de Vate en de mensen van Infra-WIS.

In de afgelopen twee jaar werden de plannen voor dit proefschrift steeds concreter. Het eerste contact dat Sylvia met Bert Holtslag had gelegd was meteen positief. Na het vertrek van Sylvia heeft Iwan Holleman het stokje van haar overgenomen wat (op de valreep) tot ons eerste gemeenschappelijk artikel heeft geleid. Iwan, bedankt voor het regelmatig uitwisselen van ideeën, het lezen van mijn manuscripten en het begeleiden van dit proefschrift. De suggestie van jou om, een week voordat het concept naar de leescommissie moest, de figuur van de “brekings-hoek” te verfraaien met een soortgelijke berekening voor de weerradar, is tekenend voor je flexibele manier van denken. (Gelukkig was het consistent met mijn berekeningen). Het afgelopen jaar hebben Hans, Iwan en Bert heel wat versies van dit proefschrift door geworsteld; geen sinecure, bedankt! De rust van Bert, zijn enthousiasme en de bemoedigende woorden tijdens ons overleg over dit proefschrift heeft een positief gevoel over het hele proces bij mij achtergelaten. Ik ben Gerrit Burgers dankbaar voor het vrijhouden van mijn tijd om het proefschrift af te ronden.

Door de jaren heen hebben we twee afdelingen verslonden (SD en RW). De naam veranderde maar aan de groepsgeest viel niet te tornen. Ik wil dan ook alle collega’s van deze afdelingen bedanken voor de gezelligheid op het werk en de uitjes. In het bijzonder Hans Roozkrans (mijn eerste projectleider en zeer kunstig schipper), Paul de Valk (dank voor het doorlezen van een deel van het proefschrift en je presentatie op onze bruiloft: we hebben het er nog over!), Frits Koek (de koffie, mp3’s en anekdotes). Frans Debie voor je avonturen tijdens congressen en de discussies wat jij nou eigenlijk met GPS-waterdamp moet. De HIRLAM’rs Sander Tijm, Toon Moene, Ben Wichers en Gerard Cats hebben me heel goed geholpen met het gebruik van de modeldata. De zeilers van het KNMI (het zijn er nogal wat) wil ik graag bedanken voor het meedoen aan de jaarlijkse KNMI-zeilwedstrijd; Anton en Gerard voor het fokken. Het is altijd leuk om “bakboord” te roepen; iets minder om het te horen. De ondersteuning (en gezelligheid) van Jacqueline en Sylvia V. is bijzonder gewaardeerd. Rob, Joeri, Leo en Olaf, dank voor de computerondersteuning. Het was (en is) elke keer een feest om de atoombunker in te gaan om te repeteren, dankzij (in alfabetische volgorde): Andre, Angèle, Bert de V., Erwin, Folkert, Gijs, Hans V., Homme, Joop, Lucas, Marian, Martin, Nico, Piet, Rene, Renske, Ria en Sylvia V. In de grootte van de groep (zeg maar een big band) toont zich de breedte van het genre (van “the Animals” tot “Rammstein”). Rock on! Folkert, het zendelingenwerk met betrekking tot Metallica heeft zijn vruchten afgeworpen, kill! Zeer goede herinneringen heb ik aan de bandjes waar Gijs me de laatste jaren mee naar toe heeft genomen!

Het was voor jullie een verrassing, Folkert en Gert-Jan; maar ook ik ben vereerd dat jullie mijn paranifmen willen zijn. Gert-Jan, bedankt voor het vinden van een aantal schrijffouten (nu de laatste nog).

Mijn schaatsvrienden uit Groningen hebben in de jaren een speciaal plaatsje gekregen. De schaatstochten, toen er nog ijs lag, waren allemaal fantastisch. De (fiets)weekendjes zijn altijd weer een feest van herkenning. Het kamperen onder primitieve omstandigheden op Lowlands werd verzacht door de aanwezigheid van Frederik en Karien. Gea en Twan, we hebben genoten

van onze zeilvakanties (wanneer gaan we weer?). Peer, mijn medeschipper van de “Reidsjonger”; het was elke keer schrikken als bleek dat er een reparatie onder de waterlijn nodig was. Maar ja, hout leeft nou eenmaal; dat maakt het extra mooi! En, er gaat niets boven samen klussen.

Tot slot de roots. Het is prettig dat mijn schoonfamilie me geaccepteerd heeft (ondanks dat ik Fries bloed heb). Vaders en moeders bedankt voor de altijd warme ontvangst! Ma, dankzij de fijne en liefdevolle opvoeding met de vrijheid die jij en pa me gaven, heb ik me kunnen ontwikkelen tot wat ik ben. Van je grote broer winnen met tafeltennis is natuurlijk altijd leuk (alleen verlies je dan ook wel eens); nu geeft samen op (flinterdun) ijs staan een zelfde gevoel. Zus (en Peter), de tijd dat we in Groningen bijna burens waren was geweldig en hebben me verder gevormd (nature/nurture). Als laatste Edith; je West-Friesche nuchterheid gebruik ik vaak om te nuanceren. Bedankt voor al je liefde, vertrouwen en steun en Iris.

Abstract

This thesis presents meteorological applications of water vapour observations from a surface network of Global Positioning System (GPS) receivers. GPS signals are delayed by the atmosphere due to atmospheric refraction and bending. Mapped to the zenith, this delay is called Zenith Total Delay (ZTD). The ZTD can be separated in a hydrostatic and a wet delay. The first can be approximated by the surface pressure, while the second is related to Integrated Water Vapour (IWV); this relation depends on the surface temperature. Currently, radiosondes are the only operational source of upper air humidity observations, however these observations are sparse in space and time. GPS IWV can fill this gap, albeit that the observable is an integral quantity. A study of the correlation of radiosonde observations and IWV shows that the change over time of IWV is closely related to the change in specific humidity at 2 km. The quality of the GPS IWV, assessed by comparison with numerical weather prediction (NWP) model and radiosonde observations, shows accuracies of 14 mm in ZTD and 2 kg m^{-2} in IWV.

In the processing of GPS signals it is assumed that the atmosphere through which the signals propagate is symmetric and close to climatology. A consequence of this assumption is that when a strong water vapour gradient is present at a GPS site, systematic errors of around -3 mm in ZTD are observed (which corresponds to approximately -0.5 kg m^{-2} in IWV).

Geostationary satellites can observe upper tropospheric water vapour in cloud free areas. Timeseries analysis of the change in GPS IWV and change in upper tropospheric water vapour gives a rough estimate of the change in vertical water vapour distribution. A spectral analysis of timeseries of the residual signal of GPS zenith delay estimates shows that there is a relation between the power of the residual signal and Convective Available Potential Energy (CAPE) from radiosonde. A correlation of 0.6 is observed which is remarkable because the power of the residual is based on a timeseries of one hour of GPS residuals while CAPE is derived from atmospheric profile information.

Real-time GPS IWV maps are constructed using a two-dimensional variational technique. These maps are validated against NWP analyses and forecast fields. The statistics show that the IWV maps are of good quality. Two thunderstorm cases show the applicability of these maps for nowcasting.

A comparison study shows that slant delay estimates from GPS contain information with a three-dimensional character. This three-dimensional character is exploited further by assimilating slant delay observations using a three-dimensional variational (3DVAR) scheme. The used GPS network had a horizontal resolution of approximately 100 km, which impaired the resolution of the analysed water vapour field. Nevertheless, when compared to independent radiosonde observations, the bias of 3DVAR GPS was smaller than the NWP six hour forecasts.

Chapter 1

Introduction

In the last decade, the influence of the Global Positioning System (GPS) on our daily life has increased; for instance car navigation and clock synchronisation both rely on GPS signals. Weather is also playing a role in navigation with GPS. The atmosphere influences the GPS signal and induces inaccuracies of the order of several metres in positioning: weather is a nuisance for navigation. This “atmospheric noise”, on the other hand, is an information source for atmospheric science and meteorology.

This thesis exemplifies meteorological applications of water vapour observations from a surface network of Global Positioning System receivers. This topic requires an introduction on both “GPS” and “Weather” and its connecting relation (i.e. atmospheric water vapour). First an introduction on atmospheric water vapour is presented. Hereafter the Global Positioning System itself is introduced. The research questions for using GPS in weather applications are discussed in the last paragraph together with the outline of this thesis.

1.1 ATMOSPHERIC WATER VAPOUR

Water vapour is one of the driving forces of convection and plays obviously a crucial role in the development of clouds and precipitation. The water vapour content is highly variable due to temperature changes, micro-physical processes (such as cloud formation) and atmospheric circulation.

Generally, water vapour is invisible to the eye; only when the amount of water vapour is very large a haze can be seen for instance around the sun. Water in liquid or solid phase is easily observed: clouds, fog, raindrops, snow etc. Although the air mass fraction of water vapour is on the order of 1%, the effect on weather is strong.

There are a number of definitions to quantify the amount of water vapour in air: water vapour density, water vapour mixing ratio, specific humidity and relative humidity. There are more definitions (e.g. dew point temperature and wet-bulb temperature) but these are not discussed here. Water vapour density (or simply water vapour) is the amount of water in gas phase in grammes per cubic metre of air. The water vapour mixing ratio in a volume of air is

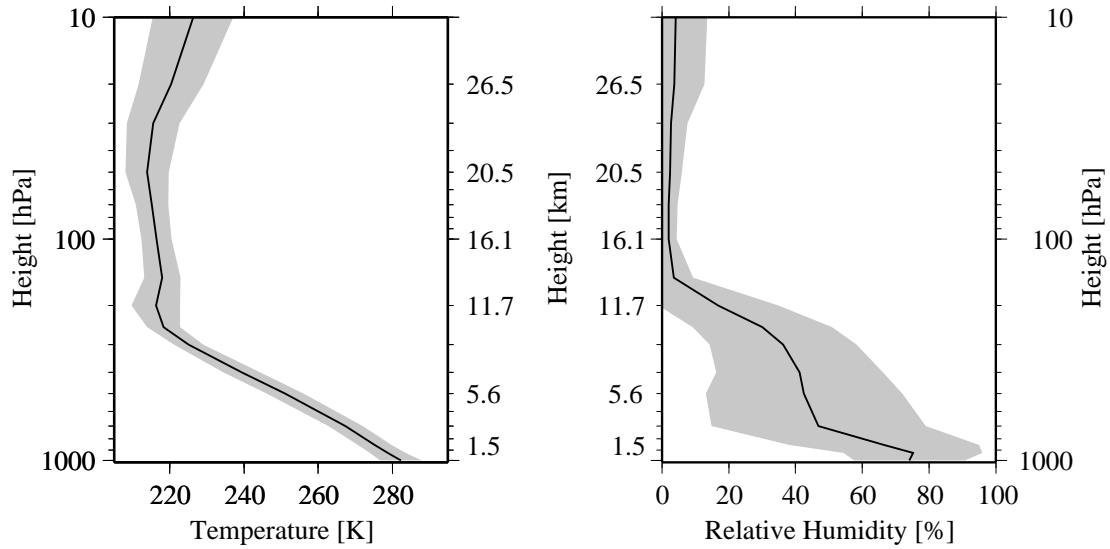


Figure 1.1: Annual mean temperature (left panel) and relative humidity (right panel) at significant levels as observed by the radiosonde in De Bilt in 2002. The shaded area indicates the standard deviation of temperature and relative humidity.

the ratio between the mass of water vapour and the mass of dry air. Specific humidity is the amount of water in gas phase in grammes of the total air volume with a mass of one kilogramme. Water vapour mixing ratio and specific humidity are clearly related; both are mass ratios. A more commonly used and known parameter is relative humidity. This parameter is the ratio of the water vapour pressure to the saturation water vapour pressure; the latter is the pressure at which all water vapour condensates. When the air has a 100% relative humidity the air is saturated with water vapour.

The total amount of water vapour in a vertical column is also a widely used parameter in meteorology and has several names: Total Precipitable Water, (Total) Integrated Precipitable Water or Integrated Water Vapour. In this thesis, the last name is used and is abbreviated as IWV. The total amount of water vapour is the integral of the water vapour density from the surface to the top of the atmosphere. The unit is kilogramme's per square metre although in some publications the unit millimetre is used (similar to rainfall) to express the total amount water in gas phase that could rain out when all of the water vapour is condensed and collected on the ground. Here the first unit (kg m^{-2}) is chosen, to distinguish the unit for IWV from the unit for length (i.e. distance).

To give some insight in the vertical humidity and temperature distribution, the annual mean temperature and relative humidity profile of radiosonde De Bilt, the Netherlands, are shown in Figure 1.1; this figure is created using radiosonde observations from 2002 at 00:00 and 12:00 UTC. From this figure, we see that the temperature has a nearly constant standard deviation over the whole profile. In the troposphere, starting at the surface the temperature is gradually decreasing with an average lapse rate of around 6 K km^{-1} . The (almost) constant temperature above 200 hPa (higher than approximately 12 km) marks the start of the stratosphere and is known as the tropopause. The mean relative humidity is decreasing with increasing height (apart from the surface). The standard deviation approaches a maximum at around 3-4 km:

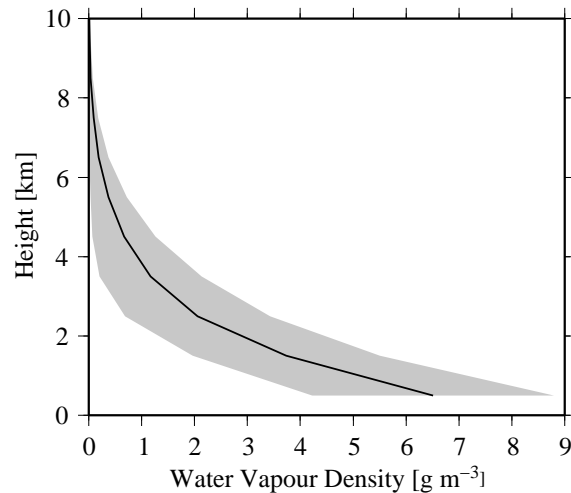


Figure 1.2: Annual mean and standard deviation of water vapour as observed by radiosonde De Bilt in 2002.

the average height of a cloud. Near the tropopause a sharp change in relative humidity is observed.

The annual profile of water vapour is shown in Figure 1.2. The mean water vapour decreases very rapidly and attains zero at a height of approximately 10 km. The standard deviation in water vapour decreases also very rapidly from values of 2.5 g m^{-3} at the surface to zero at 10 km.

When the temperature decreases the capacity of air to contain water in gas phase decreases according to the Clausius-Clapeyron relation. This can be observed in Figure 1.2 at a height from the top of the tropopause onwards where the atmosphere is very dry (with respect to water vapour) due to temperatures of around 215 K. When the temperature changes and no condensation takes place (and the mass of the air is constant) the amount of water vapour does not change although the relative humidity changes. The amount of water vapour changes when the relative humidity reaches 100%; water vapour starts to condensate. The temperature at which this occurs is called the saturation temperature. The limit of 100% relative humidity is not strict. Supersaturation, that is air with relative humidity higher than 100%, occurs regularly in clouds.

Water vapour is an important greenhouse gas. It absorbs radiation at low altitudes and emits radiation at high altitudes. As stated before, the amount of water vapour an air parcel can contain is closely related to the temperature of the air parcel. With rising temperature, a volume of air can contain more water vapour (for instance evaporated from the ocean). An increase in water vapour at low altitudes will reduce the amount of outgoing long-wave radiation and the atmospheric equilibrium temperature (corresponding to the long-wave radiation) has to rise to balance the incoming solar radiation. Climate model predictions show that almost two thirds of the global warming is attributed to this water vapour feedback (Houghton et al., 2001; Solomon et al., 2007).

When the temperature is below the saturation temperature, water vapour will behave as a trace gas. The sources of water vapour are evaporation from the surface (soil, vegetation, and

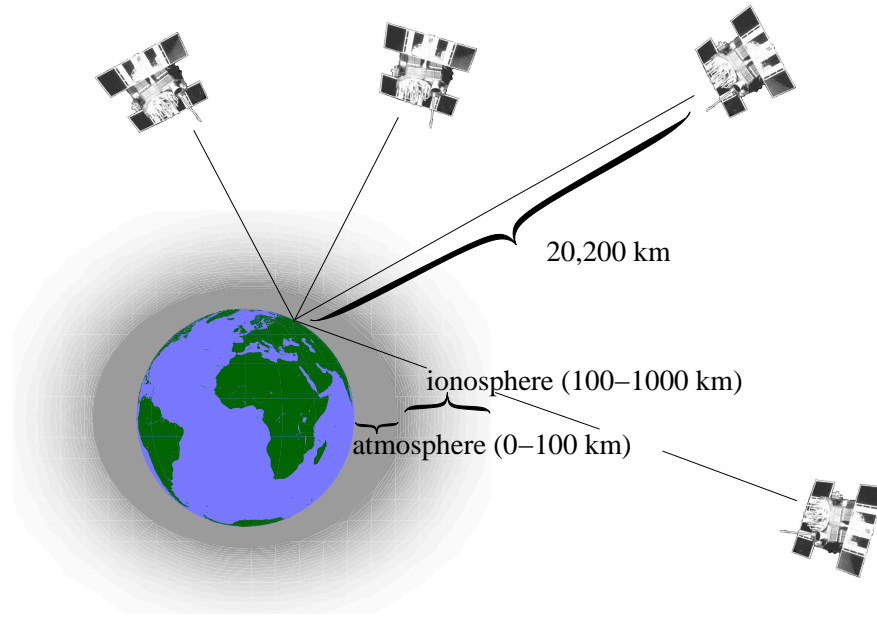


Figure 1.3: GPS satellites transmitting time coded signals and circle the earth in six orbital planes with a distance of 20,200 km from the earth. At least four satellites are in each plane ensuring visibility of at least four satellites over the entire globe. Note that the path through the atmosphere differs for different satellites .

ocean), cloud droplets or ice particles. Sinks of water vapour are condensation and absorption into surfaces (i.e. soil).

1.2 THE GLOBAL POSITIONING SYSTEM

In 1967 an early prototype of a Global Positioning Satellite called 'Timation 1' was launched into a low Earth orbit (approximately 900 km) as part of a military test program. The immediate predecessor of 'Timation 1' was the Navy Navigational Satellite System (NNSS), also called TRANSIT, with a satellite constellation of six polar orbiting satellites at a height of about 1100 km, but lacked instantaneous positioning capability. Only when the Navigation Satellite Timing and Ranging Global Positioning System (NAVSTAR GPS, or simply GPS) controlled by the U.S. Department of Defense became operational in 1995 precise time tagged and almost instantaneous three-dimensional position information accurate to several metres became available to users with a proper receiver. The positioning principle uses the distance or pseudo ranges between (minimal) four satellites and a receiver, given the positions of the satellites.

The GPS system consists of three segments: the space, ground and user segment. The space segment comprises (more than) 24 GPS satellites in orbit at a distance of approximately 20,200 km. The satellites transmit time coded signals in two frequencies with carrier wave frequencies of 1575.42 MHz (called L1) and 1227.60 MHz (called L2). On-board atomic clocks control all signal components in the satellites. The ground segment controls the satellites for orbit adjustment and provides the broadcast ephemerides, which are disseminated to the user



Figure 1.4: GPS antenna installed on a weather station in the Netherlands. The receiver is located in a nearby shed.

segment via the navigation message of the GPS signal. A GPS antenna and receiver (ground-based or space borne) form the user segment (see Figure 1.4). The receiver compares the time coded signal from the GPS satellites with its own internal clock, from which the receiver can compute the pseudo ranges to each satellite in view. When at least four pseudo ranges are observed the receiver can compute its position and the clock error of the receiver. The standard positioning technique using the time-coded signals has an accuracy of about 3-5 m.

In 1972, Counselmann along with his colleagues from the Massachusetts Institute of Technology's Department of Earth and Planetary Sciences reported on the first use of interferometry to track the Apollo 16 Lunar Rover module. The principle they described is in essence the same technique used later in developing the first geodetic GPS receiver. By tracking the carrier phase as well as the time coded signals higher precision (mm-cm) applications are possible.

Traditionally used for high precision geodesy, the GPS system emerged as a powerful tool in atmospheric studies. In fact, the geodetic and atmospheric applications cannot be separated; to get the precise location of a receiver, the delay suffered by the GPS signal, while propagating through the atmosphere, must be accurately known. The atmospheric delay is an error term in geodesy, while it contains useful information for meteorology. One of the first publications on GPS meteorology was written by Bevis et al. (1992). His group showed that one of the error terms in positioning with GPS contained information on atmospheric humidity.

By observing the phase difference $\Delta\phi = \phi_{obs} - \phi_{rec}$ of the carrier wave from the satellite signal with the reference carrier wave in the receiver, information on the range between satellite and receiver can be inferred. Phase differencing introduces an integer ambiguity j_{amb} , but has a higher accuracy than observed time code difference. Uncertainties in the clock offsets ($\tau_{sat} - \tau_{rec}$) between satellite and receiver will also be part of the observation and additional delays are

observed because the signal propagates through the atmosphere (ΔL_{atm}) and ionosphere (ΔL_{ion}). The observed phase difference (multiplied by the wavelength λ) can be written as

$$\lambda \Delta\phi = D + c(\tau_{sat} - \tau_{rec}) - \lambda j_{amb} + \Delta L_{atm} - \Delta L_{ion} + \varepsilon, \quad (1.1)$$

where c is the speed of light, λ is the wave length of the signal, D is the distance between the receiver and the satellite, and ε are the (unmodeled) errors (e.g. multipath, receiver noise). All terms in Equation 1.1, except the j_{amb} , have a time dependency. The ambiguity is constant for every satellite-receiver pair during a continuous tracking of the signal. The time scales of the other terms in Equation 1.1 are different: the range D (and observed phase difference) change rapidly because the position of the satellite changes rapidly, while the atmospheric and ionospheric terms have time scales on the order of several minutes to hours.

In general there are more unknowns than observations in the estimation of the position with one satellite-receiver observation and thus GPS positioning is based on determining the ranges D between the receiver and a number of satellites, with a priori information on the positions of the satellites. These ephemerides are in turn determined from a global tracking network of GPS receivers in the framework of the International GNSS Service (IGS). The IGS is a voluntary federation of agencies that pool resources and GPS data of a worldwide network of over 200 permanent GPS stations to generate precise GPS products. By collecting observed phase differences from different satellites over a period, a least squares estimate of the position can be established. This involves estimating or eliminating clock errors, phase ambiguity, atmospheric delay and ionospheric delay. Due to the dispersive nature of the ionosphere, ΔL_{ion} can be approximated to the first order by a linear combination of the signal received at two frequencies. Differences in time scales are used to reduce the number of unknowns. Furthermore, the atmosphere around the receiver is assumed to be horizontally homogeneous with a standard (or climatological) vertical temperature and moisture distribution. By this assumption, the atmospheric slant delays can be mapped to the zenith and thus the number of unknowns is reduced even further. The atmospheric delays are estimated for instance every 15 minutes, while the phase differences are available every observation epoch (e.g. every minute).

The atmospheric excess path is caused by refraction and bending of the signal due to the gradients in refractive index n . According to Fermat's principle this excess path is

$$\Delta L_{atm} = \int_s n ds - D + \Delta S \approx \int_s (n - 1) ds, \quad (1.2)$$

where D ($= \int_s ds$) is the geometric distance and ΔS the excess path due to bending; the latter can be neglected for elevations larger than 10 degrees. The refractivity N is defined as $N = 10^6(n - 1)$ and according to (Smith and Weintraub, 1953; Thompson et al., 1986)

$$\begin{aligned} N &= k_1 \rho R_d + \left(k_2 R_v - k_1 R_d + k_3 \frac{R_v}{T} \right) \rho_w \\ &= N_h + N_w, \end{aligned} \quad (1.3)$$

for the neutral atmosphere. Here ρ is air density [kg m^{-3}], ρ_w water vapour density [kg m^{-3}], T is temperature [K] and $R_d = 287.05$ [$\text{J kg}^{-1} \text{K}^{-1}$] and $R_v = 461.51$ [$\text{J kg}^{-1} \text{K}^{-1}$] are the gas

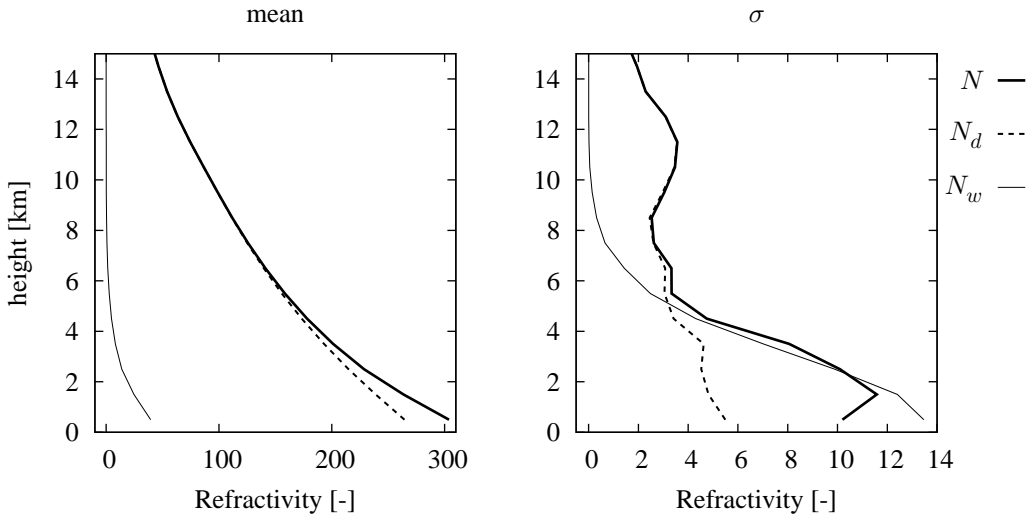


Figure 1.5: Mean (left panel) and standard deviation (right panel) of total (thick), hydrostatic (dashed) and wet (thin) refractivity with height (data from radiosonde De Bilt in 2002).

constants for dry air and water vapour. The empirical constants are (Thayer, 1974) $k_1 = 77.6$ [K hPa⁻¹], $k_2 = 70.4$ [K hPa⁻¹] and $k_3 = 373900$ [K² hPa⁻¹]. The first term in Equation 1.3 is the hydrostatic refractivity¹, N_h , and the second term is called the wet refractivity, N_w . The integrals in the zenith direction of the hydrostatic and wet refractivity are called the Zenith Hydrostatic Delay (ZHD) and Zenith Wet Delay (ZWD) respectively, that is

$$\text{ZHD} = 10^{-6} \int_z N_h dz \text{ [m]} \quad \text{and} \quad \text{ZWD} = 10^{-6} \int_z N_w dz \text{ [m]}. \quad (1.4)$$

In Figure 1.5 the mean (left panel) and standard deviation (right panel) of the total N , hydrostatic N_h , and wet N_w refractivity are shown. Above 5 km the (total) refractivity is dominated by the hydrostatic part. The wet refractivity is roughly 10% of the total refractivity N . The standard deviation of the refractivity, shown in the right panel, reveals that in the lowest 5 km the wet refractivity is more variable than the hydrostatic refractivity. Above 6 to 8 km, the standard deviation of the total refractivity is governed by the hydrostatic refractivity standard deviation. A signal with a low elevation will propagate longer through the lower parts of the atmosphere than a signal with high elevation (see Figure 1.3). The different distribution of wet and hydrostatic refractivity with height requires a separate approach of the hydrostatic and wet part of the atmospheric delay by applying different mapping functions (Niell, 1996, 2000; Boehm et al., 2006). The atmospheric delay for an elevation β can be written as

$$\Delta L_{atm} = m_h(\beta) \text{ZHD} + m_w(\beta) \text{ZWD}, \quad (1.5)$$

where m_h and m_w are hydrostatic and wet mapping functions. A mapping function is in general a fit of the ratio between the slant hydrostatic (wet) delay of and the zenith hydrostatic

¹The term N_h should not be confused with the dry refractivity, which is $N_d = k_1 \rho_d R_d$, where $\rho_d = \rho - \rho_w$ the density of dry air.

(wet) delay derived from a climatological atmosphere. Mapping functions can also be retrieved from numerical weather prediction models. Note that the atmospheric delay is assumed to be independent of the azimuth α .

The number of atmospheric unknowns seems to have doubled with the introduction of ZHD and ZWD. This is not the case because the ZHD can be approximated very accurately by the surface pressure and the latitude and height of the receiver, according to Saastamoinen (1972)

$$\begin{aligned} \text{ZHD} &= 10^{-6} k_1 R_d \int_z \rho dz \\ &\approx \frac{2.2768 \cdot 10^{-5} p_a}{1 - 2.66 \cdot 10^{-3} \cos(2\phi_{gps}) - 2.8 \cdot 10^{-7} z_{gps}} \doteq \text{ZHD}_{Saas}, \end{aligned} \quad (1.6)$$

where ϕ_{gps} is the latitude of the GPS receiver and z_{gps} the height of the receiver. The remaining atmospheric term can be rewritten as (following Davis et al. (1985))

$$\text{ZWD} = 10^{-6} \left(k_2 R_v - k_1 R_d + k_3 R_v \frac{\int_z \rho_w / T dz}{\int_z \rho_w dz} \right) \int_z \rho_w dz. \quad (1.7)$$

and by defining the weighted mean temperature as

$$T_m = \frac{\int_z \rho_w dz}{\int_z \rho_w / T dz}, \quad (1.8)$$

the equation for ZWD becomes

$$\text{ZWD} = \underbrace{10^{-6} (k_2 R_v - k_1 R_d + R_v k_3 / T_m)}_{k'(T_m)} \int_z \rho_w dz. \quad (1.9)$$

The weighted mean temperature T_m can be approximated by a function of the surface temperature T_s (Davis et al., 1985; Baltink et al., 2002); thus $k'(T_m) = k(T_s)$. The last integral is the integrated water vapour (IWV) defined by

$$\text{IWV} = \int_z \rho_w dz. \quad (1.10)$$

The above equations show that IWV can be inferred from ZWD (or ZTD) observations in the following way

$$\text{IWV} = \frac{1}{k(T_s)} \text{ZWD} = \frac{1}{k(T_s)} (\text{ZTD} - \text{ZHD}_{Saas}). \quad (1.11)$$

The ratio $k(T_s)$ between IWV and ZWD is around 6.5 [kg m⁻³]. When only ZTD delay observations are available the ZWD is calculated by subtraction of ZTD by ZHD from the approximation derived by Saastamoinen. Figure 1.6 shows a timeseries IWV for the site Cabauw, the Netherlands. Clearly visible is the variation of IWV with a seasonal signal: low values in the winter period and high values in the summer period. Nevertheless, variations of over 15 kg m⁻² during a period of a few days occur.

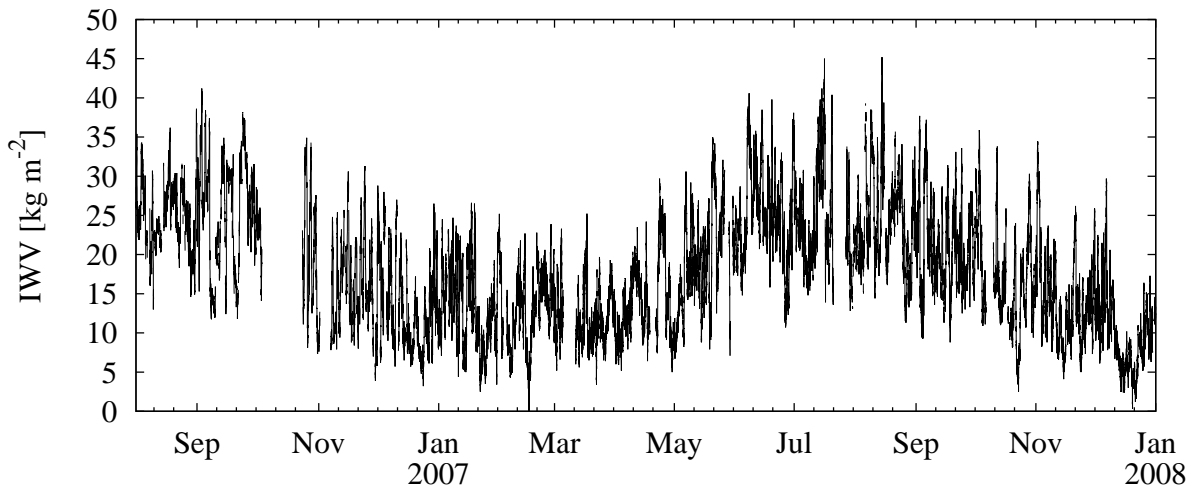


Figure 1.6: Integrated Water Vapour time series for Cabauw.

1.3 GPS METEOROLOGY

Starting in the early 90's of the previous century, the method of detecting atmospheric humidity using GPS has grown into a mature technique. Two types of meteorological observation techniques based on the reception of GPS signals can be identified: one using a ground-based surface network of GPS receivers and the other using a space-borne GPS receiver on board a low Earth orbiting (LEO) satellite.

The principle of ground-based observations was first outlined in 1992 by M. Bevis and his group (Bevis et al., 1992). This was followed by several studies (Rocken et al., 1993; Bevis et al., 1994; Rocken et al., 1995; Businger et al., 1996). In 1996, the Netherlands Remote Sensing Board (BCRS) funded a project to analyse ground-based GPS atmospheric humidity observations from the Dutch Active GPS Reference System (AGRS) network (Baltink et al., 1998, 2002). The results from this project were very promising and when in 1998 the European COST 716 action “Exploitation of ground-based GPS for operational numerical weather prediction and climate applications” started, the Koninklijk Nederlands Meteorologisch Instituut (KNMI) and the Technische Universiteit Delft (TUD) joined this action (COST is the acronym for Co-operation in the field of Scientific and Technical Research). This action brought the geodetic and meteorological communities in Europe together. The primary objective of this action was to assess the operational potential of ground-based GPS on an international scale and to provide near real-time observations for numerical weather prediction (NWP). An unforeseen spin-off of this action was the application of GPS IWV for nowcasting (de Haan et al., 2004). The action ended successfully in 2004. The EU project TOUGH “Targeting Optimal Use of GPS Humidity Measurements in Meteorology” was the follow-up of COST 716. The focus of this action was to prepare the NWP models for the use of GPS data. A new research area was addressed in this project: investigation of the possibilities to determine slant path information from GPS and to assimilate these in NWP (van der Marel and Gündlich, 2006; Eresmaa and Järvinen, 2006; Järvinen et al., 2007); KNMI was involved in this work (de Vries, 2006). This research was partly a continuation of a Netherlands Institute for Space Research

(SRON) funded project (SRON-EO-050) run by KNMI and TUD (de Haan et al., 2005). In the mean time routinely processing of a GPS network of 35 stations in the Netherlands has been realised (de Haan, 2008).

At this moment, early 2008, the production of zenith GPS observations is close to operational. Several European National Meteorological Services (NMS's) have set up processing schemes of GPS data or made agreements with an agency to produce the atmospheric delays for meteorology. In 2005 the network of European National Meteorological Services (EUMETNET) has initiated the program "E-GVAP" which plays a crucial role in the collaboration between the geodetic and meteorological communities.

A space-borne GPS receiver observes atmospheric humidity related parameters by means of the radio occultation (RO) technique. Orbital motion of the GPS satellites and the receiver produces a limb scanning geometry. Due to the difference in orbits of the GPS receiver and transmitter, global profiles of the atmospheric refractivity can be measured. As a limb sounder, its along-track, horizontal resolution is approximately 300 km while its vertical resolution is 200 m. The UCAR/NCAR GPS/MET project was the "proof of concept" where a GPS receiver was installed on board a small research satellite that was put into a relatively low orbit and delivered data from April 1995 to February 1997 (Ware et al., 1996). Since this successful project a number of space-borne GPS receivers were launched (SAC-C, CHAMP, GRACE, METOP-GRAS, COSMIC); the data of some of these satellites are assimilated in the ECMWF global NWP model (Healy et al., 2005, 2007).

Ground-based GPS and GPS RO data are valuable observations for operational meteorology. The quality of GPS RO temperature/humidity observations are generally very accurate with good global coverage; these observations are therefore assimilated operationally in global NWP models. Because of their random distribution over the globe, the footprint of about 300 km and the irregular observation times these data are less suitable for nowcasting. For short-range weather forecasting this data could be valuable when there are multiple GPS RO receivers operational. Ground-based GPS ZTD observations have a temporal resolution suitable for both NWP and nowcasting. A number of European NMS's are actually assimilating the data in their regional NWP models (Poli et al., 2007; Jupp, 2006).

This thesis focuses on the meteorological application of ground-based GPS ZTD and IWV observations and how to utilise its real-time character and good horizontal distribution over land. NWP data assimilation is generally performed with a delay of more than an hour in order to collect as many observations as possible. Thus assimilation in NWP will not exploit the real time signature of the GPS observations (which can be similar to satellite imagery and weather radar products that are available with a delay of several minutes). The present operational measurements of atmospheric water vapour by radiosondes do not possess the temporal nor the horizontal spatial resolution to infer information about the atmosphere smaller than synoptic scales. GPS ZTD (and IWV) can be estimated accurately with a temporal resolution of 15 minutes for a surface network of GPS receivers with a horizontal resolution between 50 and 100 km. In this thesis, the standalone quality of the (real time) meteorological application of GPS is assessed and to its usefulness for nowcasting is evaluated.

1.4 METEOROLOGICAL APPLICATIONS

For any practical meteorological application or product the following questions should always be addressed and should be revisited regularly:

- Is the product accurate and reliable?

Is the product “stable”? The product should be stable in the sense of accuracy. Sudden (short) decrease of the quality degenerates the applicability of a product as a whole. What are the boundary conditions of retrieving/generating the product? Are meteorological circumstances crucial (e.g. cloud contamination of satellite water vapour channels)?

- Is the product applicable, useful (or even essential)?

Does the product have an additional value with respect to the current observing system, or even, does the product fill a gap in the observing system (time/space)? The answer to this question may change during the years, for instance when new techniques or methods become available (e.g. new assimilation techniques). The user requirements for the meteorological and climatological observing system may also change during time giving reason to review this question.

- Is the product cost-effective?

Is it feasible to generate the product in an economical way? The answer to this question may also change with time (due to for example decreasing costs of equipment and/or data transport). Are there other products, which can deliver similar information more cost-effectively? Will for example the forecast of severe weather improve; will the false alarm rate be lower using the product?

With evolving observing methods, these questions should be addressed regularly. New products may replace old products, not because the old products are bad but simply because the new product is better (faster/cheaper). Answers to the questions raised above cannot be given separately. For instance, an outstanding quality product with high reliability may be too expensive to deploy.

With respect to GPS, part of the third question can be answered positively at this moment: (raw) GPS observations are made available; GPS derived atmospheric observations are generated for use in meteorology and disseminated through the meteorological data network. An important question therefore still is related to the added value of GPS for meteorology.

This thesis deals in detail with the first two questions previously stated. The product considered here is the application of water vapour observations from ground-based GPS for meteorology.

1.5 OUTLINE

The following research questions are addressed:

- a) How accurate can a ground-based GPS network estimate tropospheric delay and integrated water vapour?
- b) What meteorological information can be inferred from GPS atmospheric estimates?
- c) In what way can the atmospheric information from GPS be beneficial for nowcasting applications?

Chapter 2 answers the question on accuracy. This chapter presents background information on methods of observing atmospheric water vapour and the atmospheric variability of water vapour around the Netherlands. Chapter 3 discusses the influence of the symmetric mapping function assumption on estimation of the GPS parameters; this topic relates also to the accuracy issue.

Chapter 4 presents a first (one-dimensional) meteorological application; comparing time series of GPS IWV and water vapour brightness temperature observed by a geostationary satellite. Differences in the change of the brightness temperatures and GPS IWV reveal coarse information on the water vapour profile. Staying in the one-dimensional observation space, Chapter 5 identifies atmospheric buoyancy to spectral response of a GPS signal.

Going one dimension higher, validation and applications of two-dimensional GPS IWV maps are discussed in Chapter 6 for nowcasting of thunderstorms.

In Chapter 7 the three-dimensional space is reached: the additional information from slants is investigated. Chapter 8 describes and validates a system which estimates three-dimensional water vapour using slant GPS water vapour observations.

The last chapter contains the conclusion and an outlook to possible new applications and research topics for GPS meteorology.

Chapter 2

Background

2.1 WATER VAPOUR OBSERVATIONS

Upper air water vapour can be measured directly with radiosondes and humidity sensors on-board (commercial) aircrafts or indirectly by GPS, satellites and radiometers. The first type of measurements is in-situ while the second use remote sensing techniques and rely on parameterisations. Because the measurement technique differs, the representativity of the observed water vapour differs as well.

2.1.1 RADIOSONDE

In an operational sense, only radiosonde observations provide vertical profile in-situ information on upper atmospheric water vapour. The distribution of the radiosonde network is chosen such that synoptic scales can be observed but atmospheric water vapour variations smaller than synoptic scales are not sampled by the network. The locations where radiosondes are launched are mainly restricted to land (see Figure 2.1a), although there are a number of automatic radiosonde systems on ships and on a few offshore platforms. A radiosonde system consists of a ground segment and a balloon to which a small lightweight container is attached. The temperature and humidity sensor in the container measure the atmospheric state while a pressure sensor or a GPS receiver determines the height (and position in case a GPS is used); all information is transmitted to the ground segment where the wind speed and direction are inferred from the ground track of the balloon during its ascent (using LORAN-C when the radiosonde is not equipped with GPS). The balloon is released approximately 30 minutes before the synoptic hour to assure that it reaches the tropopause around the synoptic hour. The equipment used is in general lost and thus must be low-cost. The observation method implies that the actual observation time at a certain height does not correspond with the synoptic time. Furthermore, because of the drift of the balloon the observed profile does not correspond exactly to the profile at the launch site.

The measurement can be influenced by the atmospheric trajectory of the balloon. There are known problems with the humidity observations for instance due to ice contamination

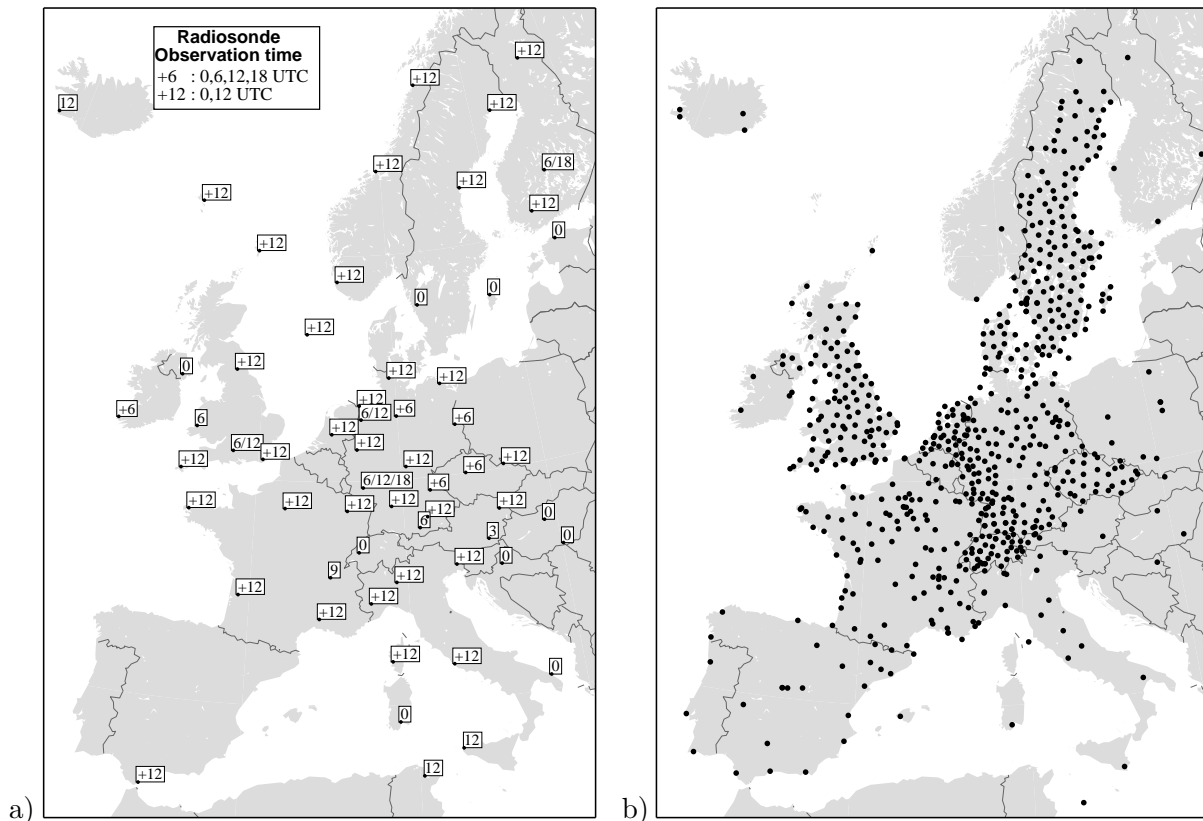


Figure 2.1: a) Locations and launch times of radiosonde observations. All observations are extracted from the Global Telecom System (GTS) database at KNMI on 30 November 2007. b) Locations of GPS sites for which at least once per hour an observation was present in the GTS database at KNMI on 30 November 2007.

or day/night inconsistencies (Lorenc et al., 1996; Leiterer et al., 1997). Turner et al. (2003) showed that calibration of the total humidity profile with a water vapour radiometer resulted in a better humidity profile. Furthermore, they showed that the age of the equipment had a negative influence on the quality of the radiosonde observation.

KNMI started radiosonde observations in 1947; currently Vaisala RS92 radiosondes are launched every 12 hours. This radiosonde has technical uncertainties of 0.1°C for temperature, 0.2 hPa for pressure and 2% for relative humidity. The previous radiosondes (RS90 and RS80) had higher uncertainties (for example 5% for humidity).

Despite the coarse temporal and horizontal resolution, radiosonde observations are a valuable source of information on temperature, humidity, and wind in the atmosphere. Nevertheless, the frequency of a large number of radiosonde launches were reduced from four times per day to two to reduce the costs of the total meteorological observing network.

2.1.2 GPS SURFACE NETWORKS

In 1992 the first Dutch GPS site was installed in Kootwijk. Since 1996, the Dutch AGRS (Active GPS Reference System) network was established, consisting of six permanent stations.

Data from this network, complemented with a number of IGS stations, was processed daily at the Delft institute for Earth Oriented Space Research (DEOS) of Delft University of Technology (TUD). When raw GPS data in a network are processed an estimate of the atmospheric delay is determined, the so-called Zenith Total Delay (ZTD). From this ZTD the total zenith Integrated Water Vapour (IWV) can be extracted when surface measurements of pressure and temperature are available. Over the years the number of GPS stations continued to grow, in particular from several commercial providers. A research GPS receiver was installed at Cabauw in 2001. In 2005, a dense network of 35 stations was installed for surveying applications by the Kadaster, the Dutch Land Registry Office. This network, abbreviated as NETPOS, is a collaboration of the Ministry of Transport, Public Works and Water Management (“Ministerie van Verkeer en Waterstaat”, abbreviated as MinVenW) and the Kadaster. KNMI, part of MinVenW, provides access to three remote weather station locations where a GPS antenna and receiver are installed (an example is shown see Figure 1.4). The NETPOS-network (also complemented with a number of IGS stations) is processed at KNMI for meteorological applications and produces, in real-time, atmospheric estimates with an observation frequency of four times per hour. On a European scale, data from a large number of GPS sites are available and are used to produce atmospheric observables. Figure 2.1b shows the locations of the available sites on 30 November 2007; the data plotted are received at KNMI through the Global Telecom System (GTS), the communication network dedicated to exchange meteorological observations.

Instead of obtaining zenith quantities, the total amount of water vapour can also be measured along a slant path between a ground-based receiver and the (transmitting) GPS satellite. By using not only the zenith atmospheric information but also the slant information the number of observations will increase by roughly a factor ten. A slant IWV on its own has a two-dimensional character, and by applying tomographic or variational algorithms a three-dimensional water vapour field can be retrieved from slant observations. Furthermore, the horizontal resolution of the retrieved water vapour field will also profit from this larger amount of observations.

GPS measured water vapour has the ability to provide the lacking moisture information over land. The strength of GPS water vapour observations from a surface network of receivers is inherited from the continuous availability of the GPS signals; the observations are all-weather with observation frequencies of every several minutes.

2.1.3 OTHER WATER VAPOUR OBSERVATIONS

Commercial aircrafts are equipped with instruments to measure wind and temperature. At present, a selection of these observations are transmitted to a ground station using the AMDAR (Aircraft Meteorological Data Reporting) system. An atmospheric profile can be observed when measurements are taken during takeoff and landing. In the near future it is expected that water vapour observations can be obtained using the AMDAR system. The locations of the observed profiles are restricted to vicinities of airports and are sparse during night times and landing restrictions (e.g. due to severe weather). In Figure 2.2a the locations and observation time of AMDAR are shown for a single day.

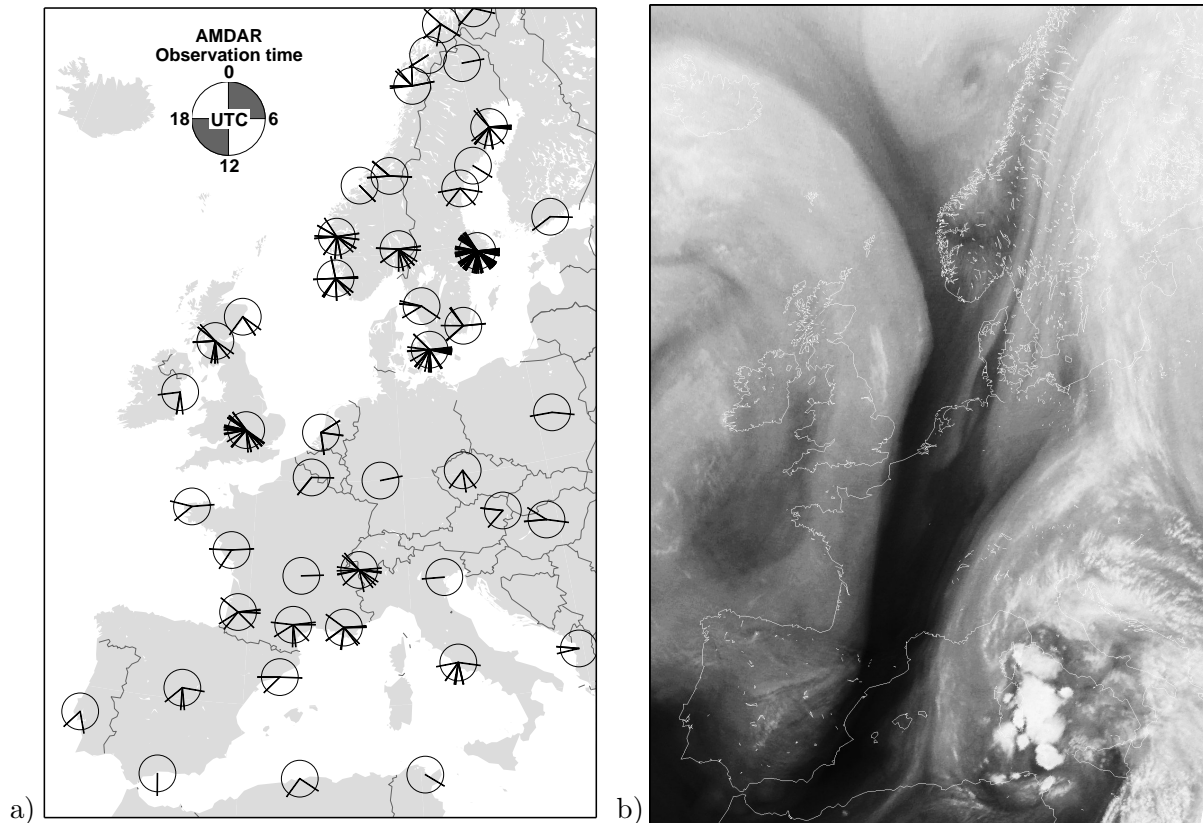


Figure 2.2: a) Locations and observation time of AMDAR observations as extracted from the GTS database at KNMI on 30 November 2007. b) Meteosat $6.7 \mu\text{m}$ water vapour image from 30 November 2007 12:00 UTC.

Satellite imagery is another source of information from which a qualitative analysis of the horizontal water vapour distribution can be obtained. The current Meteosat satellite measures the thermal emission by tropospheric water vapour in two channels ($6.7 \mu\text{m}$ and $7.3 \mu\text{m}$). The temperature of the atmosphere and the presence of clouds affect the observed thermal emission. Very coarse profile information can be retrieved from these water vapour observations in cloud free areas. The strength of these observations lies in the update frequency (every 15 minutes), good coverage (up to the mid-latitudes), and resolution.

Water vapour radiometers and water vapour lidars can also measure atmospheric water vapour, however these remote sensing techniques are still not operational; water vapour radiometers have difficulties during rainfall and lidars during daylight.

2.2 TEMPORAL VARIATIONS AND CORRELATIONS OF WATER VAPOUR

Water vapour is highly variable in time and space. In this section the temporal variation and correlation are described using water vapour observations from radiosonde De Bilt, the Netherlands and GPS IWV observations from Cabauw which lies approximately 31 km southwest of De Bilt. Radiosonde observations used in the study presented here are from 1999 and have an observation frequency of four times per day. This observation frequency enables an

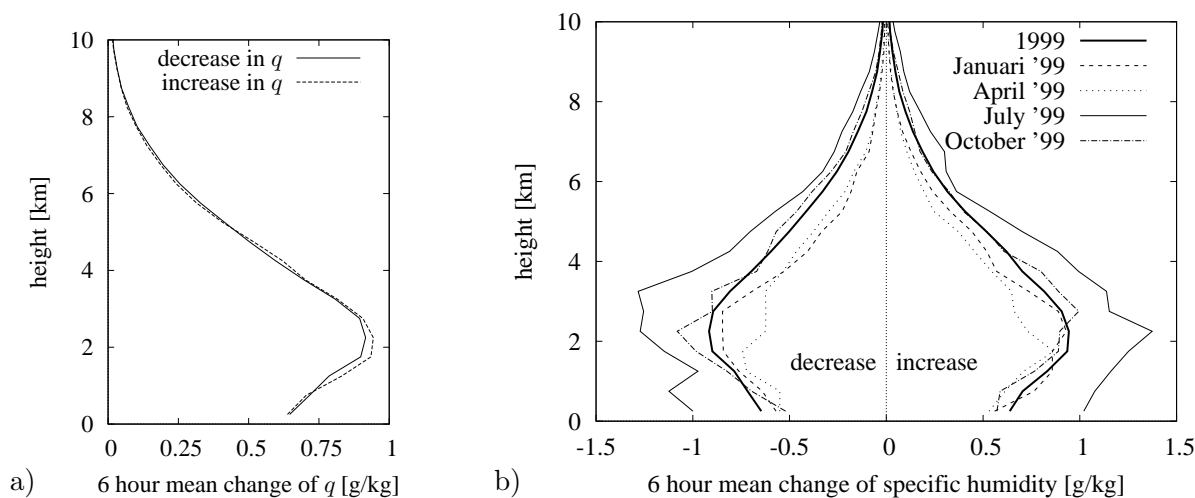


Figure 2.3: Mean increase and decrease in water vapour over six hours based on radiosonde observations in 1999: a) increase/decrease of specific humidity over the whole year; b) seasonal increase/decrease in specific humidity.

investigation of temporal variations of humidity and creates the opportunity to compare these variations to GPS IWV variations. The GPS IWV estimates are retrieved from the routinely processing scheme at KNMI. This data were collected in the period from August 2006 to July 2007.

Figure 2.3 shows the mean change in six hours in specific humidity q for different heights over one year (panel a) and the change in four different months (panel b) of the same year. The mean change is separated in a mean decrease in q (solid line in panel a and left half of panel b), and a mean increase in q (dashed line in panel a and right half in panel b). The yearly increase in q occurs in a thicker level than the yearly decrease. The mean level of the decrease lies a little higher than the mean level of increase. The six hour changes over a whole year are comparable at heights larger than 3 km.

The specific humidity changes most rapidly in the summer and the least in the spring (Fig. 2.3b). The change of water vapour near the surface is more or less equal for the spring, autumn and winter (around 0.5 g/kg). The spread in decrease in q for the seasons winter, spring and autumn is larger than the spread in increase in q for the same seasons.

The change in specific humidity is due to advection of dry or moist air or due to condensation and/or evaporation. Figure 2.3a shows that the increase of q in six hours is in general slightly higher than its decrease. This can be related to the general atmospheric circulation in the Netherlands which is from the west and advects moist air from the Atlantic Ocean and North Sea. The major increase in moisture is located above the surface layer and spread over a layer from 500 m to 2500 m; this is due to the mixing of moisture. The maximum decrease is located near the mean cloud height and is related to condensation at that height.

By examination of the autocorrelation of specific humidity between different heights insight can be gained on the variability of the humidity profile. Figure 2.4 shows the autocorrelation of specific humidity for different heights with respect to time difference. Not surprisingly all correlations decrease with time. Clearly, the specific humidity in the first kilometre of the

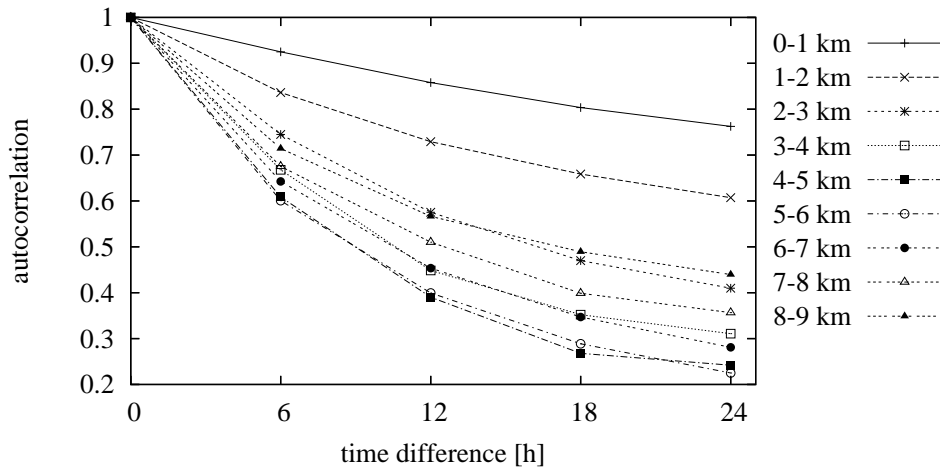


Figure 2.4: Radiosonde Water Vapour auto correlations with time for different heights (data from 1999).

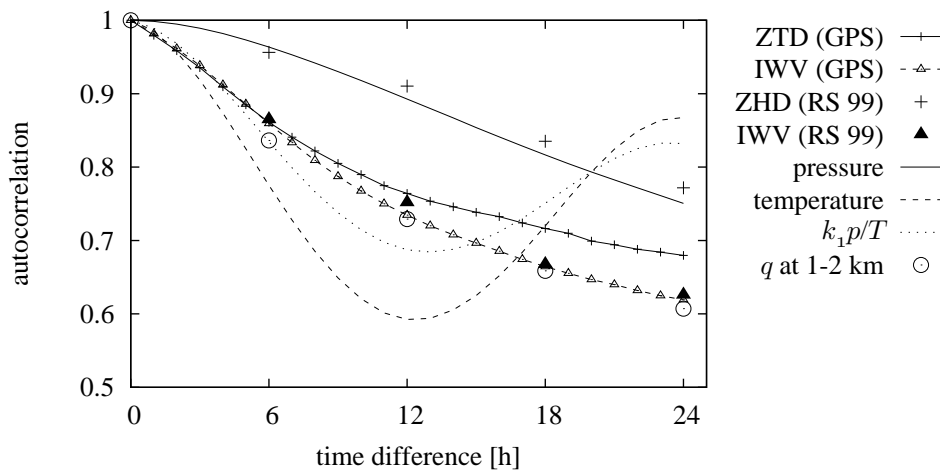


Figure 2.5: Autocorrelation of ZTD, IWV, surface temperature and pressure, hydrostatic refractivity at the surface, q at a level between 1 and 2 km height with respect to time difference and the ZHD and IWV as observed by radiosonde observations. The specific humidity autocorrelation is derived from radiosonde observations in De Bilt (1999); the other parameters are observed in Cabauw (August 2006 - July 2007).

atmosphere is highly correlated with the value at previous times. There is a clear separation in correlation strength for specific humidity above and below 3 km. The lowest correlation is observed at heights around 4 to 6 km and the autocorrelation at 9 km is similar to that at 3 km. The amounts of specific humidity at heights higher than 10 km are small, and are therefore not shown here. The clear separation in autocorrelation between heights below and above 3 km is related to the general circulation of water vapour. The largest amount of water vapour resides in the lowest kilometres, resulting in a high correlation at these levels.

Next, the autocorrelation of GPS ZTD and IWV are investigated. Both IWV and ZTD are parameters, which contain information on the complete atmospheric column; ZTD also contains hydrostatic mass information. In Figure 2.5, the autocorrelation of ZTD and IWV (solid

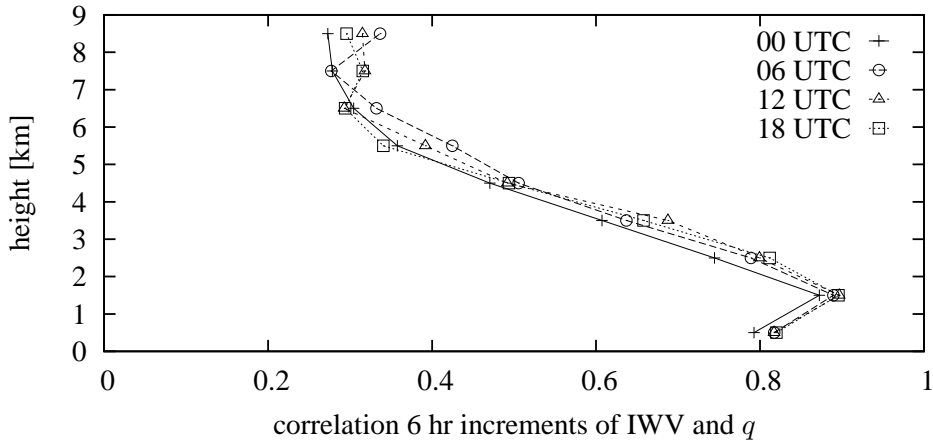


Figure 2.6: Correlation of six hour increments of IWW with increments of q for different heights; IWW is calculated from the radiosonde profile (data from 1999).

and dashed lines with symbols) are shown together with the autocorrelation of some surface parameters (pressure, temperature and hydrostatic refractivity $k_1\rho R_d \approx k_1p/T$) and the ZHD and IWW from radiosonde observations from 1999. Pressure has the highest autocorrelation; temperature shows the typical diurnal effect over a 24-hour period, which is also visible in the hydrostatic refractivity autocorrelation. The ZTD has a higher autocorrelation than IWW, which is because approximately 90% of the signal in ZTD is linearly related to pressure (i.e. the hydrostatic part, see Equation 1.3). Not surprisingly, the autocorrelation of ZHD from radiosonde is in good agreement with the autocorrelation of surface pressure. Although both data sets are from different periods (radiosonde from 1999 and GPS from August 2006 to July 2007) the agreement is reassuring. Note that also the autocorrelation of IWW from GPS and radiosonde are almost equal. Also plotted in Figure 2.5 is the autocorrelation of specific humidity at a level between 1 and 2 km (also shown in Figure 2.4). For time differences longer than 6 hours the autocorrelation of IWW and specific humidity at a level between 1 and 2 km height are very close.

To further investigate the relation between variation of IWW and specific humidity at different heights the correlation between these parameters are determined and presented in Figure 2.6. The IWW is calculated from the radiosonde profile. Correlations are determined separately for the four different observation times (00:00, 06:00, 12:00 and 18:00 UTC). The correlation is calculated using the 6-hour increment of integrated water vapour (calculated from the radiosonde profile) and the 6-hour specific humidity increment at different heights (from the same radiosonde observation). Clearly the two parameters are correlated. Remarkable is that the maximum correlation of the increment of IWW with the increment of specific humidity appears at a level between 1 and 2 km. At 00:00 UTC the correlation is the smallest of all four observation times. Below 5 km, the other three observation times show a similar correlation with height. The correlation decreases with height for all four observation times.

When the correlation is determined for positive (resp. negative) increments in IWW a different signal is visible (see Figure 2.7: left panel correlations for negative increments of IWW; right panel for positive increments). Note that the correlation for decreasing IWW at

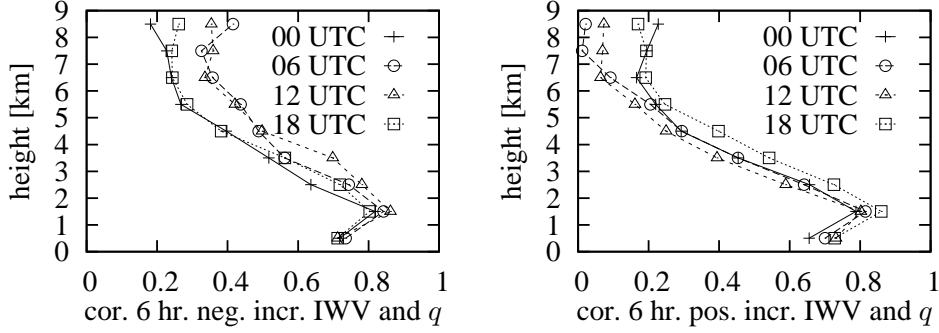


Figure 2.7: Same as Figure 2.6, except now a distinction is made between decrease in IWV (left panel) and increase in IWV (right panel).

06:00 and 12:00 UTC have a higher positive correlation with specific humidity at levels above 5 kilometres, while a positive increment of IWV is less correlated with increments in specific humidity for these times and heights. Furthermore, at 12:00 UTC (and also 06:00 UTC although less extreme) a high correlation for decreasing IWV with q at heights between 1 and 5 km is observed. For positive increments of IWV observations at 18:00 UTC show the highest correlation.

The largest variations of water vapour are observed at a level between 1 and 2 km. Because IWV has a similar autocorrelation with q at this same height, the change in IWV is for a large part caused by a change in q at this level; and vice versa.

2.3 SIGNAL DELAY FROM ATMOSPHERIC MODELS¹

In this section algorithms are presented to calculate zenith and slant delays, as well as integrated water vapour from numerical weather prediction (NWP) model data (or radiosonde profiles). An atmospheric model is the representation of the real atmosphere by three-dimensional fields of temperature, wind, humidity and other physical quantities that characterise the state of the atmosphere. Generally, the numbering of an NWP model starts at the top of the atmosphere counting down to the surface. Each level in the NWP models used in this study is bounded by pressure levels (the so-called pressure half-levels, denoted by p^h). Level j is bounded by p_j^h from above and p_{j+1}^h from below (see Figure 2.8); the temperature in level j represents the mean temperature at this level; the same yields for the other parameters. The surface pressure is equal to the pressure at the bottom of the lowest level, p_{N+1}^h , where N is the number of levels.

The gravity as a function of height z and latitude ϕ is given by (see Lide (1997) a complete definition of g_0 and r_0),

$$g(z) = g_0(\phi) \left(\frac{r_0(\phi)}{r_0(\phi) + z} \right)^2 \quad (2.1)$$

The assumption that the atmosphere is in hydrostatic balance implies that there is a relation

¹This section based on: S. de Haan, H. van der Marel, B. Gündlich, S. J. M. Barlag (2005), Resolving spatial and temporal atmospheric water vapour structures using a ground based GPS receiver network, Final Report: SRON project EO-050, *Chapter 3*.

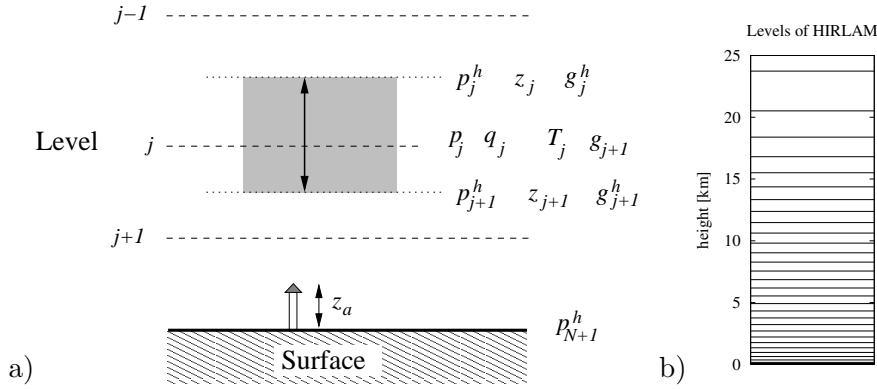


Figure 2.8: a) The vertical representation in NWP of the atmosphere; b) Example of level heights of the HIRLAM model.

between height, gravity, density and pressure given by

$$\partial p = -\rho g \partial z. \quad (2.2)$$

The universal gas law states that there is a simple relation between density ρ , pressure p and temperature T , that is

$$\rho = \frac{p}{RT} = \frac{p}{R_d T_v} \quad (2.3)$$

where $R_d = 287.05$ [J kg⁻¹ K⁻¹] is the gas constant of dry air and T_v is the so-called virtual temperature defined as

$$T_v = T(1 + \delta q), \quad (2.4)$$

where q is specific humidity, $\delta = \epsilon^{-1} - 1$ with $\epsilon = R_d/R_v = 0.62198$, is the ratio of molar weights of dry and moist air (see also Appendix A). Combining the last two equations results in an equation that expresses the thickness Δz in metres of a layer between pressures p_1 and p_2 as

$$\Delta z = - \int_{p_1}^{p_2} \frac{R_d T_v}{g} d \log p \quad (2.5)$$

In NWP models the value of physical constituencies at a certain position is the mean value of three-dimensional grid box around this position. The usual coordinate system for the vertical axis is expressed in pressure or related parameters (i.e. logarithmic of the pressure). The thickness of an NWP level is determined using the following approximation

$$\Delta z = \frac{R_d \widehat{T}_v}{\widehat{g}} \log \frac{p_1^h}{p_2^h}, \quad (2.6)$$

where \widehat{T}_v stands for the mean virtual temperature and \widehat{g} the mean gravity in the layer.

Suppose we want to calculate the height of a level z_j and we know the height of the bottom of the level (z_{j+1}). From Equation 2.1 we can calculate the gravity at this height, called g_{j+1}^h . To calculate the height of the top of the layer we first set the mean gravity equal to g_{j+1}^h determine the thickness of the level using Equation 2.6 and calculate the gravity g_j^h at the top of the level. Recalculate Δz using the mean of top and bottom the gravity as often as necessary. In this way, g_j and $z_j = z_{j+1} + \Delta z$ can be determined.

2.3.1 ZENITH ALGORITHM

The Zenith Total Delay (ZTD) and Integrated Water Vapour (IWV) are defined as

$$\text{ZTD} = \text{ZHD} + \text{ZWD} \quad (2.7)$$

$$= 10^{-6} \int_{z_a}^{\infty} k_1 R_d \rho dz + 10^{-6} \int_{z_a}^{\infty} \frac{R_d}{\epsilon} \left(k_2 - \epsilon k_1 + \frac{k_3}{T} \right) q \rho dz \quad (2.8)$$

$$\stackrel{(\text{Eq. 2.2})}{=} 10^{-6} \int_0^{p_a} k_1 \frac{R_d}{g} dp + 10^{-6} \int_0^{p_a} \frac{R_d}{\epsilon g} \left(k_2 - \epsilon k_1 + \frac{k_3}{T} \right) q dp \quad (2.9)$$

$$\text{IWV} = \int_{z_a}^{\infty} \rho_w dz \stackrel{(\text{Eq. 2.2})}{=} \int_0^{p_a} \frac{1}{g} \frac{q}{1 - q} dp \quad (2.10)$$

where q is the specific humidity, ρ is the density of the air and ρ_w is the water vapour density. The height of the location is denoted by z_a (antenna height) and p_a is pressure at this height.

In general the height z_a does not coincide with a level height and thus to numerical integrate Equations 2.9 and 2.10 the pressure at height z_a and the mean temperature and specific humidity of the level between the antenna and the bottom of the next level has to be determined. Equation 2.6 is used to calculate the pressure at antenna height from surface temperature, humidity and pressure and the height difference between the surface and the antenna. The (mean) temperature of the layer above the antenna is determined as follows. When the antenna pressure is higher than the full level pressure (i.e. the height is lower) the mean temperature above the antenna is determined by a linear approximation of the mean temperature of the current layer and the layer below the antenna. When the antenna pressure is lower than the full pressure (i.e. the antenna is higher) the mean temperature is determined using the mean of the layer temperature of the current layer and the layer above. When the antenna is in the surface layer, the surface temperature is used in the linear approximation. To estimate the humidity in the layer above the antenna, a similar method is used. When the antenna is below the NWP orography the temperature is estimated using a constant lapse rate with the relative humidity kept constant. Apart from the first integration step the calculation of ZTD, IWV and ZWD is straightforward. Suppose that in the first integration step the antenna lies inside the level j : the integration has to start at the pressure level of the antenna p_a ; the temperature, humidity and gravity in the layer above the antenna are T_a , q_a and g_a . Numerical integrating of Eq. 2.9 and Eq. 2.10 the ZHD, ZWD and IWV can be approximated by

$$\text{ZHD} \approx 10^{-6} \left(k_1 \frac{R_d}{g_a} (p_a - p_j^h) + \sum_{i=j}^N k_1 \frac{R_d}{g_i} \Delta p_i \right) \quad (2.11)$$

$$\begin{aligned} \text{ZWD} \approx & 10^{-6} \left(\frac{R_d}{\epsilon g_a} \left(k_2 - \epsilon k_1 + \frac{k_3}{T_a} \right) q_a (p_a - p_j^h) \right. \\ & \left. + \sum_{i=j}^N \frac{R_d}{\epsilon g_i} \left(k_2 - \epsilon k_1 + \frac{k_3}{T_i} \right) q_i \Delta p_i \right) \end{aligned} \quad (2.12)$$

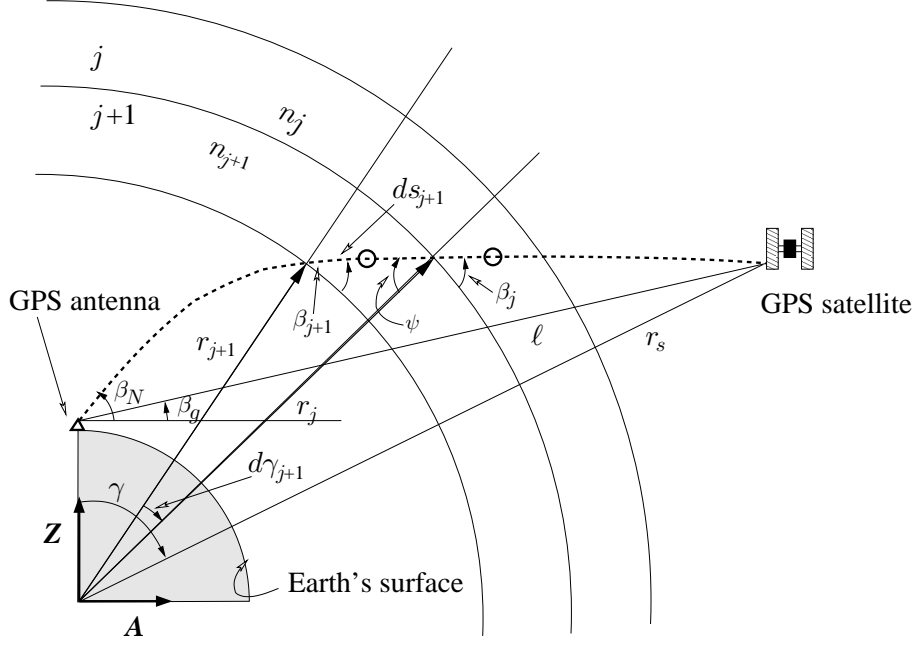


Figure 2.9: Ray tracing through a layered atmosphere.

$$\text{IWV} \approx \frac{1}{g_a} \frac{q_a}{1 - q_a} (p_a - p_j^h) + \sum_{i=j}^N \frac{1}{g_i} \frac{q_i}{1 - q_i} \Delta p_i \quad (2.13)$$

where g_i is the gravity at height p_i and Δp_i is the thickness of level i , see Fig. 2.8. The thickness of level i is defined as the difference between the pressure at half levels p_i^h and p_{i+1}^h (i.e. $\Delta p_i = p_{i+1}^h - p_i^h$).

2.3.2 SLANT ALGORITHM

The path a ray travels through the atmosphere is not straight when gradients in the refractivity field are present. The slant path through a NWP model is assumed to be piecewise linear, that is straight within each layer. Gradients in refractivity tend to bend the signal and determine a curved path, following Snell's law. In Figure 2.9, a bended ray path is shown by the dashed line. In this figure, the plane of intersection is determined by the azimuth direction \mathbf{A} of the signal and the zenith direction \mathbf{Z} at the GPS site. Both vectors are drawn in the figure starting from the earth centre. The geometric angle or true elevation β_g and the position angle γ of the satellite in the azimuth-zenith plane are related by

$$\cos(\beta_g) = \frac{r_s}{\ell} \sin(\gamma), \quad (2.14)$$

where r_s is the distance between the earth centre and the satellite and ℓ the geometric distance between receiver and satellite.

When we focus on the transition of the signal from layer $j + 1$ to j and assuming that the elevation β_{j+1} at the bottom of level $j + 1$ is known we can determine β_j through Snell's law in spherical coordinates

$$n_j r_j \cos(\beta_j) = n_{j+1} r_{j+1} \cos(\psi), \quad (2.15)$$

where ψ is the angle of the ray path with the top of the layer, n_j is the refractivity in layer j and r_j is the distance of the level j to the centre of the earth, see Fig. 2.9. This angle can be found by solving the following three geometric relations

$$\frac{\sin(\pi/2 + \beta_{j+1})}{r_j} = \frac{\sin(\psi)}{r_{j+1}} = \frac{\sin(d\gamma_{j+1})}{ds} \quad (2.16)$$

$$ds^2 = (r_{j+1})^2 + (r_j)^2 - 2r_{j+1}r_j \cos d\gamma_{j+1} \quad (2.17)$$

$$d\gamma_{j+1} + \beta_{j+1} + \psi = \frac{\pi}{2}, \quad (2.18)$$

where ds is the length of the ray path in level $j + 1$, $d\gamma_{j+1}$ is the angle between the r_{j+1} and r_j , which are the intersection points of the ray path with the bottom and top respectively of layer $j + 1$. Note that the sum of $d\gamma_j$ is equal to the (relative) position angle γ of the satellite with respect to the receiver in the azimuth-zenith plane.

Only the refractivity n_j is not determined yet. This parameter cannot be computed directly because the refractivity may change horizontally in the layer. The value of n_j is the mean of the refractivity in layer j and is determined by the location of the centre of the layer (denoted by the circle in Figure 2.9). A first estimate of the intersection of the ray path with the centre of the layer can be found by lengthening the ray path from level $j + 1$ to j . With this initial value the elevation β_j at the top of level $j + 1$ (and bottom of level j) can be determined using the above equations. With this new β_j the intersection of the ray path with the mid of level j can be determined more correctly resulting in a new value of n_j . This procedure can be repeated until n_j and β_j do not change anymore. In most cases two steps are sufficient.

As can be seen from Figure 2.9, the true elevation is not equal to the ray path elevation at the GPS receiver. The ray path elevation β is determined with an algorithm as follows. The initial guess for β^0 is the geometric angle. By determining all β_j and thus $d\gamma_j$ the position angle of the satellite can be determined and should satisfy Equation 2.14. When this is not the case the elevation is adjusted. Suppose $\hat{\beta}$ satisfies Equation 2.14, the elevation β^{i+1} is set to

$$\beta^{i+1} = \beta^i - (\hat{\beta} - \beta_g) \quad (2.19)$$

The above procedure is repeated until β^i and β^{i+1} are sufficiently close. In reality only a few steps are needed.

The last algorithm can be accelerated by using a-priori information, based on previous determined pairs of geometric and ray path elevations. For a period of four weeks the difference between the elevation and the geometric angle as observed from HIRLAM NWP is plotted against elevation for 15 GPS sites, see Figure 2.10 (dots). The solid line through the data set is a least square fit of the data points by the function

$$f(\beta_g) = a \cdot (\beta_g - 90) + b \cdot (\exp^{c \cdot \beta_g} - \exp^{c \cdot 90}), \quad (2.20)$$

with $a = -3.54 \cdot 10^{-4}$, $b = 1.83 \cdot 10^{-1}$, and $c = -9.57 \cdot 10^{-2}$. Huuskonen and Holleman (2007) determined the refraction of C-band waves as a function of true elevation using the atmospheric refraction routines of the Starlink positional astronomy library (CCLRC, 2005). These refraction curves have been calculated for the U.S. Standard Atmosphere (NOAA/NASA/USAF,

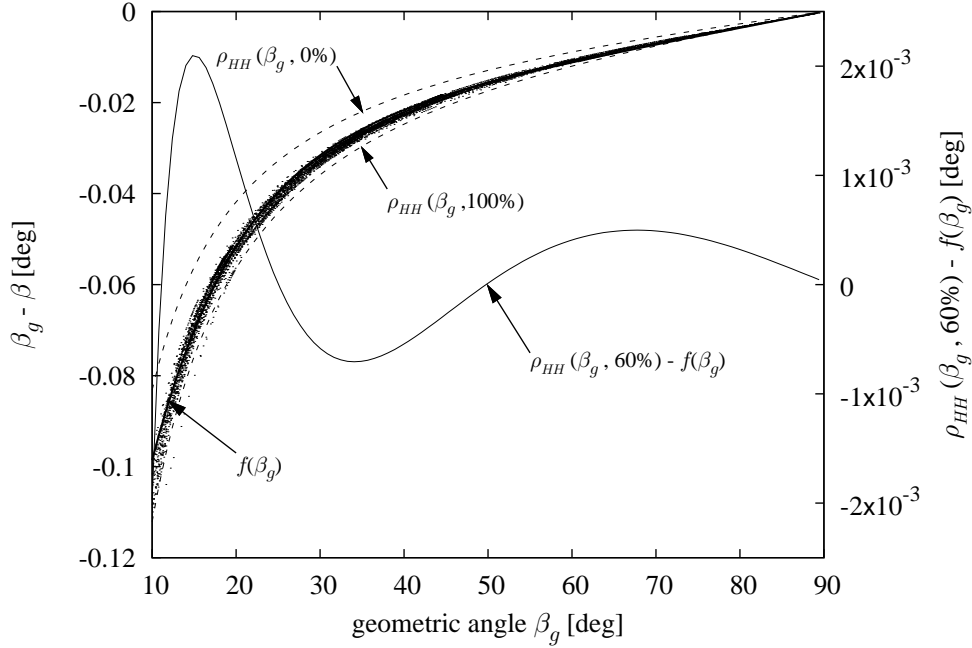


Figure 2.10: Difference between the geometric angle β_g and the elevation β from the HIRLAM NWP model using a realistic GPS satellite geometry and 15 GPS sites. Data are collected over a period of four weeks. Also plotted is a fit $f(\beta_g)$ of the data, refractivity curves for C-band waves denoted as $\rho_{HH}(\beta_g, \text{RH})$ (for $\text{RH} = 0\%$ and 100%) according to Huuskonen and Holleman (2007), and the difference between $f(\beta_g)$ and $\rho_{HH}(\beta_g, 60\%)$ (right scale).

1976) for different surface relative humidities (RH), and the resulting curves are fitted by the following function, see (Huuskonen and Holleman, 2007)

$$\rho_{HH}(\beta_g, \text{RH}) = \frac{0.0155 + 0.000054 \cdot \text{RH}}{\tan(\beta_g + 8.0/(\beta_g + 4.23))}. \quad (2.21)$$

The dashed lines mark the $\text{RH} = 0\%$ and $\text{RH} = 100\%$ refractivity curves; these lines characterise the meteorological boundaries. The few data points below the $\text{RH} = 100\%$ curve are from the GPS site ONSA. The slant algorithm was less accurate for low elevations at this GPS site because the antenna for this site was below the NWP orography. The function $f(\beta_g)$ lies close to the C-band refractivity curve of $\text{RH} = 60\%$ as can be seen in Figure 2.10, where the right-hand scale shows the difference between the two curves.

In the following the function $f(\beta_g)$ is used as initial offset for the elevation. Using this offset the algorithm converges within one or two steps. The Slant Total Delay and Slant Water Vapour is determined using the numerical integration as defined in Equations 2.11, 2.12 and 2.13 with an additional factor for each layer equal to the ratio of ds_{i+1} and $r_{i+1} - r_i$. The algorithm presented above treats the refractivity in a layer as constant. A linear approximation of the refractivity could be a refinement of the algorithm described above.

2.4 DATA QUALITY AND VALIDATION²

For the month May 2003 GPS data processed by TUD-DEOS (Delft institute for Earth Oriented Space Research, Delft University of Technology) are compared to NWP (HIRLAM analysis), another GPS processing method (precise point positioning by GFZ, Geo Forschungs Zentrum Potsdam, Germany) and two radiosondes sites (10 sec data from synoptic launches at De Bilt and 2 sec data from radiosonde observations at Cabauw from the Baltex Bridge Campaign-2 (BBC2)). The method used to derive ZTD and IWV from NWP and radiosondes is described in Section 2.3.1; the method to derive IWV from GPS ZTD is described in Section 1.2. Nowadays, the technique of retrieving IWV from GPS observations is stable. A number of studies showed that the differences between radiosondes IWV, GPS IWV and radiometers are within 2 kg m^{-2} (Rocken et al., 1993, 1995, 1997; Emardson et al., 1998, 2000; Liou et al., 2001; Niell et al., 2001; Stoew et al., 2001; Guerova et al., 2003). Niell et al. (2001) reported on an intensive study on comparison between different methods of observing ZWD. The standard deviations that were found in this study between GPS and radiosonde ZWD observations were about of 10 mm; errors between ZWD obtained from water vapour radiometer and radiosonde or GPS were roughly 7 mm.

Two data sources are used in this validation: data processed by TUD-DEOS and by GFZ. Both processing networks have an overlap but use different processing schemes. The TUD processing network that is selected for processing is a regional network of 17 stations, of which 12 stations are in or very close to the Netherlands. It is basically the same network that has been selected for the routine coordinate computations in the Netherlands (van der Marel, 2002), with the exception of a new receiver in Cabauw (abbreviated as CABW) which is added to the network for this research. The temporal resolution of these GPS estimates is 10 minutes. Data from GFZ are processed using a precise point positioning (PPP) technique as described in Zumbege et al. (1997). The temporal resolution of these GPS estimates is 30 minutes.

HIRLAM analysis are made every six hours and are based on observations of in total three hours. The main weight lies on the observations around the assimilation time. Synoptic radiosonde launches at De Bilt are conducted every 12 hours. These radiosonde observations are used in the HIRLAM assimilation scheme which produces an analysis field. The radiosonde launches performed at Cabauw were conducted within the BBC2 campaign, and were launched mainly during daytime without a specific schedule: these launches were not used in the assimilation of HIRLAM. To be able to compare the timeseries of NWP, GFZ and radiosonde with TUD data, the temporal resolution of TUD solutions is reduced from 10 minutes to 30 minutes by averaging. Comparisons of ZTD is discussed in the next subsection; hereafter IWV comparison are shown.

Here GPS slant observations are not validated because we do not have an independent slant water observation. Ware et al. (1997) obtained SWV using double differencing with precise orbits. They found a 1.3 kg m^{-2} RMS (scaled to the zenith) agreement with a pointed

²This section based on: S. de Haan, H. van der Marel, B. Gündlich, S. J. M. Barlag (2005), Resolving spatial and temporal atmospheric water vapour structures using a ground based GPS receiver network, Final Report: SRON project EO-050, *Chapter 4*.

Table 2.1: Height and differences in height of GPS antenna z_a , HIRLAM 22 km orography z_{NWP} and actual orography (GTOPO) z_{GTOPO} above mean sea level. GTOPO data are distributed by the Land Processes Distributed Active Archive Center (LP DAAC), located at the U.S. Geological Survey’s EROS Data Center <http://LPDAAC.usgs.gov>.

| Site | z_a | z_{NWP} | $z_{NWP} - z_{GTOPO}$ | $z_a - z_{GTOPO}$ | $z_a - z_{NWP}$ |
|------|----------|-----------|-----------------------|-------------------|-----------------|
| APEL | 72.49 m | 23.21 m | 9.21 m | 58.49 m | 49.28 m |
| BORK | 14.07 m | 0.21 m | 0.21 m | 14.07 m | 13.86 m |
| BRUS | 104.28 m | 72.44 m | -17.56 m | 14.28 m | 31.84 m |
| CABW | 2.00 m | 0.86 m | -0.14 m | 1 m | 1.14 m |
| DELF | 30.89 m | -0.98 m | 2.02 m | 33.89 m | 31.87 m |
| EIJS | 57.45 m | 131.28 m | 76.28 m | 2.45 m | -73.83 m |
| EUSK | 198.03 m | 214.96 m | 46.96 m | 30.03 m | -16.93 m |
| HELG | 9.26 m | -0.61 m | -0.61 m | 9.26 m | 9.87 m |
| HERS | 31.47 m | 42.18 m | 17.18 m | 6.47 m | -10.71 m |
| KOSA | 53.44 m | 30.08 m | -9.92 m | 13.44 m | 23.36 m |
| KOSG | 54.49 m | 30.08 m | -9.92 m | 14.49 m | 24.41 m |
| ONSA | 9.02 m | 16.75 m | 3.75 m | -3.98 m | -7.73 m |
| POTS | 104.11 m | 40.60 m | -23.40 m | 40.11 m | 63.51 m |
| TERS | 14.72 m | 0.56 m | 0.56 m | 14.72 m | 14.16 m |
| WSRA | 41.14 m | 12.92 m | -2.08 m | 26.14 m | 28.22 m |
| WSRT | 44.47 m | 13.22 m | -1.78 m | 29.47 m | 31.25 m |
| WTZR | 619.24 m | 594.66 m | 7.66 m | 32.24 m | 24.58 m |

radiometer for observations above 20 degrees elevation agree. A more comprehensive study by Braun et al. (2003) showed a similar result.

2.4.1 ZTD COMPARISON

In Table 2.1 the height of the GPS antenna, the height of the HIRLAM orography, and differences between the actual orography (2 km orography deduced from GTOPO) and HIRLAM orography, and differences between the height of a GPS antenna and both orographies are shown (all heights are above mean sea level). For the GPS sites BRUS and POTS the HIRLAM orography lies more than 15 m below the actual orography. For the sites EIJS, EUSK and HERS the HIRLAM orography lies more than 15 m higher than the actual orography. As a consequence, the antenna position is below the HIRLAM surface (for EIJS even more than 73 m). A large deviation between the HIRLAM orography and actual orography (negative or positive) may introduce errors, especially when the orography of HIRLAM is higher than the GPS antenna. Also shown in the one-but-last column of this table is the height of the antenna above the 2 km orography. Note that, according to the height of the antenna and the orography, ONSA antenna lies below the surface. This is probably due to the resolution of the GTOPO-data set.

In Table 2.2a the results of the statistics of two comparisons are shown: HIRLAM versus TUD and GFZ versus TUD. Table 2.2b shows the comparison statistics of time collocated data from the three sources.

Table 2.2: Statistics of comparison of ZTD estimates between TUD and HIRLAM analysis and GFZ, respectively, in [mm]; a) for all sites separately and b) for collocation in time.

| a) | | $ZTD_{NWP} - ZTD_{TUD}$ | | | $ZTD_{GFZ} - ZTD_{TUD}$ | | | |
|------|-----|-------------------------|-------|--------|-------------------------|------------------------|------|--------|
| Site | num | \overline{ZTD}_{TUD} | bias | stddev | num | \overline{ZTD}_{TUD} | bias | stddev |
| APEL | 97 | 2402.7 | -3.6 | 12.9 | 456 | 2416.3 | -1.1 | 6.8 |
| BORK | 97 | 2428.3 | -20.3 | 12.4 | | | | |
| BRUS | 97 | 2398.0 | 0.1 | 12.5 | 470 | 2410.7 | 1.4 | 6.9 |
| CABW | 97 | 2430.3 | -9.3 | 13.1 | | | | |
| DELF | 97 | 2414.3 | -5.2 | 13.3 | 475 | 2427.2 | -1.8 | 6.6 |
| EIJS | 97 | 2418.4 | -4.8 | 11.4 | 466 | 2429.0 | -2.4 | 6.3 |
| EUSK | 97 | 2397.4 | -25.2 | 13.0 | | | | |
| HELG | 96 | 2417.5 | -9.7 | 13.3 | 469 | 2425.2 | -2.7 | 7.2 |
| HERS | 97 | 2408.3 | -2.4 | 13.5 | 460 | 2426.8 | -2.8 | 7.1 |
| KOSG | 97 | 2413.3 | -8.0 | 12.8 | | | | |
| TERS | 97 | 2412.8 | -8.0 | 12.3 | 460 | 2421.5 | -2.8 | 6.2 |
| WSRA | 96 | 2415.5 | -10.6 | 12.7 | 423 | 2426.9 | -5.3 | 6.3 |
| WSRT | 97 | 2414.4 | -10.6 | 12.7 | | | | |
| WTZR | 96 | 2255.6 | 5.1 | 16.7 | 419 | 2255.1 | -0.7 | 7.0 |

| b) | | $ZTD_{NWP} - ZTD_{TUD}$ | | | $ZTD_{GFZ} - ZTD_{TUD}$ | |
|------|-----|-------------------------|-------|--------|-------------------------|--------|
| Site | num | \overline{ZTD}_{TUD} | bias | stddev | bias | stddev |
| APEL | 42 | 2413.2 | -5.8 | 12.7 | -0.3 | 5.1 |
| BRUS | 42 | 2408.1 | -1.6 | 13.2 | 1.8 | 6.0 |
| DELF | 42 | 2424.5 | -7.0 | 13.2 | -1.0 | 5.9 |
| EIJS | 41 | 2428.0 | -6.2 | 13.3 | -2.1 | 6.2 |
| HELG | 42 | 2424.5 | -10.2 | 15.3 | -2.6 | 5.7 |
| HERS | 41 | 2423.8 | -5.0 | 14.5 | -1.9 | 7.3 |
| TERS | 41 | 2422.5 | -9.7 | 15.0 | -2.7 | 5.5 |
| WSRA | 39 | 2425.5 | -11.3 | 15.3 | -4.9 | 6.8 |
| WTZR | 41 | 2253.5 | 1.7 | 17.0 | -1.1 | 7.4 |

There are two large outliers with high absolute biases between TUD and HIRLAM: BORK and EUSK. It turned out that both BORK and EUSK had problems with their antenna. The antenna on BORK did not function well and was replaced after the BBC2 campaign. Initially, for EUSK the wrong antenna type was specified in the GPS processing. This was soon discovered in the elevation plots of the residuals which had exceptionally large values, ranging from 10 mm in the zenith, down to -15 mm at 10 degrees elevation.

When the correct antenna type was set in the software, the estimated ZTD decrease by about 2 cm, and the height coordinate increased by 7 cm. This again shows the sensitivity of the results for the correct specification of the elevation dependent phase delays in the GPS antenna. The sites CABW, HELG, KOSG, TERS and WSRT and WSRA have biases around

-8 mm to -10 mm when TUD is compared to HIRLAM analysis. All other sites have smaller biases. The standard deviation for this month is around 13 mm, except for the site WTZR.

When ZTD_{TUD} is compared to GFZ we see that WSRA has a large bias. Although the bias with HIRLAM is also large, it is suspected that there were some problems with processing WSRA by TUD or GFZ. WSRT uses the same antenna as WSRA, but a different receiver, and shows nearly the same bias with HIRLAM: this site has most likely the same problems as WSRA. This bias could be related to the un-calibrated conical radome that is used on WSRT and WSRA, which results in a similar problem, but of smaller magnitude, compared to EUSK. The reason that GFZ observes a different bias is probably related to the different elevation cut-off angle that GFZ is using. The standard deviation is around 6 to 7 mm for all stations, which can be explained by the difference in temporal resolution (TUD uses 10 minutes; GFZ uses 30 minutes).

When all three data sources are compared simultaneously (Table 2.2b) we see that TUD-WSRA has a large bias with GFZ-WSRA and HIRLAM. For all GPS sites, except BRUS, ZTD_{TUD} is larger than ZTD_{GFZ} . When compared to ZTD estimates from the HIRLAM analysis ZTD_{TUD} is larger than ZTD_{NWP} , for all GPS sites except BRUS and WTZR.

2.4.2 IWV COMPARISON

The IWV comparison between TUD and HIRLAM highlights the same stations BORK and EUSK where extreme ZTD values occurred, see Table 2.3a. All stations have a standard deviation with respect to HIRLAM of around 2 kg m^{-2} , except again WTZR. Comparing GFZ and TUD, WSRA has a relatively large bias (due to the difference in ZTD). All standard deviation of the IWV comparison between GFZ and TUD are around 1 kg m^{-2} . Note that all sites, except WTZR, the IWV_{TUD} is larger than IWV_{NWP} . At first thought the IWV comparison seems a copy of the ZTD comparison, however, because the algorithm to calculate IWV from NWP is different from the calculation of ZTD from NWP this comparison is useful, which shows that the difference is related to the algorithms separately but due to the NWP model state.

The TUD solutions are a network solution constructed by the Bernese Software (Rothacher and Mervart, 1996); GFZ uses a different technique: PPP. Stoew et al. (2001) showed that biases between network and PPP solution may range from 0.03 to 0.13 kg m^{-2} and standard deviation range from 0.22 and 0.33 kg m^{-2} ; this study used data from one year and both data sets (most likely) are the same and have the same temporal resolution. The biases shown in Table 2.3 between a network solution of TUD and PPP solution of GFZ cannot be explained by this study, although part of the difference in standard deviations has its cause in the difference in temporal resolution and the length of the period.

For all valid radiosonde launches in the period under consideration, we have determined the IWV value from the two radiosonde data sets. When radiosonde IWV observations from De Bilt are compared with GPS data in DELF, a correction for the height difference of the antenna at the start of the profile is performed: the IWV value is calculated from a different starting level. For APEL a different (i.e. higher) starting height is being used, see Table 2.1. Only

Table 2.3: Statistics of comparison of IWV estimates between TUD and HIRLAM-analyses and GFZ, respectively, in [kg m^{-2}]; a) for all sites separately and b) for collocation in time.

| a) | | $\text{IWV}_{NWP} - \text{IWV}_{TUD}$ | | | $\text{IWV}_{GFZ} - \text{IWV}_{TUD}$ | | | |
|------|-----|---------------------------------------|------|--------|---------------------------------------|-------------------------------|------|--------|
| Site | num | $\overline{\text{IWV}}_{TUD}$ | bias | stddev | num | $\overline{\text{IWV}}_{TUD}$ | bias | stddev |
| APEL | 97 | 17.5 | -0.6 | 2.1 | 456 | 20.6 | 0.0 | 1.2 |
| BORK | 97 | 19.4 | -3.2 | 2.0 | | | | |
| BRUS | 97 | 17.9 | -0.1 | 2.0 | 470 | 20.6 | 0.3 | 1.1 |
| CABW | 97 | 18.9 | -1.5 | 2.1 | | | | |
| DELF | 97 | 17.7 | -0.9 | 2.2 | 475 | 20.6 | -0.2 | 1.1 |
| EIJS | 97 | 18.9 | -0.7 | 1.8 | 466 | 21.3 | -0.3 | 1.0 |
| EUSK | 97 | 21.5 | -4.0 | 2.1 | | | | |
| HELG | 96 | 17.5 | -1.4 | 2.1 | 469 | 19.7 | -0.4 | 1.1 |
| HERS | 97 | 16.6 | -0.3 | 2.2 | 460 | 20.4 | -0.5 | 1.1 |
| KOSG | 97 | 18.4 | -1.3 | 2.0 | | | | |
| TERS | 97 | 17.2 | -1.4 | 1.9 | 460 | 19.6 | -0.5 | 1.0 |
| WSRA | 96 | 18.4 | -1.7 | 2.0 | 423 | 21.1 | -0.7 | 1.0 |
| WSRT | 97 | 18.4 | -1.7 | 2.0 | | | | |
| WTZR | 96 | 16.4 | 0.5 | 2.7 | 419 | 16.4 | -0.1 | 1.1 |

| b) | | $\text{IWV}_{NWP} - \text{IWV}_{TUD}$ | | | $\text{IWV}_{GFZ} - \text{IWV}_{TUD}$ | |
|------|-----|---------------------------------------|------|--------|---------------------------------------|--------|
| Site | num | $\overline{\text{IWV}}_{TUD}$ | bias | stddev | bias | stddev |
| APEL | 42 | 20.1 | -0.9 | 2.0 | 0.2 | 0.9 |
| BRUS | 42 | 20.2 | -0.3 | 2.1 | 0.4 | 1.0 |
| DELF | 42 | 20.2 | -1.2 | 2.2 | -0.1 | 0.9 |
| EIJS | 41 | 21.2 | -1.0 | 2.1 | -0.3 | 1.0 |
| HELG | 42 | 19.5 | -1.4 | 2.3 | -0.4 | 0.9 |
| HERS | 41 | 19.9 | -0.8 | 2.3 | -0.3 | 1.1 |
| TERS | 41 | 19.9 | -1.7 | 2.5 | -0.4 | 0.9 |
| WSRA | 39 | 20.9 | -1.8 | 2.5 | -0.6 | 1.0 |
| WTZR | 41 | 16.2 | 0.0 | 2.8 | -0.2 | 1.2 |

the radiosonde Cabauw is collocated with a GPS receiver; De Bilt lies in between DELF and APEL, with distance of approximately 55 km to both sites. The distance between Cabauw and De Bilt is 31 km. From Table 2.4.2 we see that HIRLAM-analyses compared to RS Cabauw have the smallest bias. The bias between HIRLAM-analyses at APEL and radiosonde De Bilt is caused by the height of the start of the radiosonde profile, which is 58 m lower than the GPS antenna height. Moreover, between APEL and De Bilt lies a plateau with heights 100 m above mean sea level. This plateau may influence the stability of the atmospheric profile and thus change the amount of water vapour. The difference between orographic height at Delft and De Bilt is smaller and there are no large orographic obstacles between DELF and De Bilt.

The comparison between IWV_{RS} and IWV_{TUD} at Cabauw shows a large bias but a very

Table 2.4: Statistics of comparison of IWV estimates between RS and HIRLAM-analyses TUD and GFZ, respectively.

| RS | num | \overline{IWV}_{RS} | $IWV_{RS} - IWV_{NWP}$ | | Site | AC | num | \overline{IWV}_{RS} | $IWV_{RS} - IWV_{GPS}$ | |
|---------|-----|-----------------------|------------------------|--------|-------|-----|-----|-----------------------|------------------------|--------|
| | | | bias | stddev | | | | | bias | stddev |
| De Bilt | 55 | 16.4 | -0.9 | 1.7 | APEL | TUD | 46 | 17.9 | -1.5 | 1.9 |
| | | | | | | GFZ | 26 | 20.6 | -1.3 | 1.9 |
| Cabauw | 30 | 16.4 | -0.2 | 1.7 | CABW | TUD | 76 | 18.4 | -2.1 | 1.0 |
| De Bilt | 55 | 16.6 | -0.4 | 1.6 | DELFF | TUD | 46 | 18.2 | -1.5 | 1.7 |
| | | | | | | GFZ | 26 | 20.6 | -1.5 | 1.9 |

small standard deviation. It has been noted before that the IWV_{GPS} tends to be higher than the IWV_{RS} . However, the bias found here is high. The bias between GPS (both GFZ and TUD) IWV DELF and RS De Bilt is smaller than for the observed bias in Cabauw. The standard deviation is mainly due to the distance between DELF and De Bilt. The same holds for the standard deviation of the comparison between IWV_{GPS} from APEL and IWV_{RS} from De Bilt.

2.5 SUMMARY

In this chapter background information has been presented on operational observation techniques of atmospheric water vapour. The current operational network of radiosondes is distributed on a synoptic scale. Smaller water vapour scales are not sampled by radiosonde observations. At present, processed data from GPS networks are available. This data contain atmospheric humidity information. The horizontal and temporal coverage of these observations over Europe is very good, apart from the oceans. In some regions the GPS networks have a density of around 50 km.

Six-hour autocorrelation of specific humidity from radiosonde has a distinct signature below and above a height of 2 km, with the highest autocorrelation in the levels closest to the surface. The six-hour variability in IWV, as observed by radiosonde observations correlates highly with six-hour specific humidity variations as observed by radiosonde.

Ray tracing algorithms have been developed and are used to estimate ZTD, IWV and slant path information from NWP model data. These algorithms can also be used to estimate GPS related atmospheric parameters from radiosonde profiles.

The accuracy of GPS ZTD and IWV from GPS data processed by TUD (and GFZ) is as expected. Standard deviation of ZTD versus NWP analysis is around 14 mm with varying biases related to differences in height between the actual orography and the NWP model orography. The standard deviation of GPS IWV versus NWP analysis is around 2 kg m⁻². The biases change in a similar manner as for the ZTD. The accuracy of IWV is around 10% of the observed value. When compared to radiosondes, the accuracy is slightly better with values between 5-10%.

Chapter 3

The influence on GPS estimates of NWP derived mapping functions¹

When estimating zenith total delays (ZTD) from global positioning system (GPS) signals it is assumed that the atmosphere is symmetric in the horizontal plane and that delays in the signal from one of the GPS satellites to a receiver can be mapped onto the zenith direction through a known mapping function. The generally used mapping function has only a dependence on the day of the year and the latitude of the receiver. The fact that these mapping functions do not depend on the actual weather may introduce errors in estimates of the location parameters and the estimate of the ZTD. In this chapter mapping functions from numerical weather prediction (NWP) models are derived and the influence on the accuracy of location parameters and ZTD estimates is investigated during a cold front passage in the Netherlands on the 30th of October 2000. The hydrostatic mapping function computed from NWP was smaller than the Niell mapping function (0.02 at 5 degree elevation). The differences for the wet mapping function were much larger, and of opposite sign. However, since the hydrostatic delay is larger than the wet delay, we found that the geodetic parameters are mainly influenced by errors in the hydrostatic mapping function. Using an elevation cut-off error of 10 degrees, we observed systematic errors in the estimated ZTD of -2.1 to -3.1 mm, in the clock error of 6.5 to 9.2 mm and in the height of 4.8 to 6.5 mm.

3.1 INTRODUCTION

The accuracy of zenith tropospheric delay and position and height of a GPS site is closely related to the uncertainty in the (a priori) knowledge of the path delay through the atmosphere. The wet path delay is highly correlated to the (local) distribution of water vapour. The uncertainties in the characteristics of the path delay, both wet and hydrostatic, increase with decreasing elevation of the signal.

¹This chapter is previously published in *Phys. Chem. Earth*, 2004, **29**, pp 159-166, by S. de Haan and H. van der Marel.

The ratio between the delay at the elevation of observation and the zenith delay is used to characterise the influence of the atmosphere at different elevations. One of the most commonly used mapping functions is constructed by Niell (1996). Mapping functions have a hydrostatic and wet component (Davis et al., 1985). The Niell mapping functions have a dependence on site location and day of the year. Mapping functions can also be derived from numerical weather prediction (NWP) models. The atmospheric representation in NWP models are expected to be good, although (of course) not correct because a NWP model is a reconstruction of the real atmosphere.

In this chapter, we derive the hydrostatic and wet mapping functions from NWP and compare them to the Niell mapping functions and give an estimate of the influence of NWP mapping functions on the GPS position and zenith delay. Mapping functions derived from radiosonde observations are also compared with Niell mapping functions. We choose a period of 3 days (29-31th October 2000) for which the zenith total delay showed large changes due to the passing of a cold front.

3.2 MAPPING FUNCTIONS

One of the essential assumptions in the processing of GPS data is that the delay in the signal from a GPS satellite to a receiver can be mapped onto the zenith direction using a known function, the so-called mapping function. Mapping functions are different for the hydrostatic and wet delay.

3.2.1 NIELL MAPPING FUNCTION

Both Niell mapping functions, hydrostatic (m_h^{Niell}) and wet (m_w^{Niell}), are represented as a continued fraction normalised to the unity at zenith, that is

$$m(\beta) = \frac{1 + \frac{a}{1 + \frac{b}{1+c}}}{\sin(\beta) + \frac{a}{\sin(\beta) + \frac{b}{\sin(\beta)+c}}}, \quad (3.1)$$

where β is the elevation. The m_w^{Niell} has coefficients which are only dependent on latitude and day of the year. The latitude dependence is piecewise linear while the day of the year dependence is based on a cosine function. The hydrostatic mapping function has an additional linear dependence on the height above mean sea level of the GPS antenna. This height dependence is the sum of $1/\sin(\beta)$ and a continued fraction multiplied by the height of the antenna. The coefficients have been determined from radiosonde data.

In Figure 3.1 (top part) the hydrostatic and wet mapping functions are shown for the location Delft. At elevations higher than 30 degrees both mapping functions are equal. Due to the distribution of water vapour along the vertical, the difference between the hydrostatic and wet mapping function increases for decreasing elevation. In the bottom part the difference between $1/\sin(\beta)$ and the Niell mapping functions are depicted: again the difference between $1/\sin(\beta)$ increases for decreasing elevation. See Niell (1996) for more details.

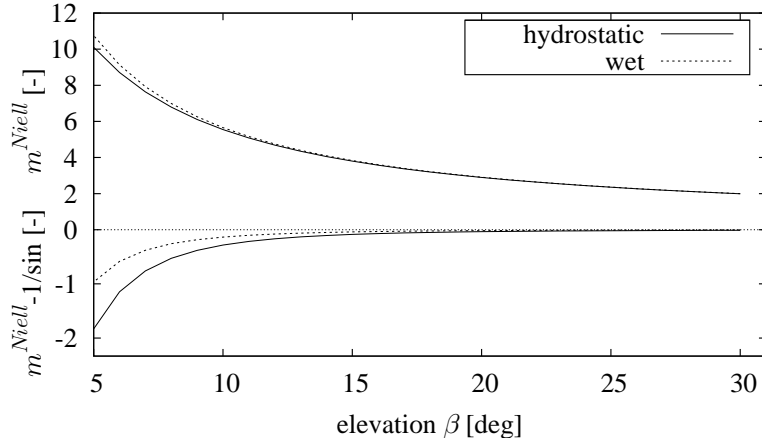


Figure 3.1: Hydrostatic and wet Niell mapping function for Delft at 2000/10/30 (top part) and the difference with $1/\sin(\beta)$ (bottom part). Note the different scales.

3.2.2 MAPPING FUNCTIONS DERIVED FROM NWP

The mapping function is defined as the ratio between slant hydrostatic (wet) delay for a certain elevation and the zenith hydrostatic (wet) delay. Both quantities can be obtained from NWP using numerical integration along a (slant or zenith) path through the model field using the theoretical definition of delay given by

$$\text{STD} = 10^{-6} \int_{z_a}^{\infty} k_1 R_d \rho ds + 10^{-6} \int_{z_a}^{\infty} \frac{R_d}{\epsilon} \left(k_2 - \epsilon k_1 + \frac{k_3}{T} \right) q \rho ds, \quad (3.2)$$

where z_a is the antenna height, R_d is the specific gas constant for dry air, q is the specific humidity and ρ is the density of the air. The constants k_1 , k_2 and k_3 have the following values (Thayer, 1974) $k_1 = 7.76 \cdot 10^{-3}$ [K/Pa], $k_2 = 7.04 \cdot 10^{-1}$ [K/Pa] and $k_3 = 3.74 \cdot 10^3$ [K²/Pa]. The constant ϵ is the ratio between the specific gas constant for dry air and water vapour, that is $\epsilon = \frac{R_d}{R_v}$.

The first term in Eq. 3.2 on the right-hand side is called the slant hydrostatic delay (SHD) and the second term is called the slant wet delay (SWD).

The NWP model we use here is a hydrostatic limited area model with a horizontal resolution of 55 km with 31 levels. The height in NWP is given in pressure and thus we rewrite Eq. 3.2 using the hydrostatic equation. For each level the hydrostatic coordinate transformation is multiplied by the ratio between the zenith height and the slant path length through the level under consideration in the case of a slant observation with an elevation lower than 90 degrees. See de Haan et al. (2002) for more details.

The accuracy of the zenith hydrostatic delay (ZHD) is determined by calculating the ZHD from NWP and compare it to the formula given by Saastamoinen (1972)

$$\text{ZHD}_{\text{Saas}} = \frac{2.2768 \cdot 10^{-5} p_a}{1 - 2.66 \cdot 10^{-3} \cos(2\phi_{\text{gps}}) - 2.8 \cdot 10^{-7} z_{\text{gps}}}, \quad (3.3)$$

where ϕ_{gps} is the latitude of the GPS receiver and z_{gps} the height of the receiver. For the complete HIRLAM grid the bias and RMS between ZHD_{NWP} and ZHD_{Saas} is calculated for all

analysis between 29 October 2000 and 31 October 2000. The bias lies between -0.068 mm and -0.052 mm and the RMS lies between 0.188 mm and 0.198 mm, no orographic signal in the difference between both ZHD estimates was observed. These values are small implying that both estimates of ZHD are close giving reason to trust the numerical integration method.

One should note that, although we call the above method to calculate the ratio between slant delay and zenith delay a mapping function, it is not really a function; it is more an algorithm. However, when we use the phrase “NWP derived mapping function at a certain elevation” we mean the outcome of the ratio for this particular elevation.

3.2.3 MAPPING FUNCTIONS DERIVED FROM RADIOSONDES

Mapping functions can also be derived from radiosondes. The radiosonde profile we used here is the operational radiosonde at De Bilt which is a Vaisala RS90. The observations were performed every 6 hours. The profile consists of a pressure, temperature and relative humidity observation performed every 10 seconds. The Vaisala RS90 radiosonde has two humidity sensors which alternately are heated to avoid contamination by freezing. Some checks may still be needed to guarantee the quality of the observations. Here, because a small number of observations were used, these checks are done manually. Comparison of the ZHD derived from radiosonde profile and the ZHD_{SaaS} was one of the checks.

From the temperature and humidity profile for a certain elevation the SHD and SWD is computed in the same way as for a NWP model. The determination of the mapping function from this radiosonde is straightforward. A single radiosonde profile used here has in general around 500 observations, which is more much more than the 31 the NWP model has. However, the levels of the model are more dense in the planetary boundary, while the radiosonde profile is almost equidistant in the vertical.

3.3 INFLUENCE OF MAPPING FUNCTIONS ON GPS PARAMETERS

To investigate the influence of the difference in mapping functions on the GPS parameters several methods can be applied. One could process the actual GPS data with the NWP derived mapping functions. Here we choose a different approach.

We assume that the NWP slant delays obtained using a realistic GPS constellation is the truth. This is of course not the case because NWP models contain errors in the water vapour distributions. Moreover, the magnitudes of these errors are not exactly known. Still, an NWP model can be regarded as the best estimate of the atmosphere using all (at the time of assimilation) available data.

Knowing the “true” slant delay (STD) we calculate the ZTD and other GPS parameters using the Niell mapping functions in the usual way. The linearised functional model for GPS

single difference observations, or Precise Point Positioning (Zumberge et al., 1997), is

$$E\{\Delta \underline{y}\} = \begin{bmatrix} \cos \alpha \cos z & \sin \alpha \cos z & \sin z & c & m_w^{Niell} & \lambda \end{bmatrix} \begin{bmatrix} \Delta N \\ \Delta E \\ \Delta U \\ \Delta \delta t_r \\ \Delta ZWD \\ \Delta A_r^s \end{bmatrix} \quad (3.4)$$

with α the azimuth of the satellite, z the zenith angle, c speed of light, m_w^{Niell} the wet Niell mapping function, λ the wavelength of the carrier phase observations, ΔN , ΔE and ΔU the unknown corrections in North, East and Up for the position, $\Delta \delta t_r$ the receiver clock correction, ΔZWD the zenith wet delay and ΔA_r^s the carrier phase ambiguity. Satellite clock errors are not present in this model, either because single difference observations are used in which the satellite clock errors are eliminated (in the single difference observations from two receivers to the same satellite are subtracted), or because the satellite clock errors and satellite orbits have been computed previously in a global adjustment. The second approach is known as Precise Point Positioning. The ‘‘observations’’ that are used in the simulation are computed from the slant delays given by the NWP as follows

$$\Delta y = \text{STD}_{NWP} - m_h^{Niell} \text{ZHD}_0 \quad (3.5)$$

with STD_{NWP} the slant delay from the NWP model, m_h^{Niell} the hydrostatic Niell mapping function and ZHD_0 an a-priori zenith hydrostatic delay. Note that in this approach the full slant delay for an individual station is taken, and not the (single) difference with some reference station. This is not a problem considering that the slant and zenith delay at the reference station act as a reference, and postulate that it must be consistent with the Niell mapping function. Actually, this approach is more typical for Precise Point Positioning.

The slant delays are generated from a NWP model using the actually observed GPS constellation. Stacking all the observations and unknowns, the following system of linear equations is obtained which can be solved by standard least-squares

$$E\{\Delta \underline{y}\} = \mathbf{A} \Delta \underline{x} = [\mathbf{A}_{coord} \quad \mathbf{A}_{clock} \quad \mathbf{A}_{ZWD} \quad \mathbf{A}_{amb}] \begin{bmatrix} \Delta x_{coord} \\ \Delta x_{clock} \\ \Delta x_{ZWD} \\ \Delta x_{amb} \end{bmatrix} \quad (3.6)$$

Receiver clock and zenith delay parameters are introduced for every epoch. The coordinates either do not change during the observation interval (static solution) or a new set of coordinates can be introduced for every observation epoch (kinematic solution). Finally, a carrier phase ambiguity parameter is introduced for every satellite pass. This system of equations is rank-defect, which we may solve simply by lumping one of the ambiguity parameters with the clock parameters. The least-squares solution is

$$\hat{\underline{x}} = (\mathbf{A}^T \mathbf{Q}_y^{-1} \mathbf{A})^{-1} (\mathbf{A}^T \mathbf{Q}_y^{-1}) \underline{y} \quad (3.7)$$

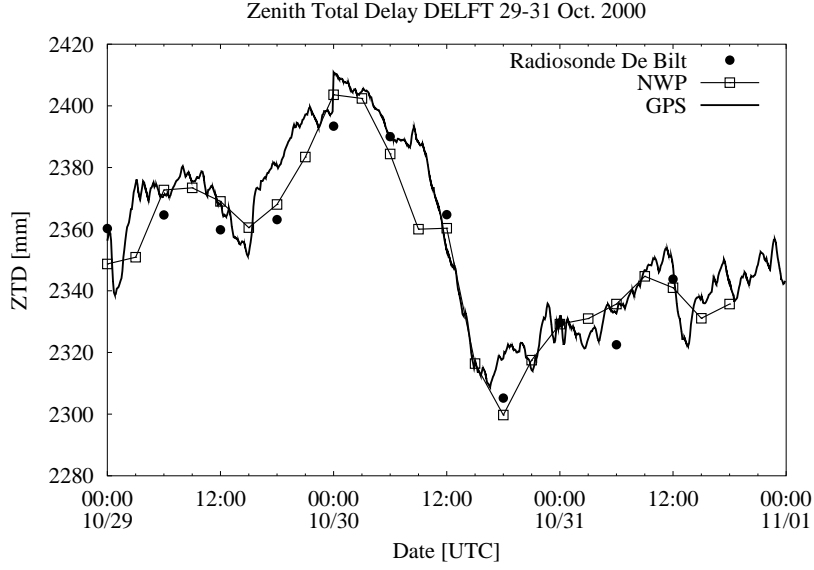


Figure 3.2: Timeseries of zenith total delay estimates from Radiosonde, GPS and NWP.

with \mathbf{Q}_y the co-variance matrix for the observations. The estimated zenith total delay (ZTD) is equal to

$$\widehat{ZTD} = ZHD_0 + \Delta ZWD \quad (3.8)$$

The error in the ZTD estimation we make as a result of the approximate nature of the mapping functions is then

$$\Delta ZTD = \widehat{ZTD} - ZTD_{NWP} \quad (3.9)$$

while, the error in the coordinates and other parameters is directly given by ΔN , ΔE , ΔU and $\Delta \delta t_r$.

3.4 CASE STUDY

On the 30 October 2000 a barotropic low passed over the North Sea. Together with this depression a cold front passed the Netherlands, which resulted in a drop in IWV from around 24 kg m^{-2} to 13 kg m^{-2} . The zenith total delay as observed by the permanent GPS network in the Netherlands showed a decay from 2400 mm to around 2320 mm within 6 hours. Time series of the ZTD for the GPS site Delft are shown in Fig. 3.2. Also shown in this figure are the estimates of the ZTD from radiosonde observations from the 6 hourly launches performed at De Bilt, some 60 km inland in the Netherlands and the ZTD estimates obtained from NWP at the GPS site. The GPS ZTD estimates are obtained using the GIPSY software at a 6 minute interval with a processing window of 24 hours. The used cut-off elevation in the processing is 10 degrees.

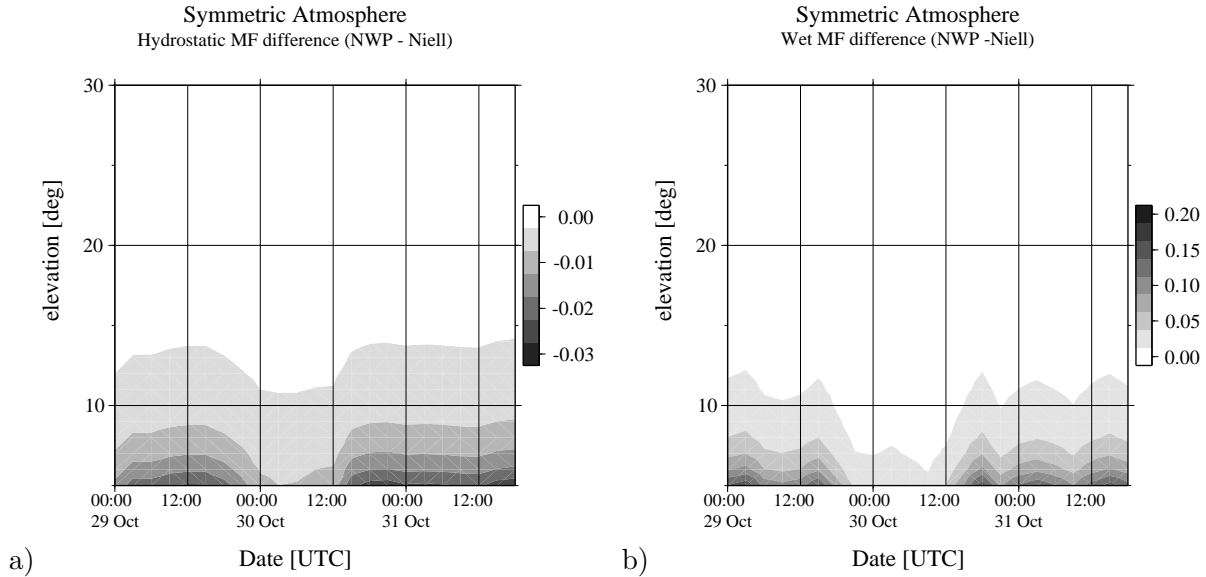


Figure 3.3: Difference between hydrostatic part, and wet part, of the Niell mapping function and the NWP mapping function. Time is on the horizontal axis and the vertical axis is the elevation. The difference between m_h^{Niell} and m_h^{NWP} is shown in panel a and the difference between m_w^{Niell} and m_w^{NWP} in panel b. The scale of the difference is shown on the right-hand-side of each panel.

3.4.1 NIELL AND NWP MAPPING FUNCTIONS DIFFERENCE

For the period from 29 October to 31 October 2000 the difference between the Niell and NWP mapping functions are determined for the GPS site Delft. Because Niell mapping functions have no azimuthal dependence, a symmetric atmosphere is constructed from the NWP model. The temperature and humidity profile above the GPS site are expanded horizontally to obtain a horizontally stratified atmosphere.

Figure 3.3a shows the difference between the symmetric m_h^{NWP} and the m_h^{Niell} for the period under consideration. On the horizontal axes is the date and on the vertical axis is the elevation. For elevations above 15 degrees the difference between both mapping functions is very small. For all times a maximum in the difference is observed at an elevation of 5 degrees. At this elevation the m_h^{Niell} is approximately 0.02 larger than the m_h^{NWP} . The moment of cold front passage is also visible in Fig. 3.3a by the increase in difference towards lower elevations.

The difference between the m_w^{Niell} and m_w^{NWP} is shown in Fig. 3.3b. The difference of the wet mapping function is a factor 15 larger than the difference for the hydrostatic mapping function. Note also that the maximum of the difference is at the lowest elevations and steadily decreasing with decreasing elevation.

Although the difference between the hydrostatic mapping functions is a factor 10 smaller than the difference in wet mapping functions, the effect on the GPS processing is approximately of the same order (at 5 degrees elevation). This is due to the fact that in the GPS processing the hydrostatic mapping function is used to map an (a priori) hydrostatic slant delay to the zenith and this value is a factor 20 larger than the wet slant delay. This implies that in the

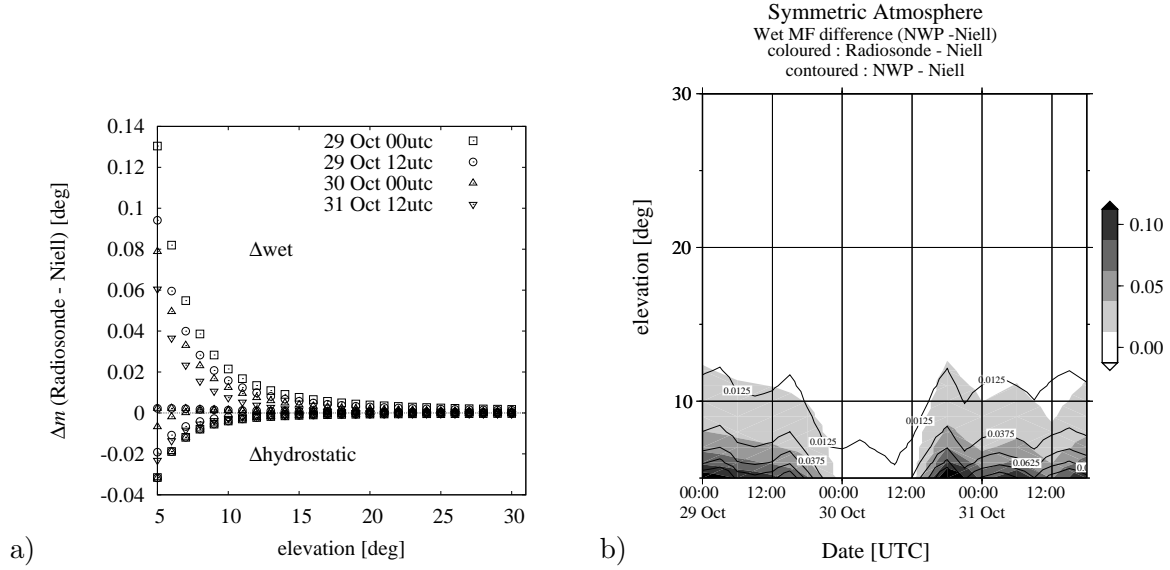


Figure 3.4: Difference in wet and hydrostatic mapping functions between Niell and radiosonde. Panel a shows both difference for four dates : 29 Oct 00:00 UTC and 12:00 UTC, 30 Oct 00:00 UTC and 30 Oct 12:00 UTC. Panel b shows the difference between m_w^{Niell} and m_w^{RS} . Time is on the horizontal axis and the elevation is on the vertical axis. The scale of the difference is shown on the right-hand-side of panel b. Contour lines of the difference between m_w^{Niell} and m_w^{NWP} are also shown in panel b.

GPS processing the error in the mapping functions could more or less cancel out, although, as we will see in Section 3.4.3, the error in the wet mapping function is not able to compensate for the error in the hydrostatic mapping function.

3.4.2 NIELL AND RADIOSONDE MAPPING FUNCTIONS DIFFERENCE

For the same period as before all radiosonde launches were used to derive mapping functions. A number of these launches had a profile that was too short, which resulted in an erroneous estimate of the ZHD. The ZWD is related to humidity information and has therefore a very small deterioration when only a short profile is observed. In Fig. 3.4a the difference between the Niell mapping function and the radiosonde mapping function for four launches is shown. Only four are shown because of a few short profiles and in order to keep the plot readable. In Fig. 3.4b a similar plot as Fig. 3.3b is shown; all 6 hourly observations with good quality were used for this plot. Also shown in this figure are contour lines of the difference between the m_w^{Niell} and m_w^{NWP} as presented in Fig. 3.3b.

The positive difference between the m_h^{Niell} and the m_h^{RS} has the same sign and magnitude as the difference between m_h^{Niell} and m_h^{NWP} . The same is true for the wet mapping functions as can be seen by comparing the grey shades in Fig. 3.3b with the contour lines in Fig. 3.4b. This is not surprising because the radiosonde observation was used in the analysis of the model, however a good radiosonde profile has around 500 observations which contains more detail compared to the NWP model which has 31 levels.

3.4.3 INFLUENCE ON GPS PARAMETERS

The influence of the NWP derived mapping function on the GPS parameters has been computed using the simulation method described in Section 3.3. Slant delays have been computed from the NWP model for the three day period of 29–31 October 2000 using the actually observed GPS constellation on these days. An elevation cut-off angle of 10 degrees was used. For the standard deviation of the observations a value of 9 mm was used, which is representative for the ionosphere free linear combination. The effect of taking single differences was taken into account by multiplying the standard deviations of the observations by a factor of $\sqrt{2}$. Although data points were generated every 6 minutes, the NWP model could only generate slant delays every 3 hours. This is often not enough to estimate the carrier phase ambiguities. Therefore, in this study we did not include the estimation of ambiguity parameters in our model and therefore we have an ambiguity fixed model. Although this is not very realistic, van der Marel and de Haan (2002) observed that, under the long observation time spans we have here, the effect of ambiguity fixing is not very significant. Nevertheless, we plan to include ambiguity estimation in future simulations.

Two types of slant delays were generated from the NWP model: i) slant delays for an asymmetric atmosphere in the model, and ii) slant delays assuming a symmetric atmosphere in the model. In case of the asymmetric atmosphere for each position crossing a pressure level the temperature and humidity is calculated using bilinear interpolation. Besides slant delays, also the ZHD and ZWD were generated from the model. The ZHD generated by the model was used as a priori (ZHD_0) in the GPS processing, the ZWD was used to compute the error in the ZWD estimation. The slant delays were generated for a single station: Delft. This implies that in a single difference set-up the reference station has a nominal behaviour according to the Niell mapping functions. More realistic would have been to compute the slant delays from the model for two stations several 100 km apart, and then use the difference, but we did not do this in this study. Our approach is more typical for Precise Point Positioning, where we use the satellite orbits and clocks from a previous global solution.

Three different runs were carried out for both the symmetric and asymmetric atmosphere. The main difference between the runs is the way in which the positions were handled: a) kinematic positions (three position unknowns every 3 hours), b) daily positions (three position unknowns every day) and c) static positions (three position unknowns over the whole interval). The clocks and ZWD were solved for every observation epoch (3 hours). The errors for the various runs are given in Table 3.1 and Fig. 3.5. In Table 3.1 the mean and the standard error of errors (with respect to the mean values) are given. The standard deviation gives an indication of the variation in time of the errors. The errors are plotted in Fig 3.5 for both the symmetric and asymmetric atmosphere. The results for the 3 day static position are not plotted, as these are not very different from the 1 day solutions. The dilution of precision (DOP) the standard deviation of the estimated parameter divided by the standard deviation of the observations plotted in Fig. 3.6.

The mapping functions computed from the NWP model are different from the Niell mapping function, resulting in significant deviations in estimated parameters if the Niell mapping func-

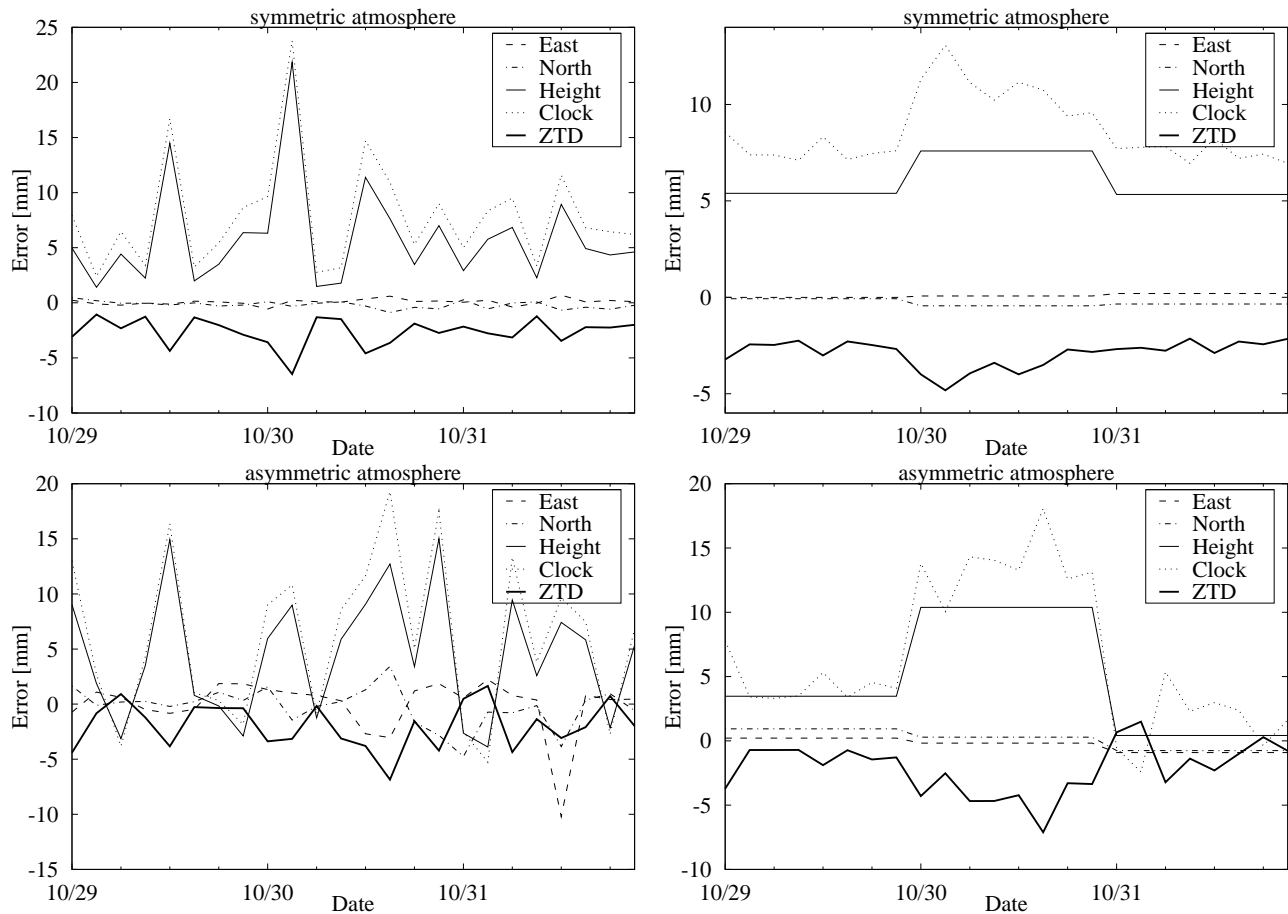


Figure 3.5: Error in the East, North, Up, Clock and ZTD parameters due to the mapping function for a symmetric atmosphere (top row) and asymmetric atmosphere (bottom row), and for a kinematic solution (left column) and 1 day static solution (right column). Time is on the horizontal axis and the vertical axis is the difference between the estimated parameters and the reference.

Table 3.1: Mean error in the GPS parameters (in [mm]).

| KINEMATIC POSITION | | | | | | STATIC 1 DAY POSITION | | | | | |
|--------------------|------|-------|-----|-------|------|-----------------------|------|-------|-----|-------|------|
| Mean | East | North | Up | Clock | ZTD | Mean | East | North | Up | Clock | ZTD |
| Symmetric | -0.1 | -0.2 | 6.2 | 8.4 | -2.8 | Symmetric | 0.1 | -0.3 | 6.5 | 9.2 | -3.1 |
| Asymmetric | 0.0 | -0.3 | 4.8 | 6.5 | -2.1 | Asymmetric | -0.3 | 0.1 | 5.1 | 7.0 | -2.3 |
| St.Dev | East | North | Up | Clock | ZTD | St.Dev | East | North | Up | Clock | ZTD |
| Symmetric | 0.3 | 0.3 | 4.9 | 5.2 | 1.3 | Symmetric | 0.1 | 0.2 | 1.1 | 1.8 | 0.7 |
| Asymmetric | 2.5 | 1.8 | 5.8 | 7.3 | 2.1 | Asymmetric | 0.5 | 0.2 | 4.3 | 5.7 | 2.0 |

| STATIC 3 DAY POSITION | | | | | |
|-----------------------|------|-------|-----|-------|------|
| Mean | East | North | Up | Clock | ZTD |
| Symmetric | -0.1 | 0.3 | 6.5 | 9.2 | -3.1 |
| Asymmetric | -0.3 | 0.0 | 5.0 | 7.0 | -2.3 |
| St.Dev | East | North | Up | Clock | ZTD |
| Symmetric | - | - | - | 0.9 | 0.6 |
| Asymmetric | - | - | - | 2.2 | 1.4 |

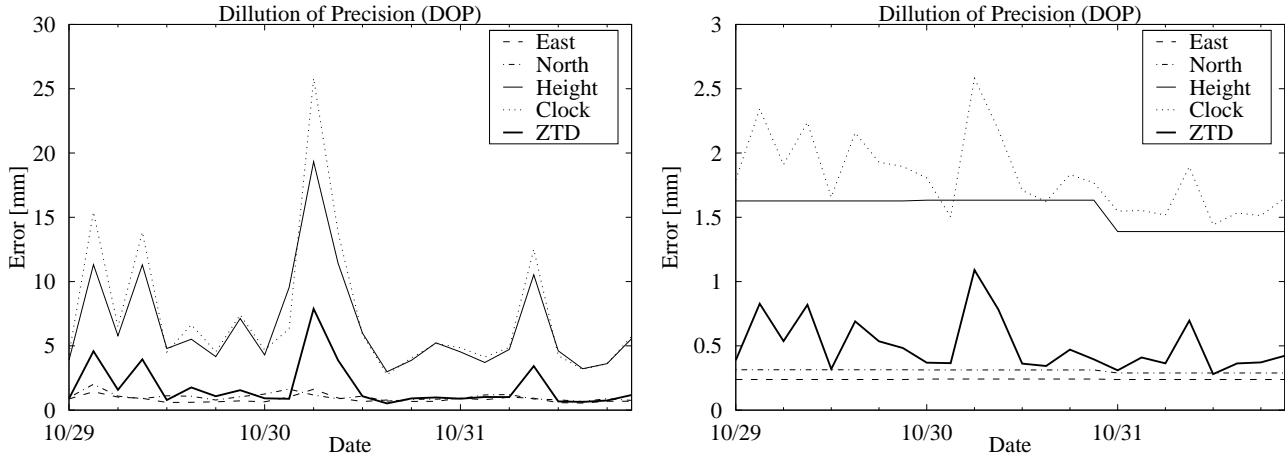


Figure 3.6: Dilution of Precision for East, North, Up, Clock and ZTD for the kinematic solution (left) and static 1 day solution (right). Time is on the horizontal axis and on the vertical axis is the standard deviation of the estimated parameters divided by the -assumed- standard deviation of the observations.

tion is used. The difference of the hydrostatic mapping function ($m_h^{NWP} - m_h^{Niell}$) is about -0.005 at low elevations, while the difference of the wet mapping functions ($m_w^{NWP} - m_w^{Niell}$) is between $0.006 - 0.020$. Taking the actual ZHD and ZWD into account, the effect on the observations is respectively -11 mm for the hydrostatic part and $1-2$ mm for the wet part. Therefore, the observations are mainly affected by the hydrostatic mapping function. The systematic error in the estimated geodetic parameters we found was -2.1 to -3.1 mm in ZTD (less than 0.5 kg m $^{-2}$ in terms of IWV), $+6.5$ to $+9.2$ mm in the receiver clock error and $+4.8$ to $+6.5$ mm in the height. When the asymmetric atmosphere is used in the simulation the variation in the estimated parameters is much larger than with a symmetric atmosphere: $2-7$ mm in ZTD, height and clock errors, however, it did not significantly affect the horizontal components. One possible explanation is that the Niell mapping functions are not representative for the three days chosen in our simulation. It is of course also possible that water vapour is not represented very well in the model, but this argument is not decisive here, as the mapping functions from radiosonde tend to agree with the NWP derived mapping functions. Final proof can only be obtained when real GPS data is processed with both Niell and NWP mapping functions over a long period, and the results are analysed carefully. However, this is outside the scope of this chapter.

3.5 CONCLUSIONS

In this chapter the influence of NWP derived slant delays on GPS parameters is discussed. A single GPS site, Delft (the Netherlands) was selected to investigate the influence. We focused on a dynamical weather system: a cold front passage on the 30 October 2000. For this case we showed that the difference between the Niell mapping functions and the NWP model and radiosonde mapping functions influence these parameters. We observed systematic errors in ZTD (-2.1 to -3.1 mm), clock error (6.2 to 9.2 mm) and height (4.8 to 6.5 mm). The systematic

error in ZTD corresponds to approximately 0.5 kg m^{-2} IWV.

We also showed that mapping functions derived from radiosonde De Bilt differ from the Niell mapping functions. Moreover and not really surprising, NWP derived mapping functions are comparable to those derived from radiosonde profiles.

The Niell mapping functions have no dependence on geographical location other than latitude. Influences on water vapour amounts related to climate or orographic effects are not included. We showed that GPS estimates are influenced by local effects which are not unusual for a sea climate. We expect that orographic effects also influence the GPS estimates.

So far only one specific case is studied. This experiment has to be repeated for more days, under various meteorological conditions, different seasons and for more stations. Also, we would like to study the effect of adding gradient parameters to the GPS estimation and introduce carrier phase ambiguities, as these might absorb some of the effects we have observed. If our findings are correct, and confirmed by other experiments, like those done by Niell (2000, 2001) and Rocken et al. (2001), the use of standard mapping functions like Niell could introduce (systematic) errors in the geodetic parameters, including ZTD which is used to estimate IWV for meteorological applications. A possible solution to this problem could be to compute station dependent mapping functions from NWP models as a service for GPS analysis centres as suggested by Niell (2000).

Chapter 4

Synergetic use of GPS water vapour and Meteosat images for synoptic weather forecasting¹

The use of integrated water vapour (IWV) measurements from a ground based global positioning system (GPS) for nowcasting is described for a cold front that passed the Netherlands during 16 and 17 May 2000. Meteosat water vapour (WV) and infrared (IR) channel measurements are incorporated to analyse this weather situation. A cloud band with embedded cumulonimbus clouds (Cb) preceded the cold front. The GPS IWV showed a clear signal at the passing time of the embedded Cb's over the GPS-sites. After the front passage a dry intrusion occurred. By comparing Meteosat WV observations collocated in time and space with GPS IWV observations a rough reconstruction of the vertical water vapour distribution can be made. The case described here shows that, in addition to Meteosat WV/IR images GPS IWV contained information for nowcasting of the probability of the occurrence of thunderstorm and heavy precipitation.

4.1 INTRODUCTION

Water vapour is one of the parameters that is highly under-determined in the current synoptic weather observations systems. Radiosonde measurements provide detailed vertical information, however, at very low temporal and horizontal resolution. Atmospheric water vapour can also be measured using water vapour radiometers which measure column integrated water vapour (IWV). These instruments are very accurate in clear sky situations but they are not 'all weather', moreover, they are very expensive. IWV can also be obtained from a network of ground based global positioning system (GPS) receivers together with a constellation of 24 GPS satellites. The temporal resolution of the observed IWV is high (5 to 15 minutes), the

¹This chapter is previously published in *J. Appl. Met.*, 2004, **43**, pp 514–518, by S. de Haan, S. J. M. Barlag, H. Klein Baltink and F. Debie.

accuracy is very good and a GPS receiver is much cheaper to deploy and maintain. Duan et al. (1996) showed that GPS IWV is in good agreement with IWV observations from water vapour radiometers with a root mean square difference around 1 to 1.5 kg m⁻². The difference between near real time GPS IWV with respect to radiosonde and water vapour radiometers is around 2 kg m⁻² (Rocken et al., 1997). The network used in this study has an agreement of 2 kg m⁻² with respect to radiosonde (Baltink et al., 2002). This is in agreement with accuracies found in other comparison studies.

Mazany et al. (2002) showed that combination of GPS IWV and other meteorological data using a statistical model increases the forecast skill and lead time of a lightning event. The study presented here differs from Mazany et al. (2002) and previous studies because it does not focus on the quantitative information of GPS IWV but more on the qualitative information.

The network of GPS receivers used in this study is constructed for geodetic research. A GPS receiver measures the delay of the GPS signal for every GPS satellite in view. By processing all observed slant delays within a certain time window errors and unknowns, such as satellite or receiver clock errors can be estimated. An estimate of the Zenith Total Delay (ZTD) for any GPS receiver is determined simultaneously. The Zenith Wet Delay (ZWD) can be computed from the signal by differencing the ZTD with the zenith hydrostatic delay (ZHD),

$$\text{ZWD} = \text{ZTD} - \text{ZHD}. \quad (4.1)$$

The ZHD can be approximated using the surface pressure (Saastamoinen, 1972), while the ZWD is associated with the vertically integrated column of water vapour overlying the GPS receiver

$$\text{IWV} = \frac{1}{k} \text{ZWD}, \quad (4.2)$$

where k depends on the weighted mean temperature of the atmosphere, which in turn can be approximated as a function of the surface temperature (Bevis et al., 1994; Baltink et al., 2002).

Upper tropospheric water vapour can be inferred by the 6.7 μm channel imager on board the Meteosat satellite. This instrument measures the thermal emission by upper tropospheric water vapour. The atmospheric temperature and clouds also affect the emission. Radiation emitted from water vapour low in the atmosphere will be absorbed by water vapour higher in the atmosphere: lower atmospheric water vapour is obscured by upper atmospheric water vapour. The geostationary satellite scans the earth every 30 minutes. The Meteosat water vapour (WV) images are widely used as 'control' observations for synoptic weather meteorology. A loop of these images reveals the movement of weather systems and the downward motion of drier stratospheric air. The Meteosat imager scans also in the visible and in the infrared (IR). The IR measures the emission of the atmosphere in a broad band around 12 μm and can therefore be used at day and night as with the WV channel. Although the 6.7 μm channel is actually a thermal infrared channel the commonly used abbreviation is WV channel. The WV and IR emission is reported in brightness temperatures (T_b) with units of K. The average absorption level of WV emission lies roughly between 300-600 hPa (Weldon and Holmes, 1991). Very low IR T_b indicates the presence of high clouds. High WV T_b implies that emission from low in the atmosphere reaches the detector, which can only occur when the upper troposphere is dry.

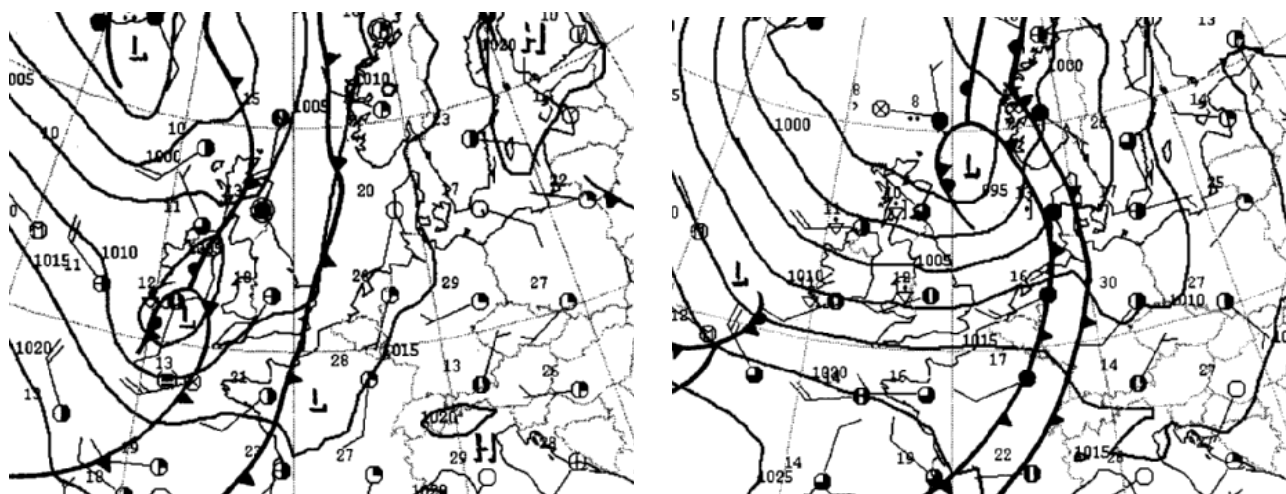


Figure 4.1: Synoptic weather situation of 16 May 12:00 UTC (left) and 17 May 12:00 UTC (right)

Another way to estimate water vapour is using the Advanced-TIROS Operational Vertical Sounder (ATOVS). This instrument is on board the NOAA polar satellites and has a frequency of passage of two times a day. Using the Advanced Microwave Sounding Unit B (AMSU-B) an estimate of the total water vapour column is only valid over the ocean (Grody et al., 2001). In this chapter this information is not used due to this temporal resolution and the restriction to ocean areas. On the other hand, ground-based GPS water vapour estimates are restricted to land areas but have, as stated before, a good temporal resolution. The case discussed here focuses on the application of the temporal resolution.

4.2 COLD FRONT PASSAGE

In the evening of 16 May 2002, a sunny period of warm weather came to an end when a cold front passed the Netherlands. Across this cold front a temperature drop of about 10 degrees K in 3 hours was observed. In Figure 4.1 the weather situations of 16 and 17 May at 12:00 UTC are shown. In the left panel of Figure 4.1, which represents the synoptic situation of 16 May 12:00 UTC, two cold fronts are heading towards the Netherlands.

The first front, which extends from Norway over the North Sea towards Bretagne, marks the leading edge of the clouds. This edge is also visible in Figure 4.2 which shows IR and WV images observed by Meteosat on 16 May 12:00 UTC. The actual active cold front is related to the low pressure south of Ireland. Between these two fronts a large cloud band exists in which air is transported northward between the two frontal systems that are propagating eastward. Instabilities occurred when this cold air was transported over the warm surface, which resulted in mixed embedded cumulonimbus clouds (Cb). Behind the second front a dry intrusion appeared, visible as a dark spot in the WV image in Figure 4.2.

The temperature and relative humidity as observed by synoptic weather stations Rotterdam, Hoogeveen and Deelen during this passage are shown in Figure 4.3 top and bottom panel respectively. Both relative humidity and temperature show a clear diurnal cycle during the

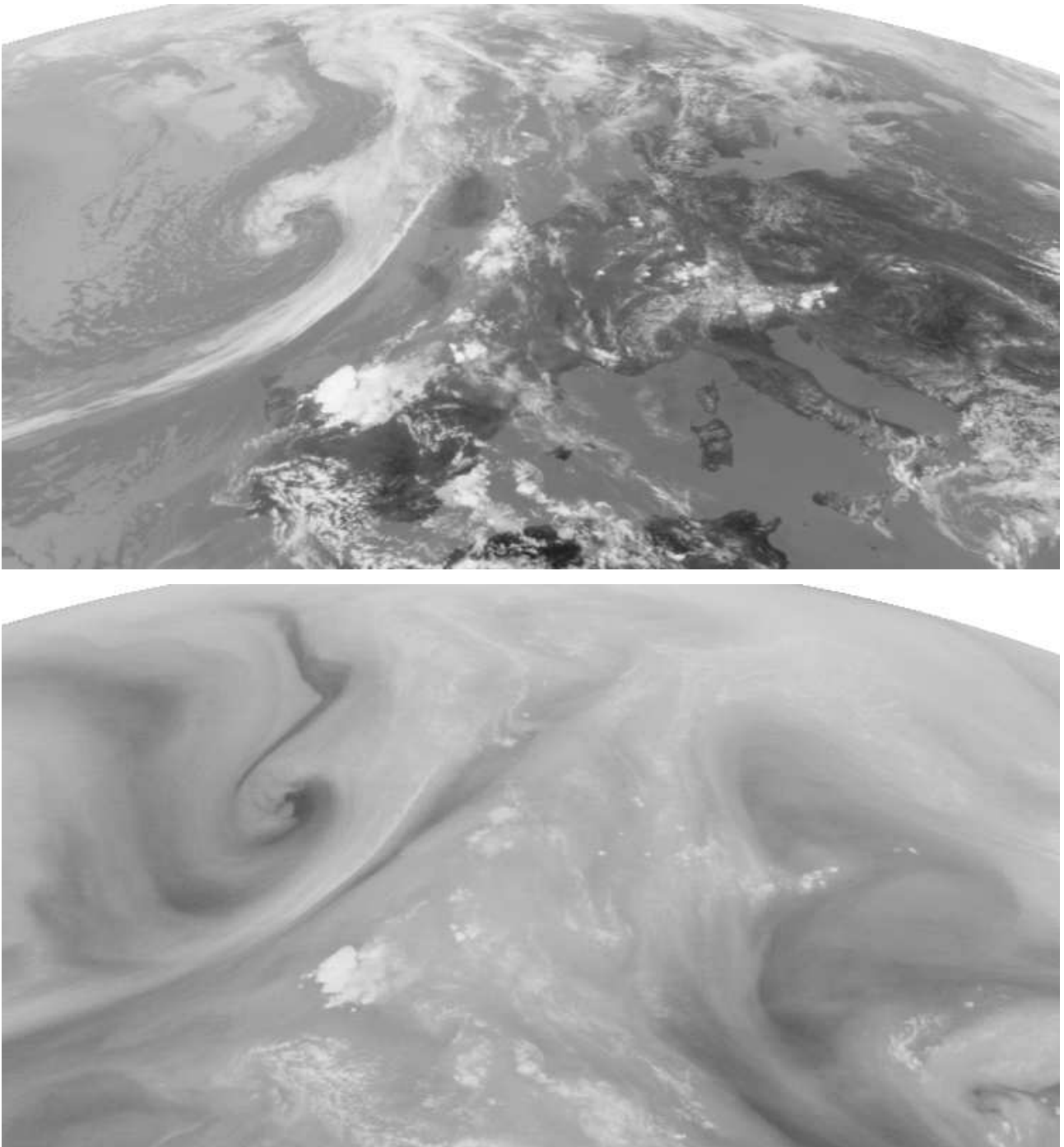


Figure 4.2: The inverted IR image (top) and WV (bottom) as observed by Meteosat. White pixels represent low T_b . Both images are retrieved at 16 May 12:00 UTC and cover Western Europe, with France in the centre. Italy, Corsica and Sardinia are visible on the IR image.

warm weather. After the frontal passage the diurnal cycle clearly weakens. In Figure 4.4 the location of these weather stations as well as nearby GPS sites are shown. The GPS receiver locations are distributed over the Netherlands with a minimum distance of approximately 100 km.

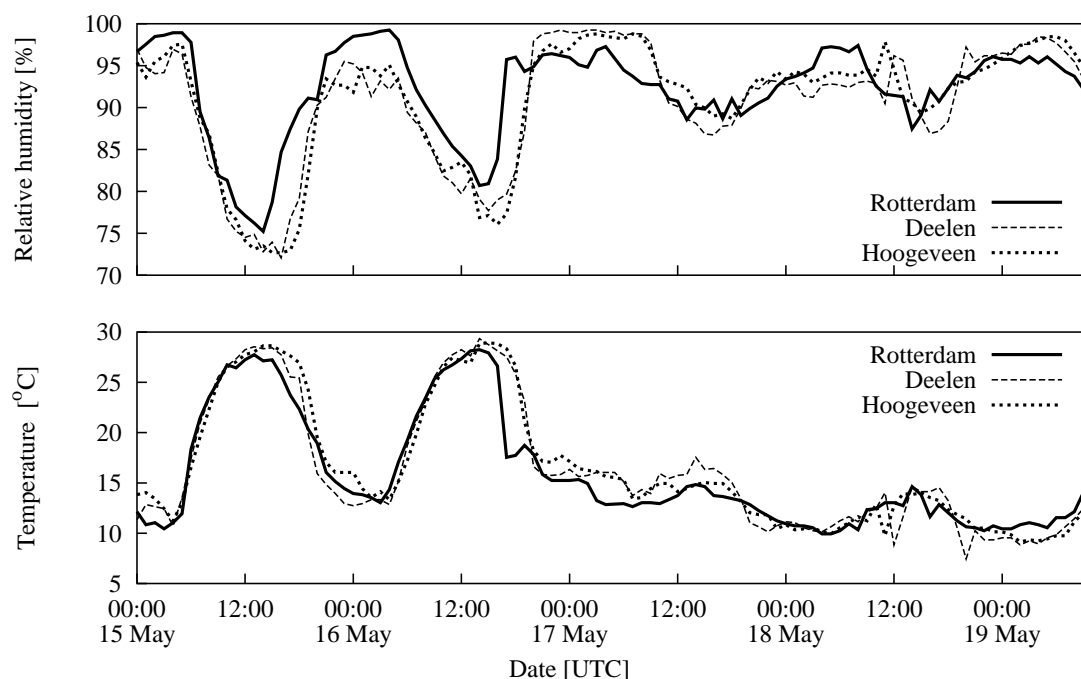


Figure 4.3: The top panel shows the relative humidity change during the front passage for three synoptic weather stations close to a GPS receiver location (see Figure 4.4). The temperature change is shown in the bottom panel.



Figure 4.4: Locations of GPS receivers and synoptic weather stations used in this study.

4.3 DISCUSSION

In Figure 4.5 the changes in WV and IR imagery overlying The Netherlands are shown. The upper half of all four panels shows the observed T_b from the water vapour channel by Meteosat

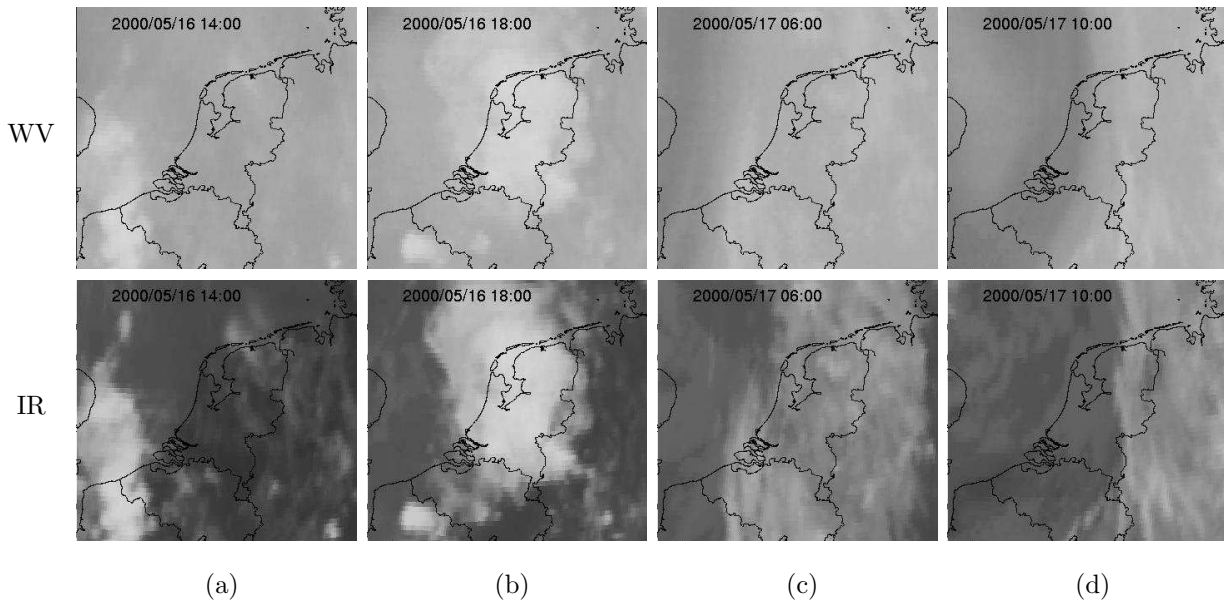


Figure 4.5: The four panels show the WV and IR as observed by Meteosat on (a) 16 May 14:00 UTC, (b) 16 May 18:00 UTC, (c) 17 May 06:00 UTC and (d) 17 May 10:00 UTC. The top sub-figure in every panel is WV and the bottom sub-figure is the IR channel. Dark grey tones indicate high T_b while lower T_b are light grey.

at subsequent times; the lower half contains T_b from the infrared channel.

On 16 May at 14:00 UTC convective clouds emerged in a region close to the west coast of Belgium and the east coast of England. These clouds are observed in both the WV image and the IR image. At this time large parts of the Netherlands are cloud free as can be seen from the IR image (Figure 4.5a bottom). These clouds marked the first front running from Norway to Bretagne (see Figure 4.1, left panel). At 18:00 UTC (Figure 4.5b) the convective clouds cover the Netherlands almost completely. These cumulonimbus clouds (Cb) move from the south-west towards the north-east. The observed temperature in Rotterdam, see Figure 4.3, dropped earlier than in Hoogeveen (the latter lies further to the east). On 17 May 06:00 UTC (Figure 4.5c) a dark band in the WV appeared west of the Dutch coast indicating a dry intrusion and the amount of water vapour high in the troposphere decreased. At 10:00 UTC this dark band has moved eastward and lies across the Netherlands. On the IR image the cloud free region in the vicinity of this dark band is visible at both times.

The timeseries of IWV as observed by the GPS receivers are shown in Figure 4.6 (solid line). Also shown in this figure are the brightness temperatures of the WV (open squares) and IR (filled triangles) channel for the same locations. The IWV is presented in kg m^{-2} with the values on the left vertical axis. The T_b shown here are between 20°C and -40°C but are plotted inversely as indicated by the values on the right axis. High T_b values indicate a low average level of WV emission.

The three panels of Figure 4.6 correspond to locations that shift in northeasterly directions when read from top to bottom. Figure 4.6 shows an increase in IWV overlying the GPS locations on 16 May between 00:00 UTC and 12:00 UTC from about 15 kg m^{-2} to 25 kg m^{-2} . The measured WV brightness temperature was nearly constant in this period. The sudden decrease of IR T_b that occurred at the same moment as a minimum in WV T_b is due to high

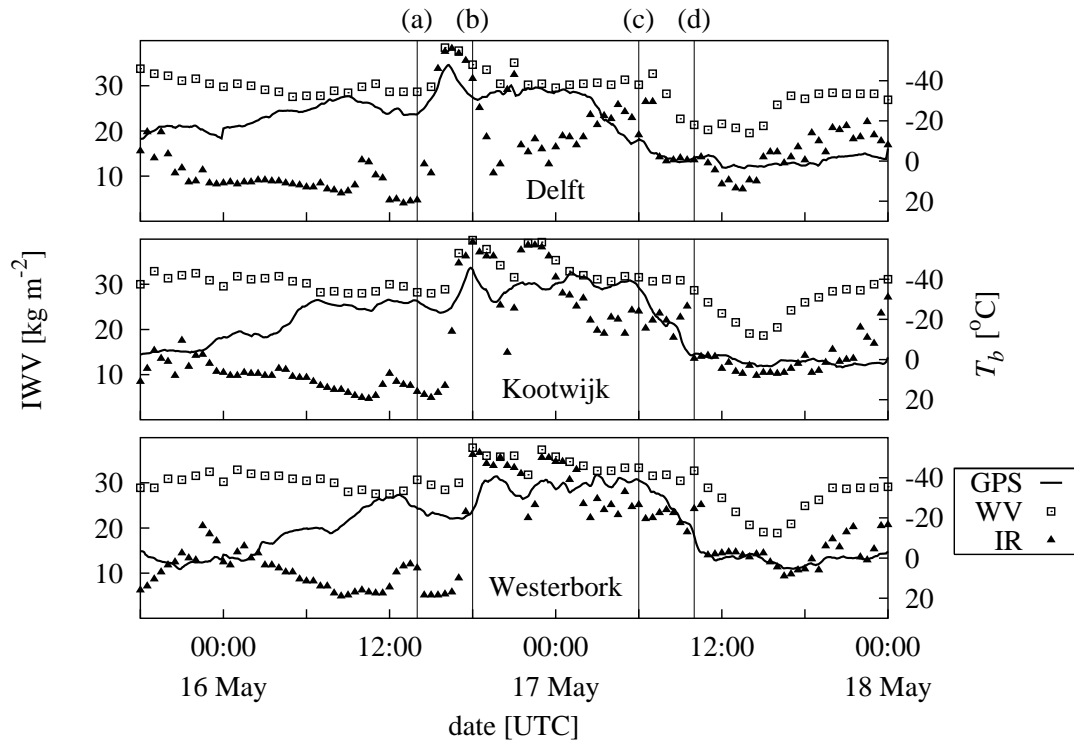


Figure 4.6: Timeseries of IWV as retrieved using GPS (solid) together with the T_b of WV (dashed) and IR (dotted) overlying the locations Delft, Kootwijk and Westerbork. The letters (a) through (d) mark the times of the image in Figure 4.5, that is : (a) 16 May 14:00 UTC, (b) 16 May 18:00 UTC, (c) 17 May 06:00 UTC and (d) 17 May 10:00 UTC.

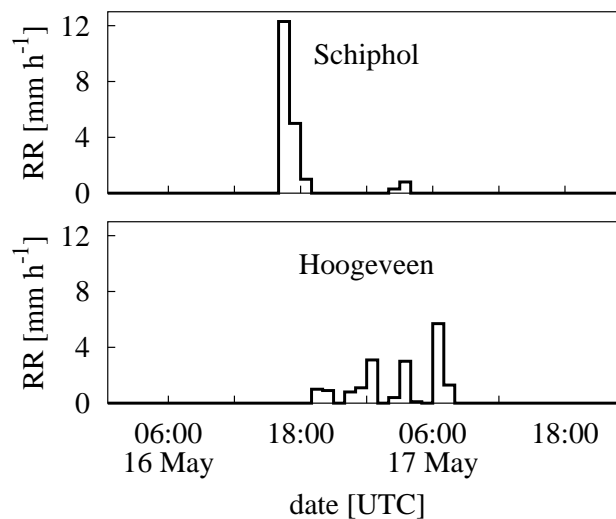


Figure 4.7: Timeseries of Rainfall (mm hour^{-1}) at Schiphol and Hoogeveen.

clouds, which contain large amounts of water vapour. The T_b attains a minimum in WV and IR at approximately 17:00 UTC in Delft, at 18:00 UTC in Kootwijk and around 18:30 UTC in Westerbork. Simultaneously a maximum GPS IWV occurred indicating that the Cb's are

heavily mixed. Note that the maximum of GPS IWV at Westerbork is less pronounced than over the other two sites. The simultaneous occurrence of high clouds (IR T_b), water vapour in the upper troposphere (WV T_b) and high GPS-IWV estimates could be an indication for the occurrence of a relatively extreme weather event. Downstream of Delft, at Schiphol a rainfall rate 12 mm h^{-1} has been observed, while near Westerbork, at Hoogeveen the rainfall is spread over a period, see Figure 4.7.

GPS IWV measured at Delft slowly decreases from 17 May 00:00 UTC to 06:00 UTC. At this time the cloud band passes the GPS site. The WV T_b showed a more or less constant value during these 6 hours, while the IR T_b did not indicate the occurrence of high clouds. This implies that the water vapour density in the top of the atmosphere is more or less constant while the total amount decreases. This indicates that the lower part of the atmosphere below 600 hPa becomes drier. This decay is also seen in the relative humidity observation for Rotterdam close to Delft (Figure 4.3 top panel the solid line). The signal is not pronounced which is due to the fact that these relative humidity measurements, which are measured at approximately 2 metres above ground, in general have a diurnal cycle. The dehydration of the atmosphere below 600 hPa is also observed over the other GPS sites, except that a delay in time is observed. The GPS IWV starts decreasing a little before 06:00 UTC for Kootwijk and a little after 06:00 UTC for Westerbork. The decrease stops at around 10:00 UTC for Kootwijk and 11:00 UTC for Westerbork. At these moments the dry intrusion sets in and the top of the atmosphere dehydrates (increase in water vapour T_b), while the total amount stays constant. Note that for all three sites the increase in brightness temperature is nearly the same but that the period is smaller for Delft than for the other two sites.

4.4 CONCLUSION

In this chapter we showed the additional information that GPS integrated Water Vapour (IWV) contains in relation to the current Meteosat Water Vapour (WV) and Infrared (IR) images. The fact that GPS IWV is an all weather system and can measure with a high temporal resolution is beneficial for interpreting the (coarse) water vapour distribution in a vertical column together with the timeseries of Meteosat WV/IR brightness temperatures (T_b). The GPS IWV system determines the total zenith water vapour column overlying a GPS site while WV T_b is related to the amount of radiance emitted from a layer of water vapour of unknown depth. The combination of this information gives a rough indication on the distribution of the water vapour in this column. Moreover the temporal changes of GPS IWV and WV T_b reveal the change in vertical distribution of WV. The case presented here shows that the amount and temporal changes of water vapour in a convective system with Cb's can be estimated by GPS, which together with information on flow gives insight in the possibility of the occurrence of a weather situation with heavy rainfall.

Chapter 5

Measuring atmospheric stability with GPS¹

Nowcasting of convective systems plays a crucial role in weather forecasting. The strength of convection depends on the (in)stability of the air column. The stability can be detected by radiosonde observations. However, these observations are not frequent (typically 2 times a day) and expensive to deploy. In this chapter a method is presented to detect the stability of the atmosphere based on high frequency Global Positioning System (GPS) path delay observations. The convection parameter derived from these observations is the power of the non-isotropic GPS path delay signal. Comparisons with the Convective Available Potential Energy (CAPE) obtained from radiosonde observations shows a correlation with the convection parameter obtained from GPS. This implies that, because of the continuous availability of GPS estimates and the good land coverage, this method of detecting atmospheric stability may be beneficial to forecasters.

5.1 INTRODUCTION

An indication of the stability of a column of air is essential to be able to forecast a strong convection event. The combination of humidity and temperature profile information determines the (static) stability of an air column. Currently, radiosonde observations provide the only operational upper air collocated measurements of temperature, humidity and wind. Temperature sensors on commercial aircrafts provide temperature soundings but (currently) no humidity observations. These observations are distributed to the users using the AMDAR (Aircraft Meteorological Data Relay) system. Currently, humidity measurements from commercial aircraft are being carried out now in the U.S. using TAMDAR (Tropospheric Airborne Meteorological Data Reporting) although these observations are not operationally available at KNMI. Moreover, information from these observations is restricted to flight routes and airports. The latter are operating at specific times during the day, which is a weakness of the system. Satellite temperature sensors, such as ATOVS (Advanced-TIROS Vertical Sounder on board the NOAA polar satellites) measure outgoing radiation at a number of wavelengths. These radiation pa-

¹This chapter is previously published in *J. Appl. Met.*, 2006, **3**, pp 467–475 by S. de Haan.

rameters are linked to upper tropospheric temperature (and humidity), but these observations need a model to be able to convert them into a temperature profile (Li et al., 2000). Another disadvantage is that satellite derived temperatures are not frequent in time, in the case of polar orbiting satellites, or have a low spatial resolution, in the case of a geostationary satellite.

Radiosonde profiles are obtained with a frequency of two or four times a day at specific times. A forecaster has to combine satellite information with numerical weather prediction (NWP) model output at times when radiosonde observations are not available. Although radiosondes are regarded as the best way of measuring profile information they should not be treated as truth profile information. For example, a radiosonde balloon rises from the surface to 15 to 30 kilometre in approximately one hour. During its ascent, the wind speed and direction are deduced by its horizontal movement. A radiosonde measurement is thus rarely a vertical profile. Moreover, there are known problems with certain type of radiosondes due to for example ice contamination of the humidity sensors or day/night inconsistencies (Lorenc et al., 1996; Leiterer et al., 1997). Radiosonde observations are also subject to biases and non-systematic errors caused by sensor malfunctions. The quality of a radiosonde observation is also depending on the age of the sensor and proper calibration before launch.

The Global Positioning System (GPS) signals are transmitted by GPS satellites and, received at the earth surface, have traversed the atmosphere. The atmosphere delays and bends the signal due to differences in density and humidity. Each received signal contains information about the temperature and humidity along the path between GPS satellite and receiver. By collecting the signal from a large number of satellite-receiver pairs for a number of receivers, the atmospheric delay can be estimates very accurately, simultaneously with the position of the receivers and other parameters (Rothacher and Mervart, 1996; Webb and Zumberge, 1993). From this atmospheric delay an estimate of the total column water vapour can be estimated when surface pressure and temperature are available (Bevis et al., 1992). The spatial coverage is (up to now) restricted to land. However, the great advantage of GPS observations is that a very high temporal resolution can be achieved (up to minutes) with reasonable accuracy. Studies have shown that GPS observations can be used for nowcasting purposes (Mazany et al., 2002; de Haan et al., 2004; Elgered et al., 2004). Because GPS delays are determined using differences in observed and expected arrival time of a signal, it is intrinsically calibrated. This makes GPS derived atmospheric information also a very good observation for climate purposes (Gradinarsky et al., 2002).

In this chapter a connection is made between GPS observations and the possibility of (strong) convection. Strong convective systems may suddenly develop. An external trigger may change a potential instable column of air into a completely unstable one. Entrainment, friction, and orographic effects can change the stability. The timescales at which this can occur are in the order of hours to several minutes. Because GPS delay signals contain moisture information and can be obtained with a high temporal resolution, these observations may reveal potential unstable air masses. During convection, air masses are constantly transported upward and downward and the frequency at which this occurs may also be apparent in the GPS signals.

5.2 DATA

GPS is a constellation of 24 satellites (which transmit radio frequency signals) and (ground-based or space-borne) receivers. The civil use of GPS has increased rapidly in the last 10 years. The receiver constellation used in this study is set up for geodetic and surveying purposes which require very accurate positional information (in the order of millimetres).

A GPS satellite transmits a radio frequency signal with a time tag and code specific for the transmitting satellite. By comparing the clock of the receiver and the time stamp of the signal, the excess path can be estimated when the position of the satellite and the receiver are known. To obtain millimetre accuracy, however, parameters such as satellite and receiver clock errors and atmospheric correction (or delay) need to be estimated. By collecting all observations in a time window from a fixed network of receivers, the estimates of these parameters can be obtained by a least squares fit. The atmospheric delay is usually determined in the zenith direction and is called zenith total delay (ZTD). The ZTD is related to refractivity N as follows

$$\text{ZTD} = 10^{-6} \int_{z_A}^{\infty} N dz, \quad (5.1)$$

where z_A is the the height of the antenna. The ZTD is normally given in metres. The refractivity N at a certain height is a function of temperature T , density ρ and water vapour density ρ_w , that is

$$N = k_1 \rho R_d + \left(k_2 R_v - k_1 R_d + k_3 \frac{R_v}{T} \right) \rho_w \quad (5.2)$$

where $k_1 = 77.6$ [K/hPa], $k_2 = 70.4$ [K/hPa] and $k_3 = 3.739 \cdot 10^5$ [K²/hPa] are constants (Thayer, 1974). The ZTD can be split up into a hydrostatic part (ρR_d -term in Eq. 5.2, called Zenith Hydrostatic Delay, ZHD) and a wet part (the rest in Eq. 5.2, called Zenith Wet Delay, ZWD),

$$\text{ZTD} = \text{ZHD} + \text{ZWD} \quad (5.3)$$

The ZTD is an estimate of the path delay for signals with zenith elevation. GPS satellites are rising or setting continuously for each receiver. When a signal reaches a receiver at a low elevation, the path through the atmosphere will be long and may span over 200 km horizontally in the troposphere. At very low elevations the ratio between wet slant delay and wet zenith delay deviates substantially from the ratio between hydrostatic slant and hydrostatic zenith delay. Therefore, the hydrostatic and wet part should be treated separately when mapping a total slant delay to the zenith. The ratios between zenith hydrostatic (wet) and slant hydrostatic (wet) delay determine the so-called Niell mapping functions. Based on radiosonde observations Niell (1996) determined a general relation between the ratio of slant and zenith delays with respect to elevation. Signals with an elevation of 50 degrees and higher are more representative for the column of air above the receiver. Although the elevation dependence of the mapping functions is still present, the differences between hydrostatic and wet mapping functions are small at these high elevations (Niell, 1996). The actual ratio between slant and zenith delay may deviate from the more or less climatological value proposed by Niell (1996). The cause of these deviations is due to gradients in humidity and pressure distribution (de Haan et al., 2002). Not surprisingly, these differences are most pronounced at low elevations.

A network of GPS receivers is used in the current study. Data from the whole network is processed using Bernese software (Rothacher and Mervart, 1996) with final orbits. The GPS data used in this study has a temporal resolution of 30 seconds. In the processing the minimum elevation is set to 10 degrees. Double differences are used to eliminate clock errors. Using zero differencing (Alber et al., 2000) an estimate of the slant total delay (STD) is obtained. From these zero differences the non-isotropic residual is estimated by

$$\delta_{non-iso} = \text{STD} - (m_h(\beta) \cdot \text{ZHD}_0 + m_w(\beta) \cdot \text{ZWD}_e - M(\alpha, \beta)), \quad (5.4)$$

where m_h and m_w are Niell hydrostatic and wet mapping functions, and $M(\alpha, \beta)$ is the multipath correction at azimuth α and elevation β (de Haan et al., 2002). ZHD_0 is an a priori estimate of the hydrostatic delay while ZWD_e is estimated in the processing.

Elosegui and Davis (2003) showed that there are some problems with the method proposed by Alber et al. (2000). The main problem lies in the fact that offsets at low elevations appear in the solutions at other locations of the network due to the zero differencing technique. The offset is spread over the network, although the magnitude of the spread will be relative to the value of the mapping functions. The magnitude of the resulting offset is expected to decrease when the difference in elevation increases. The decrease is relative to the ratio of the value of the mapping functions.

The non-isotropic residuals are mapped onto the zenith by the wet Niell mapping functions, although as said before, the difference between the hydrostatic and wet mapping function at these elevations is small. Timeseries of these (mapped) residuals will be analysed for each satellite separately. The errors due to the problems addressed by Elosegui and Davis (2003) are small because data is only used with an elevation larger than 50 degrees. This minimal elevation diminishes the influence of advection of moisture gradients.

Two periods with GPS observations are used in the study presented here: 23 October 2000 - 7 November 2000 and 1-24 May 2003. The period in 2000 was governed by a large number of cold fronts (see also de Haan et al. (2004)) passing the Netherlands. The latter period was marked by a number of thunderstorms. In this latter period, an extensive measurement campaign called BBC2 (Baltex Bridge Campaign-2) was organised in the Netherlands. Dedicated radiosonde measurements and a large number of other observations were conducted during this period. The main emphasis of this campaign was on cloud research. The primary location for this campaign was Cabauw, where the radiosondes were launched and where a GPS receiver was installed. In the first period, October-November 2000, no dedicated radiosondes were available and the GPS receiver at Cabauw was not installed at that time. Figure 5.1 shows the location of Cabauw and (part of the) GPS receiver network used to estimate the delays, as well as the radiosonde launch sites De Bilt (the Netherlands) and Brussels (Belgium) and Göteborg (Sweden). Table 5.1 shows the radiosonde sites and receiver locations.

The radiosonde data obtained at Cabauw have a high temporal resolution (2 seconds) and the launch times were chosen depending on the weather forecast. A radiosonde balloon rises with a vertical speed of approximately 5 m/s, which implies that the vertical profile resolution for the Cabauw radiosondes is approximately 10 metre. In De Bilt (the Netherlands), Brussels (Belgium) and Göteborg (Sweden), radiosonde launches are performed every 12 hours (00:00

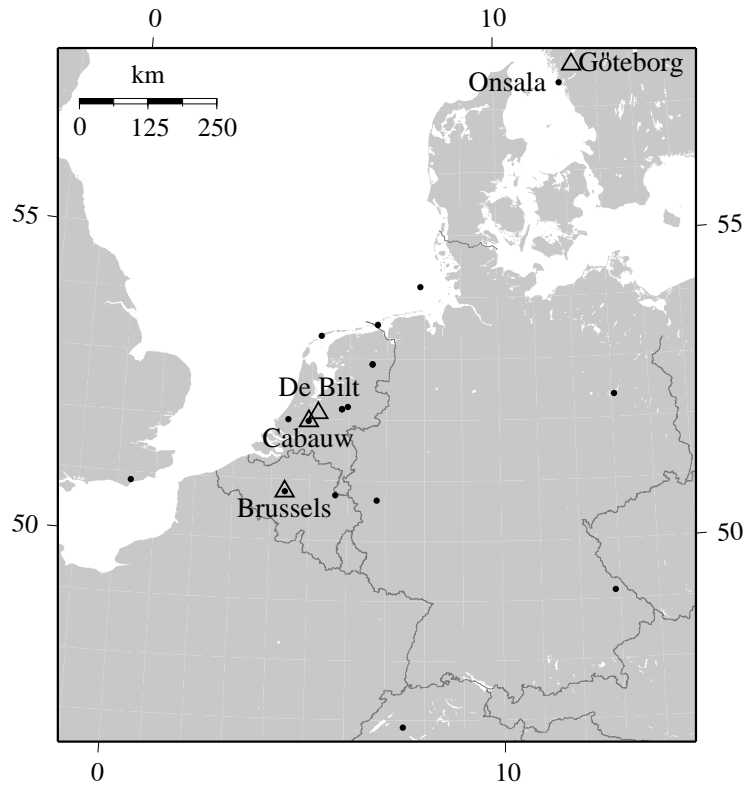


Figure 5.1: The GPS network (dots) and radiosonde launch sites (triangles).

and 12:00 UTC). The distance between the GPS sites and the radiosonde launch sites is small (within 10 km), except for Cabauw and De Bilt (distance 31 km) and Onsala and Göteborg (distance 83 km). Notice also that apart from Onsala-Göteborg height differences between GPS and radiosonde sites are small. Radiosonde observations from De Bilt have a temporal resolution of 10 seconds (vertical profile resolution of 50-60 metre). The radiosonde observations from the other two locations (Brussels and Göteborg) were obtained at so-called significant

Table 5.1: Location of the GPS receivers and radiosonde launch sites and their distance.

| | | GPS | latitude | longitude | height | | |
|----------|----------|----------|-----------|-----------|----------|--|--|
| | | | deg. | deg. | [m] | | |
| | | Brussels | 50.80 | 4.36 | 104 | | |
| | | Cabauw | 51.97 | 4.93 | 2 | | |
| | | Onsala | 57.40 | 11.93 | 9 | | |
| GPS | RS | RS. lat. | RS. long. | height | distance | | |
| | | deg. | deg. | [m] | [km] | | |
| Brussels | Ukkel | 50.80 | 4.35 | 100 | 1 | | |
| Cabauw | Cabauw | 51.97 | 4.93 | 2 | 0 | | |
| | De Bilt | 52.10 | 5.18 | 2 | 30 | | |
| Onsala | Göteborg | 57.67 | 12.30 | 155 | 83 | | |

levels, which reduces the vertical resolution drastically, retaining the main temperature and humidity inversions. On all radiosonde observations, a visual quality check was performed to remove spurious data. Moreover, for the radiosonde observations from Cabauw an extra quality check is performed by comparing the observed temperature and humidity data of the first 200 metres of the profile obtained from the measurement tower at Cabauw.

5.3 METHODOLOGY

In this section the methodology to link GPS observations to the stability of an air column is presented. A measure of static (in)stability is Convective Available Potential Energy (CAPE). CAPE is an estimate of the maximum available kinetic energy an air parcel can achieve given a certain temperature and humidity profile.

Linear or first order stability is obtained by analysis of small displacements of an air parcel. Suppose an air parcel is adiabatically displaced by z' in the vertical. Due to mechanical equilibrium, the pressure of the parcel will automatically adjust to the environment. Following Holton (1992) and Salby (1996), Newton's second law for the parcel implies,

$$\rho' \frac{d^2 z'}{dt^2} = -\rho' g - \frac{\partial p'}{\partial z'}, \quad (5.5)$$

where the primes denote the parameter corresponding to the displaced parcel. Using the hydrostatic and mechanical equilibrium this yields:

$$\frac{d^2 z'}{dt^2} = \frac{\rho - \rho'}{\rho'} g. \quad (5.6)$$

Applying the universal gas law and introducing the potential temperature θ (defined by $\theta = T(p/p_0)^\kappa$, where p_0 is usually chosen to be 1000 hPa and $\kappa = 0.286$) this results in

$$\frac{d^2 z'}{dt^2} = \frac{\theta' - \theta}{\theta} g. \quad (5.7)$$

Now θ' is the potential temperature at the displacement z' . The parcel is transported adiabatically so θ is conserved implying that

$$\theta' = \theta - \frac{d\theta}{dz} z'. \quad (5.8)$$

Combining this with Equation 5.7 yields

$$\frac{d^2 z'}{dt^2} + \mathcal{N}_{BV}^2 z' = 0, \quad (5.9)$$

where

$$\mathcal{N}_{BV}^2 = g \frac{d \log \theta}{dz}, \quad (5.10)$$

and \mathcal{N}_{BV} is known as the Brunt-Väisälä or buoyancy frequency. This frequency is approximately 1.2×10^{-2} Hz for average tropospheric conditions, which is equal to a period of around 8 minutes.

The stability is determined by the sign of \mathcal{N}_{BV}^2 : positive values determine a stable environment with oscillation at frequency \mathcal{N}_{BV} ; negative values are related to unstable environments.

Another measure of stability is CAPE, which is closely related to buoyancy through

$$\text{CAPE} = \int_{z_{LFC}}^{z_{LNB}} \frac{\rho - \rho'}{\rho'} g dz' = \int_{z_{LFC}}^{z_{LNB}} z' (-\mathcal{N}_{BV}^2) dz', \quad (5.11)$$

where z_{LFC} is the level of free condensation and z_{LNB} is the level of neutral buoyancy (Holton, 1992; Salby, 1996). Between these levels the Brunt-Väisälä frequency is negative and CAPE positive.

To obtain insight in the frequency range related to convection the time scale of free convection is very informative. A measure of the free convection time scale is defined as

$$t^* = \frac{z_i}{w^*}, \quad (5.12)$$

where z_i is the height of the lowest inversion and w^* is the scaling vertical velocity. The time scale t^* , which represents the time needed for a thermal to rise in a convective boundary layer is 5 to 10 minutes. Furthermore, because CAPE represents the maximal available potential energy, the maximal vertical velocity a parcel can achieve is:

$$\frac{w_{max}^2}{2} = \text{CAPE}. \quad (5.13)$$

The value of w_{max} is over-estimated, because not all available potential energy will be transformed into kinetic energy. Assuming that w^* is half the value of w_{max} and a CAPE of approximately $100 \text{ m}^2 \text{ s}^{-2}$ the time scale will be around 12 minutes. Moreover, for cumulus convection with a characteristic height of 1 km, and a mean vertical velocity of 1 m/s, the time scale is approximately 16 minutes.

The relation between ZTD and the Brunt-Väisälä frequency is not straightforward. Recall that the ZTD is the integral value of the refractivity N (see Equation 5.1). Replacing temperature T by potential temperature θ and water vapour pressure e by specific humidity q , the derivation of N with respect to z results in,

$$\begin{aligned} \frac{dN}{dz} = & \frac{p}{T} \left[\left(k_1 + \frac{q}{\epsilon} \left(k_2 + 2 \frac{k_3}{T} \right) \right) \left(-\frac{\mathcal{N}_{BV}^2}{g} + \frac{(1 + \kappa)}{p} \frac{dp}{dz} \right) \right. \\ & \left. + \frac{1}{\epsilon} \left(k_2 + \frac{k_3}{T} \right) \frac{dq}{dz} + k_3 \frac{q}{\epsilon T} \frac{1}{p} \frac{dp}{dz} \right], \end{aligned} \quad (5.14)$$

where $\epsilon = 0.62198$ (Sonntag, 1994). Note that not all temperatures are replaced by potential temperatures. The term \mathcal{N}_{BV}^2/g is on the order of 10^{-5} while the other term $(1 + \kappa)/p dp/dz$ is approximately 10 times larger. This term is always negative as pressure is decreasing with increasing height. The last term on the right hand side in Equation 5.14 is neglected because this term is of the order 10^{-3} smaller than the other terms. Generally the refractivity decrease with height. When the Brunt-Väisälä-frequency is negative (i.e. unstable environment) the derivative of the refractivity will be larger (less negative). When the derivative becomes positive an inversion in the refractivity profile appears. Such an inversion may cause multipath effects

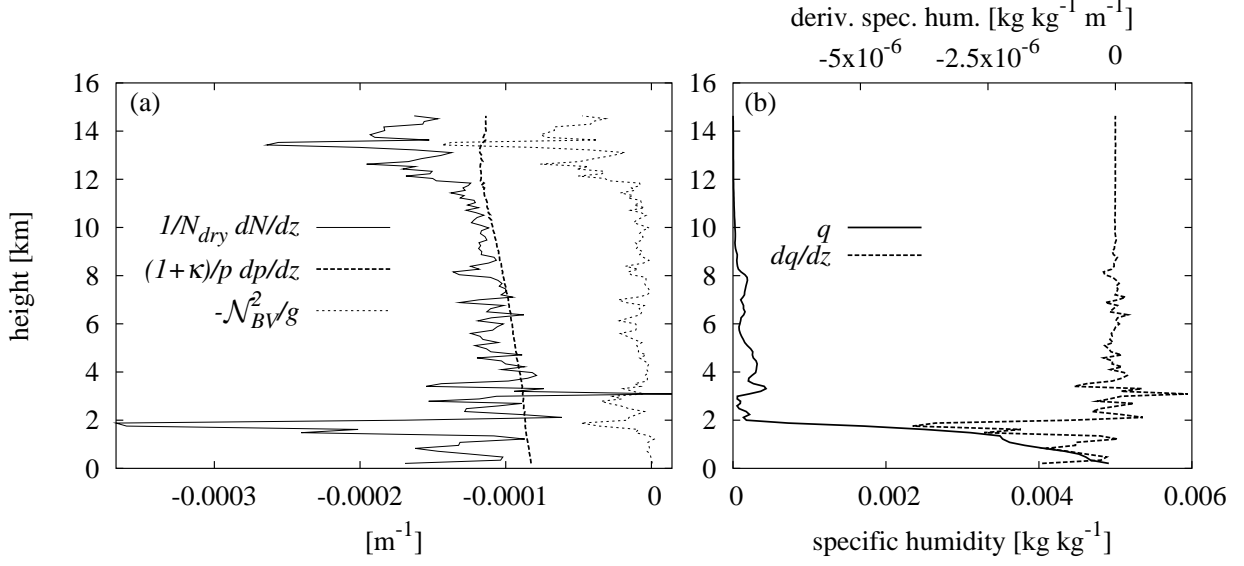


Figure 5.2: Profile data obtained from a radiosonde launch at Cabauw: a) Left-hand side of Eq. 5.16, the pressure term and Brunt-Väisälä-frequency versus height; b) Specific humidity and derivative of the specific humidity versus height. The CAPE value of the profile is 0.

of radio frequency signals (radar, GPS). Note that in hydrostatic equilibrium the pressure term can be written as

$$\frac{1}{p} \frac{dp}{dz} = \frac{d \log p}{dz} = -\frac{g}{R_d T (1 + \delta q)}, \quad (5.15)$$

where $R_d = 287.05\ J\ kg^{-1}\ K^{-1}$ is the specific gas constant dry air and $\delta = 0.6077$. For temperatures ranging from 270 to 290 K, this value will be around $1.18 \cdot 10^{-4}$ to $1.25 \cdot 10^{-4}\ m^{-1}$. Values of q are very variable: q lies generally in the range from 0 to $0.006\ kg\ kg^{-1}$. The derivative is much smaller with (absolute) maximum values of around $1 \cdot 10^{-5}\ kg\ kg^{-1}\ m^{-1}$.

By rewriting Equation 5.14 and using the approximation for $N_{dry} \approx k_1 p/T$, the following equation is obtained

$$\begin{aligned} \frac{1}{N_{dry}} \frac{dN}{dz} &\approx \left(1 + \frac{q}{\epsilon} \left(\frac{k_2}{k_1} + 2 \frac{k_3}{k_1} \frac{1}{T} \right) \right) \left(-\frac{\mathcal{N}_{BV}^2}{g} + \frac{(1 + \kappa)}{p} \frac{dp}{dz} \right) \\ &+ \frac{1}{\epsilon} \left(\frac{k_2}{k_1} + \frac{k_3}{k_1} \frac{1}{T} \right) \frac{dq}{dz} \end{aligned} \quad (5.16)$$

The order of the left hand side is $10^{-5}\ m^{-1}$. The terms on the right hand side are on the order of $10^{-5}\ m^{-1}$ as can be seen from Figure 5.2a. In this Figure the pressure term and the Brunt-Väisälä-frequency of the right-hand side of Equation 5.16 are shown together with the left-hand side for a high resolution radiosonde observation at Cabauw. Figure 5.2b shows the values of q and dq/dz for this radiosonde launch. Below a height of 5 km the derivative of q varies very rapidly which results in a equivalent variability of $1/N_{dry} dN/dz$. Above 5 km the influence of dq/dz diminishes due to small values (and thus small changes) in q . Furthermore, note that the pressure term is gradually decreasing and that the change in $1/N_{dry} dN/dz$ is

very similar to the Brunt-Väisälä frequency above approximately 6 to 7 km. Above the 12 km, \mathcal{N}_{BV} varies due to the variability in the derivation of the logarithmic of the (dry) temperature.

Thus the Brunt-Väisälä-term cannot be neglected and the above equations reveal the relation between the refractivity N and the Brunt-Väisälä frequency \mathcal{N}_{BV} . The variability in dq/dz also has a large influence on the derivative of the refractivity and, because in convective situations dq/dz will rapidly change with time, the derivative of the refractivity will also change rapidly. The ZTD is the double integral of a function which merely depends on the Brunt-Väisälä frequency and the derivative of the specific humidity.

Atmospheric time scales related to convection are around 12 minutes (frequencies of 5 h^{-1}). The part of the GPS signal with a convective origin will most likely have the same frequency. When GPS signals are influenced by convection and this influence is additional to other fluctuations of the signal, the total power of the signal will increase. Timeseries used in this study are non-isotropic estimates from satellite-receiver combination and are treated separately. Only observations with an elevation larger than 50 degrees will be used; the corresponding non-isotropic residual is mapped onto the zenith using the Niell mapping function. A quantitative value related to the signal is defined as the integral of the quadratic absolute value of the Fourier transform, that is

$$P = \int |H(f)|^2 df, \quad (5.17)$$

where $H(f)$ is the Fourier transform of the projection to the zenith of the non-isotropic residual signal $\delta_{non-iso}(t)$. The quantity P is related to the power of the signal, with unit $\text{m}^2 \text{ s}^{-1}$.

5.4 RESULTS

In this section the values of CAPE are compared to the spectral power of a GPS signal. The results are presented in two steps. First, special attention is given to a single day to set the framework and to investigate the time dependence of the frequency spectral power. Next the results are presented in more general terms for the periods in October/November 2000 and May 2003.

Power spectrum plots are derived from non-isotropic residual timeseries observed in a one hour window at Cabauw. The residual signal is shown in the top panels of Figure 5.3 for three different hours, the azimuth-elevation plot is shown in the middle panel and the corresponding power spectrum is shown in the bottom panels. Note that the elevation shown is 50 degrees and higher. The highest frequency that can be observed is the so-called Nyquist frequency, which is $1/(2 \cdot 30) \text{ s}^{-1}$ in this case, which corresponds to a cycle of 60 h^{-1} . In the first and last hour, only one satellite with an elevation higher than 50 degrees is visible for the full 60 minutes; in the intermediate hour two satellites were observed, indicated by the dashed and solid lines. The value of CAPE, as observed by the radiosonde launched at Cabauw in the same hour, is shown in the bottom panels, for the second and third hour window.

The difference for values of CAPE in spectral density distributions is remarkable. Moreover, two different satellites show almost the same spectral frequency distribution, although the signal itself differs. The power spectrum corresponding to the largest value of CAPE has a maximum

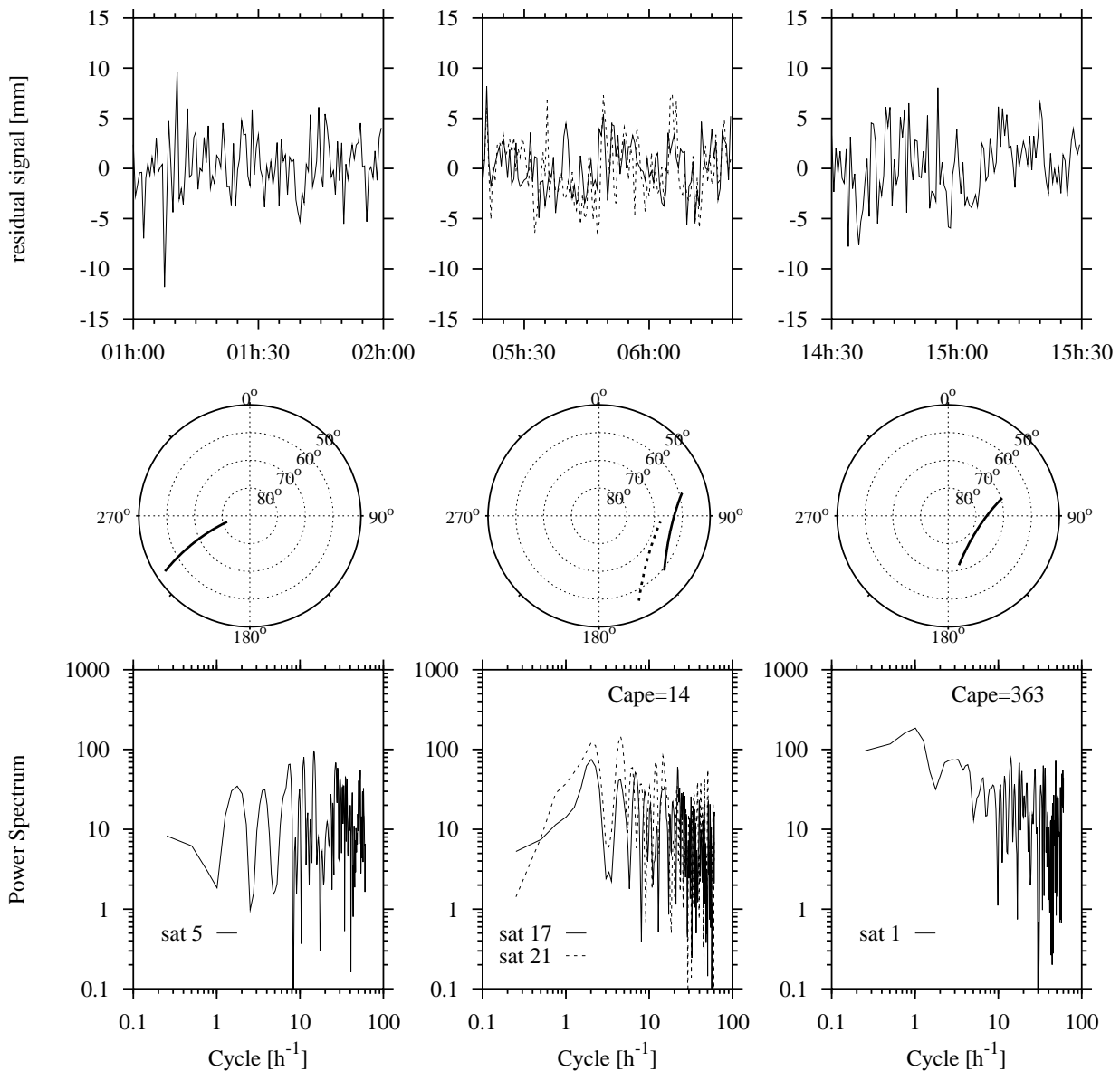


Figure 5.3: Residual signal (top panels), azimuth elevation plot (middle panels) and corresponding power spectrum plot (bottom panels) for three different hour windows on 17 May 2003 observed at Cabauw. For the last two hours the value of CAPE (obtained from the radiosonde observations in Cabauw) is shown.

of around $200 \text{ m}^2 \text{ s}^{-2}$. This maximum lies around 1 h^{-1} . There is a second broader maximum around 2 h^{-1} . The power spectrum related to CAPE values of $14 \text{ m}^2 \text{ s}^{-2}$ shows a less extreme maximum at higher frequencies.

A timeseries of P is shown in Figure 5.4. Also shown in this plot are the values of CAPE as observed by radiosonde launches at Cabauw (open circles, launched at irregular intervals) and De Bilt (crossed circles, launched every 12 hours at 00:00 UTC and 12:00 UTC). The P values are obtained every 15 minutes, through Fourier analysis of non-isotropic residual data observed in a window of one hour. The highest values of the P are observed in the afternoon, which can be related to the fact that convection is triggered by solar heating. There are two radiosondes

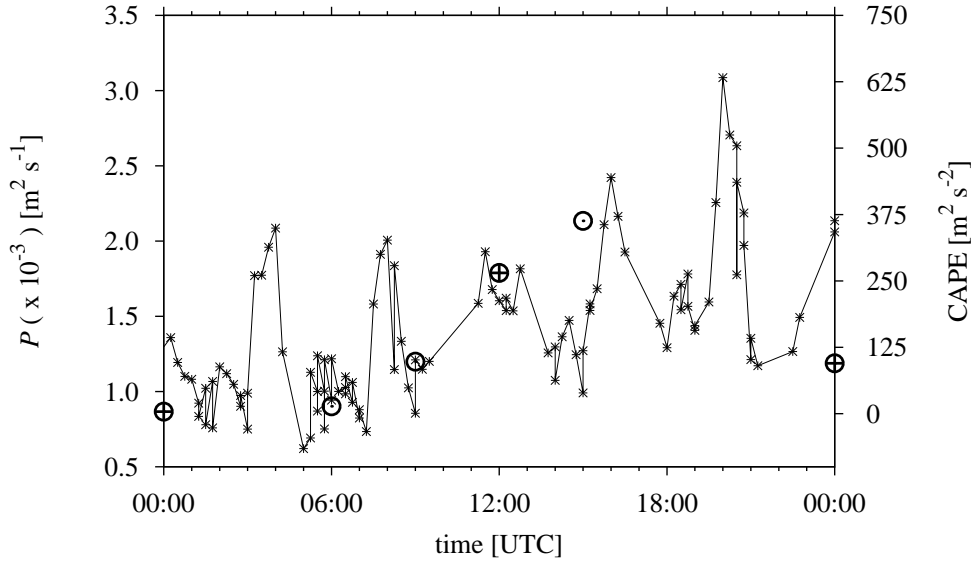


Figure 5.4: Timeseries of P for GPS site Cabauw for 17 May 2003. Also shown in this plot are the values of CAPE as obtained from radiosonde launches in Cabauw (open circles) and De Bilt (crossed circles).

launched right before the maximum at 16:00 UTC. At 12:00 UTC, the radiosonde launch of De Bilt shows a CAPE of approximately $250 \text{ m}^2 \text{ s}^{-2}$. At the same time the P is steadily increasing again and thereafter retaining at a local maximum for a few hours. At 15:00 UTC the CAPE observed by the radiosonde launched at Cabauw is $363 \text{ m}^2 \text{ s}^{-2}$. At the same time the values P are again large. Right after the launch a peak in P is observed. Notice that at 24:00 UTC CAPE from De Bilt is low while the value of P at Cabauw is relatively high. This difference can be due to the distance between De Bilt and Cabauw, which is approximately 30 km.

The trend in the P signal is most likely due to changes in vertical distribution of the humidity in the column of air above the GPS receiver. The frequencies are in atmospheric terms high (although not extreme) but in terms of the GPS signal not high at all. High frequency response might contain information on the turbulence of the atmosphere (Cornman et al., 2004; Kleijer et al., 2004). The low frequencies seem to have a convective origin, which can be explained by the fact that the ZTD is a function of the \mathcal{N}_{BV} and dq/dz (see Eq. 5.16).

Convection is often driven by solar heating and thus has a diurnal signal. Whenever P is related to convection a diurnal signal should be present. Figure 5.5 shows the diurnal cycle for P over the 24 day period for Cabauw in May 2003. The value of P is determined every 15 minutes in May 2003; hourly bins of GPS ZTD data are used. The mean and standard deviation is determined using these values P . The mean and standard deviation with respect to the time of day is shown in Figure 5.5; statistics at times when less than 10 values of P were observed are omitted. From 05:00 UTC onwards, the value of P is steadily increasing and reaches its maximum around 13:00 UTC which is close to the time of day at which in the Netherlands the convective activity is generally the largest.

In Figure 5.6 the value P is plotted versus the CAPE as observed by the radiosonde launches for the periods October/November 2000 and May 2003. The value of P is determined in a one

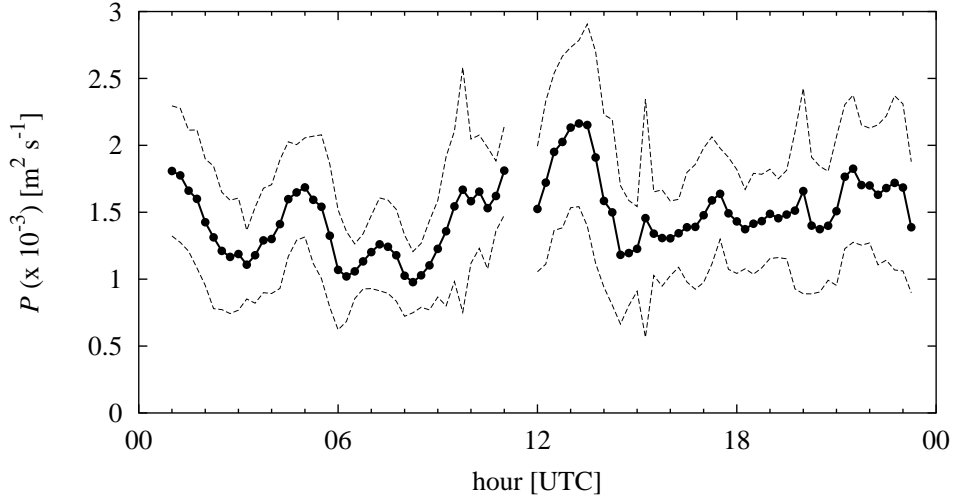


Figure 5.5: Diurnal signal of P plotted every 15 minutes derived from hourly bins of GPS ZTD observations for the month May 2003.

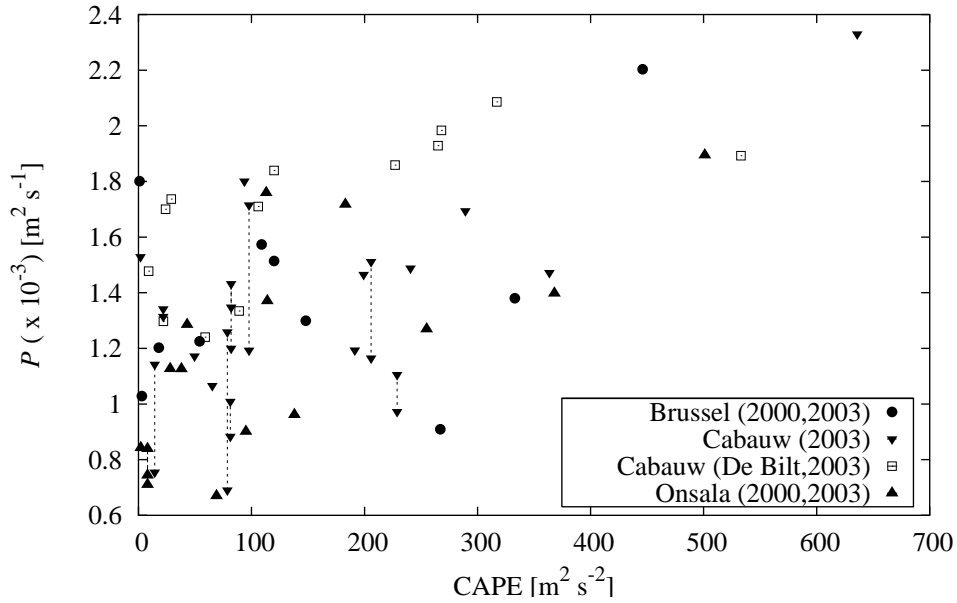


Figure 5.6: Scatter plot of frequency response P versus CAPE for the months October/November 2000 and May 2003. Data points are connected when more than one satellite was visible above 50 degrees elevation for the complete hour of comparison.

hour window starting at the radiosonde launch time. The relation between the two parameters is evident: observations of large values of CAPE are coinciding with large values of P . The relation can be traced back to the definition of CAPE which is related to a (negative) Brunt-Väisälä frequency. A negative \mathcal{N}_{BV} yields a smaller decrease in height for the refractivity N and will influence the observed ZTD in a similar way. Data points with high CAPE and low P are not observed. Note that CAPE represents the upper bound of the available potential energy. For small values of CAPE there seems to be a larger spread in P . This can be caused by fluctuations in moisture (last term of Eq. 5.16) while the profile itself is still more or less stable.

Table 5.2: Correlation of CAPE and P for all GPS receiver-radiosonde pairs.

| GPS | - | RS | Number | Correlation |
|----------|---|----------|--------|-------------|
| | | All | 66 | 0.57 |
| Brussels | - | Ukkel | 10 | 0.39 |
| Cabauw | - | Cabauw | 27 | 0.58 |
| Cabauw | - | De Bilt | 13 | 0.68 |
| Onsala | - | Göteborg | 16 | 0.69 |

The total number of data points is 66 and the correlation between CAPE and P is approximately 0.57. Table 5.2 shows the correlations separated by GPS receiver and radiosonde location combination. Except Brussels and Cabauw, all pairs have a correlation between 0.6 and 0.7. The number of comparisons for Brussels is small (10) and there is an outlier with a low CAPE and high P . Omitting this outlier results in a correlation of 0.59. Furthermore, the maximum CAPE used in the comparisons of Brussels is $450 \text{ m}^2 \text{ s}^{-2}$, while all other comparisons show some CAPE values larger than $500 \text{ m}^2 \text{ s}^{-2}$. The Cabauw-Cabauw pair (radiosonde/GPS receiver collocation) has correlation close to 0.6.

These correlations are not very high, however, keeping in mind that CAPE is obtained from a profile at a certain time and P is determined using Fourier analysis of a timeseries of one hour, the magnitude of correlations are remarkable: it indicates that there is a relation between the two parameters. The fact that there seems to be an inverse relationship between correlation and distance between radiosonde and GPS is striking and cannot be explained with the current data set.

The number of observation pairs is smaller than expected. Recall that the radiosonde launch times were, apart from Cabauw, at 00:00 and 12:00 UTC. The number of satellites with elevations above 50 degrees is small between 11:00 and 12:00 UTC; causing the gaps in the diurnal plots (Fig. 5.5). Because the GPS satellites orbits are chosen such that the observed elevation angles are repeated every day, only more satellites can fill this gap. Another solution would be to include also lower elevation angles. However, then the simple mapping of the non-isotropic residual to the zenith may fail because of differences between the dry and wet Niell mapping functions.

5.5 CONCLUSIONS

In this chapter a method for detection of convection from GPS delay signals is presented. A network of GPS receivers was used to determine the GPS atmospheric delay very accurately. Two periods October/November 2000 and May 2003, for which GPS data with a temporal resolution of 30 seconds were available, were investigated.

The GPS signals were obtained from slant delay estimates with elevations higher than 50 degrees and were projected onto the zenith using the wet Niell mapping function. The Fourier

spectrum of frequencies is related to convective available potential energy (CAPE) retrieved from radiosonde observations. The power of the signal has a diurnal signal consistent with the diurnal signal of convective activity in the Netherlands and shows to have a correlation of 0.57 with values of CAPE. The GPS constellation of satellites and a GPS network has proved to be very reliable. However, when using the algorithm described in this chapter, there are hours during the day where the number of observations with an elevation higher than 50 degrees are small and thus an accurate frequency spectrum cannot be obtained.

In this study the GPS frequency spectrum is only compared to CAPE values from radiosonde observations. By investigation of other observations related to convection, such as LIDAR or Doppler radar more knowledge can be gathered on the value of GPS frequency spectrum analysis.

Chapter 6

Real-time water vapour maps from a GPS surface network and the application for nowcasting of thunderstorms¹

In this chapter the construction of real-time integrated water vapour (IWV) maps from a surface network of Global Positioning System (GPS) receivers is presented. The IWV maps are constructed using a two-dimensional variational technique with a persistence background of 15 minutes old. The background error covariances are determined using a novel two-step method, which is based on the Hollingsworth-Lonnberg method. The quality of these maps is assessed by comparison with radiosonde observations and IWV maps from a numerical weather prediction (NWP) model. The analysed GPS IWV maps have no bias against radiosonde observations and a small bias against NWP. The standard deviation with radiosonde observations is around 2 kg m^{-2} , while the standard deviation increases with increasing forecast length (from 2 kg m^{-2} for the NWP analysis to 4 kg m^{-2} for a forecast length of 48 hours). To illustrate the additional value of these real-time products for nowcasting, two thunderstorm cases are discussed. The constructed GPS IWV maps are combined with data from the weather radar, a lightning detection network and surface wind observations. Both cases show that the location of developing thunderstorms can be identified a couple of hours prior to initiation from the convergence of moist air.

6.1 INTRODUCTION

At present, radiosonde observations are the only operational source for upper-air water vapour data. These observations are expensive and thus sparse in time and space. Global Positioning System (GPS) Zenith Total Delay (ZTD) observations contain integrated water vapour path information, which can be used in numerical weather prediction (NWP) models and for

¹This chapter is submitted as an article to *Journal of Applied Meteorology and Climate* by S. de Haan, I. Holleman and A. A. M. Holtslag.

nowcasting of severe weather. These high temporal resolution water vapour measurements are likely to have a large impact on forecasting rapidly developing systems (Mazany et al., 2002; de Haan et al., 2002; de Haan, 2006; de Haan et al., 2004).

The current measurements of atmospheric water vapour by the radiosonde network do not possess the temporal nor the spatial resolution to infer information about atmospheric scales smaller than synoptic scales. Imagery from geostationary satellites provides continuous monitoring of the atmospheric water vapour, but the use of these observations in NWP is far from straightforward due to the problems with height assignment of the observed structures and to cloud contamination. These observations are very well suited for the use in nowcasting. Due to the passive observation method, however, lower stratospheric water vapour information is hampered by overlying clouds or water vapour and is therefore only valid in cloud-free situations. GPS can observe integrated water vapour IWB continuously independent of clouds and rain.

In this chapter a method to construct GPS IWB maps from GPS observations is presented. These maps are validated with radiosonde observations, NWP derived integrated water vapour and GPS IWB estimates from independent sources. By discussing two cases the application for nowcasting of thunderstorms is demonstrated. First a description of the data used is given. Next, the method of constructing two-dimensional IWB maps based on variational techniques is introduced. This is followed by a validation of the constructed IWB maps. Hereafter, two cases of thunderstorm events in the Netherlands are presented.

6.2 OBSERVATIONS AND INFRASTRUCTURE

A GPS receiver measures the delay of the GPS signal for every GPS satellite in view. By processing all observed slant delays within a certain time window, errors and unknowns, such as satellite and receiver clock errors, can be estimated. An estimate of the Zenith Total Delay (ZTD), which is the slant delay mapped to the zenith is determined for each GPS receiver in the network. The hydrostatic part of the ZTD, called the Zenith Hydrostatic Delay (ZHD), which is the vertical integral of $k_1 \rho R_d$, can be estimated using the surface pressure (Saastamoinen, 1972). The residual part of ZTD is associated with the vertically integrated column of water vapour overlying the GPS receiver, that is

$$\text{IWB} = \frac{1}{k}(\text{ZTD} - \text{ZHD}) \quad (6.1)$$

where k depends on the weighted mean temperature of the atmosphere which in turn can be approximated by a linear function of the surface temperature (Davis et al., 1985; Bevis et al., 1994; Baltink et al., 2002).

The network of GPS double-frequency receivers used here is initially constructed for operational geodetic applications (land surveying, levelling); the network is presented in Figure 6.1 (denoted by the black dots). Data from this network are processed by KNMI every 15 minutes; the meteorological observations are available approximately 5 minutes after observation time.

In this study data from a different network are used besides the GPS data from the real-time network GPS. The additional used estimates are processed on a routinely basis by Geodetic Ob-

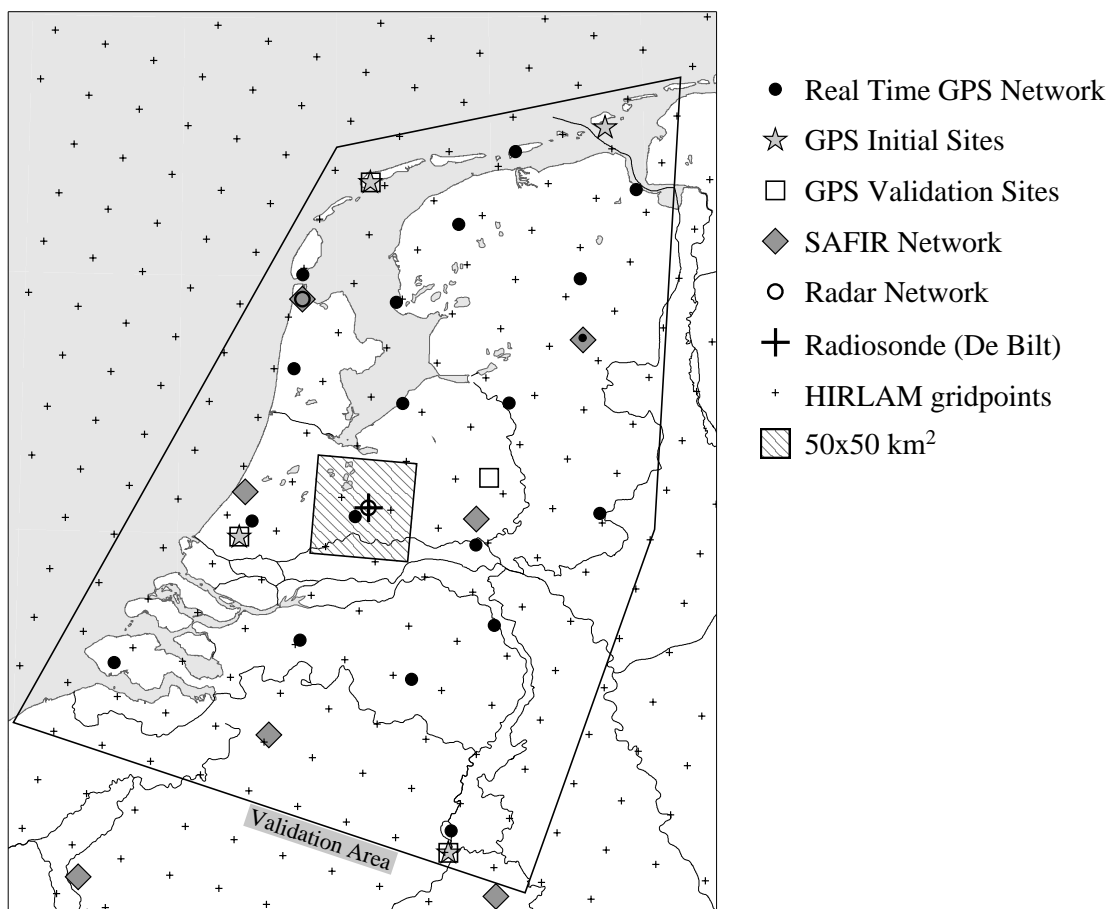


Figure 6.1: Location of GPS sites, SAFIR antennas, two weather radars and the radiosonde launch site. The crosses denote the HIRLAM grid points. Statistics against HIRLAM are derived within the validation area (large area) and the dashed area around the radiosonde launch site De Bilt is used in Section 6.2.5.

servatory Pecny, Czech Republic (GOP) within the framework of the EUMETNET programme E-GVAP. EUMETNET is the network of European National Meteorological Services. GOP estimates the atmospheric delay two times per hour; at the start and at end of each window of one hour. The network does not overlap with the real-time observations and thus samples different parts of the atmosphere and uses different GPS receivers (denoted by the stars and squares in 6.1).

6.2.1 RADIOSONDE

The current system used is a Vaisala RS92 radiosonde. This radiosonde has technical uncertainties of 0.1°C for temperature, 0.2 hPa for pressure and 2% for relative humidity and is launched in De Bilt every 12 hours at 00:00 and 12:00 UTC. The location De Bilt is denoted by the large cross in Figure 6.1. Besides measurements of temperature and humidity, information on the wind speed and direction is inferred from the change in position of the balloon during its ascent. The current system uses a GPS receiver to track the position of the balloon.

6.2.2 WEATHER RADAR

A weather radar employs scattering of radio-frequency waves (5.6 GHz/5 cm for C-band) to measure precipitation and other particles in the atmosphere (See Doviak and Zrnić (1993) for more details). The intensity of the atmospheric echoes is converted to the so-called radar reflectivity Z using the equations for Rayleigh scattering. The Rayleigh equations are valid when the wavelength of the radar is much larger than the diameter of the scatterers (maximum 6 mm for rain). In that case, the radar reflectivity depends strongly (to the sixth power) on the diameter of the rain droplets. The radar reflectivity is a good measure for the strength of the convection (up-drafts) and the amount of condensed moisture in the atmosphere.

KNMI operates two identical C-band Doppler weather radars from Selex SI. The radar in De Bilt is located at a latitude of 52.10° N and a longitude of 5.18° E. The radar in Den Helder is located at a latitude of 52.96° N and a longitude of 4.79° E. The locations of the weather radars are displayed in Figure 6.1 by the open circles. The weather radars have recently been upgraded with digital receivers and a centralised product generation. Precipitation and wind are observed with a fourteen elevation scan (between 0.3 and 25 degrees) which is repeated every 5 minutes.

From the three-dimensional scans pseudoCAPPI images, that is, horizontal cross sections of radar reflectivity at constant altitude, are produced with a target height of 800 m above antenna level and a horizontal resolution of 2.4 km. Radar reflectivity values are converted to rainfall intensities R using a $Z - R$ relationship (Marshall and Palmer, 1948):

$$Z = 200R^{1.6} \quad (6.2)$$

with the radar reflectivity Z in mm^6/m^3 and rainfall rate R in mm/h . More details on the KNMI weather radar network can be found in Holleman (2005, 2007)

6.2.3 LIGHTNING DETECTION NETWORK

KNMI maintains a SAFIR (Surveillance et Alerte Foudre par Interférométrie Radioélectrique) Lightning Detection System for monitoring (severe) convection and for feeding a climatological database. The lightning detection system consists of four detection stations located in the Netherlands and a central processing unit located at KNMI in De Bilt. In addition to the four Dutch stations raw data from three Belgian stations operated by Royal Meteorological Institute of Belgium (RMI) are processed in real-time as well. The locations of the seven detection stations are shown in Figure 6.1 (grey diamonds).

Each lightning detection station consists of three basic components: a VHF antenna array, an LF sensor, and a single-frequency GPS receiver. The VHF antenna array consists of five dipole antennas mounted on a circle and is used for the azimuth determination of discharges based on interferometry. The capacitive LF antenna is used for lightning discrimination, i.e., Cloud-Ground (CG) or Cloud-Cloud (CC) discharge, and for Time-Of-Arrival (TOA) localisation of CG discharges. The GPS receiver provides accurate time stamps for the observed discharges. The observed lightning events are localised by the central processing unit and they are distributed in real-time to the users.

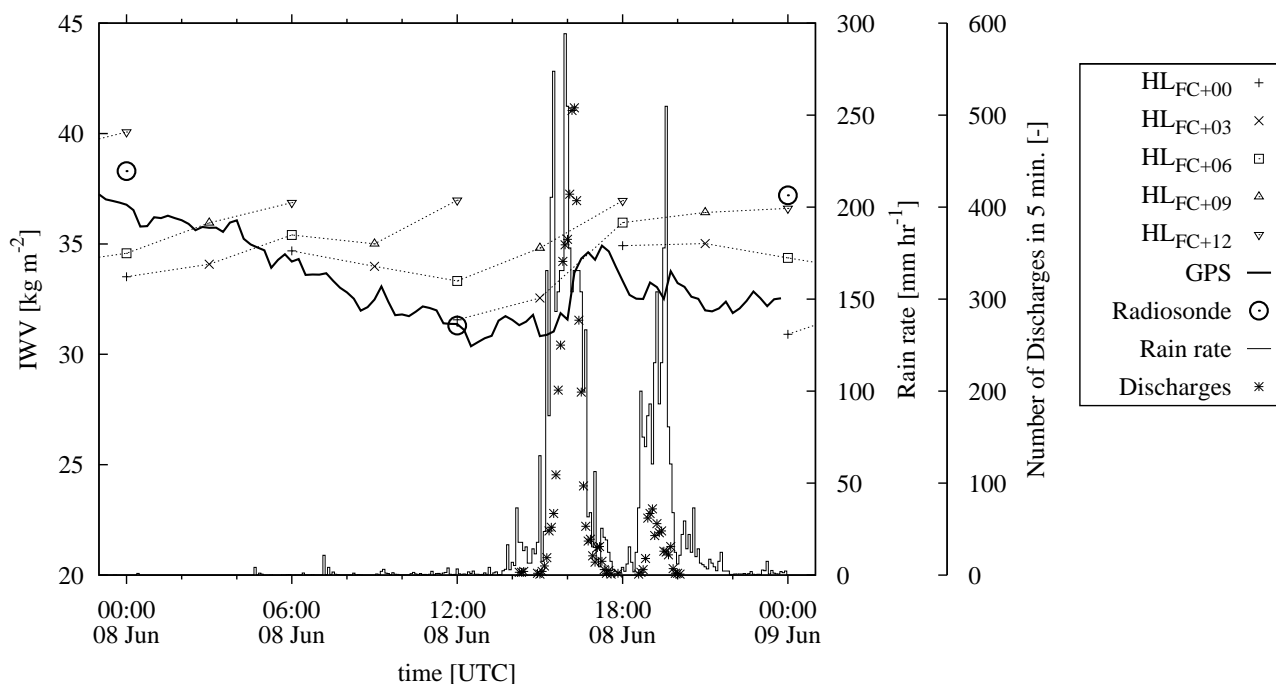


Figure 6.2: Timeseries of IWV from GPS (thick line), radiosonde (circles) and HIRLAM IWV analysis and forecasts in De Bilt (dashed lines). Maximum rain rate as observed by the radar in a $50 \times 50 \text{ km}^2$ area is depicted by a thin solid lines. The stars denotes the number of discharges in the same area; the location of the area is shown in Figure 6.1.

The localisation accuracy of the SAFIR network over the Netherlands is around 2 km. The false alarm rate of the SAFIR network has been assessed using an overlay with weather radar imagery and is less than 1%. The detection efficiency for lightning events of the network is unknown and is currently under investigation. More details on the technical layout of the SAFIR network and its performance can be found in Beekhuis and Holleman (2004); Holleman et al. (2006).

6.2.4 NUMERICAL WEATHER MODEL DATA

At KNMI a High Resolution Limited Area Model (HIRLAM, Undén et al., 2002) is run operationally. This Numerical Weather Prediction (NWP) model is started every 6 hours and has a forecast length of 48 hours. For the period under consideration, the model had a resolution of 22 kilometres and 40 vertical levels. Synoptic observations, such as wind, temperature and humidity from radiosondes and surface wind and temperature observations, are used to analyse the initial state of the atmosphere; note that no GPS data were assimilated. The previous 6-hour forecast is used as background information and, because the model is a limited area model, the forecast at the boundaries of the region is retrieved from the ECMWF forecast fields.

6.2.5 TIMESERIES ANALYSIS

An example of the data described previously is shown in Figure 6.2 for 8 June 2007. GPS IWV and HIRLAM IWV are observed at the GPS site in the centre of the square in Figure 6.1. The difference in temporal resolution is obvious. The most striking observation from this figure is the large deviation between GPS IWV and HIRLAM IWV. Furthermore, the GPS IWV and radiosonde observation are close except at 9 June 00:00 UTC where it deviates from both the HIRLAM analyses and the GPS value. In general HIRLAM analysis are close to the observed GPS IWV (except the analysis at 8 June 00:00 UTC). The forecasts show much larger discrepancies, especially the forecasts valid at 12:00 UTC. At this time the GPS and radiosonde match perfectly. From 15:00 UTC to 16:00 UTC maximum rain rates are observed up to nearly 300 mm h^{-1} (observed in a period of 5 minutes) in the area of $50 \times 50 \text{ km}^2$. In the same period a maximum of 500 discharges in 5 minutes is observed. These occurrences overlap a local increase of IWV from approximately 31 to 35 kg m^{-2} . This increase in IWV was present in the HIRLAM forecast started at 06:00 UTC and 12:00 UTC. The first forecast started with a too large amount of IWV while the second overestimated the increase from 15:00 UTC to 18:00 UTC.

Figure 6.2 shows an increase in IWV but this happens after the time the thunderstorm appeared. The occurrence of the lighting around 16:00 UTC seems to match with the increase in IWV. From the timeseries shown in this figure the thunderstorm event cannot be explained; two-dimensional representation may reveal the explanation for the occurrence of this thunderstorm. To obtain a good estimate of two-dimensional water vapour fields an assimilation system is preferred to incorporate for instance observation errors. In the next sections the description of this system is presented and validated; we will return to this case in Section 6.5.1.

6.3 INTEGRATED WATER VAPOUR FIELD ANALYSIS

An objective analysis of total water vapour columns can be constructed in various ways. The simplest method is to horizontally interpolate between the observed values. This method is straightforward but assumes that the observations do not contain an error. Because all observations contain errors, an approach that incorporates these errors and correlations thereof is more appropriate. The method chosen here is based on a variational technique (see Daley, 1991) which requires a background field and knowledge on the background error and observation error covariances. The optimal analysis \mathbf{x}_a is determined by minimisation of a cost function J ,

$$J(\mathbf{x}) = (\mathbf{x} - \mathbf{x}_b)^T B^{-1}(\mathbf{x} - \mathbf{x}_b) + (\mathbf{y} - H(\mathbf{x}))^T R^{-1}(\mathbf{y} - H(\mathbf{x})), \quad (6.3)$$

where \mathbf{x} is the state space with dimension $L = M \times N$ with grid sizes M and N , the vector \mathbf{y} of dimension K are the observations, B is the background error covariance matrix ($L \times L$), R is the observation error covariance matrix ($K \times K$) and H observation operator $H : R^L \rightarrow R^K$ which maps the state space to the observations.

The state vector \mathbf{x} represents the two-dimensional integrated water vapour field; the observations are IWV from GPS at a receiver location. This implies that the observation operator is

an interpolation of the water vapour field to the observation location. Here a bilinear interpolation is chosen which implies that the cost function J is linear and thus the optimal solution \mathbf{x}_a can be determined analytically, that is $\nabla J(\mathbf{x}_a) = 0$:

$$\begin{aligned} 0 &= B^{-1}(\mathbf{x}_a - \mathbf{x}_b) - H^T R^{-1}(\mathbf{y} - H\mathbf{x}_a) \\ \Leftrightarrow \mathbf{x}_a &= (B^{-1} + H^T R^{-1} H)^{-1}(B^{-1}\mathbf{x}_b + H^T R^{-1}\mathbf{y}) = f(\mathbf{y}, \mathbf{x}_b; R, B). \end{aligned} \quad (6.4)$$

Integrated water vapour observations are available every 15 minutes and thus an analysis with the same frequency is possible.

The matrices B and R play a key role in the analysis. Observation errors are correlated due to the method of observing (i.e. processing GPS signals). However in the following it is assumed that these correlations can be neglected. The validity on this assumption needs to be investigated but is not discussed here.

Estimation of the background error covariances is a delicate matter. A common method to determine these covariances uses a forward model (such as a numerical weather prediction model). The covariances are determined from the difference between the model forecast and the observations. This method is known as the Hollingsworth-Lonnberg-method (Hollingsworth and Lonnberg, 1986). The background error is then closely related to the forward model. For the present system, no forward model is available that can provide a background estimate at analysis time for the variational system. Instead, the variational system will be set up using a persistence background and thus the error covariances between the observations and the background should be determined with a similar relation (i.e. persistence). How can a good estimate of the background error covariance be found without a forward model? We solved this problem by applying a two-step approach for the determination of a background error covariance for a persistence variational analysis scheme. The difference between the steps lies in the origin of the background; the first background field will be a mean value valid at observation time and the second one will have a time difference of 15 minutes. The estimate of the background error covariances based on the last background field will be used in the final real-time variational analysis scheme.

In the first step the background is equal to a mean IWV value as observed by GOP (i.e. a single value for the whole domain). The locations of these GOP sites are indicated as grey stars in Figure 6.1. Timeseries of offsets between the real-time observations and this background are used to determine the initial background error covariances B^0 , that is

$$B^0 = \langle \text{IWV}_{mean}(t) - y_i(t), \text{IWV}_{mean}(t) - y_j(t) \rangle \quad (6.5)$$

The covariances are shown in Figure 6.3a. Also shown in this figure is a fit of the background error covariance. Note that the value at zero distance actually is the sum of the background error and the observation error. Using this background an initial analysis \mathbf{x}_a^0 can be constructed, that is

$$\mathbf{x}_a^0(t) = f(\mathbf{y}(t), \text{IWV}_{mean}(t); B^0, R) \quad (6.6)$$

In the second step, the background is the initial analysis as obtained in the first step (using background error covariances B^0). The timeseries of the differences between this analysis and

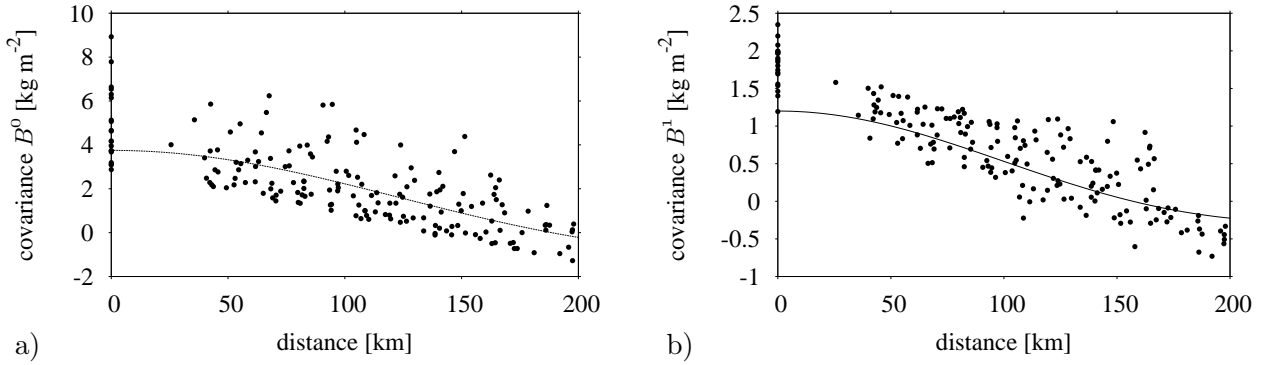


Figure 6.3: Background error covariance with a mean background (a) and a persistence background (b) with respect to site separation.

observations 15 minutes later are used to determine the background error covariances B^1 :

$$B^1 = \langle \mathbf{x}_a^0(t) - y_i(t + 15'), \mathbf{x}_a^0(t) - y_j(t + 15') \rangle \quad (6.7)$$

The results are shown in Figure 6.3b. The background error covariances B^1 will be used in the real-time variational analysis.

The period over which the background error covariances are estimated runs from January to July 2007. The background error covariance in the first step has values ranging from -2 to 6 kg m^{-2} for distances larger than zero. This is due to the coarse background field used, which is a single value for the whole region. The background error covariances decrease to values ranging from -1 to 1.5 kg m^{-2} in the second step. This decrease is the result of a better background estimate, although persistence is used and no forward model is applied. The estimate of the observation errors, which can be deduced from the covariances at zero distances ranges from 1 to 1.5 kg m^{-2} . These values have been observed in earlier studies and show that the method used here results in good covariances (Rocken et al., 1993, 1995, 1997; Emardson et al., 1998, 2000; Liou et al., 2001; Niell et al., 2001; Stoew et al., 2001; Guerova et al., 2003).

6.4 INTEGRATED WATER VAPOUR FIELD VALIDATION

The accuracy of GPS IWV is typically around 5 to 10% of the IWV value, when compared to radiosonde and NWP (Rocken et al., 1993, 1995, 1997; Emardson et al., 1998, 2000; Liou et al., 2001; Niell et al., 2001; Stoew et al., 2001; Guerova et al., 2003). Over the period May 1 to July 1 2007, the constructed IWV analyses are compared to estimates from GPS, radiosonde and NWP. First IWV estimates obtained from Geodetic Observatory Pecny, Czech Republic (GOP) are considered. Table 6.1 shows the statistics of the comparison of the two-dimensional analysis with the GPS solutions for three sites (see Figure 6.1, open squares).

The largest value of standard deviation is observed at a site with large distance to the closest GPS site used in the analysis (TERS). This is not surprising as there is no IWV information available near this site. The bias and standard deviation at the two other sites are comparable. Compared to GPS IWV from a different source, the standard deviation is around 2 kg m^{-2} .

The comparison with radiosonde observations from De Bilt is showing very good statistics. A total of 96 comparisons at 00:00 and 12:00 UTC resulted in a negligible bias (0.01 kg m^{-2}) and a standard deviation of 1.94 kg m^{-2} .

When the analysed IWV field is compared to the NWP field for the period from May 1 to July 1 for different forecast lengths, the biases show no tendency and are around -0.5 kg m^{-2} (see Table 6.2) for the forecast lengths shorter than 12 hours; for forecast lengths longer than 12 hours an increase in bias is observed. Note that the comparison is made on the validation region close to the sites (see Figure 6.1). The standard deviation shows an increase with forecast length of nearly 100% after 48 hours. An increase in standard deviation is not surprising because the NWP forecast model always loses quality with increasing forecast length. Part of this increase in standard deviation is due to phase errors in the forecasts resulting in a double penalty. Nevertheless, the sudden change in bias cannot be explained by the double penalty argument.

In Figure 6.4, the horizontal distribution of the mean IWV_{an} and the bias and standard deviation of the difference between IWV_{an} and HIRLAM analyses for the month June 2007 are shown. The signature of the bias between model and GPS analysis has a number of origins. The main cause of the difference is that the model orography and the GPS observation heights

Table 6.1: Statistics of the difference between the analysed IWV field and GPS estimates from processing GOP over a period from May-June 2007.

| site | num | mean IWV_{an} | $\text{IWV}_{an} - \text{IWV}_{GOP}$ | |
|------|------|------------------------|--------------------------------------|----------------------------------|
| | | $[\text{kg m}^{-2}]$ | bias $[\text{kg m}^{-2}]$ | σ $[\text{kg m}^{-2}]$ |
| DELF | 1342 | 21.23 | -0.25 | 2.08 |
| EIJS | 1344 | 22.32 | -0.62 | 1.87 |
| TERS | 1343 | 19.85 | -0.22 | 2.50 |

Table 6.2: Statistics of the difference between GPS and NWP IWV fields for different forecast lengths over a period from May-June 2007. Mean value of IWV_{an} is 21.77 kg m^{-2} .

| Forecast length [hrs] | num | $\text{IWV}_{an} - \text{IWV}_{NWP}$ | |
|--------------------------|-----|--------------------------------------|----------------------------------|
| | | bias $[\text{kg m}^{-2}]$ | σ $[\text{kg m}^{-2}]$ |
| 00 | 206 | -0.44 | 2.01 |
| 03 | 209 | -0.55 | 2.06 |
| 06 | 206 | -0.43 | 2.20 |
| 09 | 209 | -0.52 | 2.34 |
| 12 | 206 | -0.38 | 2.46 |
| 24 | 206 | -0.25 | 3.02 |
| 36 | 206 | -0.01 | 3.61 |
| 48 | 206 | 0.19 | 4.00 |

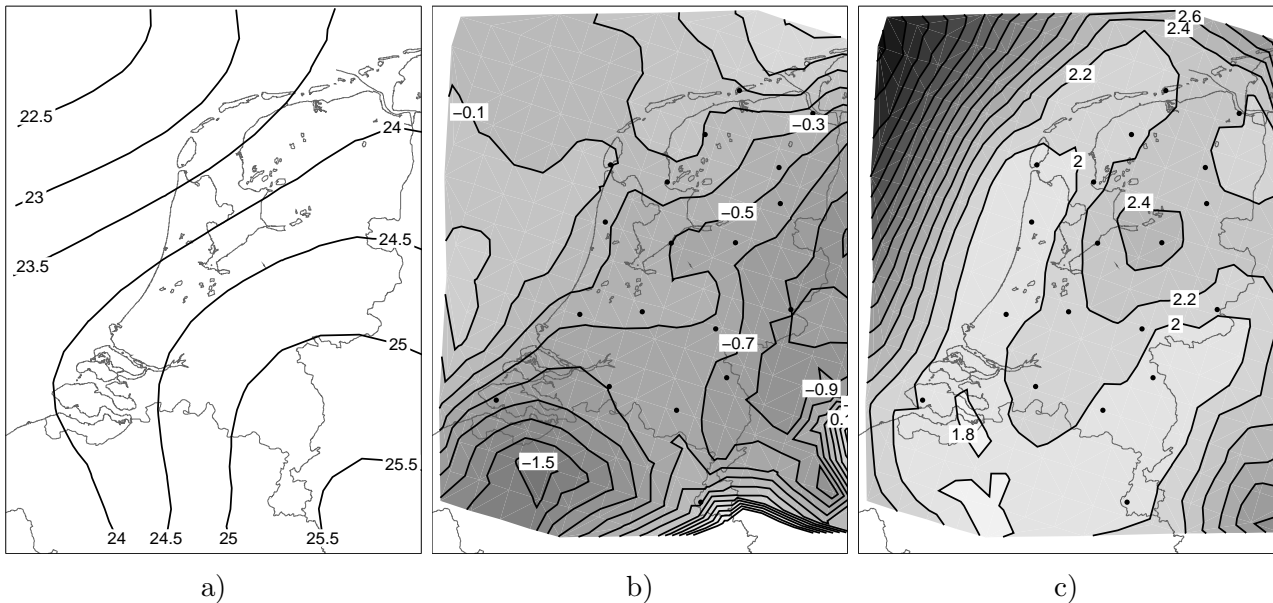


Figure 6.4: (a) Mean of IWV_{an} , and (b) bias and (c) standard deviation of the difference between IWV_{an} and HIRLAM analysis for the month June 2007.

are different. The observations are taken as is, which implies that for a GPS receiver on a tall building the total amount of water vapour in the column will be lower than when the GPS receiver is installed at the surface. The horizontal representativeness of the GPS IWV value will also be smaller in areas of variable orography (see the increase in bias at the right bottom corner in Figure 6.4b). Systematic biases may be present in both model and GPS. Note that, although there are no observations over the North Sea, the bias against the model is small. Over land, the bias increases with distance to the coast, which could be related to an orographic signal. The standard deviation increases with increasing distance to the GPS network. This is clearly visible in the top left corner and the bottom right corner. The overall bias ranges between 1.8 and 2.4 kg m^{-2} .

Figure 6.5 shows a timeseries of the mean IWV_{an} , the bias and the standard deviation of the difference between GPS IWV analysis and NWP analysis and 6 hour forecast (denoted as FC+00 and FC+06, respectively). Both the bias and standard deviation differ from time-to-time and even between analysis and forecast. Especially, during June 7 and 8 the biases of the analysis and forecast have opposite signs. On June 20 and 21 the standard deviation of the 6 hour forecast was significantly higher than the standard deviation of the NWP analysis and the biases were also of opposite sign. Note that due to problems in the GPS data exchange there are a few gaps in the timeseries.

The NWP analysis is created without GPS information: both fields can be regarded as independent. Apparently, the mean difference and standard deviation signal show that GPS IWV contains other information structures than NWP and because GPS IWV observations are accurate the IWV_{an} is expected to have an additional value.

Figure 6.6 displays the frequency distribution of IWV in 4 kg m^{-2} bins in the period May-June 2007. Panel 6.6a shows these distributions for radiosonde, NWP and IWV_{an} at 00:00

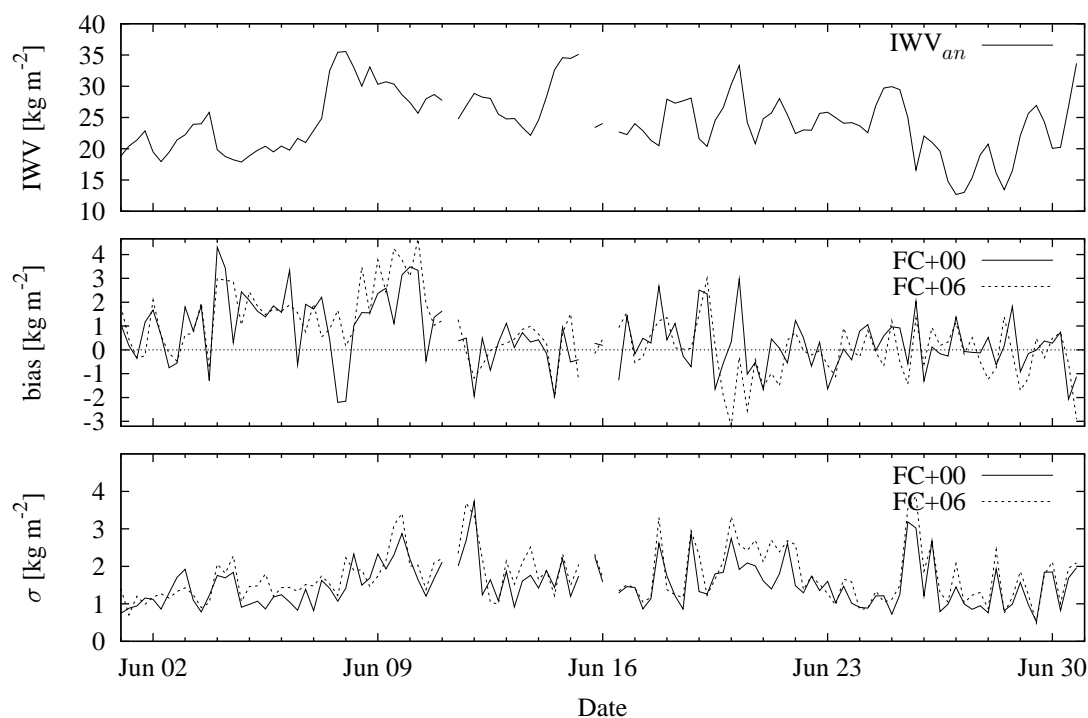


Figure 6.5: Timeseries of the bias and standard deviation of the difference between GPS IWV analysis and NWP analysis (FC+00, solid line) and 6 hour forecast (FC+06, dashed line) respectively.

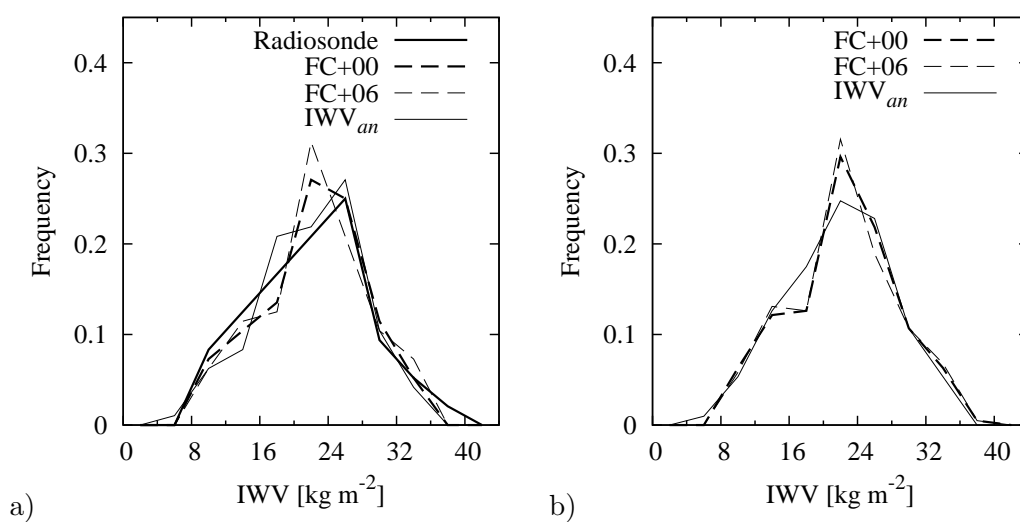


Figure 6.6: Frequency distribution of IWV in the period May-June 2007 from radiosonde (thick solid line), NWP analysis and 6 hour forecast (thick and thin dashed lines, respectively) and IWV analysis (thin solid line). Panel a shows the distribution for 00:00 and 12:00 UTC and panel b for 00:00, 06:00, 12:00 and 18:00 UTC. Note that no radiosondes are launched at 06:00 and 18:00 UTC in De Bilt.

and 12:00 UTC. Outside the range 16 to 24 kg m^{-2} these distributions do not differ much. Both the NWP analysis and 6 hour forecast show a different maximal distribution for values

between 20 and 24 kg m⁻². The distribution of the NWP analysis differs less from the radiosonde distribution because the information of these observations are assimilated in the NWP analysis, however the difference is remarkable. The distribution of the radiosonde and IWV_{an} are very close. Panel 6.6b shows the distributions for all available times (00:00, 06:00, 12:00 and 18:00 UTC). Outside 16 to 24 kg m⁻² the distributions are almost identical. For values between 16 and 24 kg m⁻² there is a shift in distribution: the NWP dataset contains less observations between 16 and 20 kg m⁻² than GPS. This difference in water vapour distributions from NWP can also be observed in panel 6.6a, although less apparent. The reason for this shift in IWV values needs further investigation.

6.5 NOWCASTING CASES

6.5.1 A SEVERE THUNDERSTORM ON 8 JUNE 2007

On 8 June 2007 a low pressure system moved towards the Netherlands from a south-east direction. Pressure values of 1012 hPa were observed in the centre of this system: the low pressure system was not well developed. Nevertheless, a local severe weather event occurred around 14:00 UTC on the eastern part of the border between the Netherlands and Belgium causing flooding in Maastricht. The thunderstorm produced rain-rates between 10 and 30 mm h⁻¹ and over 200 lightning discharges in a 10×10 km² area. A very unstable profile was observed by the radiosonde observation from De Bilt at 12:00 UTC. The lifting condensation level (LCL) was around 900 hPa and the Level of Neutral Buoyancy (LNB) was around 200 hPa. The Boyden index, defined as $BI = 0.1(z_{700} - z_{1000}) - T_{700} - 200$ (Boyden, 1963), was around 98. The Boyden index appears to be a good indicator for thunderstorm intensity: values exceeding 96 are an indication for severe thunderstorm activity (Schmeits et al., 2005). There was very little wind shear at 850 hPa where the wind direction turned from south-west to more southerly. The surface winds at 14:00 UTC show that there is a convergence zone right on the location of the thunderstorm. To the west of the convergence zone surface winds are from the west to northwest, while east of the convergence zone winds blow from the east. A dry tongue of integrated water vapour lies over the Netherlands at 14:00 UTC with low values (23 kg m⁻²) in the mid-east of the Netherlands and strong gradients to towards the south and west. Figure 6.7 shows the observed surface winds (wind barbs), GPS IWV (contours), radar rain-rates (grey scale) and lightning events (symbols) for four times starting at 14:00 UTC with a time step of one hour.

The heavy rainfall and intense lightning activity occurs right on the convergence zone of the surface wind. Air with a large amount of integrated water vapour is advected from the west to this region, while air from the east contains less moisture. Note that surface winds are not representative for wind at higher altitudes. However, most moisture resides in the lower part of the atmosphere. The convergence of the moisture increased the activity of the thunderstorm, which is clearly visible from the GPS IWV maps.

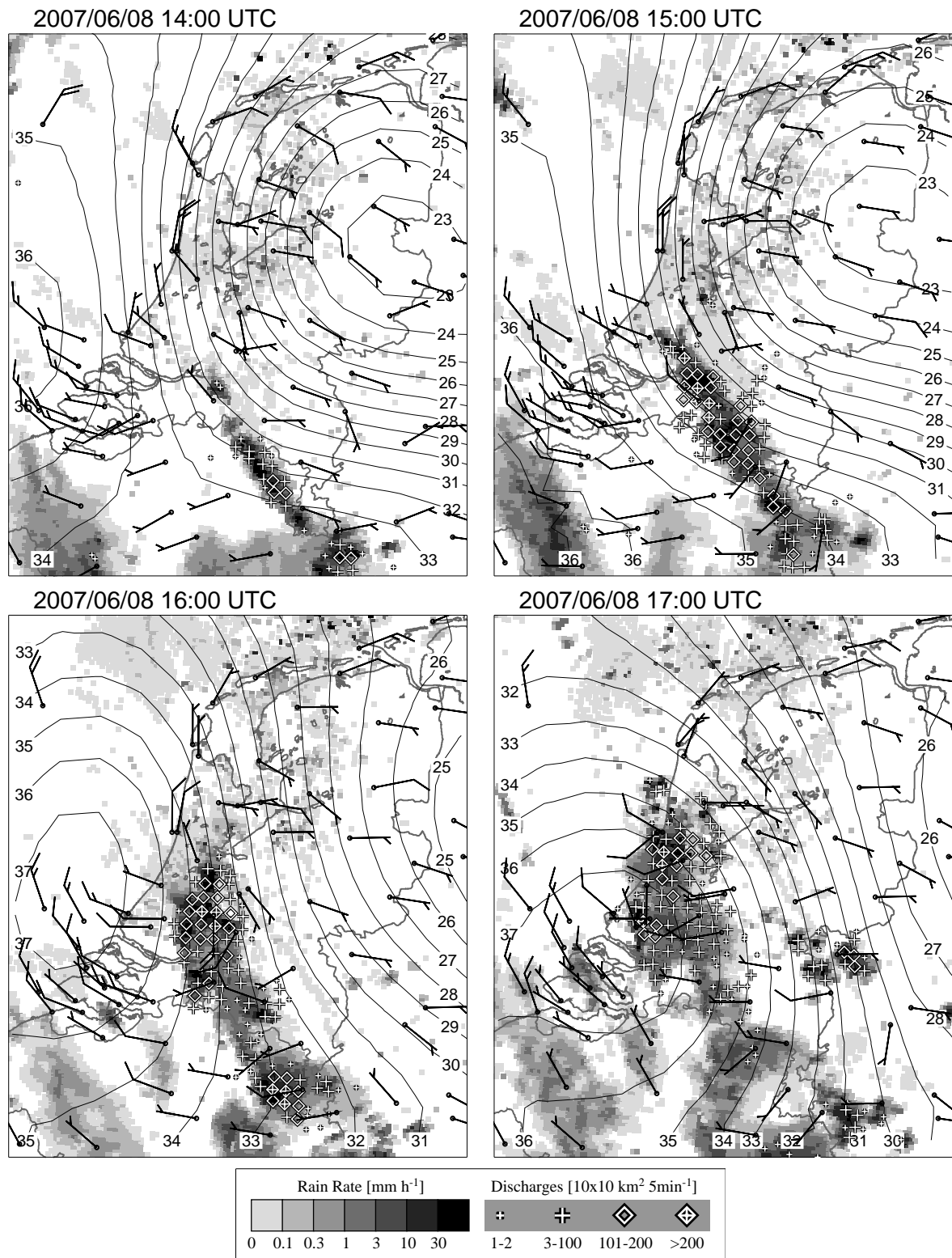


Figure 6.7: Radar rain-rate observations (grey scales), lightning discharges (crosses and diamonds), GPS IWV (contoured) and surface wind observations (wind barbs) at 08 June 2007, 14:00 UTC to 17:00 UTC with an interval of one hour.

6.5.2 TWO THUNDERSTORM EVENTS ON 20 JULY 2007

The second case describes the occurrence of two thunderstorms. A low pressure system moved north-eastward through the English Channel towards the Netherlands on 20 July 2007. A warm front, on east side of the system with an east-west direction, preceded the low pressure system. On the west side of the low pressure centre an occluded front moves to the west. At 18:00 UTC this system was situated over the mid-east of the Netherlands. The radiosonde profile from De Bilt at 12:00 UTC showed a almost completely saturated profile with a LCL at 950 hPa and a LNB around 290 hPa. The Boyden Index was 96 which implies a moderate chance of severe thunderstorms. Surface winds ahead of the low pressure system were from the north-east, while behind this system south-west winds were observed. A water vapour maximum travels from south to north over the Netherlands, entering the south at 10:00 UTC and leaving the region 19:00 UTC. The maximum value was over 40 kg m^{-2} . A large thunderstorm moves in the same direction although with a higher group velocity, the maximum activity occurs east of the water vapour maximum. The thunderstorm entered the Netherlands at 11:00 UTC and has left the country at 17:00 UTC. At that time a second line of thunderstorms developed over the middle of the Netherlands; the position of this thunderstorm coincides locally with water vapour contours at the location where the water vapour gradients are large. In Figure 6.8 the observed surface winds (wind barbs), GPS IWV (contours), radar rain-rates (grey scale) and lightning events (symbols) for four times with a time step of tow hours are shown.

It appears that the intense lightning of the first thunderstorm occurred to the east of the water vapour maximum. The thunderstorm overtakes the water vapour maximum and then weakens. The second thunderstorm developed in a zone of surface wind convergence which was present more than two hours prior. Moist air is advected from the maximum (which lies north of the convergence zone) to this region resulting in an increase in the intensity of the thunderstorm (Banacos and Schultz, 2005). Thus again, the IWV fields provide useful information.

6.6 CONCLUSIONS

In this chapter a method is presented to construct real-time two-dimensional water vapour maps from Integrated Water Vapour (IWV) observations obtained from a surface network of GPS receivers. The analysis method is based on a two-dimensional variational technique with a persistence background. Every variational analysis system requires knowledge on the observation and background error covariances. The observation error covariances are assumed to be uncorrelated between different locations. Background error covariances are determined based on Hollingsworth-Lonnberg method (Hollingsworth and Lonnberg, 1986). The method described in this chapter uses a two step technique to avoid the use of a forward model. In the first step the background map is retrieved from an independent GPS data source valid at the same time of observation over a period from January to July 2007. The difference between the mean value of the region under consideration and the observed real-time GPS IWV observations determines the first set of background error covariances. Next these background error covariances are used together with real-time observations to obtain an analysis map. This

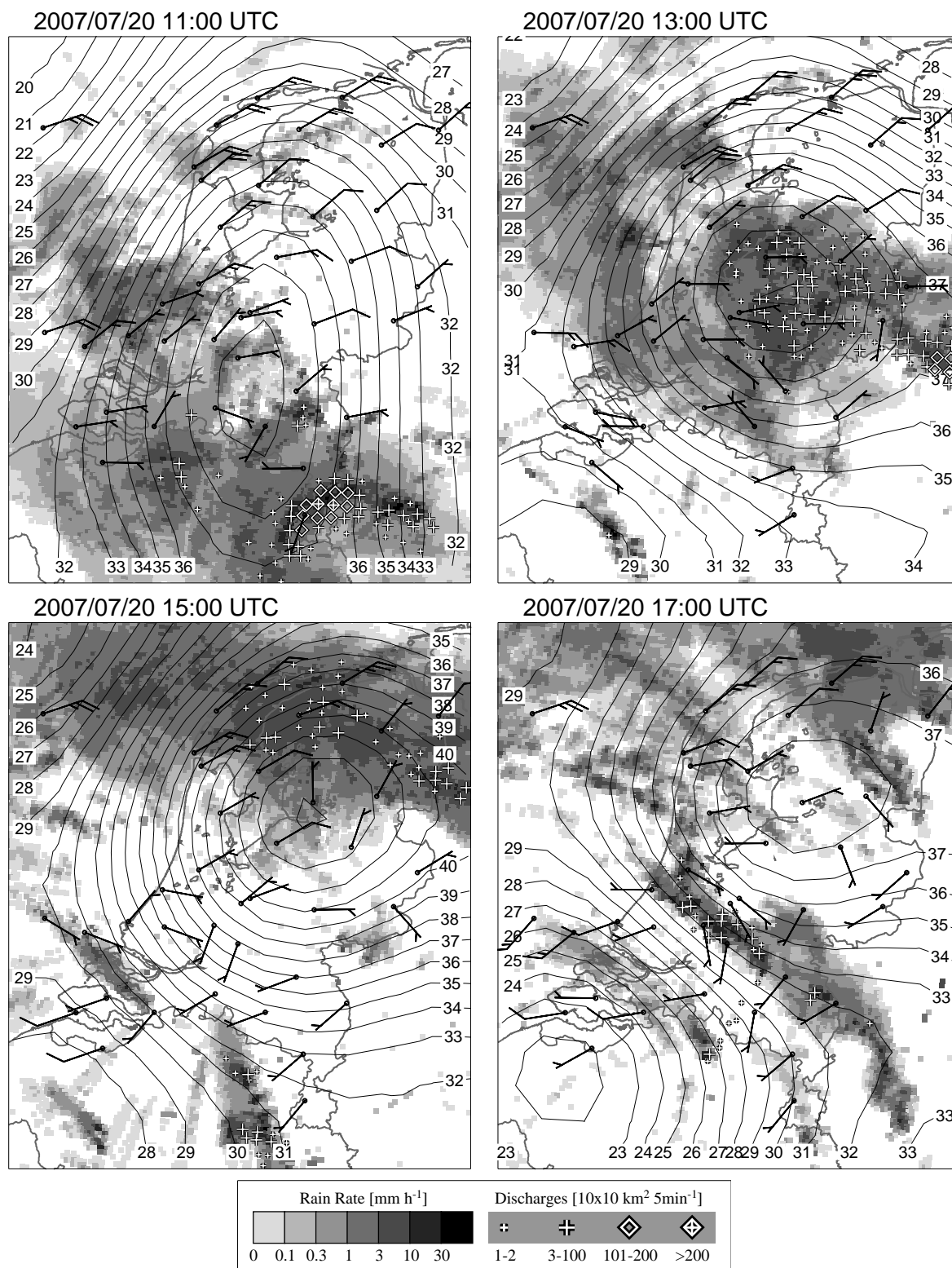


Figure 6.8: Radar rain-rate observations (grey scales), lightning discharges (crosses and diamonds), GPS IWV (contoured) and surface wind observations (wind barbs) at 20 July 2007, 11:00 UTC to 17:00 UTC with an interval of two hours.

map is then used to determine the background error covariances with real-time observation 15 minutes later.

The maps are validated with HIRLAM IWV analysis and forecast maps and radiosonde observations. The mean difference between radiosonde and GPS IWV maps is negligible, while the standard deviation is less than 2 kg m^{-2} . The bias between HIRLAM and GPS IWV is between 0.4 and 0.6 kg m^{-2} while the standard deviation increases from 2 to 4 kg m^{-2} with increasing forecast length to 48 hours. This is due to the fact that the forecast skill decreases with increasing forecast length. The horizontal distribution of the difference between one month of HIRLAM IWV and GPS IWV shows a small signal of increasing bias with increasing distance to the coast. The standard deviation increases dramatically with the increasing distance from the observation network. Histograms of the IWV values of HIRLAM are different from those observed with radiosonde and GPS. The occurrence of IWV values around 16 kg m^{-2} and around 20 kg m^{-2} for HIRLAM seems to be shifted towards the higher values compared to both radiosonde and GPS.

By examining two cases the additional value of the real-time GPS IWV maps for nowcasting is illustrated. Both cases show that the convergence of moist air contains information on the location of developing thunderstorms.

Altogether it is concluded that the real-time GPS IWV maps constructed using a two-dimensional variational method are of good quality and can be helpful for nowcasting of severe thunderstorms.

Chapter 7

Comparison of GPS slant delay measurements to a numerical Model: case study of a cold front passage¹

GPS water vapour measurements are expected to have the ability to fill the lack of moisture information in Numerical Weather Prediction (NWP) and nowcasting. Zenith Total Delays (ZTD) are obtained by mapping signal delays in the line of sight to the vertical in the processing of the GPS data. The estimated zenith integrated water vapour (IWV) can be extracted from this ZTD when surface pressure and temperature is available. This method is valid under the assumption that the atmosphere is layered and horizontally stratified. When a cold front passes the observation sites, this assumption is not valid. In this chapter a case study of such a cold front passage is examined. Slant delays from GPS and from a high resolution NWP model HIRLAM (High Resolution Limited Area Model) are derived, and the non-stratified slant wet delay components from GPS are compared with HIRLAM. Furthermore, GPS derived zenith IWV measurements are compared to HIRLAM. Meteosat water vapour channel information together with IWV derived from GPS and HIRLAM are used for interpreting the results. The additional information of slant measurements for use in synoptic forecasting and NWP is briefly discussed.

7.1 INTRODUCTION

Since the mid 1990's networks of ground based GPS receivers have been used to retrieve Integrated Water Vapour (IWV) (see e.g. Bevis et al., 1992; Rocken et al., 1995). The signal delay in the zenith direction, the so-called Zenith Total Delay (ZTD), is one of the parameters that is routinely estimated by the GPS analysis software, together with other parameters such as coordinates, satellite- and receiver clock errors, ionospheric delays and phase ambiguity parameters.

¹This chapter is previously published in *Phys. Chem. Earth*, 2002, **27**, pp 317–322, by S. de Haan, H. van der Marel and S. J. M. Barlag.

The ZTD can be converted into IWV using measurements of surface pressure and temperature (Bevis et al., 1994), or directly assimilated into Numerical Weather Prediction (NWP) models. This method is valid under the assumption that the atmosphere is layered and horizontally stratified, and that the actually observed signal delays in the line of sight can be mapped to the zenith direction using dry and wet mapping functions. Unfortunately, this assumption is not always valid, for example when a cold front passes the observation sites the water vapour shows strong horizontal gradients.

More recently, several groups have started to estimate additional gradient parameters in their analysis (Bar-Sever et al., 1998) or directly to estimate delays along the line of sight (Alber et al., 2000; Braun et al., 2001). This is an important development, as it will not only improve the geodetic parameters, but also provide information on the intensity and timing of humidity gradients in the model humidity field for high resolution NWP models.

In this chapter a case study of a cold front passage is examined using slant delay estimates from GPS and a high resolution NWP. On the 30th October 2000 a barotropic low passed over the North Sea, which resulted in some exceptional weather with very strong gradients in IWV. In this chapter estimates of the non-stratified slant wet delay (SWD) component derived from the NWP model HIRLAM (High Resolution Limited Area Model), and a GPS network in the Netherlands, are compared for this special case. Also, we describe the method we used to derive slant delay estimates from GPS and the NWP model.

7.2 COMPUTATION OF SLANT DELAYS FROM GPS

In this case-study we have chosen to compute the wet delay along the line of sight, the so-called Slant Wet Delay (SWD). Three days of data from our routine analysis of a GPS network for the retrieval of Integrated Water Vapour in the Netherlands were used (Baltink et al., 2002). The Zenith Total Delay is estimated at 6 minute intervals for a network of 6 stations in the Netherlands and a further 10 stations distributed over the Northern hemisphere, using the GIPSY-OASIS software. The elevation cut-off angle was 10 degrees. The slant delays were computed for three days, 29, 30 and 31 October 2000, using the least-squares residuals from the routine processing.

The least-squares residual computed by GIPSY-OASIS is actually the ionospheric free linear combination of phase observations, minus the observation computed from the estimated parameters (positions, satellite and receiver clocks, zenith wet delays and phase ambiguities). These residuals contain a number of effects that have not yet been modelled: site multipath, unmodeled antenna phase delays, non-stratified slant delay components and measurement noise. The first two effects, multipath and unmodeled antenna phase delays, depend mainly on the receiver-satellite geometry, are relatively constant in time and do not depend on the atmosphere. The non-stratified slant delay component is defined as the actually observed slant delay minus a slant delay computed from the mapping function and estimated zenith total delay (ZTD). The non-stratified slant delay is therefore also affected by differences in the vertical layering of the atmosphere with respect to the model used by the mapping function.

In order to separate the non-stratified slant delay component from multipath and antenna

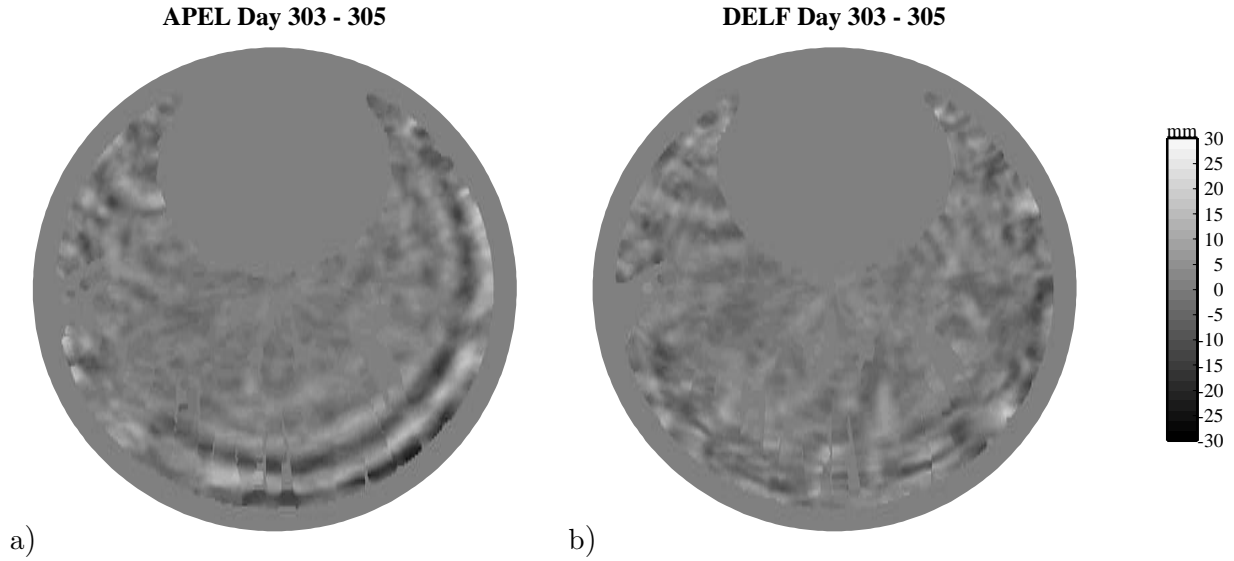


Figure 7.1: Signal delays due to multipath and other site effects at (a) Apeldoorn, and (b) Delft. For the areas in grey no data was available. Zenith angle is plotted on the radial axis and azimuth angle is plotted on the angle axis.

phase delays, first a map of the site-multipath is computed for every station, using the least-squares residuals of the full three day period. Each map $M_i(\alpha, \beta)$ consists of a 0.5×0.5 degree grid in azimuth α and elevation β . The maps have been computed using the “adjustable tension continuous curvature surface gridding algorithm” of GMT (Smith and Wessel, 1990; Wessel and Smith, 1991), using block mean averages of the residuals as input. As can be seen from the examples in Fig. 7.1 the multipath is considerable, especially at small elevation angles, ranging sometimes up to ± 30 mm. This is very significant compared to the measurement noise of roughly 6 – 9 mm which can be expected for the ionosphere free linear combination.

The least-squares residuals, corrected for multipath, can be interpreted as the non-stratified part SWD_{non} of the slant delay

$$\text{SWD}_{non}^{\text{GPS}} \doteq r - M_i(\alpha, \beta) \quad (7.1)$$

with r the least-squares residuals of the ionosphere free linear combination of GPS phase observations, and $M_i(\alpha, \beta)$ the multipath map for the station in question. The slant delay STD, as computed from GPS, is then

$$\text{STD} = m_h(\beta) \cdot \text{ZHD}_0 + m_w(\beta) \cdot \text{ZWD}' + \text{SWD}_{non}^{\text{GPS}} \quad (7.2)$$

with ZHD_0 the a-priori zenith hydrostatic delay computed using the model of Saastamoinen, ZWD' the zenith wet delay as estimated by GIPSY², $m_h(\beta)$ and $m_w(\beta)$ the hydrostatic and wet mapping functions of Niell (1996), and $\text{SWD}_{non}^{\text{GPS}}$ the multipath corrected residuals, or non-stratified slant wet delay, of Equation 7.1.

²Actually, ZWD' is not truly a wet delay, but only a correction to an approximate hydrostatic delay ZHD_0 . When we compute IWV from GPS, ZHD_0 is replaced by a ZHD computed from barometric pressure measurements at the GPS site or from the synoptic network.

The current procedure is only a first attempt at estimating slant delays and multipath, and further improvements are certainly possible. For example, we expect to improve the multipath maps and slant delay estimates when we increase the sampling rate, use more days, introduce a dynamical model for the slant delays and use more rigorous mathematical and numerical procedures.

7.3 DERIVATION OF SLANT DELAYS FROM NWP

The theoretical zenith total delay (ZTD) at a GPS location with height z_a due to the refractivity of the atmosphere overlying the GPS location is

$$\text{ZTD} = 10^{-6} \int_{z_a}^{\infty} k_1 R_d \rho dz + 10^{-6} \int_{z_a}^{\infty} \frac{R_d}{\epsilon} \left(k_2 - \epsilon k_1 + \frac{k_3}{T} \right) q \rho dz, \quad (7.3)$$

where R_d is the specific gas constant for dry air, q is the specific humidity and ρ is the density of the air. The constants k_1 , k_2 and k_3 have the following values (Bevis et al., 1994) $k_1 = 7.76 \cdot 10^{-3}$ [K/Pa], $k_2 = 7.04 \cdot 10^{-1}$ [K/Pa] and $k_3 = 3.74 \cdot 10^3$ [K²/Pa]. The constant ϵ is the ratio between the specific gas constant for dry air and moist air, that is $\epsilon = R_d/R_v$.

The first term on the left hand side of Equation 7.3 is called the zenith hydrostatic delay (ZHD) and the second term, which contains a temperature and humidity dependence, is called the zenith wet delay (ZWD).

In general, fields values in numerical weather prediction models (NWP) are given with pressure as the vertical coordinate. The integral of Equation 7.3 can be rewritten under the assumption that the atmosphere is in hydrostatic equilibrium, that is obeying the hydrostatic equation

$$\partial p = -\rho g \partial z, \quad (7.4)$$

where g is the gravity. This coordinate transformation is only valid for zenith estimates. Furthermore in strong convective situations together with a high resolution NWP model the hydrostatic assumption may fail. In these cases a non-hydrostatic model description is required and the numerical estimate of Equation 7.3 is more complicated. The horizontal model resolution we use here (12 km) allows us to use the hydrostatic approximation.

Numerical integrating the first term of Equation 7.3 and using the hydrostatic assumption, the ZHD can be approximated by

$$\text{ZHD} \approx 10^{-6} \sum_{i=1}^{31} k_1 \frac{R_d}{g_i} \Delta p_i, \quad (7.5)$$

where the model consist of 31 levels, with layer thickness Δp_i . Numerically integration of ZWD is performed analogously. The values of temperature and specific humidity at a specific pressure level are the mean quantities representative for the layer. The thickness of a level is estimated using the increments of pressure at half levels. HIRLAM uses hybrid coordinates in the vertical, meaning a constant pressure at the top of the model, in this case around 0.1 hPa. The top level therefore contributes very little to the ZHD. The gravity g_i can be approximated by a function

of height z (see for details Lide, 1997). Note that the hydrostatic equation describes a relation between gravity and height z at each model level. By solving both equations from the surface to the top level in the model simultaneously an estimate of both height z of the layer and the value of the gravity is obtained.

The theoretical definition of the slant total delay is similar to the zenith delay, with the difference being that the vertical coordinate ' z ' is replaced by the slant coordinate ' s '. When estimating slant delays using a hydrostatic NWP model, the hydrostatic coordinate transformation needs to include the slant path length coordinate ' s '. The slant path is defined by a given elevation and azimuth angle. For each level the crossing with the next level is determined by 'ray tracing' taking into account the curvature of the earth. This implies that the path length extends for lower elevations in the top levels more than high elevations. Assume that the slant path length in level i is Δs_i and the height of this level is Δz_i , then our approximation of the hydrostatic coordinate transformation for this layer and slant path becomes

$$\partial p = -\rho g \partial z \frac{\Delta s_i}{\Delta z_i} \quad (7.6)$$

and thus the slant hydrostatic delay (SHD) is approximated by

$$\text{SHD} \approx 10^{-6} \sum_{i=1}^{31} k_1 \frac{\Delta s_i}{\Delta z_i} \frac{R_d}{g_i} \Delta p_i \quad (7.7)$$

Due to the curvature of the earth the ratio $\frac{\Delta s_i}{\Delta z_i}$ will change for higher altitudes. The approximation of the SWD is obtained similarly. Note that due to the slant path horizontal interpolation of the field parameters is needed.

We investigate the influence of the horizontal stratification assumption on the slant delay estimates obtained from GPS. A slant delay estimate obeying this assumption is created using a symmetric atmosphere overlying the GPS location by assuming that the temperature and humidity profile of the atmosphere is equal to the profile overlying the GPS location. We call this estimate the stratified slant delay.

The actual slant delay estimate is the sum of a stratified delay and a non-stratified delay, that is the slant wet delay can be written as

$$\text{SWD}^{\text{NWP}} = \text{SWD}_{\text{strat}}^{\text{NWP}} + \text{SWD}_{\text{non}}^{\text{NWP}} \quad (7.8)$$

In the next section we compare non-stratified SWD derived from NWP and observed by GPS.

7.4 NON-STRATIFIED SLANT WET DELAY COMPARISON

The estimates of non-stratified SWD derived from NWP model HIRLAM and GPS are compared for a special case. On the 30 October 2000 a barotropic low passed over the North Sea causing strong winds at the Dutch coast and short lived strong winds near the English coast. The Meteosat Water Vapour (WV) images from 30 October 15 UTC reveals part of this low as a black region in the top of Figure 7.2. In the same figure the integrated water vapour

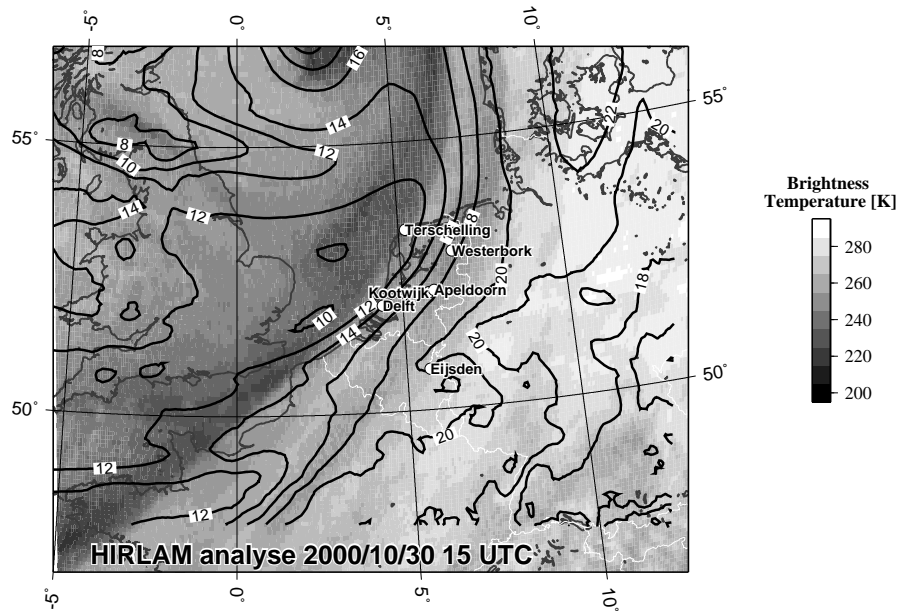


Figure 7.2: Meteosat Water vapour image of 30 October 2000, 1500 UTC, together contour lines of the integrated water vapour of HIRLAM analysis at the same time.

of HIRLAM analysis of 15 UTC is shown as contour lines together with the locations of the GPS sites in the Netherlands used for this study. The water vapour field is obtained from surface observations and radiosonde measurements through an optimal interpolation assimilation scheme. In the current assimilation scheme only surface wind observations are assimilated; humidity and temperature surface observations are not used.

The dark band in the WV image in this figure is a dry intrusion which is the result of subsiding cold upper atmospheric air. This dry intrusion lies almost parallel to the Dutch west coast. The WV channel ($6.7 \mu\text{m}$) measures the emittance of water vapour from the complete under-lying column. Emittance from water vapour lower in the atmosphere may be absorbed by water vapour higher in the atmosphere and thus not observed by the WV detector. Water vapour high in the atmosphere is less obscured by over-lying water vapour and is emitted to the detector: the WV channel measures mainly upper tropospheric water vapour. In Figure 7.2 regions of low water vapour emittance are shaded black and high water vapour emittance are coloured white. The source level of the water vapour emittance is hard to estimate without prior information, (see Weldon and Holmes, 1991; de Haan et al., 2004).

Comparing Meteosat WV and HIRLAM IWV we notice that the model gradient coincides with the boundary of the dry intrusion near Delft, however the dry intrusion lies a little more to the west near Terschelling. This may be caused by a lack of upper air humidity observations in the assimilation scheme. The nearest radiosonde site to Delft and Terschelling is situated in De Bilt, which lies between Delft and Kootwijk. Near Delft the IWV values drop from 23 kg m^{-2} to 13 kg m^{-2} over a distance of approximately 100 km. The same drop can be observed in the time series of the IWV as observed by GPS and HIRLAM in Figure 7.3. This corresponds to a change of 15 cm to 8 cm in the zenith wet delay as observed by GPS within a few hours.

The moisture field is clearly non-isotropic at 15 UTC near the Dutch coast. When the

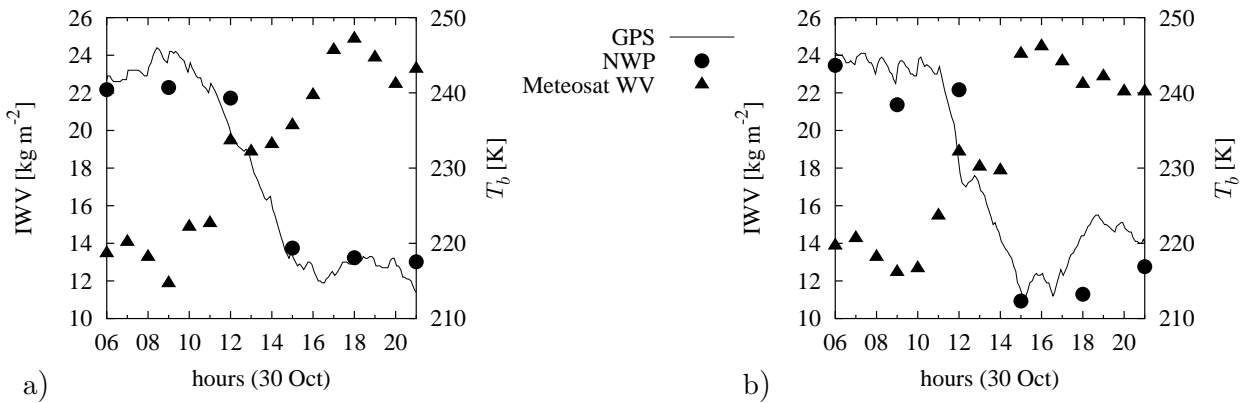


Figure 7.3: Time series of Integrated water vapour as retrieved from GPS (solid line) and NWP (dots) for GPS sites (a) Delft and (b) Terschelling. The triangles represent the brightness temperature as observed by Meteosat.

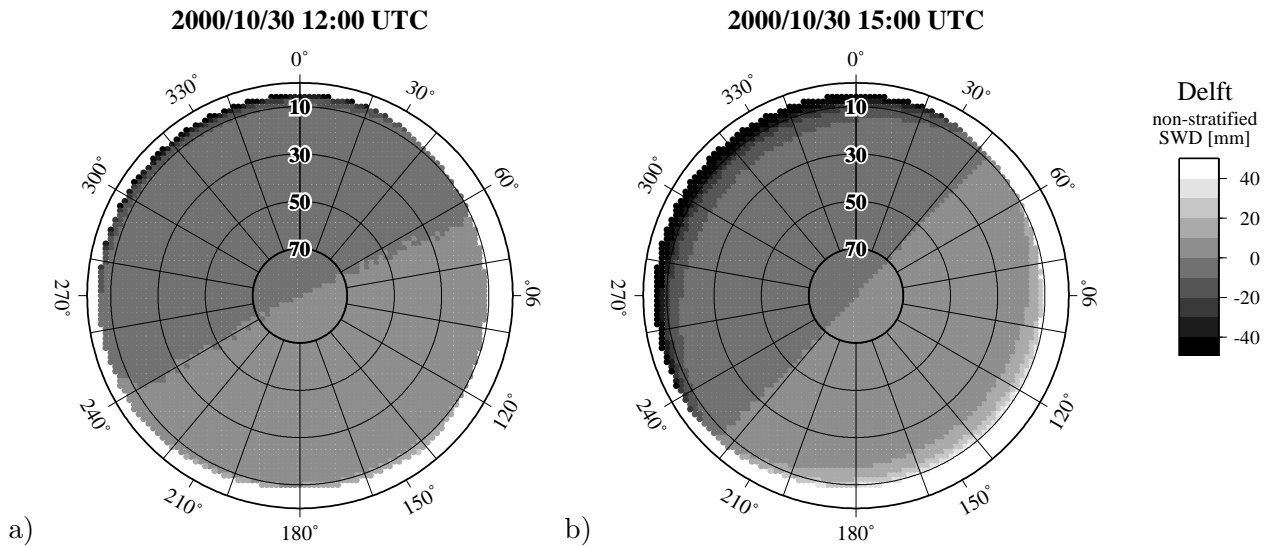


Figure 7.4: Azimuth-elevation polar plot of the non-stratified slant wet delay component obtained from HIRLAM analysis at GPS site Delft for three times: (a) 12 UTC, (b) 15 UTC and (c) 18 UTC (Figure continues on next page). The elevation angle is plotted on the radial axis and the azimuth on the angle axis.

non-stratified SWD is determined from NWP for all realistic azimuth and elevation angles this non-isotropy is observed as a gradient, with the most pronounced gradient at 15 UTC, see Figure 7.4 for three consecutive assimilation times 12 UTC, 15 UTC and 18 UTC. Elevations larger than 20 degrees have a non-stratified SWD which is in absolute value smaller than 5 mm, which is negligible considering the noise of the GPS observations (the step size in the figure is only 10 mm). Note also that the water vapour gradient is visible at 12 and 15 UTC, while at 18 UTC it has disappeared.

Comparison of the non-stratified SWD from NWP with the actual non-stratified SWD from GPS for Delft and Terschelling at 15 UTC is shown in Figure 7.5. The GPS data from 14:30 UTC up to 15:30 UTC and the SWD_{non} from NWP at 15 UTC are plotted. Every

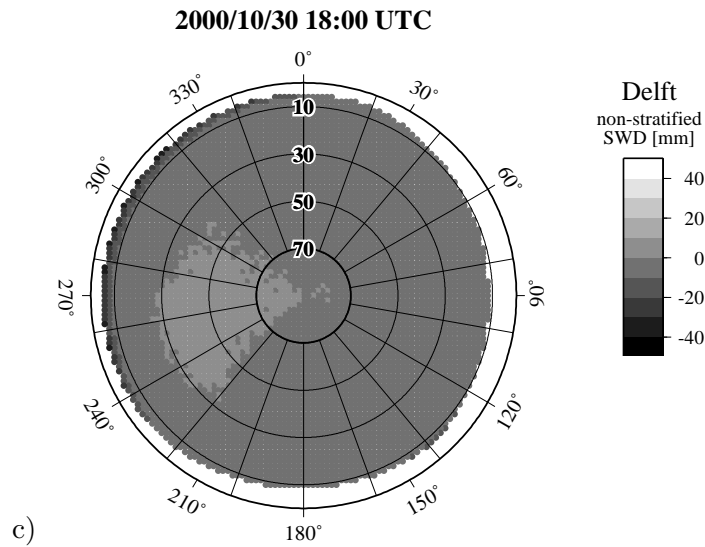


Figure 7.4: continued.

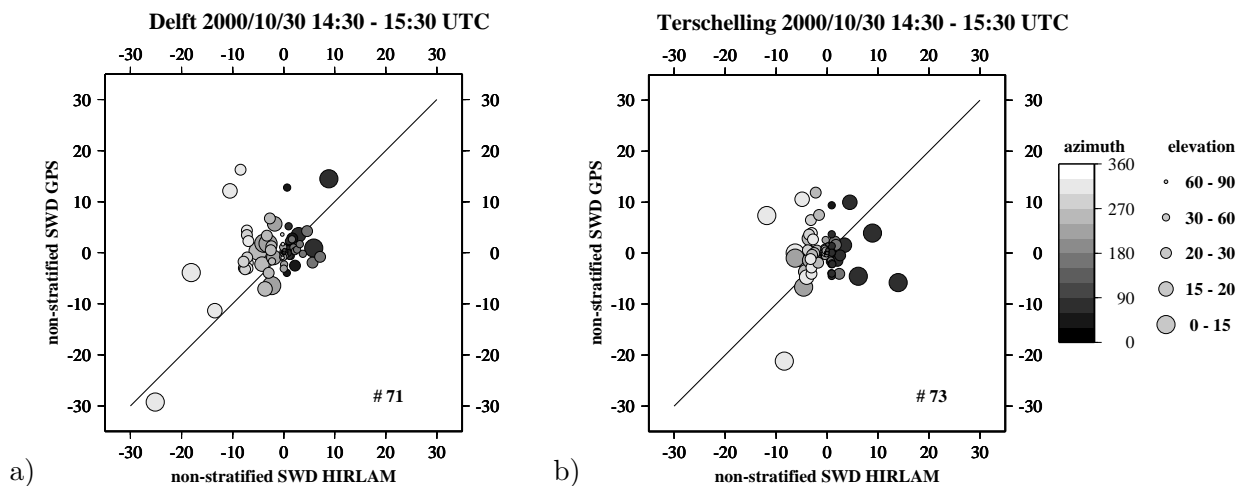


Figure 7.5: Scatter plot of non-stratified SWD from GPS versus HIRLAM for GPS sites Delft (a) and Terschelling (b). The grey scale is related to the azimuth angle and the size of the circle is related to the elevation angle.

point represents a 6 minute interval, corresponding to the observation interval of GPS. On the average, between 7 and 8 satellites were visible during this period. The size of the circle is related to the elevation angle and the grey scale to the azimuth angle.

The scatter plot of Delft (Fig. 7.5a) shows that low elevations with a westward azimuth (large light circles) have a negative non-stratified SWD component for both GPS and HIRLAM and that low elevations with a eastward azimuth (large dark grey circles) have positive values. From the scatter plot of non-stratified SWD for Terschelling (Fig. 7.5b) the same pattern can be observed, although less convincing, which is a possible indication of a mismatch between the NWP model and GPS. In Figure 7.3 the time series of the GPS-IWV as observed by NWP and GPS has been plotted. Compared with Delft, the decrease of IWV for Terschelling is more abrupt (Figure 7.3b) than for Delft (Fig. 7.3a). Moreover, from the time series of Meteosat WV

(triangles in Fig. 7.3) shows a quicker increase in brightness temperature from values around 220 K to 245 K for Terschelling than for Delft. The increase in brightness temperature is caused by the dry intrusion behind the front. The IWV values derived from the model do not show a large difference with respect to a sudden decrease in NWP-IWV. Note that the NWP field values can be regarded as the mean of the grid box and thus will smooth out strong gradients.

Therefore we think that a misalignment of the water vapour gradient by the model may be the reason for the difference in non-stratified SWD. This can be observed from Figure 7.2 as well, where we noticed before that the model gradient coincides well with the boundary of the dry intrusion near Delft, but at Terschelling the dry intrusion lies a little more to the west.

7.5 CONCLUSIONS

In this chapter we compared slant delay observations derived from GPS with slant delay estimations from NWP. We focused on the deviation of the slant wet delay (SWD) from a horizontally stratified atmosphere, the so-called non-stratified slant wet delay component. A first attempt was made to derive non-stratified slant delays from GPS while taking care of the multipath effects at the observation site. We found that for a special case, a cold front passage with a strong water vapour gradient, the non-stratified SWD observed by GPS compared well with the non-stratified SWD computed from the high resolution NWP model HIRLAM at one of the sites, and less well for another site.

This difference can be explained by the fact that NWP models fields are an estimate of the state of the atmosphere and most likely contain errors due to the chosen resolution, lack of information or even wrong assimilated information. Furthermore NWP models are smoothing all information and therefore extreme strong gradients (relative to the model resolution) are hard to be captured. GPS on the other hand, has a very high temporal resolution and should be able to capture strong gradients very well.

It is not feasible to use slant wet delays directly for operational forecasting due to difficulties in interpreting the observations as such. Assuming GPS slant wet delay estimates have a reasonable error, and systematic errors such as multipath can be accurately modelled, comparison with NWP estimates may reveal errors in the model humidity field with respect to for instance timing of a gradient passage or intensity of the humidity gradient. A derived product (i.e. three-dimensional water vapour fields from GPS slant estimates and combined use of Meteosat Water Vapour images) may provide additional information for interpreting NWP models on accuracy and correctness.

Chapter 8

Observing three-dimensional water vapour using a surface network of GPS receivers¹

Atmospheric water vapour is highly variable both in space and time. In an operational sense, only radiosonde provide vertical information on water vapour. Radiosondes are generally launched two to four times per day at synoptic times and sample primarily synoptic scales. For nowcasting purposes these observations are very valuable but obviously lose their importance with elapsing time. Water vapour observations from a surface network of Global Positioning System (GPS) receivers can fill this information gap. In this chapter, a GPS network is used to observe integral water vapour quantities along the line of sight, so-called Slant Water Vapour (SWV). Using a variational technique (3DVAR) a three-dimensional water vapour field is reconstructed and its performance is investigated using an Observation Simulation System Experiment (OSSE) in which the complete atmosphere and observations were simulated (so-called nature run). The forecasts from a high resolution limited area model (HIRLAM) embedded in the synthetic atmosphere of the nature run is compared to the separate GPS-3DVAR estimates. This experiment showed that assimilation of SWV resulted in a smaller bias and standard deviation than the HIRLAM forecast with the nature run. Besides simulated data, real SWV observations are used to assess impact. Two experiments were conducted; one with a HIRLAM six hour forecast as a background field (updated every six hours) and one with persistence as background (updated every hour). The first experiment showed a reduction of the bias between radiosonde observations compared to HIRLAM forecast. The second experiment, which has no information inherited from HIRLAM, showed to have smaller biases with independent radiosonde observations than the HIRLAM analysis. The used network, however was too sparse to detect water vapour inversions correctly.

¹This chapter is submitted as an article to *Atmos. Chem. Phys.* by S. de Haan and H. van der Marel.

8.1 INTRODUCTION

Currently, radiosonde observations are one of the few information sources for upper tropospheric humidity (i.e. water vapour). These observations are sparse in time and space and expensive to deploy. The current measurements of atmospheric water vapour by radiosonde networks do not possess either the temporal nor the spatial resolution to infer information about atmospheric scales smaller than synoptic scale. Imagery from geostationary satellites provides continuous monitoring of the atmospheric water vapour, but the use of these observations in numerical weather prediction (NWP) is far from straightforward due to the problems with height assignment of the observed structures and with clouds.

Global Positioning System (GPS) Zenith Total Delay (ZTD) observations contain integrated water vapour (IWV) path information which can be used in NWP models and forecasting applications. The temporal resolution of GPS ZTD is in the order of 15–60 minutes, which is a significant advantage over radiosonde observations. High temporal water vapour measurements are likely to have a large impact on forecasting rapidly developing weather systems (see previous chapters). However, at best GPS ZTD can only provide two-dimensional integrated water vapour fields, and lacks information on the vertical distribution of water vapour.

MacDonald et al. (2000) showed that three-dimensional analysis of slant integrated water vapour can be used to construct a three-dimensional water vapour distribution. Single path phase delays can be obtained from GPS double differences (Alber et al., 2000). The root mean square errors of this method are 1.3 kg m^{-2} (in IWV content) where the 'normal' content is approximately 30 kg m^{-2} near zenith. At low slant path elevations angles (10 degrees or less) a root mean square error of 9.1 kg m^{-2} is observed, see Braun et al. (2001). The errors increase with decreasing elevation due to the contributions of ground reflected multipath and antenna phase centre errors.

In this chapter, GPS data of the AGRS (Active GPS Reference System) network complemented with a number of International GPS Service (IGS) stations are processed at the Delft institute for Earth Oriented Space Research (DEOS) of Delft University of Technology (TUD). Timeseries of the tropospheric delay estimates are calculated from this network every 10 minutes with a standard deviation in the integrated water vapour of 2 kg m^{-2} (Baltink et al., 1998). These errors satisfy almost the WMO requirements for use of water vapour measurements, which are 5% of IWV (CBS-WMO, 1996).

Instead of obtaining zenith quantities, IWV can also be measured along a slant path from a ground-based receiver to a GPS satellite. By using not only the zenith IWV of a receiver but also the slant IWV's the number of observations will increase by roughly a factor ten. A slant IWV on its own has a two-dimensional character. However, by applying tomographic (Nilsson et al., 2007) or variational algorithms (Liu et al., 2007) a three-dimensional water vapour field can be retrieved from slant observations from a network of receivers. Furthermore, the horizontal resolution of the retrieved water vapour field will also profit from this larger amount of observations.

In the approach presented here a three-dimensional water vapour field is reconstructed using a three-dimensional variational method with real data. The approach presented here is different

from Liu et al. (2007) in the sense that we do not use flow-dependent background errors. The results from Liu et al. (2007) show that the retrieval improves using flow-dependent background error especially for fine-scale structures. The data used here are not able to detect such fine-scale structures and therefore flow-dependency of the error structure will have a minor effect on the results presented here.

This chapter is organised as follows. First the method of observing IWV and SWV from GPS observations is explained. Next the variational analysis system is explained and the background error covariances are presented. The section hereafter shows the results of two types of experiments: an Observation Simulation System Experiment (OSSE) and an analysis with real SWV observations.

8.2 WATER VAPOUR OBSERVATIONS FROM GPS

A GPS receiver measures the delay of the GPS signal for every GPS satellite in view. By processing all observed delays within a certain time window errors and unknowns, such as satellite and receiver clock errors, position of the receiver, atmospheric delay and ionospheric delay, can be estimated or eliminated. The ionospheric delay in particular is eliminated by using a linear combination of observations on two different carrier frequencies. The receiver and satellite clock errors are often eliminated by forming so called double differences between satellites and receivers. The other parameters, including atmospheric delay parameters in the form of zenith total delays, are estimated from a network of GPS receivers using a least-squares inversion process.

The atmospheric delay along the signal path is due to refraction and bending, using Fermat's principle,

$$\delta L = \int_s n ds - G + \delta S \approx \int_s (n - 1) ds, \quad (8.1)$$

where n is the refractive index, $G (= \int_s ds)$ is the geometric distance and δS the effect of bending; the latter can be neglected for elevation higher than 10 degrees. The refractivity is defined as $N = 10^6(n - 1)$ and can be approximated by

$$N = k_1 \rho R_d + (k_2 R_v - k_1 R_d + k_3 R_v T^{-1}) \rho_w, \quad (8.2)$$

where ρ is the density of air, ρ_w is the water vapour density, T is the temperature and k_1 , k_2 and k_3 are constants (see Thayer, 1974). The Zenith Hydrostatic Delay (ZHD) and Zenith Wet Delay (ZWD) are now defined as

$$\text{ZHD} = 10^{-6} \int_z k_1 \rho R_d dz \quad \text{and} \quad \text{ZWD} = 10^{-6} \int_z R_v (k_2 - k_1 R_d R_v^{-1} + k_3 T^{-1}) \rho_w dz \quad (8.3)$$

The observed delay in the line of sight, or slant total delay, is

$$\text{STD} = m_h(\beta) \text{ZHD} + m_w(\beta) \text{ZWD} \quad (8.4)$$

with m_h and m_w the so called hydrostatic and wet mapping functions, which express the relation between slant and vertical atmospheric delay.

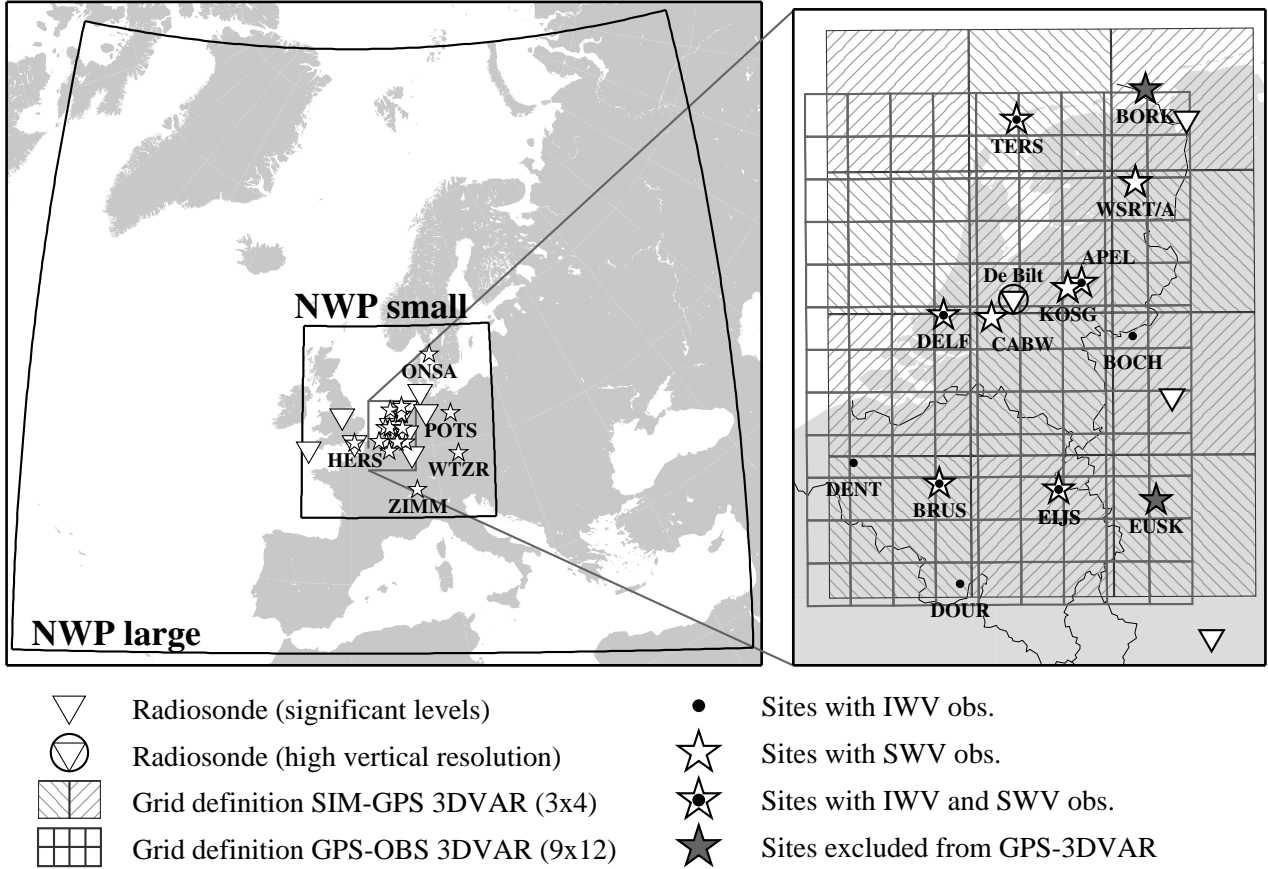


Figure 8.1: The GPS network, with on the left the IGS and EPN stations involved in the network and on the right a detail of the Netherlands.

An estimate of the Zenith Total Delay (ZTD) for each receiver, which is the sum of ZHD and ZWD, is obtained along with other parameters in the GPS estimation process, whereby the mapping functions are assumed to be known. The ZHD can be approximated using the surface pressure (Saastamoinen, 1972) and is denoted as ZHD_{Saas} . The ZWD is associated with the vertically integrated column of water vapour overlying the GPS receiver

$$IWV = \frac{1}{k} (ZTD - ZHD_{Saas}) \quad (8.5)$$

where k depends on the weighted mean temperature of the atmosphere T_m . The T_m can be approximated as a linear function of the surface temperature (Davis et al., 1985; Bevis et al., 1994; Baltink et al., 2002)

Data from the network shown in Figure 8.1 (denoted by the stars) are processed using Bernese GPS processing software (Rothacher and Mervart, 1996) with final orbits. The GPS data used in this study have a temporal resolution of 30 seconds. In the processing the minimum elevation is set to 10 degrees. The ionospheric free linear combination of GPS carrier phase observations are used as observations. The clock errors are eliminated using double differences. The station positions are estimated once per day and ZWD parameters are estimated every 20 minutes using a least-squares inversion of the double differenced ionosphere free linear

observations, using an elevation dependent weighting scheme for the observations and proper modelling of the correlations introduced by the double-differencing process.

The Slant Total Delay is computed by (van der Marel and Gündlich, 2006)

$$\text{STD} = m_h(\beta) \text{ZHD}_a + m_w(\beta) \text{ZWD}_e - M(\alpha, \beta) + \delta_{non-iso}, \quad (8.6)$$

where m_h and m_w are Niell hydrostatic and wet mapping functions, and $M(\alpha, \beta)$ is the multipath correction at azimuth α and elevation β which is computed from the zero difference residuals $\delta_{non-iso}$ over a period of several days (de Haan et al., 2002). ZHD_a is an a priori estimate of the hydrostatic delay while ZWD_e is estimated in the processing. The zero-difference $\delta_{non-iso}$ residual is the difference between the observed ionosphere free linear combination and an ionosphere free “observation” computed from the previously determined parameters. The zero-difference residuals are computed from double difference residuals, computed by the Bernese GPS software, using the procedure as outlined by Alber et al. (2000) and van der Marel and Gündlich (2006). The difference between Slant Total Delay (STD) and Zenith Total Delay (ZTD) is thus (i) STD is mapped to the slant direction, (ii) zero difference residuals are included in the STD and (iii) STD is corrected for multipath effects. Another way of writing Eq. 8.6 is

$$\text{STD} = \Phi_{iono-free} - f(x^s, x_r, \delta t_r, \delta t^s, A_r^s, \dots) - M(\alpha, \beta), \quad (8.7)$$

with $\Phi_{iono-free}$ the ionosphere free linear combination of GPS carrier phase observations and $f(x^s, x_r, \delta t_r, \delta t^s, A_r^s, \dots)$ the range computed from all estimated parameters except the tropospheric delays. In other words, STD is the GPS observation with all non tropospheric delay effects (including site multipath) removed, leaving only tropospheric delay.

However, the degree of freedom in the STD is smaller than the original observations as the same observations have been used to estimate the other parameters such as receiver position, satellite and receiver clock errors. In this case the satellite and receiver clock parameters are the most numerous and important, as for every epoch one clock parameter for each receiver and satellite in the network is computed (minus one for a rank defect). For a network with R receivers and S satellites, only $(R - 1) * (S - 1)$ out of $R * S$ STD observations per epoch are truly independent. The same is also apparent from the residuals $\delta_{non-iso}$ as certain linear combinations of the residuals are zero. This are exactly the same conditions as that have been used to convert double-difference residuals into zero-difference residuals. For instance, Elosegui and Davis (2003) showed that offsets at low elevations at one site appear in the solutions at other sites of the network due to the applied differencing technique. The offset is spread over the network, although the magnitude of the spread will be relative to the value of the mapping functions and number of stations that have been used in the network. This effect is most severe in STD parameters that are estimated for each epoch (once every 30 seconds), but will be reduced when the STD is averaged over time intervals of several minutes. In this chapter five minute averages are used.

Another effect is that the STD is not truly independent of the chosen mapping functions. The mapping functions play a role in the estimation of the clock errors and other parameters, thereby, if during the GPS processing a different mapping function is adopted this will affect the other parameters and thereby propagate into the estimate of STD.

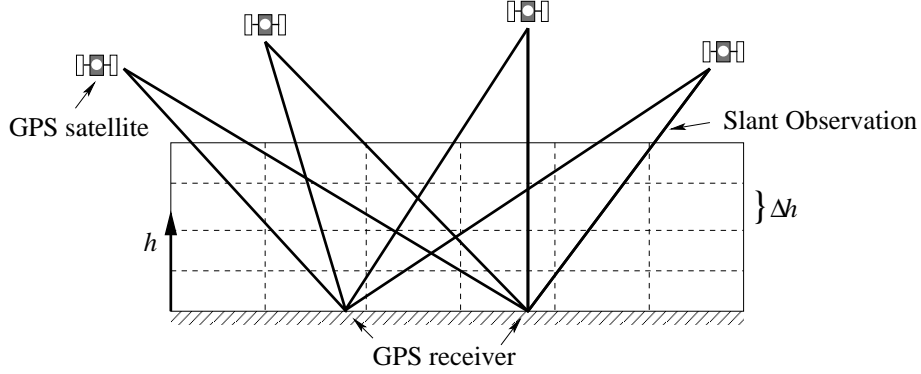


Figure 8.2: Schematics representation of the three-dimensional model space.

SWV observations are determined in a similar manner as IWV observations, with this difference that a correction for the elevation β is applied:

$$\text{SWV} = \frac{1}{k} (\text{STD} - m_h(\beta) \cdot \text{ZHD}_{\text{Saas}}) \quad (8.8)$$

Correlated errors may be introduced in the conversion from GPS STD to SWV. This conversion uses synoptic observations of temperature, relative humidity and pressure. Because we use synoptic observations, we assume that these observations do not have systematic errors and are not correlated.

8.3 VARIATIONAL ANALYSIS METHOD

In this section the SWV analysis method is presented. To stay as close as possible to the observation, water vapour density is chosen as the state parameter and the vertical parameter is in metres. The state vector will thus be water vapour density x_{ijn} [kg m^{-3}], where ij are horizontal coordinates and n the vertical coordinate. The integrated water vapour defined in terms of this state vector is

$$\text{IWV}_{ij} = \sum_{n=1}^N x_{ijn} \Delta h_n, \quad (8.9)$$

where Δh_n is the layer thickness in metres. A schematic representation of the model space is shown in Figure 8.2

The method to derive an estimate of the true state of the atmosphere is based on three-dimensional variational technique as described in Daley (1991). The observations \mathbf{y} are combined with a background \mathbf{x}_b , such that the analysed field \mathbf{x}_a minimises the following cost function

$$J(\mathbf{x}) = (\mathbf{x} - \mathbf{x}_b)^T B^{-1} (\mathbf{x} - \mathbf{x}_b) + (\mathbf{y} - H(\mathbf{x}))^T R^{-1} (\mathbf{y} - H(\mathbf{x})), \quad (8.10)$$

where the number of observations is K , and the dimension of the state vector is L and

$$\begin{aligned} B &= \text{background error covariance matrix } (L \times L) \\ R &= \text{observation error covariance matrix } (K \times K) \\ H &= \text{observation operator } H : \mathfrak{R}^L \longrightarrow \mathfrak{R}^K. \end{aligned}$$

The observation operator expresses the relation between the state space and the observations. Equation 8.9 is an example of an observation operator of an IWV observation. The observation operator for a SWV observation is defined as

$$\text{SWV} = \sum_{n=1}^N \frac{x(p_n)}{\sin(\beta(p_n))} \Delta h_n, \quad (8.11)$$

where p_n is the position of the ray at the middle of level n , $x(p_n)$ is the bilinear approximation of the state of the atmosphere at level n and location p_n and $\beta(p_n)$ is the elevation at location p_n and level n .

The observation operator H is linear and thus the minimum of the cost function J can be found by solving $\nabla J(\mathbf{x}) = 0$ analytically. The vector \mathbf{x} must be non-negative (negative water vapour amounts are impossible), however it is possible that an element of the solution becomes negative. To cure this problem a simple algorithm is applied to guarantee non-negative solutions. Suppose x_{ijk} is negative, then the profile x_{ijn} , $n = 1..N$ is adjusted in the following manner. The negative value of x_{ijk} is added to $x_{ij(k+1)}$ and $x_{ij(k-1)}$, subject to $x_{ijn} \geq 0$ and the profile sum remains unchanged. Another method would be to introduce a penalty function $J_p(\mathbf{x})$ such that J_p is small for non-negative vectors and J_p is large otherwise. This method is not used here because any penalty function will destroy the linearity.

8.3.1 BACKGROUND ERROR COVARIANCES

One of the methods widely used to estimate the background error covariances is the method developed by Hollingsworth and Lonnberg (1986). This method uses differences between observations and forecasts fields from NWP. By studying differences between the background state vector \mathbf{x} and observations with the same physical quantity (in our case water vapour density) background error covariances can be examined. By comparing the difference between observations (SWV) and the model ($H\mathbf{x}$) observation error covariances can be examined.

A data set of 18 months of radiosonde observations from launches in the vicinity of the Netherlands and (at least) 24 hour ECMWF forecasts from the operational 4DVAR model are selected. Radiosonde observations from De Bilt contain 10 seconds profile data; for the other radiosonde observations profile information on significant levels is used. The radiosondes selected here, other than De Bilt, had more than 25 vertical levels; the locations of the radiosonde launch sites are shown in Figure 8.1 (inverse triangles).

We assume that the background error covariance matrix C can be separated into a product of a function C_{vH} of height h and distance r , and a factor f incorporating the behaviour of the covariance between different levels

$$C(r, h_1, h_2) = C_{vH}(r, \frac{1}{2}(h_1 + h_2)) \cdot f(h_1, h_2), \quad (8.12)$$

where h_i are heights; f is decreasing with increasing difference in h_1 and h_2 and f is equal to 1 for $h_1 = h_2$.

Radiosonde De Bilt observations measure temperature and humidity every 10 seconds. This implies that roughly every 50 metres a measurement is performed. From these measurements the water vapour amount for layers with a thickness of 1 kilometre is calculated.

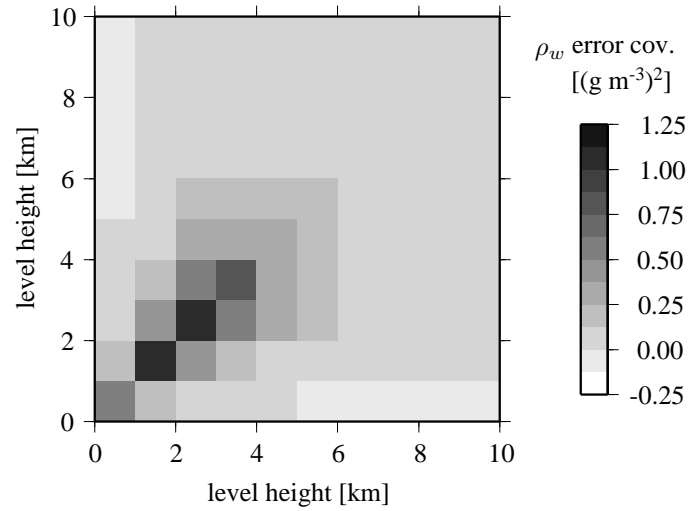


Figure 8.3: Vertical water vapour density background error covariance for departures from the ECMWF 24 hour forecast based on radiosonde observation from De Bilt for an 18 month period.

For 1 kilometre levels up to 10 kilometres, the background error covariance with ECMWF 24 hours forecast is shown in Figure 8.3. The maximum covariance lies around 3 to 4 km, decaying very quickly to small numbers for levels higher than 6 km. On the diagonal the covariance is a mixture of observation error $\sigma_o^2(h)$ and background error $\sigma_b^2(h)$. When we assume that the observations are independent, the off-diagonal elements are pure background error covariances. This may of coarse not be the case, and is most likely not true here for individual observations in a profile because this profile is measured with the same equipment. However, because the layer is integrated over a height of 1 kilometre, we assume that the observation error covariances are small compared to the background error covariances.

For the determination of the horizontal background error covariance, a similar procedure is followed as described above. Pairs of two radiosonde observation departures from the background at the same level over an 18 month period are used to determine the covariance. This covariance is plotted versus the distance between the two radiosonde launch sites. The sites used are denoted by inverse triangles in Figure 8.1. In Figure 8.4 the covariance-distance plot is shown for a few levels.

Each panel shows the background covariance for two levels, denoted by open circles (the lowest of the two levels) and triangles. Also shown in these panels are the variances as obtained from computation of the vertical background error covariances in De Bilt (denoted by the solid circles and triangles). These values are the diagonal elements in Figure 8.3.

It turned out that an exponential decay in both vertical/horizontal covariances, as well as the function which connects different levels, resulted in a good fit. Using exponential decay of covariances is not uncommon in numerical weather prediction.

The solid and dashed lines in Figure 8.4 are the fit of the data points versus the distance. Note that data with zero distance are omitted from the fitting procedure because, as said before, the variance consists of a background error part and an observation part. The function we used

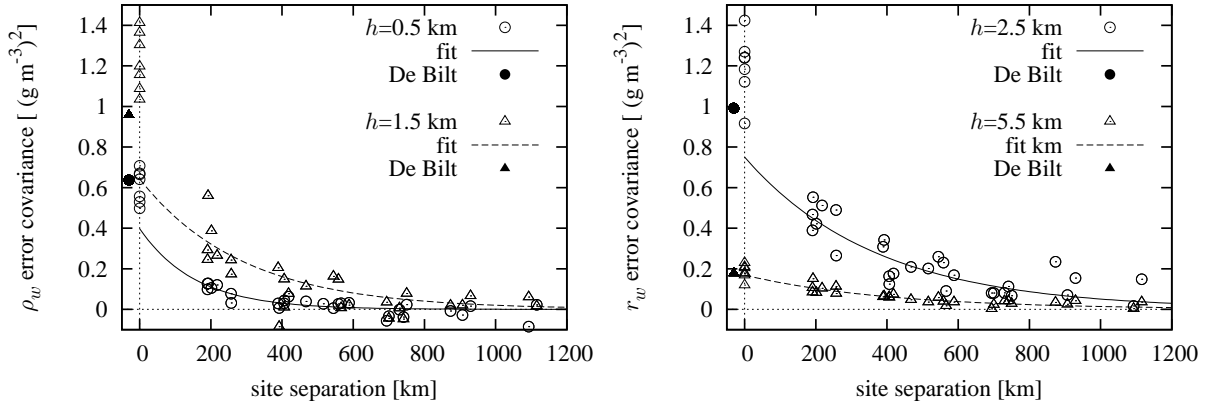


Figure 8.4: Horizontal water vapour density background error covariance for departures from the ECMWF 24 hour forecast based on significant level radiosonde observations from 9 sites for an 18 month period. Also plotted near the y-axis is the ρ_w error covariance (at the specific height) as determined using 10 second data from radiosonde De Bilt (conform Fig. 8.3). The solid and dashed lines is the fit of the background error covariances.

to fit is a function of height h and distance r is defined by

$$\begin{aligned}
 C_{vH}(r, h) &= \exp\left(a_1 + a_2 h + a_3 h^2 - (b_1 + b_2 \exp(b_3 h^2))^{-1} r\right), \\
 f(h_1, h_2) &= \exp\left((c_1 + c_2(h_1 + h_2) + c_3(h_1 + h_2)^2)|h_1 - h_2|\right)
 \end{aligned}
 \quad (8.13)$$

The coefficients used are given in Table 8.1.

8.3.2 SLANT OBSERVATION ERROR COVARIANCES

For all SWV observations from the period between 1st May and 25th May 2003 the difference between GPS-SWV and NWP-SWV is determined. A time window of one hour around the NWP valid time is chosen (i.e plus and minus 30 minutes). The distributions of the difference are mapped to the zenith by the Niell wet mapping function; these are shown in Figure 8.5 for four selected sites. Extreme outliers are immediately detected. For example APEL has a number of negative mapped differences around -20 and -30 $kg m^{-2}$. These outliers occur also at other sites (TERS has some outliers which are around 10 $kg m^{-2}$). BORK (not shown here) and EUSK still have a skew distribution due to the antenna problems (van der Marel and Gündlich, 2006). For these two sites, the difference between NWP forecast and GPS SWV is more complicated than a bias multiplied by the Niell wet mapping function. Apart from these

Table 8.1: Coefficients of the background error covariance fit as defined in Equation 8.13.

| | a_i | b_i | c_i |
|---------|---------------------------|--------------------------|---------------------------|
| $i = 1$ | -1.726400 | $-3.19943 \cdot 10^2$ | $-8.212579 \cdot 10^{-1}$ |
| $i = 2$ | $9.678325 \cdot 10^{-1}$ | $-2.57259 \cdot 10^{-1}$ | $2.959536 \cdot 10^{-2}$ |
| $i = 3$ | $-1.626992 \cdot 10^{-1}$ | $4.03587 \cdot 10^2$ | $9.014327 \cdot 10^{-4}$ |

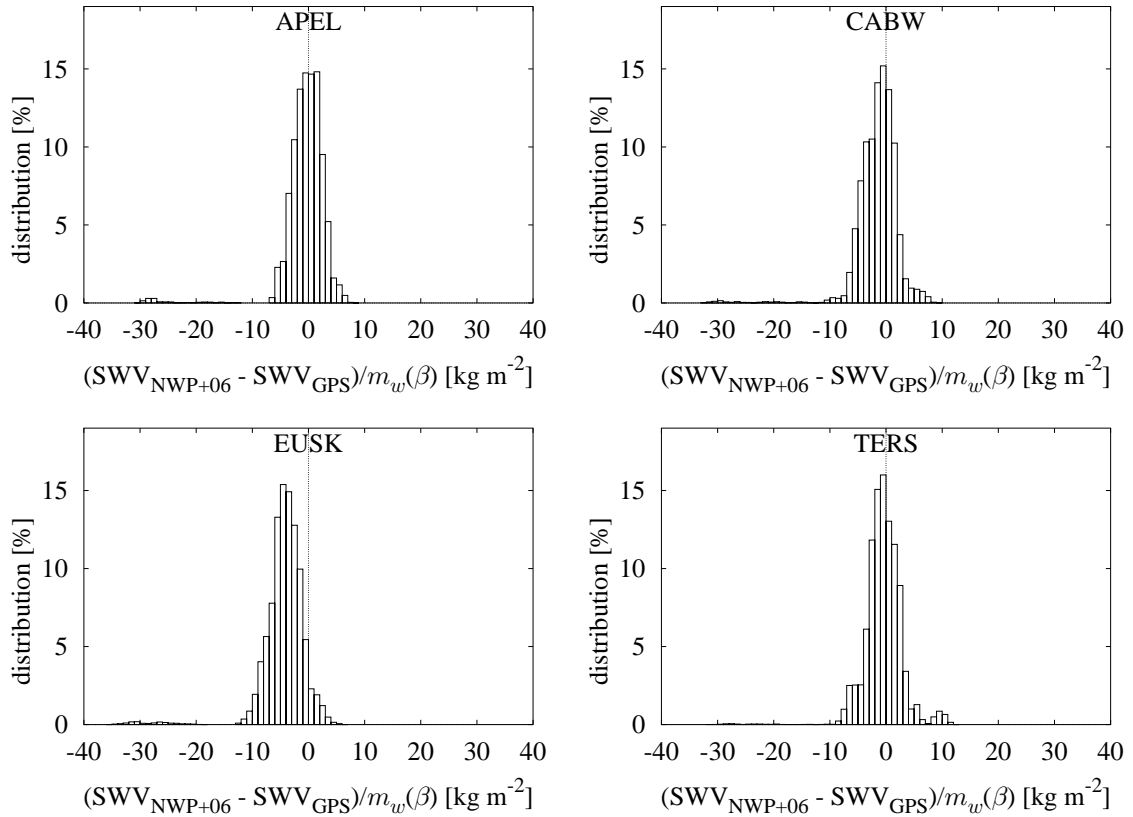


Figure 8.5: Distributions of the mapped difference between SWV NWP 6 hour forecast and GPS SWV. The Niell wet mapping function is used.

two stations, the bias between NWP SWV and GPS SWV can be denoted as a site-dependent constant multiplied by the Niell wet mapping function. The mapped difference can be expressed by a normal distribution with a site-dependent bias and a standard deviation of around 2.5 kg m^{-2} based on a sample rate of 30 seconds which is larger than the IWV standard deviation (approximately 2 kg m^{-2}); the latter is based on a 10 minute sample rate.

8.3.3 SYSTEMATIC OBSERVATION ERROR CORRELATIONS

The bias in SWV observed above can be regarded as a systematic error. For an elaborate study of systematic STD error correlations long time series are needed. At present, we do not have a long time series of slant total delay (or slant water vapour) estimates from GPS. We therefore focus on GPS ZTD estimates and use the relation between ZTD and SWV. The GPS ZTD data is obtained within the European COST716 action (Elgered et al., 2004) and is processed by Geo Forschungs Zentrum, Potsdam, Germany (GFZ), for which a time series of over 18 months is available. The background error covariances are again determined using ECMWF forecast fields.

In Figure 8.6a GPS ZTD background error covariances are shown with respect to GPS site separation and its fit. The background error decreases to zero for large distances. This implies that the GPS ZTD observation error correlations, independent of the location, are small

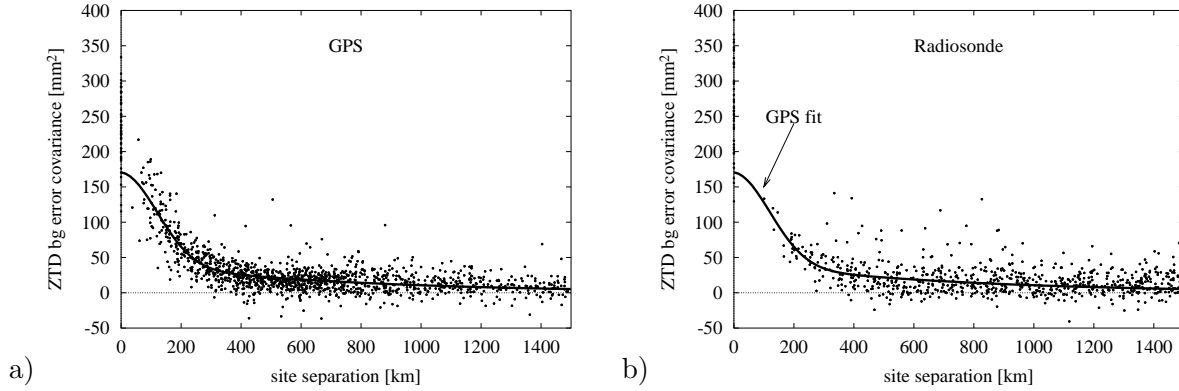


Figure 8.6: Background error covariances in ZTD from a) GPS and b) RS with ECMWF forecast of at least 24 hours for the period 2001/07/01 and 2002/11/01. The fit is defined by $\rho(r) = 126 \exp^{-(r/170)^2} + 44 \exp^{-r/700}$.

compared to the covariance of background errors which depend on the distance.

In Figure 8.6b RS ZTD the background error covariances are shown with respect to radiosonde site separation. The solid line is the background error covariance fit from GPS. The difference between the background error covariance fit from GPS and radiosonde background error covariances is similar to that of the differences between the fit and the actual data as shown in Figure 8.6a and b. Because no offset at large distances is observed systematic ZTD error covariances are small. There can of course be errors from day to day or even within a solution for the whole network at a certain time, but these errors are not systematic.

Based on the distributions as shown previously and the absence of a clear systematic error we assume that the observation correlation matrix R is diagonal, with only elevation dependent (co)variances. In the following GPS-3DVAR experiments we took a standard deviation of 2.5 kg m^{-2} at zenith elevation; for an SWV observation this standard deviation was set to $2.5/\sin(\beta) \text{ kg m}^{-2}$ for an elevation β .

8.4 VARIATIONAL ANALYSIS EXPERIMENTS

Two types of experiments are conducted for which the quality of the analysed water vapour are assessed. Comparisons are made between the analysed water vapour fields and NWP analyses and forecasts using the HIRLAM system (Undén et al., 2002). The NWP analysis is obtained through assimilation of conventional observations by the HIRLAM analysis system (version 6.2). The experiments are:

- assimilation of simulated observations by a three-dimensional variational technique. The observations are extracted from a pure synthetic atmosphere obtained from a nature run at ECMWF. The background field for the GPS 3DVAR scheme is a OSSE NWP forecast. These experiments are denoted as SIM-GPS,
- assimilation of real SWV observations with two different background fields:
 - OBS-GPS-F: background operational NWP 6 hour forecast
 - OBS-GPS-P: background is the previous 3DVAR analysis (persistence).

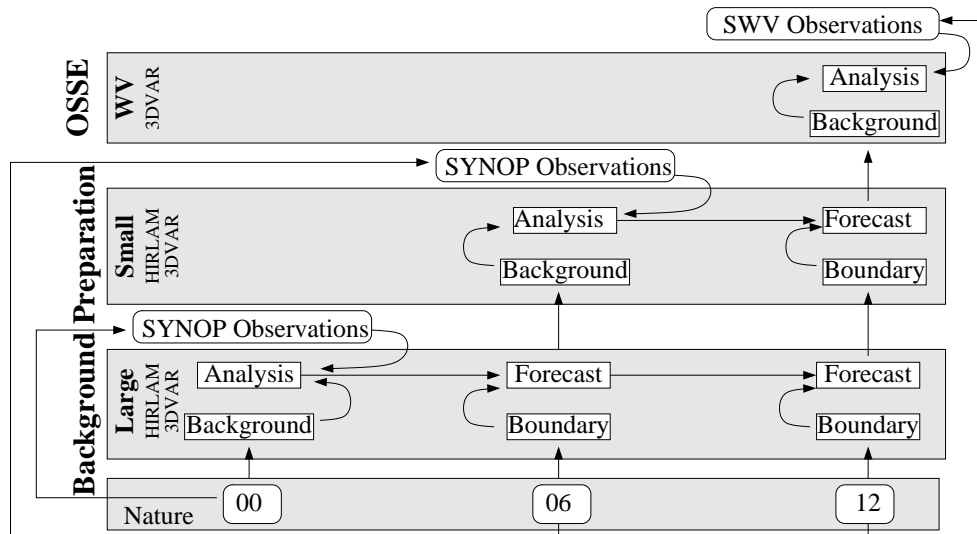


Figure 8.7: Schematic representation of the data flow for the OSSE experiment.

To assess the additional slant information both experiments are performed with only zenith observations and with both zenith and slant observations.

8.4.1 OBSERVATION SIMULATION SYSTEM EXPERIMENT

OSSEs can be used to assess the impact of a new observation system. Everything is simulated and thus there are almost no limitation to the observations, other than a relation between the observed parameter and the model parameters should exist. Generally, an OSSE consists of a data assimilation system, a nature run (or “truth”), and a database with simulated observations (conventional meteorological and new observations). An extensive description of the nature run and the observation database can be found in Stoffelen et al. (1994) and Becker and Roquet (1995).

OSSE SETUP

The OSSE used in this study is based on a forecast of one month of the operational global ECMWF model, performed in 1993 (Stoffelen et al., 1994; Becker and Roquet, 1995). This run is called the nature run or “truth”. The vertical resolution of the nature run is 31 levels with a horizontal resolution of 110 km. From this nature run all kinds of observations are extracted at observation locations. Realistic errors are added to these observations. Given a background field, these observations can be used in an assimilation scheme to derive the state of the atmosphere based on the (simulated) observations. Knowing the true state (i.e. the nature run) an assessment of the quality of the assimilation scheme can be made. Usually a background is a 6 or 12 hours forecast field valid at assimilation time.

To stay as close as possible to a configuration of an operational system a special procedure is followed, avoiding the use of boundary values from the nature run in the forecast. This is essential because the forecast will be used as a background in the variational analysis of GPS

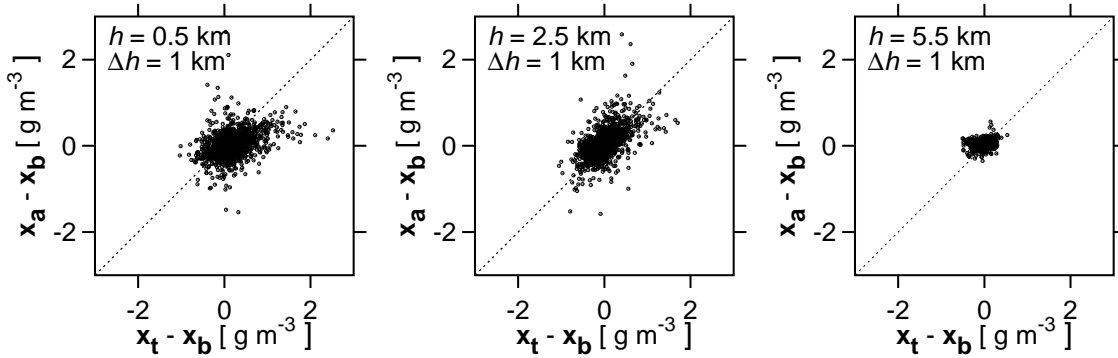


Figure 8.8: Scatter plot of the water vapour difference between the truth (nature run, \mathbf{x}_t) and the background \mathbf{x}_b against the innovation (SIM-GPS SWV solution \mathbf{x}_a minus background \mathbf{x}_b) for three selected levels.

observations. Therefore two NWP runs, one nested in the other, are deployed. The largest uses the boundaries as determined by the nature run analysis. The smallest uses the 6 hour forecast fields from the largest NWP run as boundaries, see Figure 8.7. Because the smallest of the two lies entirely inside the largest, the boundary values used for the smallest NWP can be regarded as un-coupled with the boundaries originating from the nature run.

GPS observations of SWV (and IWV) are not assimilated into the NWP system, instead the previously described 3DVAR system is fed with observations derived from the nature run, based on realistic GPS satellite configurations with additional errors as described in Section 8.3.2. The background field used for this experiment is the 6 hour (nested) NWP forecast valid at the time of assimilation, with background error co-variance from Section 8.3.1.

In Figure 8.1 the grid used for the GPS-3DVAR experiment is shown (left panel, the shaded (3×4) grid). The top of the SIM-GPS model is at 16 km, much lower than the top of the atmosphere in an NWP model (which is at approximately 25 km). However, the amount of water vapour above 16 km is almost zero and thus the atmosphere above 16 km can be neglected. The choice of a coarse grid (shifted pole projection with a grid box distance of 1 degree, corresponding to approximately 110 km resolution) was made to stay within the resolution of the nature run. Note that the ray paths are almost “solitary”, implying that the distribution of the slant water vapour information will mainly be determined by the background error covariance.

RESULTS

The results of one month of data from the SIM-GPS experiment are shown in Figure 8.8 for three selected levels. Each panel in this figure shows, for different level heights, a scatter plot of the error in the background field (horizontal axis) versus the innovation (i.e. the difference between the SIM-GPS SWV solution and the background). Ideally, the scatter plot would be the dashed straight line. From Figure 8.8 we see that for the first level, from ground to 1 kilometre height, the SIM-GPS innovations are more or less comparable to the background error although the correlation is not high. For levels higher in the atmosphere, the background error and innovation has a better correlation. This is encouraging, because the information

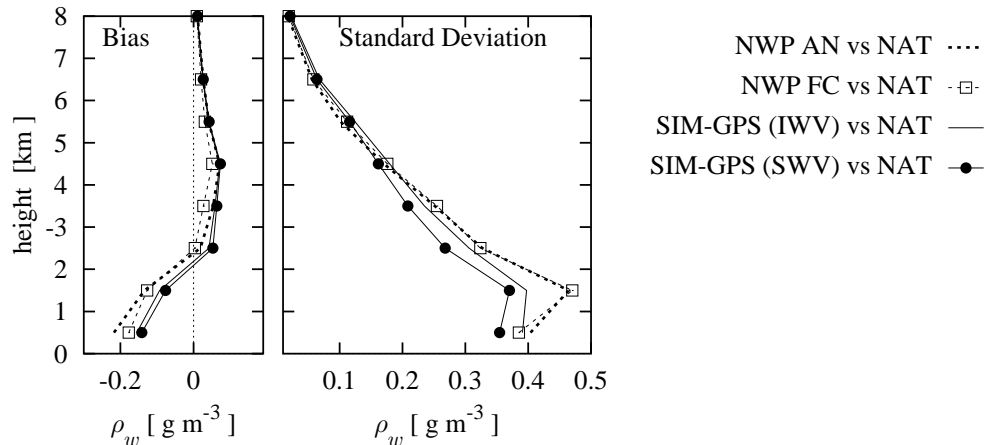


Figure 8.9: Statistics of the water vapour difference between truth (nature run) and SIM-GPS SWV (solid line with solid circles), SIM-GPS IWV (solid line), NWP analysis (dashed line) and NWP forecast (dashed line with boxes), respectively.

from the simulated observations appears to be used correctly.

In Figure 8.9 a comparison is shown between the nature run and solutions from SIM-GPS (SWV and IWV) and NWP (analysis and forecasts). In the left panel the bias between the nature run and SIM-GPS (solid lines) and NWP (dashed lines) for one month is shown over the whole three-dimensional area for which the SIM-GPS experiment was set up. The right panel shows the standard deviation between the nature run and the GPS and NWP solution. From this figure we see that NWP analysis and NWP forecast have nearly the same standard deviation and bias with respect to the nature run. The bias of SIM-GPS (both SWV and IWV) is slightly more positive than is observed for NWP analysis and forecast. The standard deviation of SIM-GPS is smaller compared to NWP analysis and forecast. Note that the forecast is used as background in SIM-GPS. It is reassuring that the standard deviation from SIM-GPS is smaller than for the background (i.e. NWP forecast). The information from the observations is used correctly. The standard deviation of SIM-GPS (SWV) is smaller than SIM-GPS (IWV), which shows the potential of the SWV observations.

8.4.2 REALISTIC EXPERIMENTS

For the period from 1 May 12:00 UTC to 25 May 23:00 UTC two different OBS-GPS assimilation schemes are conducted on GPS water vapour observations. During this period an intensive observation campaign, called BBC2, was held in the Netherlands. The campaign was mainly focusing on clouds, although also a large number of radiosonde observations were performed at Cabauw. These radiosonde observations were not used in the operational weather models, and can therefore be regarded as independent validation observations for both NWP model and GPS analysis system.

The background fields used in the first experiment are obtained from NWP forecasts, which allows us to compare the result with the SIM-OBS experiment previously discussed. This experiment is abbreviated as OBS-GPS-F. The second type of experiment differs from the first

in the sense that the background field is now the solution of the 3DVAR system of the previous hour and the updating frequency once every hour (called OBS-GPS-P).

EXPERIMENTS SETUP

For the whole period the previously described GPS analysis system was fed by actual GPS observations. Each experiment is run twice: one run with only zenith water vapour information and one with slant water vapour information to assess the impact of slant information over zenith information.

The chosen horizontal grid is identical for both experiments. The horizontal grid distance is 0.3 degrees, which results in grid boxes of approximately 30 km. The vertical discretisation is in 8 levels: the first 6 levels have a 1 kilometre thickness, the last two levels have a thickness of 3 and 6 kilometre respectively. GPS IWV observations from processing centres GFZ and GOP (Geodetic Observatory Pecny, Pecny, Czech Republic) collected within the COST716 NRT demonstration campaign are added. Furthermore, we have removed two sites (BORK and EUSK) due to antenna problems. The sites used for this experiment are shown in Figure 8.1: stars are sites for which SWV observations are used and at the sites denoted by a solid circle IWV estimates are assimilated. Only IWV observations from GFZ and GOP are used, although IWV observations from TUD are available at all sites with SWV observations. An STD estimate was available every 30 seconds. To diminish the noise of the STD observations a smoothing of the observations is applied: six STD observations from the same receiver to one satellite are averaged; the standard deviation of these six STD observations mapped to the zenith should not exceed 12 mm.

A bias correction is performed on the GPS observations. The SWV is mapped to the zenith and the bias with the state vector \mathbf{x} obtained from NWP analysis is calculated for the first two weeks of the period under consideration. The bias correction algorithm is applied because we know from previous work (Elgered et al., 2004; Ridal and Gustafsson, 2006; Poli et al., 2007) that biases exist between models and observations due to for instance differences between actual and modelled orography. SWV observations are bias corrected using the observed bias mapped to the slant by the Niell wet mapping function.

EXPERIMENT RESULTS WITH NWP BACKGROUND

For this experiment, called GPS-OBS-F, the background field from operational NWP 6 hour forecast is used. Consequently, the updating frequency is also 6 hours. This experiment is performed to obtain insight in the difference between assimilating slant observations and zenith observations and to compare to the previous purely synthetic experiment. We therefore restrict the locations to those where both IWV (from GFZ and GOP) and SWV were available (the stars in Figure 8.1, right panel).

The assimilation in NWP uses radiosonde information and other surface synoptic observations. The radiosonde information is only present at 00:00 and 12:00 UTC while at other times no upper level humidity information is available. Therefore the NWP analysis at 00:00 and 12:00 UTC can be regarded as generally better with respect to the upper atmosphere, than

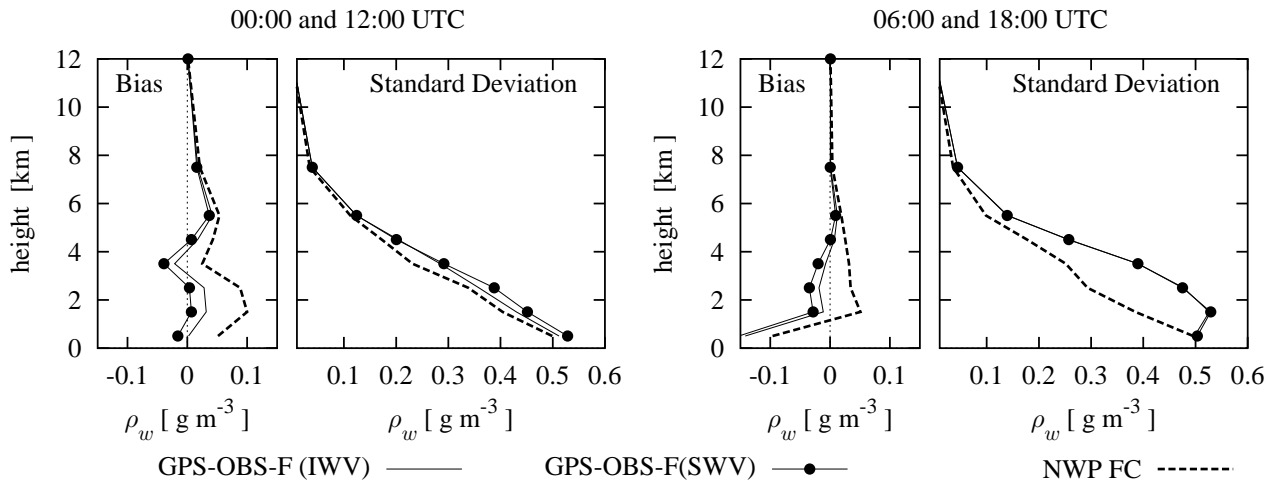


Figure 8.10: Statistics of the water vapour difference between NWP analysis and OBS-GPS-F SWV (solid lines with circles), IWV (solid lines) and NWP 6-hour forecast (dashed line) for two different time pairs: left panel shows the difference at 00:00 and 12:00 UTC, right panel 06:00 and 18:00 UTC.

those at the other times (06:00 and 18:00 UTC). The 6 hour forecast valid at 06:00 and 18:00 UTC contains information from radiosonde observations although this information is advected and spread.

In Figure 8.10 the statistics are shown for the difference at two time pairs between NWP analysis and OBS-GPS-F SWV (solid lines with circles), IWV (solid lines) and NWP 6-hour forecast (dashed line). In the left panel the statistics of the comparison is shown at 00:00 and 12:00 UTC; the right panel shows the differences at 06:00 and 18:00 UTC. The bias between SWV and IWV is small and the standard deviation is comparable to the standard deviation of the background. The bias of the background is larger than both OBS-GPS-F solutions. The NWP analysis at 00:00 and 12:00 UTC contain information of radiosonde observations; the bias between NWP 6 hour forecast and NWP analysis is the result of the analyses of new radiosonde information.

A different figure is obtained when the statistics are determined for 06:00 UTC and 18:00 UTC, see Figure 8.10 (right panel). Most striking in this figure is the difference between the standard deviation of the background and OBS-GPS-F (both SWV and IWV). The analyses at these times have no upper level humidity observations and are thus of lower quality. Note also that the standard deviation between NWP analysis and OBS-GPS-F are equal at the surface level. The biases at the surface are more negative than shown in Figure 8.10 (right panel). At the majority of the higher levels the bias between NWP forecast and analysis at 06:00 and 18:00 UTC is smaller than at the other times. This is most likely caused by the lack of upper humidity observations at 06:00 and 18:00 UTC, and thus the analysis will stay close to the background field. Apart from the lowest level, the bias is relatively small. One should keep in mind that the quality of the background field is of major importance in any analysis scheme: a bad background will result in a bad analysis, especially when the observations are sparse and the observed quantity is very variable. For both times, the bias of OBS-GPS-F is small,

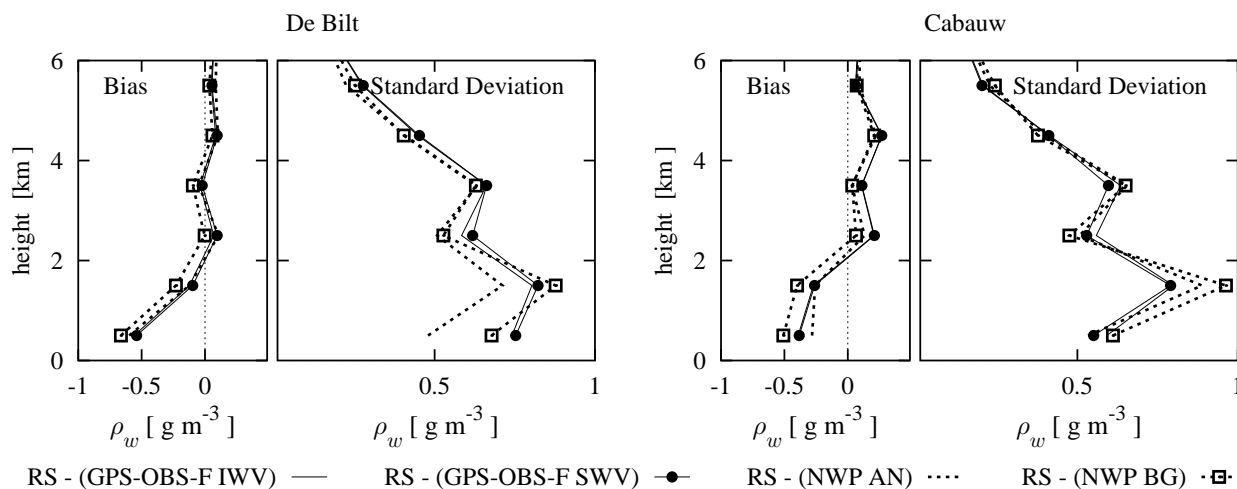


Figure 8.11: Bias and standard deviation between radiosonde water vapour observations and NWP analysis/forecast and GPS-OBS-F (IWV/SWV with NWP background): left panels radiosonde De Bilt, right panels radiosonde Cabauw. The dashed line represents the bias and standard deviation from NWP analysis; dashed line with boxes is the bias and standard deviation from NWP forecast; solid line with circles show the statistics from GPS-OBS-F SWV; the solid line the statistics of OBS-GPS-F IWV.

apart from the surface level at 06:00 and 18:00 UTC. There is some difference in the solution of assimilation of SWV and IWV, however this difference is not very clear.

The statistics of comparisons between radiosonde observations (De Bilt and Cabauw) and NWP and OBS-GPS-F are shown in Figure 8.11. NWP and OBS-GPS fields are interpolated to the location of the radiosondes. The bias for radiosonde De Bilt decrease from zero to approximately -0.6 for all model types. The OBS-GPS has a bias which lies closer to zero than NWP. The standard deviation increases, as would have been expected, from top of the atmosphere to the surface. The standard deviation at the lowest two levels of NWP analysis is smaller than at the others, which is not surprising because radiosonde observations are used in the assimilation of NWP. The standard deviation of OBS-GPS is comparable to NWP background. Again no large difference between OBS-GPS IWV and OBS-GPS SWV is observed. The comparison between water vapour profiles from NWP, OBS-GPS and radiosonde observation from Cabauw are shown in Figure 8.11, right panel. The bias of OBS-GPS lies close to the bias of the analysis for the lowest levels. The standard deviation of OBS-GPS is smaller at the lowest levels than for both analysis and forecast. Moreover, apart from the second level the standard deviation of OBS-GPS SWV is smaller than that of OBS-GPS IWV.

Resuming, the bias against NWP analysis is small (apart from the first level at 06:00 and 18:00 UTC) which implies that GPS data are used in a sensible way. The bias with radiosonde however still remains and the signature at both radiosonde locations is nearly the same; the same signature is observed in the OSSE experiment. The reason for this may lie in the quality of radiosonde observation or in the chosen vertical resolution. The fact that the OBS-GPS standard deviation in De Bilt is close to the background, while at Cabauw the standard deviation is smaller than the background, can be explained because a GPS antenna is installed in Cabauw: assimilation of SWV observations have a local effect.

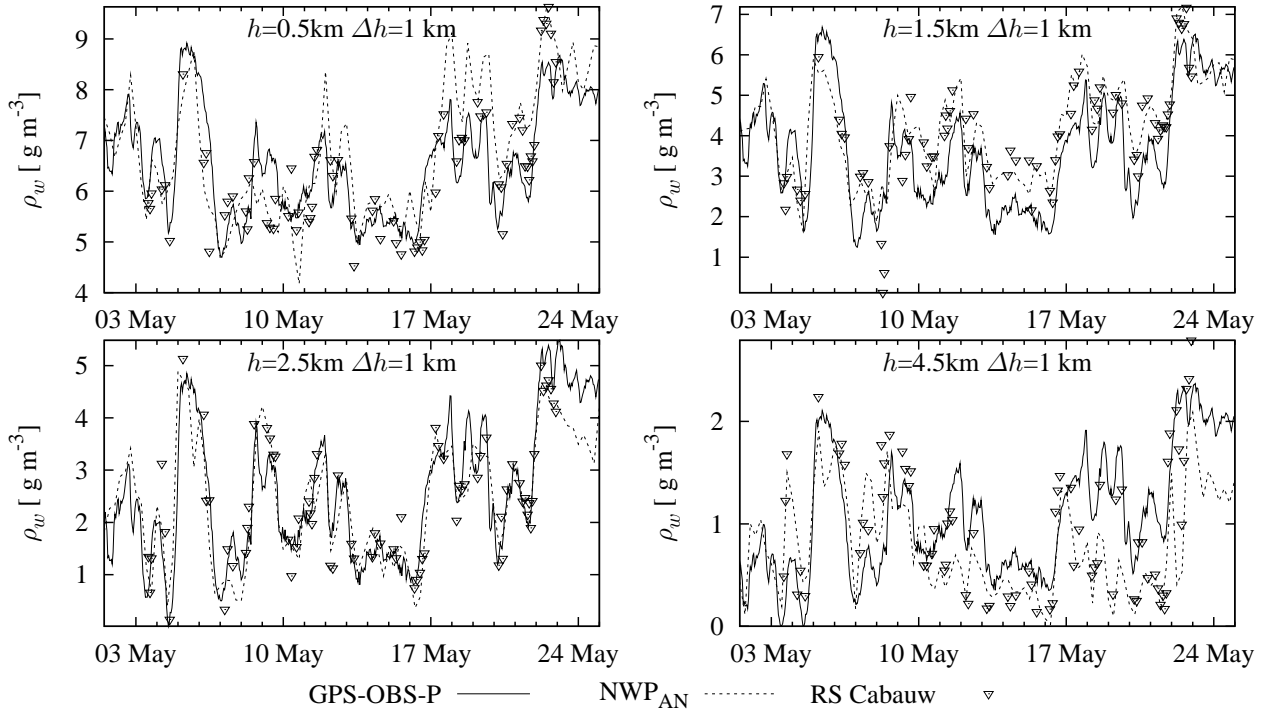


Figure 8.12: Water vapour time series at location Cabauw of OBS-GPS-P (SWV) (solid line), operational NWP analysis (dashed line) and Radiosonde Cabauw (stars) at four selected heights.

EXPERIMENT RESULTS WITH A PERSISTENT BACKGROUND

The difference between the experiment described here and the previously described experiment is the origin of the background field. Except for the first assimilation step, the solution of the GPS analysis system of the previous hour is used as the background field in the 3DVAR system. The first background field is a 6 hour forecast of the operational NWP model (valid at 1 May 12:00 UTC).

For the site Cabauw the resulting estimates at different levels are shown in Figure 8.12 for the whole period under consideration. The solid line is the solution of OBS-GPS-P, the dashed line is the NWP analysis solution at the location Cabauw and the stars are the radiosonde observations from Cabauw. Figure 8.12 shows that the timeseries for the lowest four levels of NWP, GPS and RS are close to each other. There are periods where GPS lies closer to the the largest RS observations while NWP follows the lowest observations (e.g. 10-11 May, levels 4.5km and 5.5 km and 17-23 May, same levels). The sharp gradients observed in the radiosonde observations (e.g. May 4th, May 16th and May 20th) are also visible in both GPS and NWP. On May 8th, two radiosonde observations have a very dry layer at 1.5 km height, while both GPS and NWP are much wetter.

In Figure 8.13 the bias and standard deviation of water vapour observations from radiosondes De Bilt and Cabauw (synoptic times) with NWP analysis, NWP forecast and OBS-GPS-P (IWW and SWV) are shown. Note that radiosonde observations from De Bilt are used in the NWP analysis and thus the bias and standard deviation between radiosonde and NWP anal-

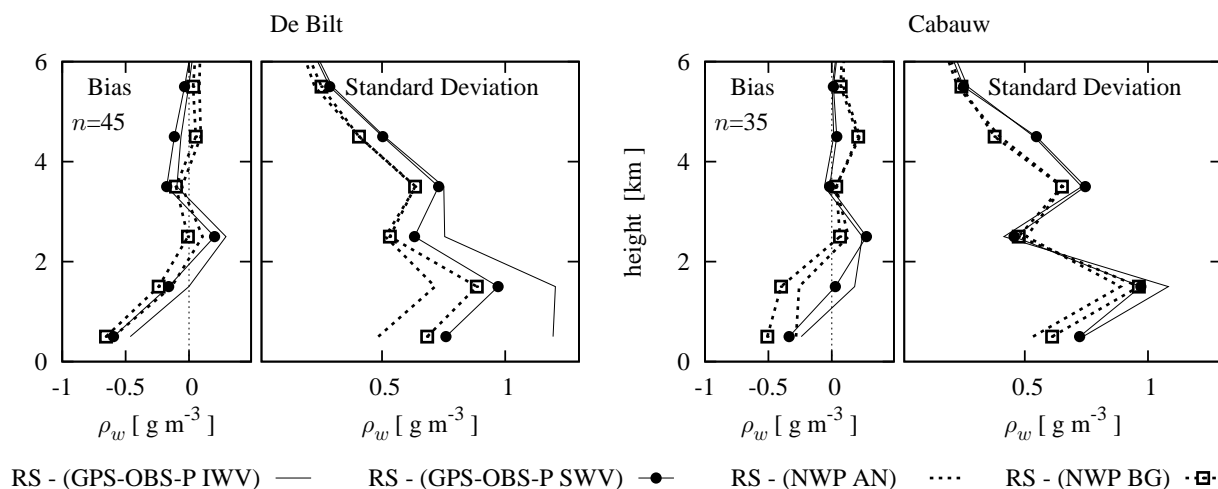


Figure 8.13: Bias and standard deviation between radiosonde water vapour observations and NWP analysis and 3DVAR-GPS (IWV/SWV with background from previous hour): left panels radiosonde De Bilt, right panels radiosonde Cabauw. The dashed line represents the bias and standard deviation from NWP analysis; solid line with circles show the statistics from 3DVAR-GPS SWV and the solid line the statistics of OBS-GPS-P IWV.

ysis are better than when compared to NWP background. The bias and standard deviation of OBS-GPS-P SWV for De Bilt are similar to the statistics for OBS-GPS-F SWV shown in Figure 8.11. The standard deviation of GPS-OBS-P IWV is much larger for the lowest 3 levels when an hourly persistence background is used than when a NWP forecast background is used (compare the solid curves in Figures 8.11 and 8.13). The reason for this is because no extra vertical information is introduced when only IWV observations are assimilated. SWV observations introduce extra vertical information which spread in the horizontal by the background correlation matrix and thus the whole model area will benefit from this additional information. Looking at the standard deviation at Cabauw in Figure 8.13 between RS and OBS-GPS-P IWV and OBS-GPS-P SWV, one observes that both standard deviations are close, although the standard deviation at the second level is smaller for OBS-GPS-P SWV. Again, the standard deviation is larger, for both SWV and IWV with an hourly background than with a NWP forecast as background. The bias, however, is better when a hourly background is used. Note that the standard deviation for GPS SWV with both radiosonde locations is comparable, indicating that the resulting three-dimensional water vapour fields have roughly the same quality over the model grid area. Furthermore, the variational run with a persistence background is completely independent from the numerical model (apart from the first time step). A standard deviation comparable to the NWP background (i.e. forecast) and a better bias shows that the 3DVAR system has a good performance.

The radiosonde Cabauw is launched at different times than the normal synoptic times and comparison with the hourly OBS-GPS-P SWV/IWV results in a double number of collocations, see Figure 8.14. The statistics do not change very much when compared to the synoptic collocations shown in Figure 8.13.

We may conclude from these figures that the SWV observations have a positive effect, although due to the horizontal distribution of the GPS receivers the effect of the extra slant

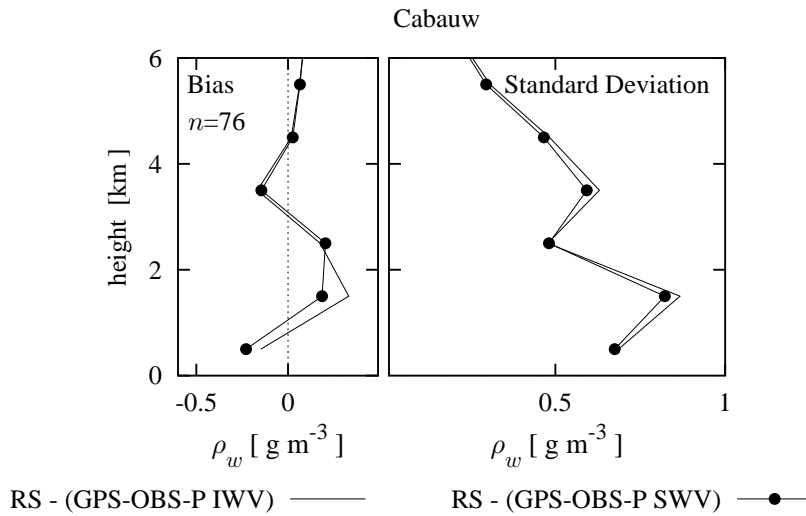


Figure 8.14: Bias and standard deviation between all radiosonde water vapour observations Cabauw 3DVAR-GPS (IWV/SWV with background from previous hour) for radiosonde Cabauw. The solid line with circles show the statistics from 3DVAR-GPS SWV and the solid line the statistics of OBS-GPS-P IWV.

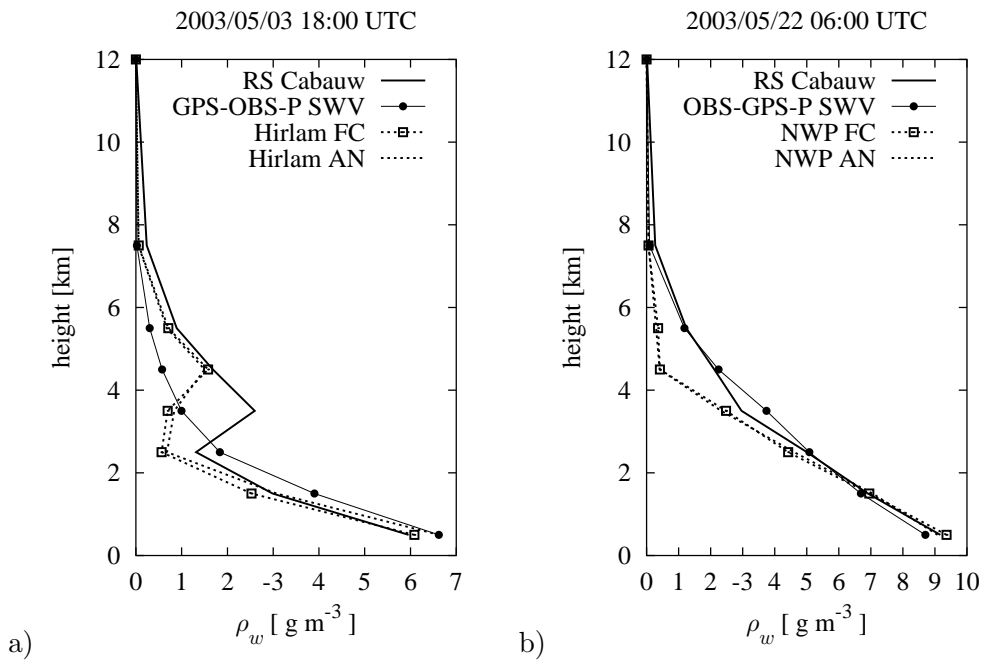


Figure 8.15: Water vapour profile of NWP (analysis and forecast), OBS-GPS-P (SWV) and radiosonde observations at Cabauw at a) 2003/05/03 18:00 UTC and b) 2003/05/22 06:00 UTC.

observation is small. The 3DVAR system performs well due to the background error covariance matrix. However, with the current distribution of GPS sites, “inversions” in ρ_w are not determined as can be seen in Figure 8.15a. For this case NWP has a local maximum in ρ_w at the wrong height, compared to the radiosonde. An example of a profile where OBS-GPS-P SWV lies closer to the radiosonde solution than NWP is shown in Figure 8.15b.

8.5 CONCLUSIONS

Despite the difficulties in interpreting slant delays the benefits of using slant total delays (STD) compared to zenith total delays (ZTD) are impressive. First of all, using slant delays one has information on gradients and non-isotropic delays in the atmosphere. Secondly when slant delays are used the part of the atmosphere that is sampled is exactly known. For example, in the Netherlands the sky is not sampled homogeneously and there is always an area in the northern sky without satellites. Moreover the satellite constellation is changing continuously, which will affect the ZTD estimation. Slant delays are much more accurate in this respect, as we know precisely the elevation and azimuth of the underlying observations. Thirdly, there are simply more STD observations than ZTD observations.

A three-dimensional variational (3DVAR) assimilation system has been developed. Background error covariance matrix were constructed using 18 months of high resolution radiosonde observations. An estimate of the observations error is made, however due to the length of the current dataset an extensive investigation of the observation error covariance matrix of slant water vapour could not be performed.

Two types of experiments were presented: an Observation System Simulation Experiment (OSSE) which is a complete simulated environment and two experiments with real GPS SWV data.

The use of slant observations in an OSSE results in a smaller standard deviation than when only zenith observations are used; the biases are similar. Slant observations have a positive effect on the standard deviation, even though the distribution of the GPS locations is (relatively) sparse with respect to the intersection between the ray-path and 3DVAR-grid. The limitation of the OSSE resolution, approximately 110 km, lays a constraint on the maximal horizontal resolution that can be resolved. The OSSE experiment shows that the GPS-3DVAR system is capable of reconstructing the three-dimensional water vapour structures. In the lowest levels, the GPS-3DVAR system does not calculate the expected innovations perfectly. Compared to the HIRLAM-3DVAR analysis solution, GPS-3DVAR has a similar bias and better standard deviation. Note that for this experiment 6 hour forecasts from HIRLAM-3DVAR are used as background information. Moreover, the period for which the nature run is valid is a winter period in the Northern hemisphere, which may explain the overall small standard deviation.

The experiments with real data and a HIRLAM 6 hour forecast as a background showed a similar result, although a little less positive, however because in this case real data is used the results are encouraging. Standard deviations between GPS-3DVAR solutions and Cabauw radiosonde observations are smaller than the standard deviations observed between HIRLAM analysis and radiosonde observation. When radiosonde observations from De Bilt are compared to GPS-3DVAR we see that the bias improves but the standard deviations lie close to the standard deviation of the background field. In Cabauw a GPS receiver is installed; slant information from this GPS receiver has a positive impact on the GPS-3DVAR derived three-dimensional water vapour. In De Bilt, no slant information was available and the GPS-3DVAR water vapour field was a little worse at this location. A small improvement of the standard deviation at a height of 2 to 4 km was observed when slant water vapour observations were used

in stead of zenith water vapour observations. The fact that the bias between radiosonde and any other system is negative at the surface does not necessarily point towards problems with the models (both NWP and GPS) but may be due to an observation bias in the radiosonde: further research is needed to understand this bias.

The last experiment presented was “stand alone” in the sense that only for the first analysis a HIRLAM background was used. All successive analysis used the previous solution of the GPS-3DVAR system as the background (persistence). The time step between successive analysis is set to one hour. When only zenith observations are used a large standard deviation in the lowest 3 km with radiosonde De Bilt was detected. This standard deviation becomes smaller, and more in line with values found in previous experiments, when slant water vapour observations are used. At Cabauw a small decrease in standard deviation, at a height of 1 to 2 km is observed when the results of the assimilation of slant observations and zenith observations are compared.

Two examples of a comparison between water vapour profiles from Cabauw and NWP show that the NWP model is not always capable to “reconstruct” the correct profile. One example shows that the NWP profile has an inversion, however it is located at a wrong height. The other example shows that the amount of water vapour in the top of the atmosphere is not correct. In the first example, GPS-3DVAR profile does not show an inversion at all; in the second example the profile of GPS-3DVAR is closer to the observed profile. The GPS-3DVAR system with the current distribution of (operational) GPS receivers is not capable of reconstructing strong water vapour inversions, without prior (background) or additional observations (radiosonde, water vapour radiometer, surface relative humidity). Nevertheless, the GPS-3DVAR system presented here is capable to estimate three-dimensional humidity with an accuracy comparable to a 6 hour NWP forecast. The GPS-3DVAR system will benefit from a denser network of GPS receivers.

Chapter 9

Summary, outlook and recommendations

The GPS system and ground-based networks are operational and well organised. This thesis shows that atmospheric applications of the GPS system are numerous; some are already in a mature state, while others are emerging. In this last chapter we return to the questions addressed in the first chapter. Topics relevant to these questions are discussed in Chapters 2 to 8; the final conclusions are stated here.

9.1 CONCLUSIONS

The questions raised in Section 1.5 are summarised here and are answered for one-, two- and three-dimensional GPS water vapour estimates.

a) How accurate can a ground-based GPS network estimate atmospheric delay and integrated water vapour?

The atmospheric zenith total delays (ZTD) can be measured accurately by processing raw GPS data from a ground-based GPS network. The conversion into integrated water vapour (IWV) values is straightforward. The GPS ZTD (with typical values of 2-3 m) has an accuracy of around 15 mm compared to the HIRLAM numerical weather prediction (NWP) model. The accuracy of GPS IWV (with typical values between 0 and 40 kg m⁻² at our latitudes) is about of 2 kg m⁻², when compared to NWP model and radiosonde observations. Note that radiosonde information are assimilated into the NWP model, and thus create a dependency between the two. There are biases, which can partly be explained by the difference in height between the actual orography and the NWP orography. The accuracy of GPS ZTD is also influenced by assumptions in the processing. One of these assumptions is that the atmosphere overlying a GPS antenna is homogeneous (i.e. independent of azimuth angle) with a climatological pressure, temperature and humidity profile. Thus, when the atmospheric profile differs from the climatology for example, when large gradients in the atmospheric parameters are present this assumption fails. The case presented in Chapter 3 showed that systematic errors were observed in ZTD (-2.1 to -3.1 mm), clock (6.5 to 9.2 mm) and height (4.8 to 6.5 mm). The

systematic error in ZTD corresponds to less than 0.5 kg m^{-2} IWV. This case was selected because a cold front passed the GPS network, a very common meteorological phenomenon in the Netherlands.

Two-dimensional maps are constructed using a variational assimilation scheme with an update frequency of 15 minutes. The two-dimensional water vapour maps have a good accuracy compared to NWP analysis maps and radiosonde observations. The mean difference between radiosonde and GPS IWV maps is negligible, while the standard deviation is less than 2 kg m^{-2} . The mean difference with NWP analysis is less than 3%; the standard deviation increases from 2 kg m^{-2} for NWP analysis to 4 kg m^{-2} for a 48 hour forecast of the NWP model. This confirms once again the importance of the near-real time character of the IWV maps: it provides more up to date information on rapid developing weather systems than a NWP forecast, and it can also act as a verification of the NWP forecast in almost real-time.

Slant GPS observations are exploited to determine three-dimensional water vapour fields. However, no slant observations are validated with independent slant water vapour observations in this thesis. Comparison with NWP shows that the extra information contained in slant GPS observations is present at one site and not at another. A three-dimensional variational (3DVAR) assimilation system is developed. When slant information is assimilated with a background field from a six-hour NWP forecast, the resulting GPS water vapour analysis has similar bias and slightly better standard deviation than the NWP analysis compared to independent radiosonde observations from Cabauw (which were not assimilated in the NWP analysis). When a persistence background (with an age of one hour) is used, the statistics of GPS WV analysis and NWP analysis compared to independent radiosonde observations show a smaller bias for the GPS WV analysis and a similar standard deviation. The above findings show that the constructed three-dimensional variational scheme produces a water vapour analysis comparable to a NWP analysis. It should be noted that these findings are based upon comparison of a GPS receiver in Cabauw which is collocated with a radiosonde location and that these observations are not used in the NWP analysis. The accuracy of this variational system is closely related to horizontal density of the ground-based GPS network. The network used in this thesis has a horizontal resolution of approximately 100 km; the current operational network has a resolution of 50 km, which will improve the estimation of three-dimensional water vapour.

b) What meteorological information can be inferred from GPS atmospheric estimates?

GPS can observe the total amount of water vapour in the column above the antenna. One of the advantages of GPS is the observation frequency. Raw GPS observations are collected every second but are commonly smoothed to 30 seconds. GPS ZTD is generally estimated with a frequency of once to four times per hour. KNMI is processing raw GPS data in real-time with a temporal frequency of four times per hour. The atmospheric residuals can be observed with a frequency of the raw observations.

The autocorrelation (with respect to time) of GPS IWV and the specific humidity at 2 km height show a dependency. The six-hour change in integrated water vapour is highly correlated with the six-hour change in specific humidity at a height of 2 km.

The horizontal distribution of water vapour obtained by GPS gives a good impression of the variability of water vapour. The observation frequency of four times per hour with a latency of several minutes opens the possibility for operational nowcasting applications.

In this thesis a special case of a cold front passage with a strong water vapour gradient is described. This case shows that the inhomogeneous part of the slant wet delay observed by GPS compared well with inhomogeneous (also called non-stratified) slant wet delay computed from a high resolution NWP model at one of the sites, and less well for another site. This difference is explained by the argument that NWP model fields are an estimate of the state of the atmosphere and most likely contain errors due to the chosen resolution, lack of information or even wrong assimilated information. Furthermore, NWP models are smoothing all information and therefore extreme strong gradients (relative to the model resolution) are hard to be captured. GPS on the other hand, has a very high temporal resolution and should be able to capture strong gradients very well.

c) In what way can the atmospheric information from GPS be beneficial for nowcasting applications?

Exploiting the temporal observation frequency GPS IWV is beneficial for interpreting the (coarse) water vapour distribution in a vertical column when combined with time-series of Meteosat water vapour and infrared brightness temperatures. The combination of this information gives a rough indication of the change in distribution of the water vapour in the column. Spectrum analysis of the residual GPS signal reveals a relation to convective available potential energy (CAPE) retrieved from radiosonde observations. The power of the signal shows to have a correlation of 0.57 with values of CAPE. The correlation is remarkable despite that the two measurements spaces are distinct (i.e. CAPE based on a profile at a single time; the power of the residual signal is a single value for the vertical over a period of an hour).

The two-dimensional maps that are produced in real-time can be helpful to detect regions of convective initialisation and can therefore be very valuable for nowcasting these severe thunderstorms as is shown by two cases presented in this thesis.

9.2 OUTLOOK

The work that is presented in this thesis has large potential for nowcasting. The research on applications of GPS in meteorology is ongoing. For instance, a better understanding of the interaction between atmosphere and GPS signals is an interesting area. Increasing this knowledge can be used in operational meteorology for nowcasting or validation applications. In this section this issue and some of other open issues are discussed which would be interesting to answer.

ONE-DIMENSIONAL WATER VAPOUR

The relation between GPS ZTD residuals and atmospheric stability needs further research. At the Cabauw research site, currently three GPS receivers are installed: two at the ground

and one in the top of the observation tower, which is 213 m high. The tower is equipped with meteorological sensors (wind, temperature, humidity) and at the site a number of other remote sensing systems are present (e.g. water vapour radiometer, 35 GHz radar, etc.). The collocation of all these measurement systems can be exploited to investigate the disturbances of the GPS signal at (currently) unresolved frequencies (i.e. minutes) especially when combining the difference in signal observed at the bottom of the tower with the signal observed at the top. When the relation of ZTD residual and atmospheric stability is better understood, this knowledge can be translated to the complete GPS network.

TWO-DIMENSIONAL WATER VAPOUR

The two-dimensional water vapour maps can be improved. By using a re-analysis of older but at the time of (the real-time) processing not yet available data, a better analysis with a larger coverage can be achieved; using this field as a background will improve the two-dimensional water vapour field. Furthermore, the current number of GPS sites in the real-time processing scheme is limited by available computer power. An increase in processing capacity will improve the resolution of the two-dimensional maps.

MOISTURE FLUX CONVERGENCE

The cases presented in Chapter 6 already showed an application of the two-dimensional water vapour maps when combined with a (surface) wind field. From a wind field and a humidity field the moisture flux can be estimated. Moisture flux convergence (MFC) is known to be related to the onset of convection (Banacos and Schultz, 2005). The MFC is defined as

$$\text{MFC} = -\nabla \cdot (qV_h) = -u \frac{\partial q}{\partial x} - v \frac{\partial q}{\partial y} - q \left(\frac{\partial u}{\partial x} + \frac{\partial v}{\partial y} \right), \quad (9.1)$$

where q is the specific humidity and $V_h = (u, v)$ is the horizontal wind. The integrated moisture flux convergence is defined as the integral of the last equation over the atmospheric profile

$$\text{IMFC} = \int_z \left(-u \frac{\partial q}{\partial x} - v \frac{\partial q}{\partial y} - q \left(\frac{\partial u}{\partial x} + \frac{\partial v}{\partial y} \right) \right) dz \quad (9.2)$$

$$\approx -u_h \frac{\partial \text{IWV}}{\partial x} - v_h \frac{\partial \text{IWV}}{\partial y} - \text{IWV} \left(\frac{\partial u_h}{\partial x} + \frac{\partial v_h}{\partial y} \right), \quad (9.3)$$

where (u_h, v_h) is the “mean” horizontal wind. The approximation fails inevitably when there is a very strong wind shear in the lower part of the troposphere. To show that this IMFC has (at least some) information on convective initiation, the IMFC fields are plotted for the two cases described previously (See section 6.5.1 and 6.5.2).

An estimate of the wind field is created using the surface wind observations by simply interpolating the wind velocity and wind direction separately. This is certainly not a perfect method and can be improved. Using this wind field and the real-time GPS IWV field the IMFC is calculated; the result is shown in Figure 9.1 where IMFC values larger than $1.15 \cdot 10^{-4} \text{ kg m}^{-2} \text{ s}^{-1}$ are plotted. Van Zomeren and van Delden (2007) showed that this was the optimum

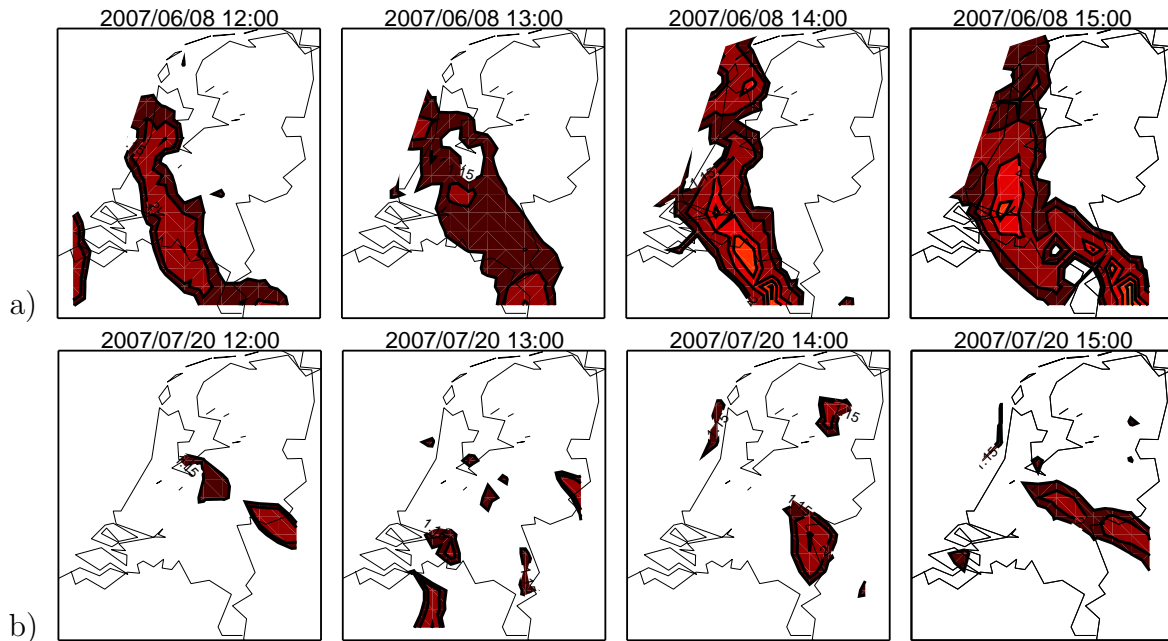


Figure 9.1: Approximation of IMFC using surface wind observations and the real-time GPS IWV field for a) 08 June 2007 and b) 20 July 2007.

threshold determined by the highest Heidke Skill Score (HSS). The HSS presents the skill as a percentage improvement over the skill expected due to random chance (Wilks, 2006). The performance of the IMFC was rather poor in their case; their study had high percentage of false alarm rates. On 08 June 2007 (Fig. 9.1a) at 12:00 UTC a region of high IMFC can be identified. The location of this region matches almost perfectly with the actual position of the thunderstorms that appeared three hours later (at 15:00 UTC, see also Fig. 6.7 on page 79). The intensification of the thunderstorms at 17:00 UTC can also be detected from the IMFC a few hours prior. The second case (Fig. 9.1b) shows the location of the line of thunderstorms at 15:00 UTC which appeared two hours later (see also Fig. 6.8 on page 81).

Because a good wind field is necessary, further research is needed that focuses on the determination of this field; the GPS IWV field has the desired accuracy (see Chapter 6). A simple scheme to construct a wind field from surface observations already demonstrates the potential for nowcasting severe weather but the method described above needs to be investigated properly based on a large number of cases. Also interesting is to compare IMFC from a three-dimensional model (using Eq. 9.2) with the approximated IMFC (Eq. 9.3) from the same model to assess the validity of the approximation.

THREE-DIMENSIONAL WATER VAPOUR

The method to estimate slant total delays is not yet implemented in the processing scheme at KNMI. Because the currently available GPS network processed at KNMI consists of 35 stations in the Netherlands, implementation will definitely improve the 3DVAR analysis. When available, slant GPS observations can also be assimilated in numerical weather prediction models. The framework for slant assimilation in HIRLAM has been set up already (Eresmaa and

Järvinen, 2006; Järvinen et al., 2007).

Knowledge on the water vapour budget can be improved by combining all types of humidity and cloud information. Observations of the liquid water path by satellite or ground based remote sensing instruments combined with weather radar and GPS water vapour can learn us more on the atmospheric water vapour balance. The HIRLAM model may also profit from this knowledge to solve the observed drift in bias shown in Table 6.2.

Near-surface refractivity in between GPS sites is not sampled by slant GPS exists due to the observation technique. Modern weather radars have sufficiently accurate time bases and digitising equipment to observe small changes in the travel time to a fixed target and back. Fabry et al. (1997) showed that a surface refractivity field around the radar can be inferred from the phase information from ground targets and its time evolution as a proxy for the changes in travel time of radar waves. These observations can fill the information gap in refractivity between the GPS sites.

IMPROVING GPS ATMOSPHERIC OBSERVATIONS

In the assimilation of GPS observation, the observation error correlation assumed to be small. However, these correlation are present as a consequence of the observation method (i.e. the processing of raw data from a network over a time window). More knowledge on these correlations would increase the applicability of these observations, especially for numerical weather prediction.

In the processing setup at KNMI GPS the only atmospheric parameter that is estimated is ZTD. However, using a slightly different setup also local gradients of ZTD can be estimated. The use of this information in NWP and nowcasting is not trivial but could be an intermediate step between using zenith and slant estimates in meteorology.

At present, the routinely processed data by KNMI from the NETPOS network is assimilated in the regional model at the UK MetOffice and Météo France. The coverage of the GPS observations is ideal for regional models but the strength lies in the observation frequency of at least once per hour. At KNMI, the first assimilation trial with GPS ZTD is in progress. An operational GPS processing chain will eventually be compulsory to guarantee the GPS ZTD data flow for the NWP model and other meteorological partners.

Because the GPS ZTD observations can be available in real-time, the opportunity to apply a rapid update cycle with a update frequency of every hour (or quicker) of an atmospheric model is possible. This model can be (or perhaps should be) nested in the operational NWP model chain as a “quick” analysis, relying on boundaries from “synoptic” runs.

9.3 RECOMMENDATIONS

The processing system run routinely at KNMI is not operational. The next step will be placing the system in the operational chain. The implemented method is stable and requires minimal human interaction, nevertheless there will be changes in the future: antenna and/or receiver changes, new software versions, more data (European GALILEO, Russian Glonass), more sites.

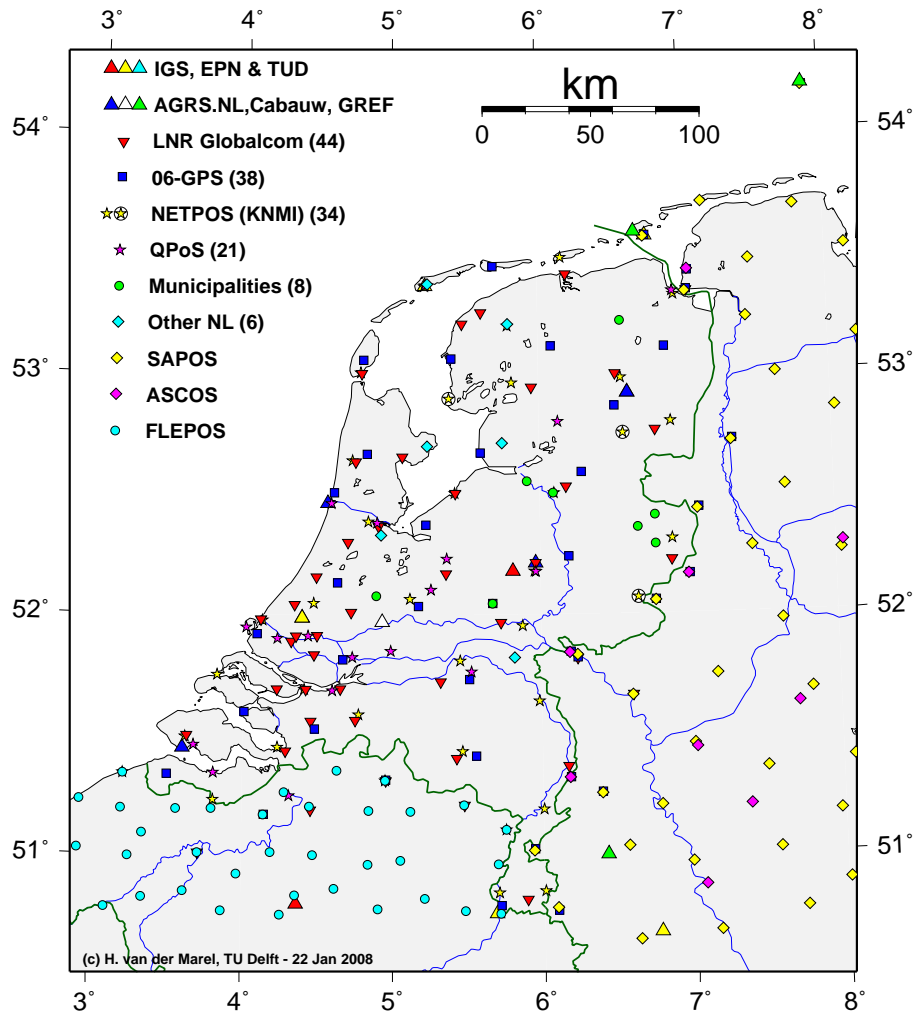


Figure 9.2: GPS sites in the vicinity of the Netherlands. Plot courtesy of H. van der Marel, TUD.

At the same time the processing system could be extended with (new) nowcasting modules (two-dimensional water vapour maps and, later, Integrated Moisture Flux Convergence).

Time should be spent on implementation of the slant GPS processing scheme at KNMI. Chapter 8 showed that using slant data three-dimensional water vapour structures can be recovered. The constructed 3DVAR system will benefit from a denser network. Late 2005, a dense GPS network with a resolution of approximately 50 km became available for meteorology in the Netherlands. This is not the only GPS ground-based network in the Netherlands: there are a number of commercial companies maintaining GPS-networks for geodetic purposes (see Figure 9.2). In total there are over 150 sites in the Netherlands alone. The potential for meteorology of the coverage of the sites is huge, especially when slant information could be derived in real-time from all of these sites. Note the high density in the southern coastal areas of the Netherlands.

The techniques constructed in Chapter 8 should be applied to the data from the operational network and will most likely result in a better vertical quality of the 3D water vapour field.

When slant observations are available assimilation in NWP is a natural step. This requires still some research especially in background error correlations and observation error correlations. When this data would be available in real-time (which is feasible) it may serve as crucial data source for a rapid update model.

Processing of GPS data will benefit from more a-priori information. A first choice might be the use of better hydrostatic and wet mapping functions, which could be obtained from long time series of NWP analysis (i.e. climatology) or NWP forecasts (Boehm et al., 2006). And secondly a-priori pressure information could be used to improve the skill of the processing.

Because the European global positioning system GALILEO will have the same frequencies (and more) as GPS today, data from this system, when available, can and should be incorporated in the current processing to improve the positioning and consequently the estimate of the atmospheric term will be more accurate.

The continuous observation of atmospheric water vapour can be used to quality control the radiosonde observations. Installation of a GPS receiver at radiosonde launch sites is preferred for this reason. Note that modern radiosonde systems are already equipped with a single frequency GPS receiver for tracking the ascending balloon. Another region that is not well sampled with upper air observations in the North Sea. In the North Sea several platforms are equipped with meteorological sensors and even some perform radiosonde launches. Installation of a GPS receiver at offshore platforms or access to raw data from existing receivers will fill the gap of moisture information over the North Sea.

The unique research constellation at Cabauw, with a GPS receiver at the top of the mast and two receivers at the ground should be exploited to help to understand (and thus quantify) the atmospheric fluctuations in GPS signals.

Finally, the meteorological use of the atmospheric “error” in GPS precise positioning is a nice illustration of recycling of information. Recycling is cost effective and expands, in this case, your scientific horizon. It is therefore worthwhile to explore other examples.

References

- Alber, C., and R. Ware, and C. Rocken, and J. Braun, 2000: Obtaining single path phase delays from GPS double differences, *Geophys. Res. Lett.*, **27**, 2661–2664.
- Baltink, H. Klein, and H. J. P. Derks, and A. C. A. P. van Lammeren, and B. A. C. Ambrosius, and A. G. A. van der Hoeven, and H. van der Marel, and F. Kleijer, and A. J. M. Kusters, 1998: GPS water vapor meteorology, *Technical Report Report 98-27*, Netherlands Remote Sensing Board (BCRS).
- Baltink, H. Klein, and H. van der Marel, and A. G. A. van der Hoeven, 2002: Integrated atmospheric water vapor estimates from a regional GPS network, *J. Geophys. Res.*, **107**, (3-1)–(3-8), ACL.
- Banacos, P.C., and D.M. Schultz, 2005: The use of moisture flux convergence in forecasting convective initiation: Historical and operational perspectives, *Weath. Forec.*, **20**, 351–366.
- Bar-Sever, Y. E., and P.M. Kroger, and J. A. Borjesson, 1998: Estimating horizontal gradients of tropospheric path delay with a single GPS receiver, *J. Geophys. Res.*, **103**, 5019–5035.
- Becker, B., and H. Roquet, 1995: Extension of the OSSE database to scatterometer and ATOVS data, Final Report Part II, *Technical report*, ECMWF, Reading.
- Beekhuis, H., and I. Holleman, 2004: Upgrade and evaluation of a lightning detection system, International Lightning Detection Conference (ILDC), 2004, Helsinki, Väisälä.
- Bevis, M., and S. Businger, and T.A. Herring, and C. Rocken, and R.A. Anthes, and R.H. Ware, 1992: GPS meteorology: Sensing of atmospheric water vapor using the global positioning system, *J. Geophys. Res.*, **97**, 15787–15801.
- Bevis, M., and S. Businger, and S. Chiswell, and T. A. Herring, and R. A. Anthes, and C. Rocken, and R. H. Ware, 1994: GPS meteorology: Mapping zenith wet delays onto precipitable water, *J. Appl. Met.*, **33**, 379–386.
- Boehm, J., and B. Werl, and H. Schuh, 2006: Troposphere mapping functions for GPS and very long baseline interferometry from European Centre for Medium-Range Weather Forecasts operational analysis data, *J. Geophys. Res.*, **111**, B02406.
- Boyden, C. J., 1963: A simple instability index for use as a synoptic parameter, *Meteor. Mag.*, **92**, 198–210.

- Braun, J. J., and C. R. Rocken, and R. H. Ware, 2001: Validation of line-of-sight water vapor measurements with GPS, *Radio Sci.*, **36**, 459–472.
- Braun, J. J., and C. R. Rocken, and J. Liljegren, 2003: Comparisons of line-of-sight water vapor observations using the global positioning system and a pointing microwave radiometer, *J. Atmos. Ocean. Technol.*, **20**, 606–612.
- Businger, S., and S.R. Chiswell, and M. Bevis, and J. Duan, and R.A. Anthes, and C. Rocken, and R.H. Ware, and M. Exner, and T. VanHove, and , and F.S. Solheim, 1996: The promise of GPS in atmospheric monitoring, *Bull. Amer. Meteor. Soc.*, **77**, 5–18.
- CBS-WMO, J. Eyre (chair), April 1996, Working group on satellites second session, final report.
- CCLRC, , 2005, Starlink project, <http://star-www.rl.ac.uk>.
- Cornman, L. B., and R. Frehlich, and E. Praskovskaya, 2004: Detection of upper level turbulence via GPS occultations methods, *OPAC-1 workshop proceedings*, Kirchengast, G., and U. Foelsche, and A. K. Steiner, (eds), Springer Verlag, 365–374.
- Daley, R., 1991: *Atmospheric data analysis*, Cambridge University Press, 457 pp 2nd edition.
- Davis, J.L., and T.A. Herring, and I.I. Shapiro, and A.E.E. Rogers, and G. Elgered, 1985: Geodesy by radio interferometry: Effects of atmospheric modeling errors on estimates of baseline length, *Radio Sci.*, **20**, 1593–1607.
- Doviak, R. J., and D. S. Zrnić, 1993: *Doppler Radar and Weather Observations*, Academic Press, 562 pp , 2nd edition.
- Duan, J., and M. Bevis, and P. Fang, and Y. Bock, and S. Chiswell, and S. Businger, and C. Rocken, and F. Solheim, and T. Van Hove, and R. H. Ware, and S. Mc-Clusky, and T. A. Herring, and R. W. King, 1996: GPS meteorology: Direct estimation of the absolute value of precipitable water, *J. Appl. Met.*, **35**, 830–838.
- Elgered, G., and H.-P. Plag, and S. Barlag, and J. Nash, 2004: *COST716 final report*, European Union, 252 pp.
- Elosegui, P., and J. L. Davis, 2003: Accuracy assessment of GPS slant-path determination. Extended abstracts, In *International Workshop on GPS Meteorology - GPS Meteorology: Ground-Based and Space-Borne Applications*, Tsukuba, Japan, 1–35–1 – 1–36–6.
- Emardson, T. R., and G. Elgered, and J. M. Johanson, 1998: Three months of continuous monitoring of atmospheric water vapor with a network of global positioning system receivers, *J. Geophys. Res.*, **103**, 1807–1820.
- Emardson, T. R., and J. M. Johanson, and G. Elgered, 2000: The systematic behaviour of water vapor estimates using four years of GPS observations, *Trans. IEEE Geosci. and Rem. Sensing*, **GE-3**, 324–329.

-
- Eresmaa, R., and H. Järvinen, 2006: An observation operator for ground-based GPS slant delays, *Tellus*, **58A(1)**, 131–140.
- Fabry, F., and C. Frush, and I. Zawadzki, and A. Kilambi, 1997: On the extraction of near-surface index of refraction using radar phase measurements from ground targets, *J. Atmos. Ocean. Technol.*, **14**, 978–987.
- Gradinarsky, L. P., and J.M. Johansson, and H. R. Bouma, and H.-G. Scherneck, and G. Elgered, 2002: Climate monitoring using GPS, *Phys. Chem. Earth*, **27**, 225–340.
- Grody, N., and J. Zhao, and R. Ferraro, and F. Weng, and R. Boers, 2001: Determination of precipitable water and cloud liquid water path over oceans from the NOAA 15 advanced microwave sounding unit, *J. Geophys. Res.*, **D3**, 2943–2953.
- Guerova, G., and E. Brockmann, and J. Quiby, and F. Schubiger, and C. Mätzler, 2003: Validation of NWP mesoscale models with Swiss GPS network AGNES, *J. Appl. Met.*, **42**, 141–150.
- Haan, S. de, 2006: Measuring atmospheric stability with GPS, *J. Appl. Met.*, **3**, 467–475.
- Haan, S. de, 2008: GPS processing, *Technische Rapport*, Koninklijk Nederlands Meteorologisch Instituut.
- Haan, S. de, and H. van der Marel, and S. Barlag, 2002: Comparison of GPS slant delay measurements to a numerical model: case study of a cold front passage, *Phys. Chem. Earth*, **27**, 317–322.
- Haan, S. de, and S. J. M. Barlag, and H. Klein Baltink, and F. Debie, 2004: Synergetic use of GPS water vapor and meteorosat images for synoptic weather forecasting, *J. Appl. Met.*, **43**, 514–518.
- Haan, S. de, and H. van der Marel, and B. Gündlich, and S. Barlag, 2005, Resolving spatial and temporal atmospheric water vapour structures using a ground based GPS receiver network, Final Report: SRON project EO-050.
- Healy, S. B., and A. M. Jupp, and C. Marquardt, 2005: Forecast impact experiment with GPS radio occultation measurements, *Geophys. Res. Lett.*, **32**.
- Healy, S.B., and J. Wickert, and G. Michalak, and T. Schmidt, and G. Beyerle, 2007: Combined forecast impact of GRACE-A and CHAMP GPS radio occultation bending angle profiles, *Atmos. Sci. Lett.*, **8**, 43–50.
- Holleman, I., 2005: Quality control and verification of weather radar wind profiles, *J. Atmos. Ocean. Technol.*, **22**, 1541–1550.
- Holleman, I., 2007: Bias adjustment and long-term verification of radar-based precipitation estimates, *Meteor. Appl.*, **14**, 195–203.

- Holleman, I., and H. Beekhuis, and S. Noteboom, and L.G. Evers, and H. W. Haak, and H. Falcke, and L. Bühren, 2006: Validation of an operational lightning detection system, International Lightning Detection Conference (ILDC), 2006, Tucson/Az, Väisälä.
- Hollingsworth, A., and P. Lonnberg, 1986: The statistical structure of short-range forecast errors as determined from radiosonde data. Part I: The wind field, *Tellus*, **38A**, 111–136.
- Holton, J. R., 1992: *An Introduction to Dynamic Meteorology*, Academic Press, 511 pp.
- Houghton, J.T., and Y. Ding, and D.J. Griggs, and M. Noguer, and P.J. van der Linden, and X. Dai, and K. Maskell, and C.A. Johnson, (eds), 2001: *Climate Change 2001: The Scientific Basis. Contribution of Working Group I to the Third Assessment Report of the Intergovernmental Panel on Climate Change*, Cambridge University Press, Cambridge, UK.
- Huuskonen, A., and I. Holleman, 2007: Determining weather radar antenna pointing using signals detected from the sun at low antenna elevations, *J. Atmos. Ocean. Technol.*, **24**, 476–483.
- Järvinen, H., and R. Eresmaa, and H. Vedel, and K. Salonen and S. Niemelä S, and J. de Vries, 2007: A variational data assimilation system for ground-based GPS slant delays, *Q. J. Roy. Met. Soc.*, **133**, 969–980.
- Jupp, A., 2006: Met Office assimilation results, *TOUGH Deliverable D48*, Danish Meteorological Institute, <http://tough.dmi.dk>.
- Kleijer, F., and P. Elosegui, and J. L. Davis, 2004: Characterizing atmospheric turbulence with GPS, *AMS Conference*.
- Leiterer, U., and H. Dier, and T. Naebert, 1997: Improvements in radiosonde humidity profiles using RS80/RS90 radiosondes of Vaisala, *Beitr. Phys. Atmosph.*, **124**, 319–336.
- Li, J., and W. W. Wolf, and W. P. Menzel, and W. Zhang, and H.-L. Huang, and T. H. Achtor, 2000: Global soundings of the atmosphere from ATOVS measurements: The algorithm and validation, *J. Appl. Met.*, **39**, 1248–1268.
- Lide, D. R., 1997: *Handbook of Chemistry and Physics*, CRC Press, 78th edition.
- Liou, Y. A., and Y. T. Teng, and T. van Hove, and J. C. Liljegren, 2001: Comparison of precipitable water observations in the near tropics by GPS, microwave radiometer, and radiosondes, *J. Appl. Met.*, **40**, 5–15.
- Liu, H., and M. Xue, and R. J. Purser, and , and D. F. Parrish, 2007: Retrieval of moisture from simulated GPS slant-path water vapor observations using 3DVAR with anisotropic recursive filters, *Mon. Wea. Rev.*, **135**, 1506–1521.
- Lorenc, A.C., and D. Barker, and R.S. Bell, and B. Macpherson, and A.J. Maycock, 1996: On the use of radiosonde humidity observations in mid-latitude NWP, *Meteor. Atmos. Phys.*, **60**, 3–17.

- MacDonald, A. E., and X Yuanfu, and R. H. Ware, July 2000: Diagnosis of three-dimensional water vapor using slant observations from a GPS network, In *COST 716 Action Workshop*, Oslo.
- Marel, H. van der, December 2002: Processing of the AGRS.NL network with the Bernese GPS software, *Internal report*, Delft University of Technology.
- Marel, H. van der, and Brigitte Gündlich, 2006: Development of models for use of slant delays, slant delay retrieval and multipath mapping software, *TOUGH Deliverable D33*, Danish Meteorological Institute, <http://tough.dmi.dk>.
- Marel, H. van der, and S. de Haan, 2002: The use of ground based GNSS networks for meteorology, In *Proc. of the 1st ESA Workshop on Satellite navigation user equipment technology Navitec 2001*.
- Marshall, J. S., and W. M. Palmer, 1948: The distribution of raindrops with size, *J. Atmos. Sci.*, **5**, 165–166.
- Mazany, R. A., and S. I. Gutman S. Businger, and W. Roeder, 2002: A lightning prediction index that utilizes GPS integrated precipitable water vapor, *Weath. Forec.*, **17**, 1034–1047.
- Niell, A. E., 1996: Global mapping functions for the atmospheric delay at radio wavelengths, *J. Geophys. Res.*, **101**, 3227–3246.
- Niell, A. E., 2000: Improved atmospheric mapping functions for VLBI and GPS, *Eart Planets Space*, 699–702.
- Niell, A. E., 2001: Preliminary evaluation of atmospheric mapping functions based on numerical weather models, *Phys. Chem. Earth*, **26**, 475–480.
- Niell, A. E., and A. J. Coster, and F. S. Solheim, and V. B. Mendes, 2001: Comparison of measurements of atmospheric wet delay by radiosonde, water vapor radiometer, GPS, and VLBI, *J. Atmos. Ocean. Technol.*, **18**, 830–850.
- Nilsson, T., and L. Gradinarsky, and G. Elgered, 2007: Water vapour tomography using GPS phase observations: Results from the ESCOMPTE experiment, *Tellus*, **59A**, 674–682.
- Poli, P., and P. Moll, and F. Rabier, and G. Desroziers, and B. Chapnik, and L. Berre, and S. B. Healy, and E. Andersson, and F.-Z. El Guelai., 2007: Forecast impact studies of zenith total delay data from European near real-time GPS stations in Météo France 4DVAR, *J. Geophys. Res.*, **112**, 1–16.
- Ridal, M., and N. Gustafsson, 2006: A bias reduction scheme and its impact on ZTD assimilation, *TOUGH Deliverable D16-17*, Danish Meteorological Institute, <http://tough.dmi.dk>.
- Rocken, C., and R. Ware, and T. VanHove, and F. Solheim, and C. Alber, and J. Johnson, and M Bevis, and S. Businger, 1993: Sensing atmospheric water vapor with the global positioning system, *Geophys. Res. Lett.*, **20**, 2631–2634.

- Rocken, C., and T. Van Hove, and J. Johnson, and F. Solheim, and R. Ware, and M. Bevis, and S. Chiswell, and S. Busingerb, 1995: GPS/STORM - GPS sensing of atmospheric water vapor for meteorology, *J. Atmos. Ocean. Technol.*, **12**, 468–478.
- Rocken, C., and S. Sokolovskiy, and J. M. Johnson, and D. Hunt, 2001: Improved mapping of tropospheric delays, *J. Atmos. Ocean. Technol.*, **18**, 1205–1213.
- Rocken, C. R., and T. van Hove, and R. H. Ware, 1997: Near real-time GPS sensing of atmospheric water vapor, *Geophys. Res. Lett.*, **24**, 3221–3224.
- Rothacher, M., and L. Mervart, 1996: Bernese GPS software version 4.0, *Technical report*, Astronomical Institute, Berne University, Switzerland.
- Saastamoinen, J., 1972: Atmospheric correction for the troposphere and stratosphere in radio ranging of satellites, *Geoph. Monograph Series*, **15**, 247–251.
- Salby, M. L., 1996: *Fundamentals of Atmospheric Physics*, Academic Press, 627 pp.
- Schmeits, M. J., and K. J. Kok, and D. H. P. Vogelezang, 2005: Probabilistic Forecasting of (Severe) Thunderstorms in the Netherlands Using Model Output Statistics, *Weath. Forec.*, **20**, 134–148.
- Smith, E. K., and S. Weintraub, 1953: The constants in the equation for atmospheric refractive index at radio frequencies, *Proc IRE*, **41**, 1035–1037.
- Smith, W. H. F., and P. Wessel, 1990: Gridding with continuous curvature splines in tension, *Geophysics*, **55**, 293–305.
- Solomon, S., and D. Qin, and M. Manning, and Z. Chen, and M. Marquis, and K.B. Averyt, and M. Tignor, and H.L. Miller, (eds), 2007: *Climate Change 2007: The Physical Science Basis. Contribution of Working Group I to the Fourth Assessment Report of the Intergovernmental Panel on Climate Change*, Cambridge University Press, Cambridge, United Kingdom and New York, NY, USA, 996 pp. pp.
- Sonntag, D., 1994: Advancements in the field of hygrometry, *Meteor. Zeitschrift*, **3**, 51–66.
- Stoew, B., and G. Elgered, and J. M. Johansson, 2001: An assesment of estimates of integrated water vapour from ground based GPS data, *Meteor. Atmos. Phys.*, **77**, 99–107.
- Stoffelen, A., and B. Becker, and J. Eyre, and H. Roquet, 1994: Theoretical studies of the impact of doppler wind lidar data - preparation of a database, *Technical Report ESA-CR(P)-3943*, ESA.
- Thayer, G.D., 1974: An improved equation for the radio refractive index of air, *Radio Sci.*, **9**, 803–807.
- Thompson, A. R., and J. M. Moran, and G. W. Swenson, 1986: *Interferometry and Synthesis in Radio Astronomy*, John Wiley and Sons, New York, 720 pp.

- Turner, D. D., and B. M. Lesht, and S. A. Clough, and J. C. Liljegren, and H. E. Revercomb, and D. C. Tobin, 2003: Dry bias and variability in RS80-H Radiosondes: The ARM experiment, *J. Atmos. Ocean. Technol.*, **20**, 117–132.
- Undén, P., and L. Rontu, and H. Järvinen, and P. Lynch, and J. Calvo, and G. Cats, and J. Cuhart, and K. Eerola, 2002: HIRLAM-5 scientific documentation, *Technical report*, HIRLAM-project, Norrköpping, <http://hirlam.knmi.nl>.
- Vries, J. de, 2006: Expected impact of tropospheric slant delays, *TOUGH Deliverable D40*, Danish Meteorological Institute, <http://tough.dmi.dk>.
- Ware, R., and C. Rocken, and F. Solheim, and M. Exner, and W. Schreiner, and R. Anthes, and D. Feng, and B. Herman, and M. Gorbunov, and S. Sokolovskiy, and K. Hardy, and Y. Kuo, and X. Zou, and K. Trenberth, and T. Meehan, and W. Melbourne, and , and S. Businger, 1996: GPS soundings of the atmosphere from low earth orbit: Preliminary results, *Bull. Amer. Meteor. Soc.*, **77**, 19–40.
- Ware, R. H., and C. Alber, and C. R. Rocken, and F. Solheim, 1997: Sensing integrated water vapor along GPS ray paths, *Geophys. Res. Lett.*, **24**, 417–420.
- Webb, F. H., and J. F. Zumberge, 1993: An introduction to GIPSY/ OASIS-II, *JPL publication D-11088*, Jet Propulsion Laboratory, Pasadena, California.
- Weldon, R. B., and S. J. Holmes, 1991: Water vapor imagery. interpretation and applications to weather analysis and forecasting, *NOAA technical report NESDIS*, US Department of Commerce National Oceanic and Atmospheric Administration, Washington DC.
- Wessel, P., and W. H. F. Smith, 1991: Free software helps map and display data, *EOS Trans. AGU*, **72**, 445–446.
- Wilks, D. S., 2006: *Statistical methods in the atmospheric sciences*, Academic Press, 627 pp second edition.
- Zumberge, J. F., and M. B. Heflin, and D. C. Jefferson, and M. M. Watkins, and F. H. Webb, 1997: Precise point positioning for the efficient and robust analysis of GPS data from large networks, *J. Geophys. Res.*, **102**, 5005–5017.
- NOAA/NASA/USAF, *United States Committee on Extension to the Standard Atmosphere*, 1976, U.S. Standard Atmosphere, U.S. Government Printing Office, Washington D.C.

Samenvatting

Het gebruik van het Global Positioning System (GPS) is bijna niet meer weg te denken uit onze huidige samenleving: klokken worden er mee gesynchroniseerd, vliegtuigen berekenen hun positie er mee en (veel) automobilisten komen dankzij het systeem op de plaats van bestemming. De methode om de positie te bepalen is gebaseerd op het meten van de afstand tussen de ontvanger en (minimaal) vier GPS-satellieten. In dit proefschrift wordt een ander gebruik van het GPS uitgelicht: de meteorologische. Het signaal dat de GPS-satellieten uitzenden en dat met een GPS-ontvanger op aarde wordt ontvangen, wordt “verstoord” door de atmosfeer. Deze verstoring heeft tot gevolg dat eenvoudige ontvangers een nauwkeurigheid van enkele meters hebben. Met behulp van een vast netwerk en geavanceerde GPS-ontvangers kan de verstoring van de atmosfeer geschat worden waardoor de positie zeer nauwkeurig kan worden bepaald. Voor landmeetkundige toepassingen van GPS is de atmosfeer een foutenbron; voor de meteorologie blijkt de foutenbron waardevolle informatie over de hoeveelheid vocht in de atmosfeer te geven. De grootte van de verstoring van het GPS-signaal door de atmosfeer, ook wel totale vertraging genoemd, wordt direct bepaald door de temperatuur, vocht en dichtheid van lucht waar het signaal doorheen gaat. Het blijkt dat de verstoring kan worden opgedeeld in een hydrostatisch deel en een “nat” deel. Het hydrostatische deel is nauwkeurig te benaderen met behulp van de luchtdruk aan de grond. Het natte deel heeft een vrijwel lineair verband met de totale hoeveelheid waterdamp in de atmosfeer.

In dit proefschrift staan de volgende onderzoeksvragen centraal:

- a) Hoe nauwkeurig kan een GPS grondnetwerk de totale vertraging en waterdampkolom schatten?
- b) Welke meteorologische informatie kan worden afgeleid uit GPS?
- c) Hoe kan deze meteorologische informatie gebruikt worden voor “nowcasting”?

Waterdamp is één van de cruciale krachten bij de ontwikkeling van wolken, neerslag en onweer. Hoewel de totale massa van de lucht slechts voor één procent uit waterdamp bestaat is het effect op het weer zeer groot. Het huidige operationele netwerk van vochtwaarnemingen in de bovenlucht bestaat eigenlijk alleen uit radiosondes (weerballonnen). Deze worden over het algemeen elke 6 tot 12 uur opgelaten en hebben een zodanige bedekking dat voornamelijk grootschalige meteorologische systemen worden waargenomen. Kleinere systemen, belangrijk voor de weersverwachting op de korte termijn kunnen moeilijk worden gedetecteerd vanwege de lage waarneemfrequentie en horizontale verdeling van de radiosondewaarnemingen. De totale waterdampkolom uit GPS kan elke 15 minuten worden bepaald met een horizontale resolutie van

100 km (regionaal zelfs minder) en een bedekking van bijna geheel Europa, zoals in hoofdstuk twee wordt beschreven.

Hoofdstuk twee van dit proefschrift laat verder zien dat de verandering in de totale waterdampkolom in een periode van zes uur een hoge correlatie heeft met de verandering van specifieke vochtigheid op twee kilometer hoogte. Hoofdstuk twee beschrijft ook het algoritme om de totale vertraging en totale waterdampkolom uit het numerieke weermodel af te leiden, gegeven de positie van de satelliet en de positie van de ontvanger. Dit algoritme is gebruikt in de resterende hoofdstukken. Het pad dat het signaal aflegt wordt door de atmosfeer afgebogen; de hoek waaronder het signaal wordt ontvangen is anders dan de hoek van de zichtlijn naar de satelliet. Het verschil tussen de hoeken komt zeer goed overeen met het verschil dat geschat is met behulp van een standaard atmosfeer met variërende luchtvochtigheid. De kwaliteit van de GPS-waarnemingen die zijn gebruikt in dit proefschrift is bepaald door deze te vergelijken met het numerieke weermodel HIRLAM en radiosondewaarnemingen. De bepaalde standaardfouten van ongeveer 14 mm voor de totale vertraging en 2 kg m^{-2} voor de totale waterdamp kolom komen overeen met eerdere studies.

Om met de ruwe GPS-data de positie nauwkeurig te bepalen worden alle schuine vertrageningen op het zenit afgebeeld met zogenaamde mapping functies. Hierbij wordt een onderscheid gemaakt tussen het hydrostatische deel en het natte deel omdat de verdeling van vocht over de verticaal anders is dan de verdeling van de “droge” massa: waterdamp bevindt zich voornamelijk, op onze breedtegraad, in de onderste twee tot drie kilometer. Om deze functies eenvoudig te houden is een klimatologische beschrijving gemaakt die afhangt van de breedtegraad, de hoogte van het station en de dag van het jaar. Echter, bij een sterke vochtgradiënt zal de werkelijke verdeling van vocht van de klimatologische waarde afwijken. Door het gebruik van de klimatologische mapping functies heeft dit een effect op de schatting van de totale vertraging. Een uitgewerkt voorbeeld laat zien dat systematische fouten van ongeveer twee tot drie millimeter vertraging kunnen optreden, wat overeenkomt met ongeveer 0.5 kg m^{-2} totale waterdamp.

Eén van de eerste meteorologische toepassingen van GPS-waarnemingen wordt beschreven in het vierde hoofdstuk: het analyseren van tijdreeksen van de totale waterdamp. Atmosferisch vocht wordt ook waargenomen met de geostationaire satellieten, echter wolken verhinderen een eenduidige interpretatie van de waarnemingen. Een bijkomend probleem hierbij is dat de hoogte van het vochtprofiel niet nauwkeurig is te bepalen. De geostationaire satelliet, die ten opzichte van de aarde stil staat, ziet voornamelijk het vocht dat zich op een hoogte hoger dan ongeveer vijf kilometer in de atmosfeer bevindt. Door de verandering van de waterdampkolom (uit GPS) en de hoeveelheid waterdamp in de bovenlucht (uit de geostationaire satellieten) in de tijd te volgen voor een bepaalde locatie, kan een ruwe schatting gemaakt worden hoe de verticale verdeling van waterdamp veranderd is. Omdat beide tijdreeksen een waarneemfrequentie hebben van elke 15 minuten kunnen ze gemakkelijk worden vergeleken.

In hoofdstuk vijf wordt de hoge temporele resolutie van het GPS-signaal bekeken. De ruwe GPS-data hebben over het algemeen een tijdsresolutie van 30 seconden. In de processing wordt uit deze ruwe data de totale vertraging berekend met een tijdsresolutie van enkele minuten (dat wil zeggen een gemiddelde totale vertraging over deze tijdsperiode). Het verschil tussen

de geschatte waarde en de ruwe data, gecorrigeerd voor lokale effecten zoals multi-pad, wordt het residu genoemd. Spectrale analyse van het residu toont een relatie aan tussen “Convective Available Potential Energy” (CAPE) en het vermogen van het residu signaal. CAPE is een parameter die gerelateerd is aan verticale beweging en dus aan convectie en het vermogen van een signaal is de integraal van de spectrale dichtheid over de frequenties. Tussen het vermogen van het residu en CAPE is een correlatie van 0.6 gevonden. De grootte van correlatie is opmerkelijk omdat de meetruimtes verschillend zijn: de spectraal analyse is uitgevoerd op een tijdreeks van de waterdampkolom over een periode van een uur, terwijl de CAPE is bepaald uit radiosondewaarnemingen en dus berekend wordt uit profielinformatie van een enkel tijdstip.

Hoofdstuk zes bespreekt de toepassing van tweedimensionale GPS-waterdamp in de kortetermijnweersverwachting. De tweedimensionale GPS-waterdampbeelden worden berekend met behulp van een variationele assimilatietechniek. De beelden zijn “real-time” beschikbaar (d.w.z. vijf minuten na waarneemtijd) met een verversingsfrequentie van 15 minuten, hetgeen vergelijkbaar is met de weerradar en geostationaire satellietwaarnemingen. De waterdampbeelden zijn gevalideerd met waterdampvelden uit numerieke weermodellen en waterdampkolomwaarnemingen uit radiosonde. De statistieken laten zien dat de waterdampbeelden van goede kwaliteit zijn. Twee gevallen van onweerssituaties laten de bruikbaarheid van deze waterdampbeelden, gecombineerd met oppervlaktewindwaarnemingen, zien voor de kortetermijnweersverwachting.

Tot slot wordt in de hoofdstukken zeven en acht het driedimensionale karakter van de GPS-waarnemingen onderzocht. In hoofdstuk zeven wordt het residu van de totale vertraging uit GPS vergeleken met het residu uit een numeriek weermodel in een situatie waarbij een sterke gradiënt in het vochtveld aanwezig was. Het blijkt dat de vergelijking voor de waarnemingen in Delft redelijk waren, maar voor een ander station (Terschelling) weken de twee type residuen duidelijk van elkaar af. In hoofdstuk acht wordt het driedimensionale karakter van de GPS-waarnemingen gebruikt door de schuine waterdampwaarnemingen te assimileren en zo een driedimensionale verdeling van het waterdampveld te berekenen. Het gebruikte GPS-netwerk heeft een resolutie van ongeveer 100 km wat een beperkende invloed heeft op de nauwkeurigheid van de analyse van de driedimensionale GPS-waterdamp. Echter, het blijkt dat de gemiddelde afwijking van de driedimensionale GPS-analyse van onafhankelijke radiosondevochtwaarnemingen beter scoort dan de weermodelanalyses en zes-uurs voorspellingen; de standaardfouten zijn vergelijkbaar.

Appendix A

Constants and definitions

A.1 CONSTANTS

| | |
|--|---------------------------------------|
| $R_d = 287.0586$ [J kg ⁻¹ K ⁻¹] | Specific gas constant of dry air |
| $R_v = 461.5125$ [J kg ⁻¹ K ⁻¹] | Specific gas constant of water vapour |
| $\epsilon = R_d/R_v = 0.62198$ | Ratio of molar weights Sonntag (1994) |
| $\delta = 1/\epsilon - 1 = 0.6078$ | |
| $k_1 = 77.6$ [K hPa ⁻¹] | Thayer (1974) |
| $k_2 = 70.4$ [K hPa ⁻¹] | Thayer (1974) |
| $k_3 = 373900$ [K ² hPa ⁻¹] | Thayer (1974) |

A.2 SATURATED WATER VAPOUR PRESSURE

According to Sonntag (1994) the saturated water vapour pressure for a temperature T [K] is given by:

$$e_{satw}(T) = \exp(a_0 T + a_1 + a_2 T + a_3 T^2 + a_4 \log T) \quad (\text{A.1})$$

$$\left. \begin{array}{l} a_0 = -6096.9385 \\ a_1 = 16.635794 \\ a_2 = -2.711193 \cdot 10^{-2} \\ a_3 = 1.6739521 \cdot 10^{-5} \\ a_4 = 2.433502 \end{array} \right\} \text{for } T > 0^\circ\text{C}$$

$$\left. \begin{array}{l} a_0 = -6024.5282 \\ a_1 = 24.7219 \\ a_2 = 1.0613868 \cdot 10^{-2} \\ a_3 = -1.3198825 \cdot 10^{-5} \\ a_4 = -0.49382577 \end{array} \right\} \text{for } T < 0^\circ\text{C} \quad (\text{A.2})$$

Appendix B

Acronyms

| | |
|-------------|--|
| AC | Analysis Centre |
| AGRS | Active GPS Reference System |
| AMDAR | Aircraft Meteorological Data Reporting |
| AMSU | Advanced Microwave Sounding Unit |
| APEL | Apeldoorn, NL (GPS-site) |
| ATOVS | Advanced TIROS Operational Vertical Sounder |
| BBC2 | Baltex Bridge Campaign-2 |
| BI | Boyden Index |
| BCRS | Netherlands Remote Sensing Board |
| BORK | Borkum, D (GPS-site) |
| BRUS | Brussels, B (GPS-site) |
| CABW | Cabauw, NL (GPS-site) |
| CAPE | Convective Available Potential Energy |
| COST | Co-operation in the field of Scientific and Technical Research |
| DELFT | Delft, NL (GPS-site) |
| DEOS | Delft institute for Earth Oriented Space Research |
| E-GVAP | EUMETNET GPS water vapour programme |
| EIJS | Eijsden, NL (GPS-site) |
| EUMETNET | Network of European National Meteorological Services |
| EUSK | Euskirchen, D (GPS-site) |
| GALILEO | European Global Navigation Satellite System |
| GFZ | Geo Forschungs Zentrum, Potsdam, Germany |
| GIPSY-OASIS | GPS-Inferred Positioning System Orbit Analysis Simulation Software |
| GLONASS | Russian Global Global Navigation Satellite System |
| GNSS | Global Navigation Satellite System |
| GOP | Geodetic Observatory Pecny, Pecny, Czech Republic |
| GPS | Global Positioning System (USA) |
| GTS | Global Telecom System |
| HELG | Helgoland, D (GPS-site) |
| HERS | Hersmonceaux, GB (GPS-site) |
| HIRLAM | High Resolution Limited Area Model |
| IGS | International GNSS Service |
| IMFC | Integrated Moisture Flux Convergence |
| IR | (Meteosat) Infra Red |

| | |
|---------|--|
| IWV | Integrated Water Vapour |
| KNMI | Koninklijk Nederlands Meteorologisch Instituut |
| KOSA/G | Kootwijk, NL (GPS-site) |
| LEO | Low Earth Orbit |
| LCL | Lifting Condensation Level |
| LIDAR | LIght Detection And Ranging |
| LNB | Level of Neutral Buoyancy |
| LORAN-C | Long Range Navigation |
| MFC | Moisture Flux Convergence |
| MSG | Meteosat Second Generation |
| NAVSTAR | Navigation Satellite Timing and Ranging Global Positioning System |
| NETPOS | Netherlands Positioning Network |
| NIVR | Netherlands Agency for Aerospace Programmes/ Nederlands Instituut voor Vliegtuigontwikkeling en Ruimtevaart |
| NMS | National Meteorological Service |
| NNSS | Navy Navigational Satellite System |
| NOAA | National Oceanic and Atmospheric Administration |
| NRT | Near real-time |
| NWP | Numerical Weather Prediction |
| ONSA | Onsala, S (GPS-site) |
| OSSE | Observation Simulation System Experiment |
| POTS | Potsdam, D (GPS-site) |
| PPP | Precise Point Positioning |
| RH | Relative Humidity |
| RMI | Royal Meteorological Institute of Belgium |
| RMS | Root Mean Square |
| RO | Radio Occultation |
| RS | Radiosonde |
| RT | Real-time |
| SHD | Slant Hydrostatic Delay |
| SRON | Netherlands Institute for Space Research/ Stichting Ruimte Onderzoek Nederland |
| STD | Slant Total Delay |
| SWD | Slant Wet Delay |
| SWV | Slant Water Vapour |
| TAMDAR | Tropospheric Airborne Meteorological Data Reporting |
| TERS | Terschelling, NL (GPS-site) |
| TIROS | Television Infrared Observation Satellite |
| TOUGH | Targeting Optimal Use of GPS Humidity Measurements in Meteorology |
| TUD | Technische Universiteit Delft (Delft Univeristy of Technology) |
| WMO | World Meteorological Organization |
| WSRA/T | Westerbork, NL (GPS-site) |
| WTZR | Wetzell, D (GPS-site) |
| WV | (Meteosat) Water Vapour |
| ZHD | Zenith Hydrostatic Delay |
| ZTD | Zenith Total Delay |
| ZWD | Zenith Wet Delay |

List of Publications

PEER-REVIEWED

- Haan, S. de, and H. van der Marel, and S. Barlag, 2002: Comparison of GPS slant delay measurements to a numerical model: case study of a cold front passage, *Phys. Chem. Earth*, **27**, 317–322.
- Haan, S. de, and H. van der Marel, 2004: The influence on GPS estimates of NWP derived mapping functions, *Phys. Chem. Earth* **29**, 159–166.
- Haan, S. de, and S. J. M. Barlag, and H. Klein Baltink, and F. Debie, 2004: Synergetic use of GPS water vapor and meteosat images for synoptic weather forecasting, *J. Appl. Met.*, **43**, 514–518.
- Haan, S. de, 2006: Measuring atmospheric stability with GPS, *J. Appl. Met.*, **3**, 467–475.
- Hersbach, H., and A. Stoffelen, and S. de Haan, 2007: An Improved C-band scatterometer ocean geophysical model function: CMOD5, *J. Geophys. Res.*, **112**.
- Stoffelen, A. C. M., and G. J. Marseille, and F. Bouttier, and D. Vasiljevic, and S. de Haan, and C. Cardinali, 2006: ADM-Aeolus Doppler wind lidar Observing System Simulation Experiment, *Quart. J. Royal Meteor. Soc.*, **132**, 1927–1947.
- Haan, S. de, and I. Holleman, and A. A. M. Holtslag, 2008: Real-time Water Vapour Maps from a GPS Surface Network and the Application for Nowcasting of Thunderstorms, *J. Appl. Met. Clim.*, Submitted.
- Haan, S. de, and H. van der Marel, 2008: Observing Three-dimensional Water Vapour using a Surface Network of GPS Receivers, *Atmos. Chem. Phys.*, Submitted.

PUBLICATIONS IN CONFERENCE PROCEEDINGS

- Haan, S. de, 1999: Validation of NOAA-AVHRR Sea Surface Temperatures for Use in NWP-Models, In *The 1999 Meteorological Satellite Data Users' Conference*, Copenhagen, Denmark. EUMETSAT, 410–416.
- Haan, S. de, 2000: The Impact of NOAA-AVHRR SST Data Assimilation in the HIRLAM NWP model, In *The 2000 EUMETSAT Meteorological Satellite Data Users' Conference*, Bolonga, Italy. EUMETSAT, 675–682, ISBN 92-9110-037-4.
- Haan, S. de, and A. C. M. Stoffelen, 2001: Ice detection with a scatterometer: exploiting the full 3D measurement space, In *The 2001 EUMETSAT Meteorological Data Users' Conference*, Antalya, Turkey. EUMETSAT, 144–151, ISBN 92-9110-044-7.

Lindenbergh, R., and H. van der Marel, and M. Keshin, and S. de Haan, 23-27 April 2007: Towards sequential water vapor predictions based on time series of GPS and MERIS observations. In *Proceedings of Envisat Symposium* Montreux, Switzerland

Marel, H. van der, and E. Brockmann, and S. de Haan, and J. Dousa, and J. Johansson, 14-17 January 2003: COST-716 Near Real-Time Demonstration Project, *International Workshop on GPS Meteorology: Ground-Based and Space-Borne Applications*, R.A. Anthes et. al, (ed).

Verspeek, J. A., and A. C. M. Stoffelen, and S. de Haan, 15-17 March 2005: C-band sea ice model, In *Ocean and Sea Ice second workshop*, Perros-Guirec, France. EUMETSAT, ISBN 92-9110-072-2.

REPORTS

Haan, S. de, 2000: The Impact of Remotely Sensed Sea Surface Temperature on a Numerical Weather Prediction Model, SRON Final Report , project No. 1.1/AP-08, 97 p.

Haan, S. de, 2005: Global Maps from GPS Radio Occultation Data, *Scientific Report No. 05-08*, Danish Meteorological Institute.

Haan, S. de, and J. C. W. de Vries, 2005: Applications of GPS Radio Occultation for Climate and Numerical Weather Prediction, SRON Final Report , project No. E0-043, 74 p.

Haan, S. de, and H. van der Marel, and B. Gündlich, and S. Barlag, 2005, Resolving spatial and temporal atmospheric water vapour structures using a ground based GPS receiver network, Final Report: SRON project EO-050.

Haan, S. de, 2006: National/regional operational procedures of GPS water vapour networks and agreed international procedures, *WMO/TD No. 1340*, WMO.

Haan, S. de, 2008: GPS processing, *Technische Rapport*, Koninklijk Nederlands Meteorologisch Instituut.

Haan, S. de, and A. C. M. Stoffelen, 2001: CMOD5, *SAF/OSI/KNMI/TEC/TN/140*, EUMETSAT.

Haan, S. de, and A. C. M. Stoffelen, 2001: Ice Discrimination using ERS scatterometer, *SAF/OSI/KNMI/TEC/TN/120*, EUMETSAT.

Marseille, G. J., and A. C. M. Stoffelen, and F. Bouttier, and C. Cardinali, and S. de Haan, and D. Vasiljevic, 2000: Impact Assessment of a Doppler Wind Lidar in Space on Atmospheric Analyses and Numerical Weather Prediction, *Technical report*, KNMI, KNMI report in respons to ESA study.

Stoffelen, A. C. M., and S. de Haan, and Y. Quilfen, and H. Schyberg, 2000: ERS Scatterometer Ambiguity Removal Scheme Comparison, *OSI SAF*, EUMETSAT.

POPULAR SCIENTIFIC

Haan, S. de, en S. J. M. Barlag 2002: De Toegevoegde Waarde van GPS-Waterdamp voor de Weersvoorspelling: een voorbeeld *Meteorologica*, **11**(1) (in Dutch)

Curriculum Vitae

Siebren de Haan is geboren op 5 juni 1968 in Enschede. Het VWO-diploma behaalde hij in 1986 aan Het Drachtster Lyceum te Drachten, waarna met de studie Wiskunde aan de Rijks Universiteit Groningen werd begonnen. Tijdens de studie heeft een Erasmus-beurs het mogelijk gemaakt om, in 1991, vijf maanden aan het Nonlinear Systems Laboratory van University of Warwick te studeren. Na het afstuderen in 1992 wachtte de dienstplicht welke werd vervangen door werkzaamheden aan de vakgroep Econometrie van de RUG. In 1995 werd de opleiding tot eerstegraads wiskundeleraar met succes afgesloten, maar voor een carrière als leraar werd niet gekozen. In plaats daarvan ging hij aan de slag als tweejarig aio bij de groep “Wiskunde voor de Industrie” aan de Technische Universiteit Eindhoven. Na deze opleiding werd hij op 1 april 1998 aangesteld op het KNMI als projectmedewerker bij de afdeling “Satelliet Data”. In deze functie heeft hij op verschillende terreinen gewerkt: zeewatertemperatuur, wind uit satellieten, zee-ijsdetectie en (“space-borne” en “ground-based”) GPS. Dit laatste onderwerp heeft hij uit kunnen bouwen tot het proefschrift dat u nu in uw handen heeft.

Acknowledgement

Part of the research presented in this thesis is funded by the Netherlands Institute for Space Research (SRON, project EO-050) and the Netherlands Agency for Aerospace Programmes (NIVR, project GO-53517KN). The remaining part is sponsored by the Royal Netherlands Meteorological Institute (KNMI). I would like to thank my GPS colleagues who helped me to understand how GPS and the atmosphere are related. First of all I am Jan Douša (GOP) very grateful for providing me with basic near real-time processing scheme, which formed the starting point of the current processing scheme implemented at KNMI. I thank Andre van der Hoeven (DEOS, DUT) for processing the GPS data in Fig. 3.2 with GIPSY and for providing the least-squares residuals from GIPSY used in Chapter 7. The organisers and participants of the BBC2 campaign are also thanked for kindly providing access to their radiosonde data. All participants in the COST716, TOUGH and E-GVAP projects are thanked for the discussions and organising the workgroup meetings (and of course the social events!). Especially Henrik Vedel (DMI) and Jonathan Jones (UKMetOffice) are thanked for the joined effort to establish an operational GPS observation system within E-GVAP. Processing GPS data for meteorology is not possible without raw GPS data from distant GPS stations and IGS satellite orbits; the anonymous GPS data providers are kindly thanked for the use of their data. The BKG-NTRIP group is thanked for providing streaming-software to collect *real* real-time GPS data. Mark Greaves from the Ordnance Survey (UK) is thanked for providing GPS data in 15 minutes batches for the South England region, such that the region of the real time water vapour map could be extended to the west.